Traditional and Novel Approaches in Ångstchemistry: A Step into Postmodernism

by

Anton Oliynyk

A thesis submitted in partial fulfillment of the requirements for the degree of

Doctor of Philosophy

Department of Chemistry
University of Alberta

Abstract

This thesis focuses on the experimental and theoretical study of various rare-earth transition-metal germanides that contain three or four components. Ternary and quaternary germanides were synthesized through various methods, including direct reaction of the elements, arc-melting, and flux growth. Several new series – $RE_4M_2InGe_4$, RE_4MInGe_4, $RE_3M_2Ge_3$, $RE_{2+x}MnGe_{2+y}$ – were identified which contain characteristic structural motifs in common. These motifs can then be regarded as design elements to derive new structures. The crystal structures of these compounds contain many types of building units, leading to diverse physical properties (electrical and thermal transport, magnetic properties) amenable to a broad array of materials applications. For example, the complex structures of some germanides give rise to surprisingly low thermal conductivity, suitable for thermoelectric materials, and the interaction of f-electrons on rare-earth atoms with d-electrons on transition-metal atoms generates interesting magnetic behaviour.

To guide experimental attempts to thinking "outside of the box," data-driven machine-learning tools have been applied to identify new germanides, and to predict their likelihood to display favourable thermoelectric properties. A recommendation engine was first tested on a previously known intermetallic compound, $Gd_{12}Co_5Bi$, which was suggested to be a counterintuitive candidate for thermoelectric materials. Property measurements on this compound revealed promising performance and suggested that this may be a member of a new class of thermoelectric materials. This approach was then extended to find new germanides with low thermal conductivity (<10 mW/K), which is

highly unusual for intermetallic compounds. The total thermal conductivities vary from ~20 to <2 mW/K, which are unprecedentedly low for unoptimized and metallic compounds (cf., typical values for thermal conductivity for metals are ~100 mW/K).

Prediction of crystal structures and physical properties is still an unsolved problem. To address this challenge, the machine-learning strategies described above have been complemented with statistical methods (principal component analysis, support vector machines) and applied to simple binary intermetallics as well as more complex ones (Heusler phases and equiatomic ternary phases). This approach may greatly accelerate the search for new materials and minimizes the risks in exploratory synthesis.

Preface

This thesis summarizes the research that I have performed within the Mar research group in the Department of Chemistry at the University of Alberta, from January 2012 to May 2016. My contributions are described in detail within the thesis and are briefly summarized below.

Chapter 2 of this thesis has been published as Oliynyk, A. O.; Stoyko, S. S.; Mar, A. "Ternary rare-earth ruthenium and iridium germanides $RE_3M_2Ge_3$ (*RE* = Y, Gd–Tm, Lu; *M* = Ru,Ir)," *J. Solid State Chem.* **2013**, *202*, 241–249. My contribution to this study includes synthesis, data collection, analysis, characterization, and preparing the draft for the manuscript. S. Stoyko assisted with synthesis and characterization, and A. Mar, the supervisory author, was involved in manuscript composition and submission process.

Chapter 3 of this thesis has been published as Oliynyk, A. O.; Djama-Kayad, K.; Mar, A. "Ternary rare-earth manganese germanides $RE_3Mn_2Ge_3$ (*RE* = Ce–Nd) and a possible oxygen-interstitial derivative $Nd_4Mn_2Ge_5O_{0.6}$," *J. Alloys Compd.* **2014**, *602*, 130–134. My contribution to this study includes synthesis, data collection, analysis, characterization, and preparing the draft for the manuscript. K. Djama-Kayad assisted with synthesis, and A. Mar, the supervisory author, was involved in manuscript composition and submission process.

Chapter 4 of this thesis has been published as Oliynyk, A. O.; Mar, A. "Rare-earth manganese germanides $RE_{2+x}MnGe_{2+y}$ (*RE* = La, Ce) built from four-membered rings and *stellae quadrangulae* of Mn-centred tetrahedra," *J. Solid State Chem.* **2013**, *206*, 60–65. My contribution to this study includes synthesis, data collection, analysis,

characterization, and preparing the draft for the manuscript. A. Mar, the supervisory author, was involved in manuscript composition and submission process.

Chapter 5 of this thesis has been published as Oliynyk, A. O.; Djama-Kayad, K.; Mar, A. "Investigation of phase equilibria in the quaternary Ce–Mn–In–Ge system and isothermal sections of the boundary ternary systems at 800 °C," *J. Alloys Compd.* **2015**, *622*, 837–841. My contribution to this study includes synthesis, data collection, analysis, characterization, and preparing the draft for the manuscript. K. Djama-Kayad assisted with synthesis, and A. Mar, the supervisory author, was involved in manuscript composition and submission process.

Chapter 6 of this thesis has been published as Oliynyk, A. O.; Stoyko, S. S.; Mar, A. "Quaternary Germanides $RE_4Mn_2InGe_4$ (*RE* = La, Nd, Sm, Gd–Tm, Lu)," *Inorg. Chem.* **2013**, *52*, 8264–8271. My contribution to this study includes synthesis, data collection, analysis, characterization, and preparing the draft for the manuscript. S. Stoyko assisted with synthesis and characterization, and A. Mar, the supervisory author, was involved in manuscript composition and submission process.

Chapter 7 of this thesis has been published as Oliynyk, A. O.; Stoyko, S. S.; Mar, A. "Many Metals Make the Cut: Quaternary Rare-Earth Germanides $RE_4M_2InGe_4$ (*M* = Fe, Co, Ni, Ru, Rh, Ir) and $RE_4RhInGe_4$ Derived from Excision of Slabs in RE_2InGe_2," *Inorg. Chem.* **2015**, *54*, 2780–2792. My contribution to this study includes synthesis, data collection, analysis, characterization, and preparing the draft for the manuscript. S. Stoyko assisted with synthesis and characterization, and A. Mar, the supervisory author, was involved in manuscript composition and submission process.

Chapter 8 of this thesis has been published as Gaultois, M. W.; Oliynyk, A. O; Mulholland, G. J.; Mar, A.; Sparks, T. D.; Meredig, B. "A Recommendation Engine for Suggesting Unexpected Thermoelectric Chemistries, with Experimental Validation", arXiv:1502.07635v1. The manuscript has been submitted to APL Materials. My contribution to this study includes structural experimental section data collection and characterization. A. Mar and M. W. Gaultois were involved in manuscript writing. T. D. Sparks was responsible for thermoelectric property characterization. G. J. Mulholland and B. Meredig developed and described the recommendation engine. Also the following publication was an invited review article that summarizes possible applications of the recommendation engine: Sparks, T. D.; Gaultois, M. W.; Oliynyk, A. O.; Brgoch, J.; Meredig, B. "Data mining our way to the next generation of thermoelectrics" *Scr. Mater.* 2016, 111, 10–15. My contribution to this study includes writing the section about directing the exploration of intermetallic phase space. All other sections are written by M. W. Gaultois, T. D. Sparks, J. Brgoch, and B. Meredig.

Chapter 9 of this thesis has been submitted to *Chem. Mater.* as Oliynyk, A. O.; Antono, E.; Sparks, T. D., Ghadbeigi, L.; Gaultois, M. W.; Meredig, B.; Mar, A. "Deceptively Simple and Endlessly Complicated: Machine Learning Prediction and Experimental Confirmation of Novel Heusler Compounds." My contribution to this study includes data extraction, synthesis and characterization, preparing the draft, and the original idea of structure predictor. L. Ghadbeigi and T. D. Sparks did thermal conductivity characterization and analysis. E. Antono, B. Meredig, and M. W. Gaultois contributed to the development of machine learning algorithm. A. Mar edited, composed, and submitted the manuscript.

Chapter 10 of this thesis has been submitted to *Chem. Mater.* as Oliynyk, A. O.; Adutwum, L. A.; Harynuk, J. J., Mar, A. "Classifying Crystal Structures of Binary Compounds AB through Cluster Resolution Feature Selection and Support Vector Machine Analysis." My contribution to this study includes data extraction, synthesis and characterization, preparing the draft, and the original idea of structure predictor. L. A. Adutwum contributed by running machine-learning algorithms and writing technical details about the computational methods. J. J. Harynuk and A. Mar edited the manuscript. A. Mar held the submission process.

Ångstchemistry [æŋ(k)stˈkɛm.ɪ.stri]: *noun*

1. The synthesis, analysis, and characterization of chemical compounds at the Ångström scale.
2. The branch of chemistry that evokes irrational fear and anxiety, unlike 10 Å-scale chemistry.

Acknowledgements

I would want to express my sincere gratitude to Prof. Arthur Mar, my supervisor, teacher, and mentor. He is the one who inspired me, guided, and assisted through my studies at University of Alberta. I am so glad to have such a wise, hard-working, and understanding supervisor. Arthur is responsible for setting up a desire for studies in my heart, making me feel that I want to do nothing else but research for the rest of my life. Being a true researcher and incredible scientist, Arthur inspires every student in his research group.

I am also obligated to the infinite list of collaborators that helped me with their scientific and personal support. I wish to express my gratitude to Dr. Norman Gee, my teaching assistant coordinator. I really appreciate his mentoring which helped me to develop my teaching skills. I am also thankful to all my groupmates – Brent, Stanislav, Krishna, Mansura, Abishek, Xinsong, and Wenlong. I would want to thank the faculty and staff in the Chemistry Department. Special thanks go to my committee members – Dr. Steven Bergens and Dr. Alex Brown, who agreed readily to be my exam committee members starting in my first year of studies, and Dr. Eric Rivard and Dr. Vadim Kravchinsky for their assistance at my candidacy exam.

I also wish to acknowledge my parents and family members. Probably there is no need to say that without them I couldn't accomplish even a single thing in my studies. They have supported me from the first days of my life, have been around when I failed and succeeded. I hope that they are proud of me, since I am truly their accomplishment.

The research was funded by the University of Alberta, the Natural Sciences and Engineering Research Council of Canada, NSERC CREATE-IRTG ATUMS.

Well, I am quite sure that I forgot to mention everyone on this acknowledgement page, but be sure that I am very thankful to every person I have met in my life, especially you, my dear reader.

Table of Contents

List of Tables

List of Figures

List of Symbols and Abbreviations

α	Thermal diffusivity
θ	Angle of reflection; Take-off angle
κ	Thermal conductivity
λ	Wavelength; Inelastic mean free path
ρ	Density
χ	Electronegativity; Magnetic susceptibility
μ	Absorption coefficient
μ_{eff}	Effective magnetic moment
1D	One dimensional
2D	Two dimensional
3D	Three dimensional
$a\ b\ c\ \alpha\ \beta\ \gamma$	Unit cell parameters
AFM	Antiferromagnetism
APS	Advanced Photon Source
ASA	Atomic sphere approximation
C_p	Heat capacity
COHP	Crystal orbital Hamilton population
COOP	Crystal orbital overlap population
CVT	Chemical Vapour Transport
CW	Curie-Weiss
d_{hkl}	d- spacing
DFT	Density functional theory
DOS	Density of states
DSC	Differential scanning calorimetry

e^-	Electron
E_F	Fermi level
EDX	Energy dispersive X-ray analysis
FC	Field-cooled
FM	Ferromagnetism
FWHM	Full-width-at-half-maximum
H	Magnetic field
hkl	Miller indices
IR	Infrared
j	Angular momentum
k	Wave vector
l	Orbital angular momentum
LDA	Local density approximation
LMTO	Linear muffin-tin orbital
M	Magnetization; Metal
n	Principal quantum number; Number of valence electrons
PCA	Principal component analysis
PM	Paramagnetism
PPMS	Physical property measurement system
r_{cov}	Covalent radius
RE	Rare-earth
SEM	Scanning electron microscope
SVM	Support vector machine
T	Temperature; Lattice translations
T_c	Critical temperature; Curie temperature

T_N	Néel temperature
TB	Tight-binding
TM	Transition metal
TM-DSC	Temperature modulated differential scanning calorimetry
V	Cell volume; applied voltage
XRD	X-ray diffraction
Z	Atomic number; nuclear charge
Z_{eff}	Effective nuclear charge

Chapter 1

Introduction

1.1 Intermetallics and germanides

Compounds formed by metals or metalloids are called intermetallic compounds (or colloquially, intermetallics). Typically a mixture of metallic phases or solid solution of metals is called an alloy. But the term "intermetallics" is used to describe a compound with definite crystal structure and stoichiometry. The history of mankind and the development of our civilizations were highly dependent on metals, and even the latest discoveries would not be possible without metals.[1] It all started with gold used for jewelry around 8000 years ago. Later, around 6000 years back, use of copper and silver dominated over the use of polished stones and flint axes. It is not surprising that metal tools were highly appreciated by people of the most developed empires, from Roman to Chinese. Even some material design ages are now associated with the time when some metals and their alloys were discovered, like Bronze Age (discovery of copper, 3300–1200 BC, depending on region) or Iron Age (1200–200 BC, depending on region). Even now, space shuttles, rocket science, synchrotrons, and everyday electronics could not function without metals. Also, not so many of material classes are to be intuitively trusted in our everyday life. Maybe, only ceramics and intermetallics are honoured to have the "safest" reputation when we talk about chemicals. Intermetallics are familiar to us from an early age: metal tools, electronics, medical equipment, musical instruments, heaters, refrigerators, cellphones, and computers, and so on. The exciting properties of

metals and their compounds depend on their structures and the nature of the chemical bonding within. Metallic bonding involves a delocalized sea of valence electrons to which the positively charged incores are attracted. However, the actual bonding that occurs within intermetallic compounds often contains a combination of ionic, covalent, and metallic interactions.[2]

The definition of intermetallics is often extended to include not only metals, but also metalloids, such as boron, silicon, germanium, arsenic, antimony, tellurium, and polonium. This study will focus mostly on the solid-state chemistry of germanides. Germanium, a critical and strategic metalloid, and its compounds have been used as the first transistors in electronics and as optical glass in infrared night-vision systems.[3,4] However, the full potential of germanides has not yet been reached. Recent studies suggest that solid-state germanides could be used in: (1) thermoelectric materials (e.g., $RE_3M_4Ge_3$), which convert a temperature difference into electric voltage, which can be used for energy harvesting,[5,6] (2) magnetocaloric materials (e.g., $GdRu_2Ge_2$), which are used in fluid-free refrigerators that can attain extremely low (milliKelvin) temperatures,[7] and (3) superconducting compounds (e.g., $RE_2Ir_3Ge_5$), allowing resistanceless flow of electricity and magnetic levitation (e.g. Maglev trains).[8,9] Despite this potential, there is no clear understanding of how these properties can be improved by modifying the structures and compositions of these germanides, largely because the chemistry of germanides is not well developed.

1.2 Synthesis of intermetallic phases

A major problem in synthesizing intermetallics is that in order for the component metals to react, the atoms have to overcome significant kinetic barriers for diffusion, which requires quite high temperatures. To avoid reaction with oxygen, an inert atmosphere is essential. Several methods are appropriate for the synthesis of germanides (Figure 1-1).[10]

The most straightforward method is to react the elements directly followed by sintering to ensure sample homogeneity.[11] Typically, the reactants are finely ground to small pieces or powders in order to maximize surface area. The mixture can be pressed into a pellet to promote better contact between reactant particles. The choice of an appropriate container is crucial and depends on its reactivity with the components. Except for certain rare-earth metals (Eu, Yb), fused silica tubes are compatible with a mixture of rare-earth metals, transition metals, and germanium. When more active metals are present (e.g., alkali and alkaline-earth metals), alumina crucibles or welded niobium or tantalum tubing can be used. In either case, the tube must be evacuated. The reactants are then heated to promote diffusion. A high temperature is desirable but this is limited by the softening point of the container (~1200 °C for fused silica). Furthermore, to avoid volatilization losses, the heating may need to be done gradually. To improve phase purity, the heat treatment may be repeated several times. Sintering of solids normally requires a long time (several days to as much as months), so increasing the temperature to attain a melt can accelerate reactions.

Although melting can certainly be achieved in a standard furnace, an attractive method is use of an electric arc furnace.[12] Here, an electric arc is generated by a high

potential within an inert atmosphere and is directed toward the reactants to melt them almost instantaneously (i.e., within a few seconds). To remove all traces of oxygen within the chamber, a Ti ingot which is first melted acts as a getter. (The colour of the Ti ingot changes due to the formation of suboxides.) The sample is flipped over and the melting is repeated to ensure homogeneity. The arc-melted ingot is then placed within an evacuated tube and annealed within a normal high temperature furnace to attain equilibrium. The annealed ingot is removed from the furnace and quenched in cold water. This method is the standard procedure for establishing phase equilibria at a specified temperature to construct phase diagrams systematically and to rapidly identify new phases. Arc melting works well for components that do not volatilize readily. However, slightly volatile elements (like Mn or Bi) can still be used if a small excess is added to compensate for the loss. Lastly, arc melting is generally not a good method for obtaining single crystals, although in fortuitous cases, small crystals can sometimes be found within an ingot.

Because all the components used are metals, an attractive method for melting is induction heating, in which an electrically conducting sample can be rapidly heated by a high frequency alternating current generated by electromagnetic induction.[13] The major advantage is that this is a non-contact method and does not require use of a crucible. Although a very high temperature can be attained, it cannot be controlled directly. The temperature can be measured optically through a pyrometer but the readings are not very accurate and can deviate widely.

All these synthetic methods can yield single crystals if luck prevails but they are not specifically designed to promote crystal growth. The most straightforward method to

obtain single crystals is simply to cool slowly from the melt. However, more specialized methods can be applied to grow large single crystals, when these are needed. Use of a flux (a high temperature solvent) involves addition of large quantities of a substance with a low melting temperature.[14] A flux can be many types of chemical substances but for intermetallic reactions, low melting metals (Al, Ga, In, Sn, Pb, Bi, or Hg) are often used. Moreover, an excess of one reacting component can act as a self-flux. In the heat treatment, the temperature is increased to above the melting point of the flux. Then, as the sample is slowly cooled, crystals form through spontaneous nucleation and precipitation. While the sample is molten any crystals that are formed can be separated from the flux by centrifugation. Because the flux method operates under non-equilibrium conditions, the disadvantages are that there is a high risk of non-reproducibility, metastable phases are sometimes formed, and the composition of the final product cannot be directly controlled. The surface of crystals obtained may need to be cleaned to remove residual flux, usually by treatment with dilute acid (e.g., HCl or acetic acid) for sufficient time to clean but not etch the crystals.

Chemical vapour transport is an interesting crystal growth method involving gas-phase intermediates.[15] A small amount of a vapour transport agent (e.g., few mg of I_2) is added to the reaction mixture in the container. When a temperature gradient is applied in the furnace, the transport agent participates in gas-phase reactions which are reversible and eventually leads to deposition of crystals at the opposite side of the tube. The important criterion is that the gas-phase reactions are close to equilibrium conditions, but what the optimum temperatures are have to be determined by trial-and-error. Often the natural temperature deviations in the furnace are sufficient to promote crystal growth.

This method is suitable for recrystallizing an already synthesized material and is probably a better choice than flux growth.

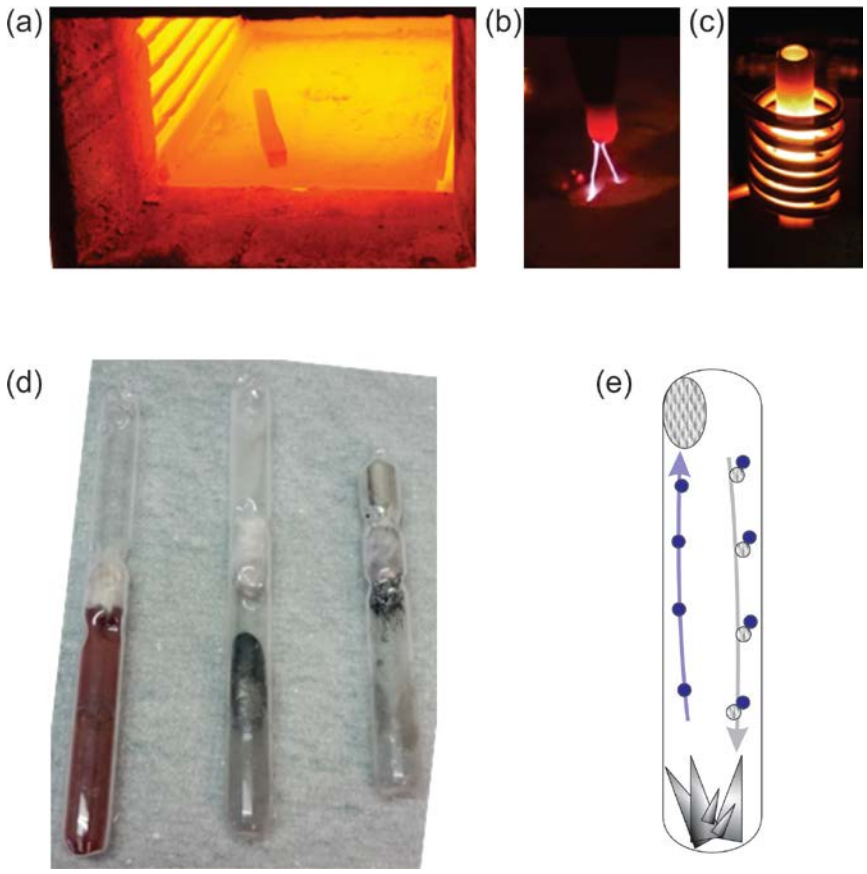

Figure 1-1 Synthesis of intermetallic phases: (a) sintering, (b) arc-melting, (c) induction heating, (d) flux growth, (e) chemical vapour transport.

Depending on the purpose intended for the synthesized material, the means of characterization, and the nature of the reactants, intermetallics can be prepared in various ways. The two most commonly used methods in this thesis are sintering and arc-melting because they are simple, reliable, reproducible, and fast; they satisfy the purpose of investigating new germanides and systematically studying ternary and quaternary intermetallics.

1.3 X-ray diffraction methods

Since the time when X-rays were first discovered, many techniques have now been developed to exploit this wonderful radiation. The unique property of this radiation is its wavelength, which is comparable to atomic length scales and can be used to explore the Ångström world (Figure 1-2). Only hard X-rays have practical application, whereas soft X-rays are usually absorbed, even in air. Hard X-rays are widely used in medical diagnostics and security screening, as well as in scientific investigations. The wavelength from 2 to 0.3 Å is typically used for diffraction methods.

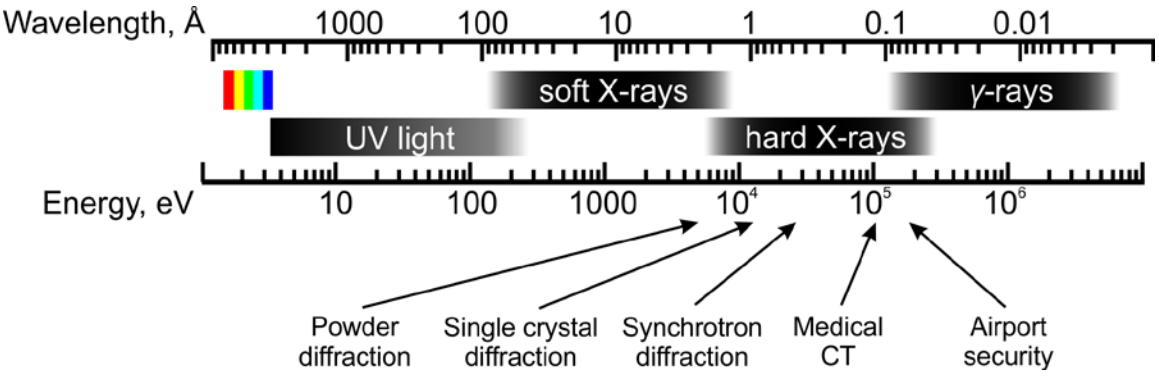

Figure 1-2 X-ray wavelength and its application.

X-ray diffraction[16,17] is a non-destructive technique to extract information about atomic arrangement and crystal structure within a material in a form of a single crystal or polycrystalline sample (Figure 1-3). In contrast to spectroscopic techniques, which detect absorbed or emitted radiation due to transitions between energy levels, diffraction methods detect the direction and intensity of elastically scattered radiation. The

directions of scattered radiation are related to where the atoms are located and their intensities to what kind of atoms are there.

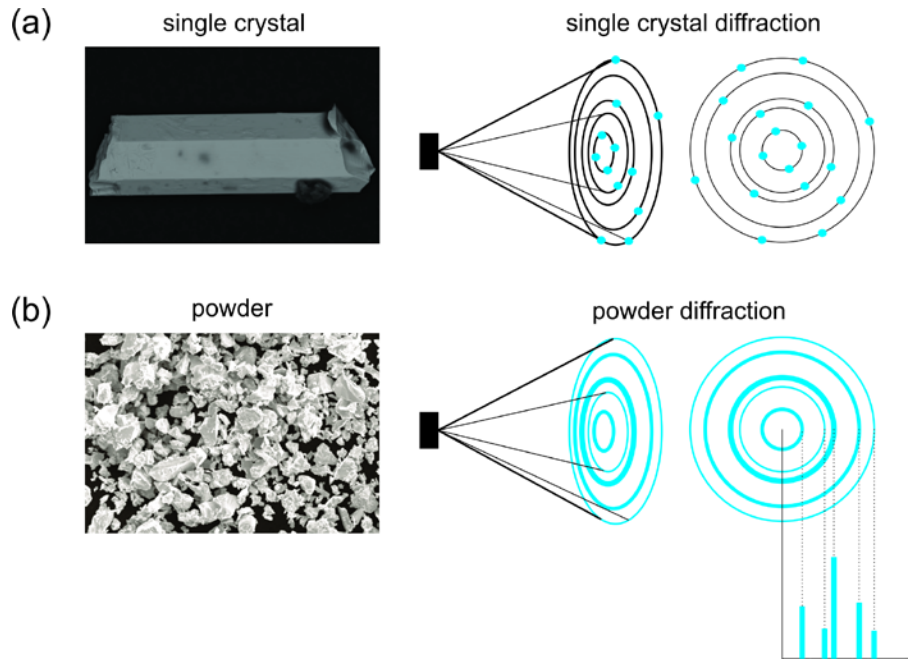

Figure 1-3 X-ray diffraction methods: (a) single crystal diffraction, (b) powder diffraction.

A powder sample consists of many small crystallites, each of which could be used for a single crystal experiment, except that they are oriented randomly. The X-ray diffraction pattern of a powder is a one-dimensional projection of many scattered X-rays which would normally be resolved in three-dimensional space for a single crystal. Powder and single crystal X-ray diffraction can both be used to identify the structure of a sample but the detailed atomic arrangement is easiest to deduce from single crystal data.

X-rays are a form of electromagnetic radiation with high energies and short wavelengths. They are produced when electrons accelerated by an electric potential strike a metal target (e.g., Cu, Ag, Mo, Fe). The X-ray spectrum consists of a continuum of white radiation, caused by inelastic collisions, superimposed by a few highly intense

characteristic lines, caused by elastic collisions (Figure 1-4). The characteristic lines are generated when electrons from core levels are ejected and higher energy electrons descend into the hole; this electronic transition is accompanied by emission of X-rays with specific wavelengths.

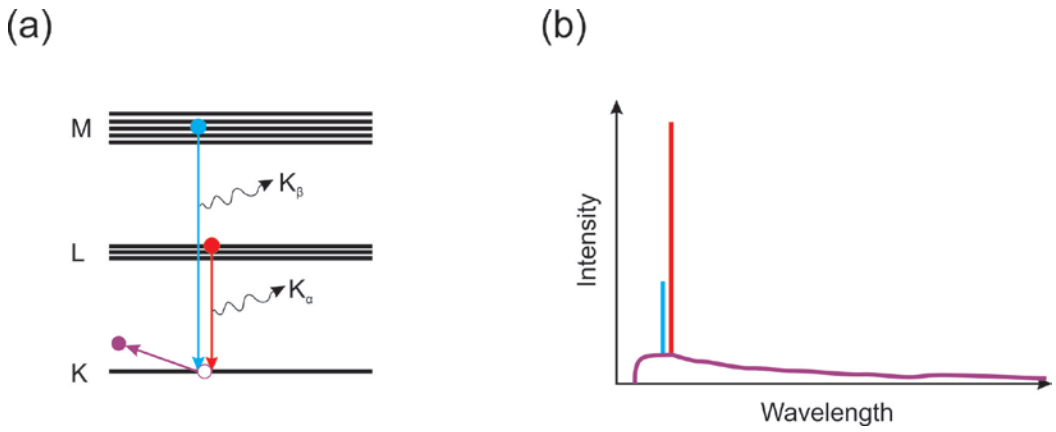

Figure 1-4 Schematic representation of X-ray generation principle (a) and spectrum (b)

Highly monochromatic radiation is needed for the diffraction experiment. The characteristic lines are actually split into doublets ($K_{\alpha1}$, $K_{\alpha2}$) arising from spin-orbit coupling: electrons have slightly different energies on the same orbital (*n*, *l*, and *s* quantum numbers are the same, but *j* numbers are different). For powder diffraction, it is desirable to use only $K_{\alpha1}$ radiation obtained through monochromatization.

1.3.1 Single crystal diffraction

The best way to determine crystal structure is by single-crystal X-ray diffraction. A crystal consists of a periodic arrangement of atoms whose translational and point symmetry can be described in terms of a lattice (a set of points with the same environment around each point) and basis (a set of atoms located with respect to each lattice point). Lattice planes are a set of equally spaced parallel planes such that all

lattice points fall on some member plane. Every set of lattice planes is described by Miller indices (*hkl*) with neighbouring planes separated by a constant spacing (*d*).[16,17] Diffraction occurs when incident X-rays are scattered by these lattice planes and undergo constructive interference as can be analyzed by two equivalent approaches.

In 1912, Laue proposed that each line of atoms within a three dimensional array that is irradiated with an incident X-ray beam produces a cone of scattered X-rays according to a specific mathematical condition so that constructive interference occurs when these cones intercept.[18] Solution of the Laue equations gives the angles at which diffraction occurs for a given set of lattice planes (Figure 1-5a).

(a) Laue diffraction

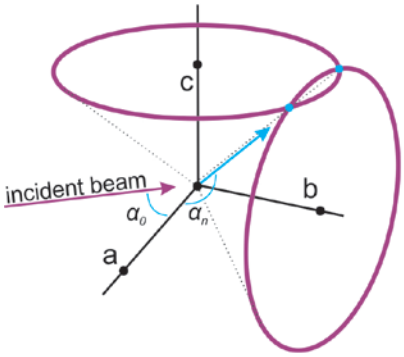

$$a \cdot (\cos\alpha_n - \cos\alpha_0) = n_x\lambda = h\lambda$$
$$b \cdot (\cos\beta_n - \cos\beta_0) = n_y\lambda = k\lambda$$
$$c \cdot (\cos\gamma_n - \cos\gamma_0) = n_z\lambda = l\lambda$$

a, b, c – distances between lattice points in three directions, α, β, γ – angles of incident beam and diffraction directions, n – diffraction order, λ – wavelength, h,k,l – Miller indices

(b) Bragg diffraction

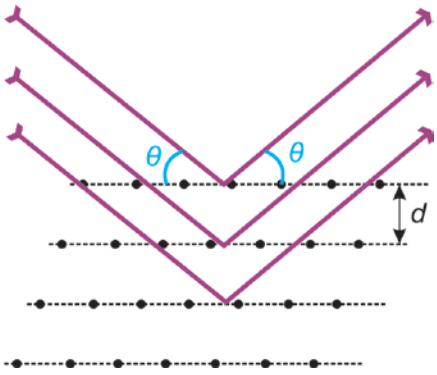

$$n\lambda = 2d\sin\theta$$

n – diffraction order, λ – wavelength, d – spacing, θ – diffraction angle

Figure 1-5 X-ray diffraction principle for (a) Laue diffraction and (b) Bragg diffraction.

In 1913, the Braggs (*père* and *fils*) proposed the diffraction phenomenon can be represented equivalently by reflection of X-rays by the lattice planes (Figure 1-5b).[19] Although physically dubious (because the X-rays are not really reflected, but rather scattered), the mathematical analysis is simpler.

The procedure for an X-ray diffraction experiment requires, above all else, a suitable crystal. The typical size of a crystal is between 0.1 to 0.01 mm, and depends on a compromise to maximize scattering intensity while minimizing absorption. The crystal is mounted on a glass fiber glued to a pin which is placed on a goniometer. A Bruker PLATFORM diffractometer was used, which was equipped with a SMART APEX II CCD area detector and a Mo Kα X-ray source. At different goniometer positions, frames of reflections are collected (Figure 1-6), usually for 10–15 seconds each, resulting in a dataset containing several thousand reflections indexed by *hkl*, in the form of their intensities I_{hkl} and direction cosines.

The intensity of a reflection *hkl* is the square of the structure factor F_{hkl}, which is function of the positions and scattering ability of atoms, as well as other parameters such as thermal displacements and site occupancies. A Fourier transform of the F_{hkl} gives the electron density, which is interpreted as the crystal structure. Unfortunately, because the phases of structure factors are experimentally unattainable ("the phase problem"), the electron density function cannot simply be calculated directly to obtain the crystal structure.[16] In practice, models are proposed or guessed through probablilistic methods for trial solutions and their calculated structure factors are compared with the observed ones. The structural models are refined until the calculated structure factors best agree with the observed structure factors. This is accomplished through a least-squares method,

in which the sum of the deviations between the squares of the calculated and observed intensities is minimized, as gauged by an agreement or residual factor (*R*-factor) and the goodness of fit. Modern crystal structures are typically refined to $R < 0.05$.[16]

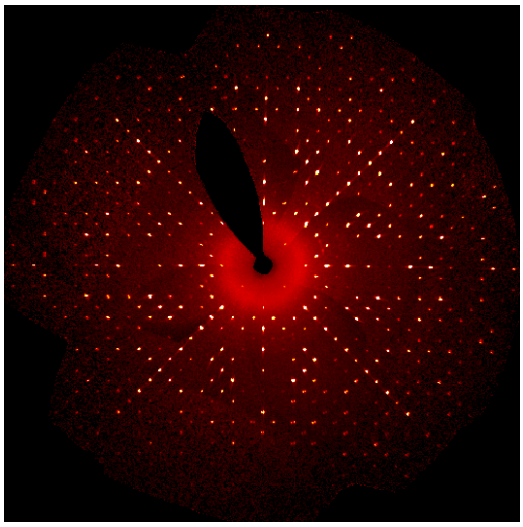

Figure 1-6 Typical image of reflections in reciprocal space collected on single crystal diffractometer.

1.3.2 Powder diffraction

X-ray diffraction on a powder sample proceeds from the same principles as above except that symmetry equivalent reflections (or those that coincidentally give rise to the same *d*-spacings) cannot be resolved and angular distribution is lost. The information contained in a powder X-ray diffraction pattern consists of the Bragg angles (2θ) and intensities of reflections (Figure 1-7).[20] The sample is ground finely into powder and rotated on a sample stage to ensure a random distribution of crystallite orientations. The experimental powder pattern is typically compared with a simulated one from a structural model.

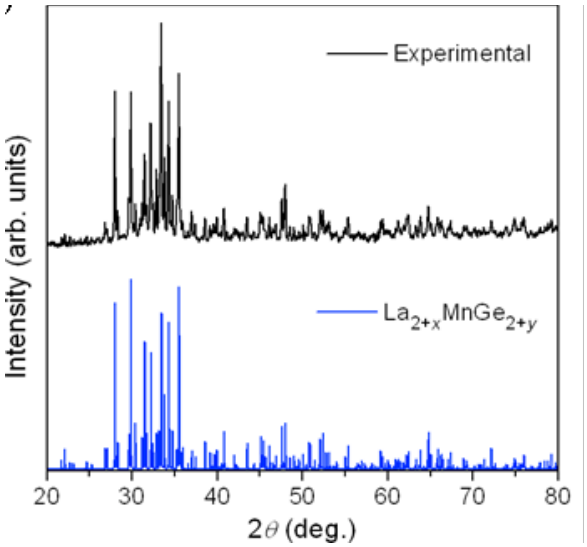

Figure 1-7 Typical powder diffraction pattern compared with simulated pattern.

The normal applications of powder diffraction are identifying phases and refining cell parameters. Other applications include checking crystallinity and determining particle sizes but they are not used here. An advanced application is to perform a structural refinement (Rietveld refinement).[21]

Powder X-ray diffraction is essential for constructing a phase diagram, which provides information about what phases are present under equilibrium conditions. Phase diagrams are valuable in chemistry, metallurgy, and physics, giving guidance about the best preparative conditions and the presence of possible secondary phases. A typical sample may contain many phases, the number of which is dictated by the Gibbs condensed phase rule (which applies when gases are not involved): $F = C - P + 2$, where F is the number of degrees of freedom (composition, temperature, pressure), C is the number of components, and P is the number of phases in thermodynamic equilibrium.[22] The relative abundance of phases present in a sample can be estimated by the peak intensities in the powder X-ray diffraction pattern. For example, in a three-component system at constant temperature and pressure, the maximum number of phases that can be

present in the sample is given by $2 = 3 - P + 2$, or $P = 3$. To illustrate, a portion of the Gd–Co–Bi phase diagram can be constructed by analyzing the powder X-ray diffraction patterns of different samples; sample 3 contains two phases ($Gd_{12}Co_5Bi$ and Gd_3Co) which establishes a tie-line in the phase diagram (Figure 1-8).[23]

(a)

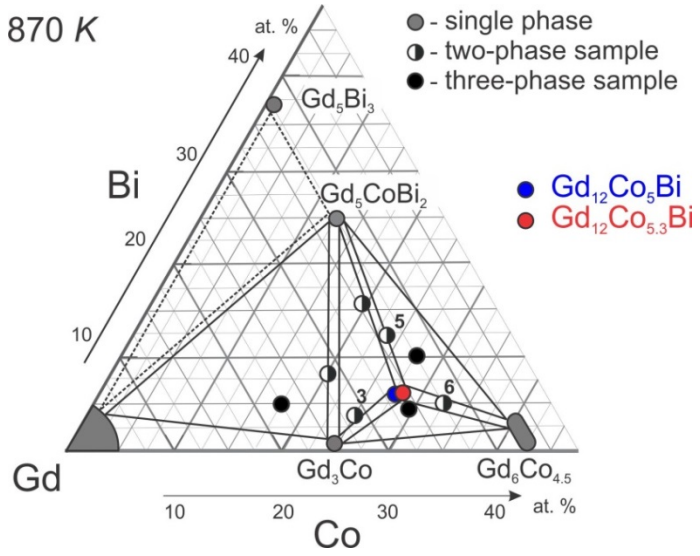

(b)

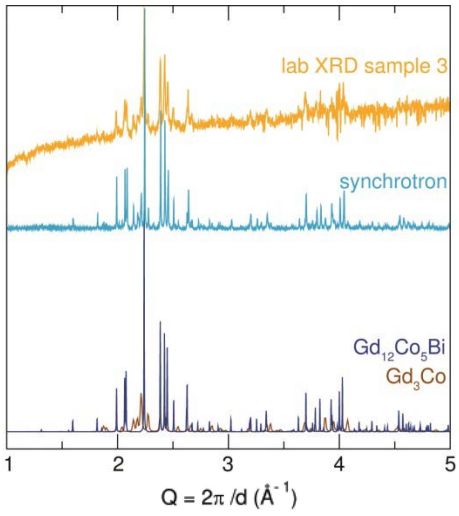

Figure 1-8 (a) Part of the Gd–Co–Bi ternary phase diagram. (b) Powder X-ray diffraction patterns for a two-phase sample, where experimental patterns are at the top, and simulated powder patters is at the bottom.

After phases are identified in a powder X-ray diffraction pattern, it is useful to refine their unit cell parameters. The experimental powder pattern for a given phase is fitted to a simulated one based on information about cell parameters, space group, and atomic coordinates; each peak must be correctly matched with the appropriate *hkl* indices, a procedure called indexing the powder pattern. However, because the unit cell only affects the peak positions and not their intensities, only the Bragg angles 2θ need to be measured accurately. This can be done by estimating the centre of each peak, or more systematically by fitting the peak profiles to well defined functions (e.g., pseudo-Voigt profile, a weighted Lorentzian/Gaussian peak shape), possibly modified by asymmetry effects. For example, a typical peak fitting routine in the WinCSD program suite is shown (Figure 1-9).[24]

(a)

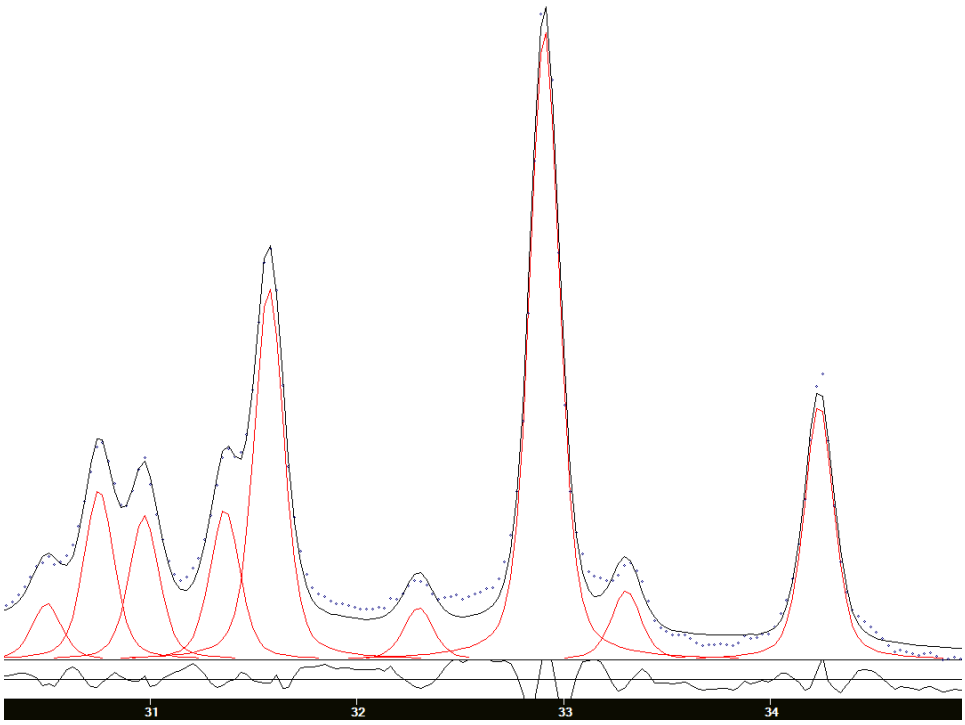

(b)

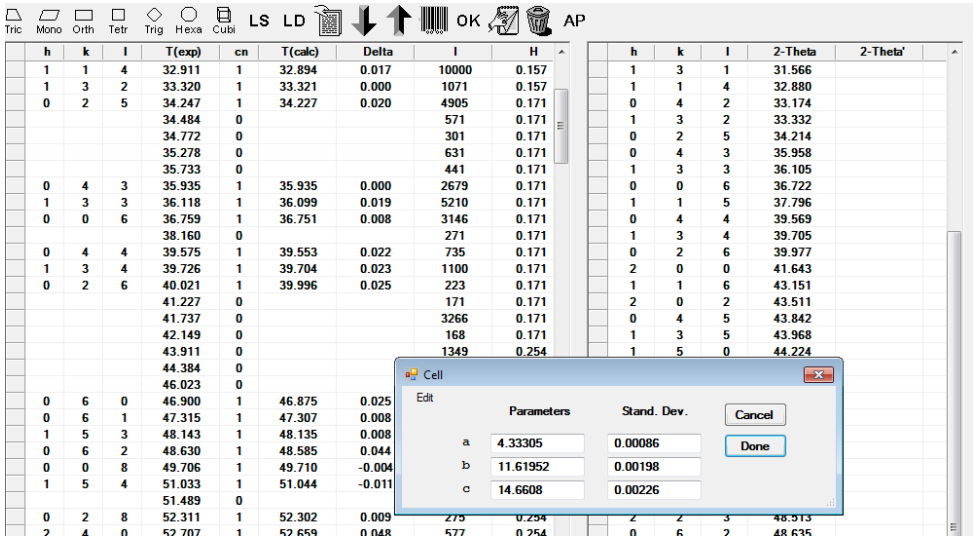

Figure 1-9 (a) Peak indexing: dotted line is the data from experiment, red lines represent individual peaks, solid black line shows a combined simulated diffraction pattern. (b) Cell parameter refinement in WinCSD environment.

From the peak profile fitting, the intensities of peaks can be determined by integrating their areas, which can be used to refine the structure further. In Rietveld refinement, various parameters such as background, peak profile, atomic positions, displacement parameters, and possibly others, are adjusted until the difference between calculated and experimental powder patterns is minimized.

Although powder diffraction is routinely performed with laboratory X-ray sources, occasionally synchrotron-based X-ray sources are exploited to overcome problems such as severe absorption or poor resolution. Synchrotron X-rays are highly intense sources that can offer tunable and highly monochromatic wavelengths, resulting in well resolved diffraction patterns with very low background. For example, the powder pattern for the two-phase sample examined earlier is much sharper and well resolved with synchrotron data (collected at 11BM-B at Argonne National Laboratory) than with laboratory based Cu Kα radiation (Figure 1-8b).

1.4 Scanning electron microscopy

Electron microscopy is useful in solid state studies for imaging; if X-ray spectroscopy is applied, chemical compositions can also be determined.[25] High spatial resolution down to tens of Ångströms is a big advantage over optical microscopy. The image is produced by detecting backscattered or secondary electrons emitted as a result of incident beam electrons interacting with a material (Figure 1-10). The instrument used here was a JEOL JSM-6010LA scanning electron microscope (SEM), typically with

accelerating voltage of 20 kV. The SEM images are examined to study surface morphology of samples and to identify impurities.

Three possible mechanisms can be exploited to identify the composition of a sample (Figure 1-10).

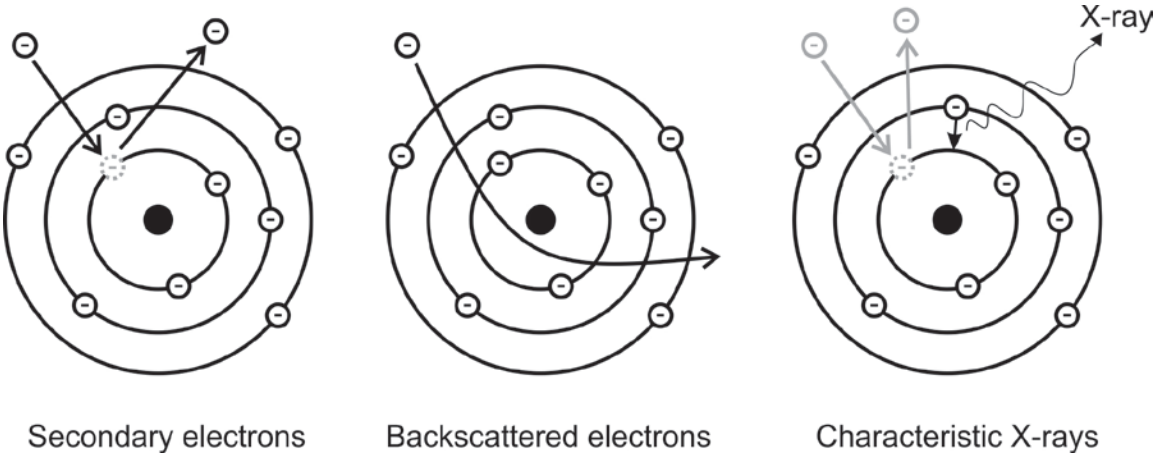

Figure 1-10 Secondary, backscattered electron, and characteristic X-ray phenomenon used for electron microscopy.

Secondary electrons are ejected when incident electrons undergo inelastic scattering and collide with atoms of the material. Backscattered electrons are deflected when elastic scattering occurs. Both depend on the type of atom but backscattered electrons are used to detect different phases and morphology in a sample because of better mass contrast (with phases containing heavier elements appearing lighter). This information is important for systematic study of phase diagrams by revealing the number, crystallinity, and composition of phases present, as illustrated by a three-phase Ce–Mn–Ge sample (Figure 1-11).

Characteristic X-rays are produced when the electron beam ejects core electrons from an atom in the material and the filling of the hole by higher level electrons is accompanied by emission of a wavelength of radiation specific to the element. A typical EDX spectrum contains many characteristic peaks belonging to different elements, the relative intensity of which is a measure of their amount in the sample (Figure 1-11).[26] The accuracy of EDX analysis can vary depending on the sample and possible peak overlaps, but is usually ~2 wt. % for a given element. For a complete phase analysis, EDX must be combined with XRD.

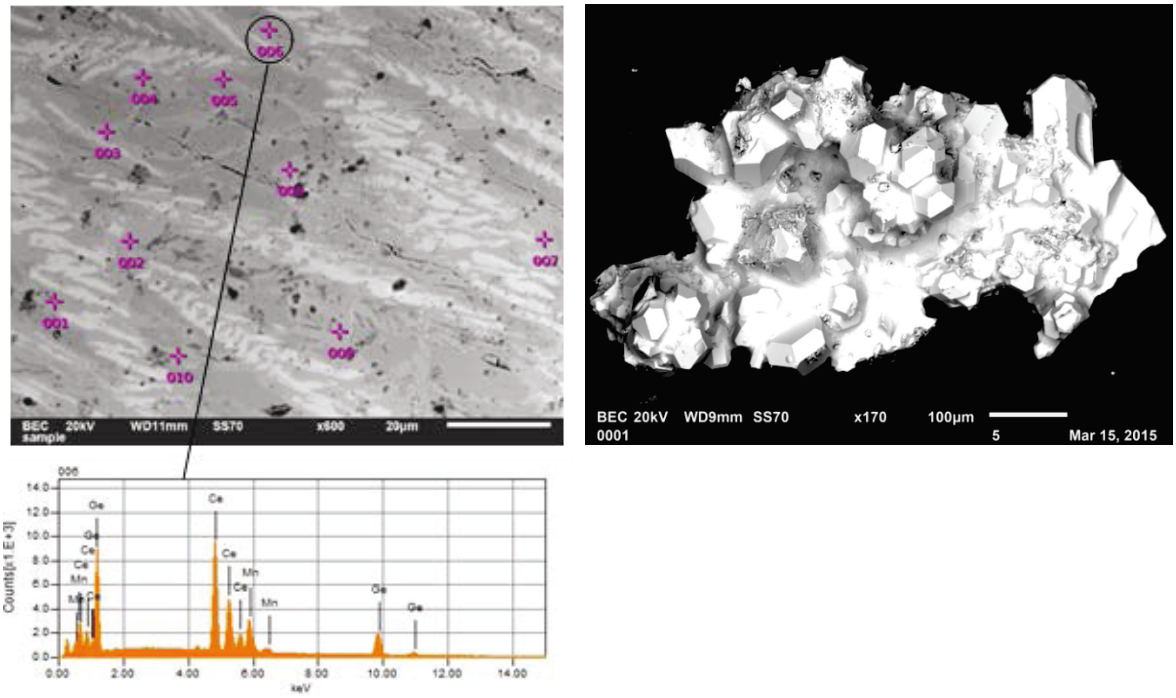

Figure 1-11 Backscattered electron image of polished multiphase sample (left) and crystal agglomeration (right). Energy dispersive spectrum for composition identification is shown in the bottom.

1.5 Band structure calculations

The electronic structure of a crystalline solid can be calculated from first principles (Schrödinger equation) to determine the total energy and to analyze the bonding between atoms.[27] In an extended solid, there are many energy levels so closely spaced that it is more convenient to represent them as energy continua called bands. A plot of the density of states shows the number of electronic states for a given energy interval (Figure 1-12).[28] These states are filled with electrons up to the Fermi level, which is often conveniently set to zero on the energy scale. There is no gap at Fermi level for a metal, a small gap for a semiconductor, and a large gap for an insulator. The density of states can be decomposed into orbital contributions of specified atoms to understand bonding interactions further.

In contrast to molecules, extended solids consist of a very large number of atoms, essentially infinite. However, because the atomic arrangement is periodic, it is sufficient to know the contents of the smallest repeat unit, or the unit cell. Similarly, the potential energy expressed in the Schrödinger equation is a periodic function. In a many-electron system, electron-electron interactions are equally important as nuclear-electron interactions. To overcome the difficult problem of specifying the numerous electron-electron interactions in a solid, density functional theory (DFT) offers a simplification in which one equation combines the Hartree potential, Coulomb potential of nuclei, and the exchange-correlation potential.[29] In other words, the problem involves treating electrons separately transforming into one-electron kind of system. As in molecular orbital calculations, the Bloch functions appearing in the Schrödinger equation for a solid

involve linear combinations of atomic orbitals. Symmetry operations are applied to further simplify the problem.

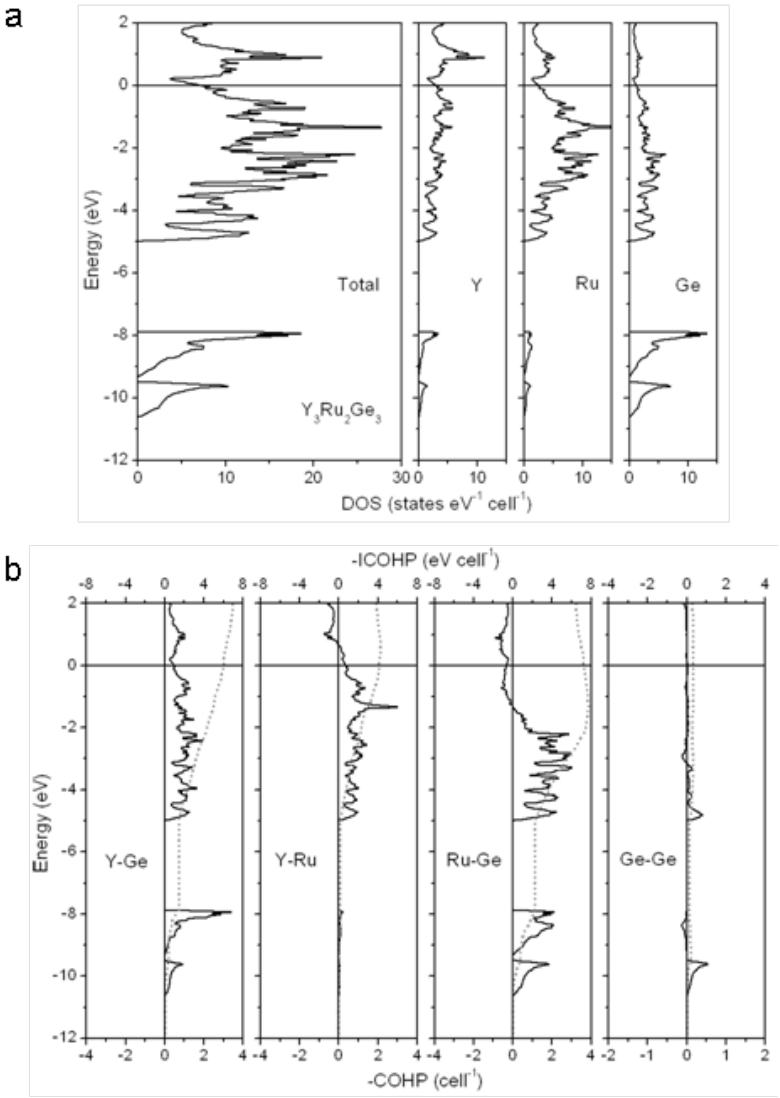

Figure 1-12 (a) Density of states and (b) Crystal Hamilton Population diagram for a typical extended solid – $Y_3Ru_2Ge_3$.

The calculations were performed with the tight-binding linear muffin-tin orbital (TB-LMTO) program package.[29] The potential energy function felt by the electrons, which becomes infinitely negative at locations of the positively charged ion cores, is truncated to a constant value within a sphere around the nuclei so that the shape of this

function resembles "muffin tins." To ensure that the potential energy function is continuous over all space, empty spheres with zero potential may need to be introduced. The atomic sphere approximation (ASA) and the local density approximation (LDA) are applied to describe exchange correlation energy. In addition to generating the density of states, the program can also be used to evaluate bonding interactions between specified atoms through their crystal orbital Hamilton population (COHP).[30] A plot of COHP reveals the bonding or antibonding nature of states, and the strength of interactions. With modern computational facilities, these calculations are now routine and subject to limitations in the maximum number of atoms treated. These calculations are helpful for rationalizing observed structures.

1.6 Physical properties

Measuring physical properties is essential to discovering potential applications of a synthesized material and to developing a fundamental understanding of structure-property relationships. Unusual behaviour can lead to design of new functional devices or to improvement of the performance of existing materials. Germanides have been implicated as potential magnetocaloric materials,[7] superconductors,[8,9] and thermoelectrics.[5,6] Most of the properties reported here were measured on a Quantum Design Physical Property Measuring System (PPMS).

1.6.1 Electrical transport

The electrical resistivity (or its inverse, electrical conductivity) provides information about the electronic structure of a solid. The absolute values of the resistivity reflect how well charge carriers move within the solid, and the temperature dependence of the resistivity reveals whether the sample is metallic or semiconducting (Figure 1-13).[28] Other information, such as defect concentrations and phase transitions, can also be inferred from the resistivity.

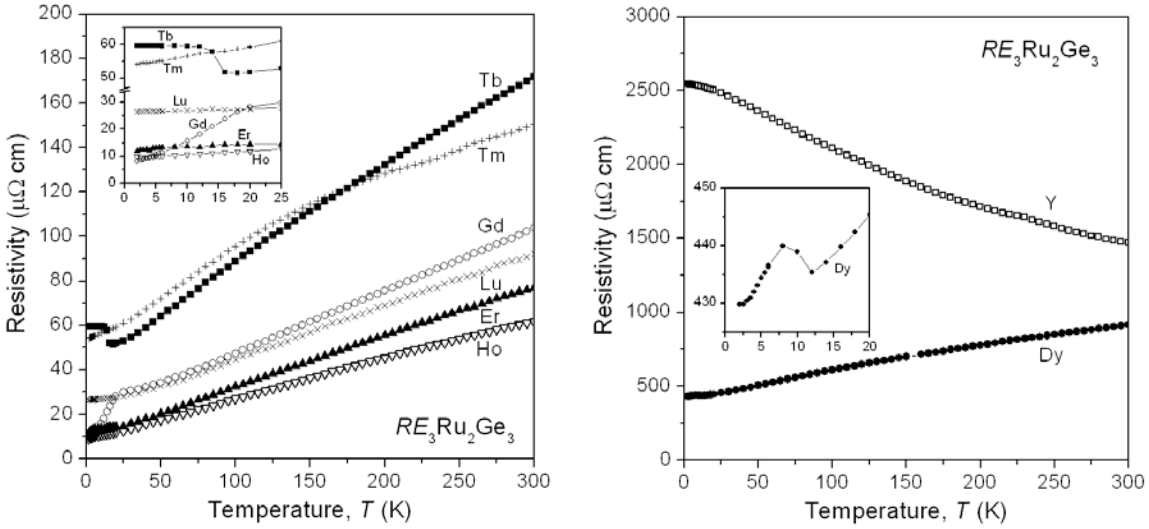

Figure 1-13 Electrical resistivity behaviour for $RE_3Ru_2Ge_3$ series of intermetallic germanide compounds. Left side shows a typical trend for metallic compounds, with various magnetic transitions at low temperature. Right side reveals semiconductor-like behaviour of $Y_3Ru_2Ge_3$ compared to metallic behaviour of $Dy_3Ru_2Ge_3$.

A typical setup for a resistivity measurement involves four probes, two at the extremeties to provide contacts for the flow of current (*I*-, *I*+) and two in the middle across which a potential difference (*V*+, *V*-) is measured. The size of the sample, which could be a single crystal or an ingot, can range from a few millimeters to 50 microns. These measurements were performed with the ac transport controller (Model 7100) on

the PPMS, with the current usually set at 100 μA and the frequency at 16 Hz, over a temperature range from 2 to 300 K.

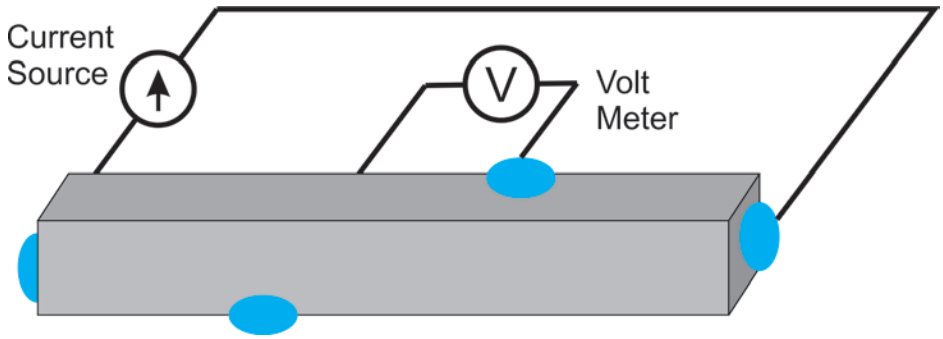

$$\rho = \frac{VS}{Il} \quad [\Omega\cdot\text{cm}]$$

ρ – Resistivity (Ω·cm)
l – Volt meter probe spacing (cm)
S – Cross section area of a sample (cm^2)
V – Voltage between the inner probes (V)
I – Current through the outer probes (A)

Figure 1-14 Correct probe placement on a sample for a four probe resistivity measurements.

Three possible types of behaviour (metallic, semiconducting, and superconducting) can be suggested by the temperature dependence of electrical resistivity; in special cases, transitions can occur between these types.[17] The electrical resistivity is inversely proportional to the concentration and mobility of charge carriers. In metals, the charge carriers are modeled as free electrons which experience zero potential and move freely within the solid. The concentration of free electrons is very high and their mobility is mainly affected by scattering with lattice vibrations (phonons). At higher temperatures, the enhanced vibrations reduce the mobility and the resistivity is higher. At lower temperatures, the resistivity is lower but reaches a limiting value

determined by defects. In semiconductors, the charge carriers are created by promotion through thermal activation from the valence to the conduction band, so that their concentration increases at higher temperature. Thus, the temperature dependence of the resistivity of a semiconductor is opposite that of a metal. In superconductors, the charge carriers are correlated electron pairs that move through the solid with no energy dissipation so that the resistance is zero (below the critical temperature, T_C). Above T_C, superconductors exhibit normal metallic behaviour.[17]

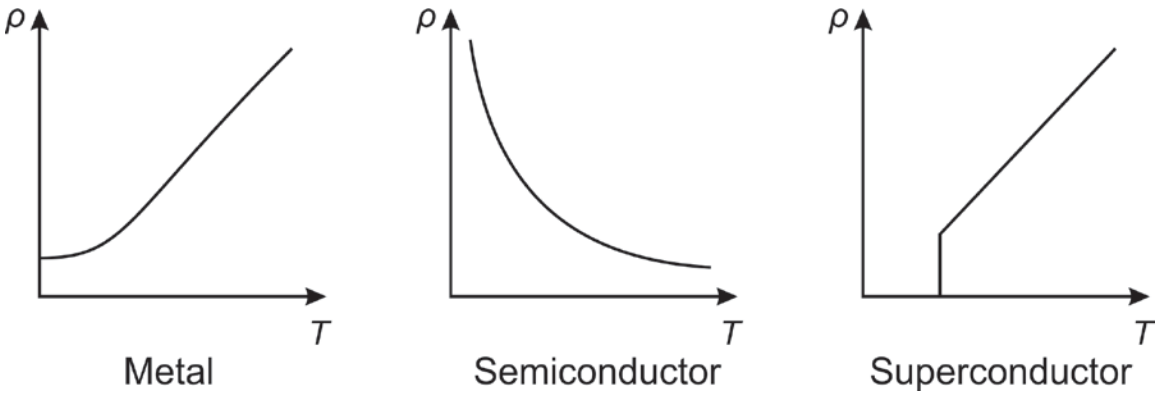

Figure 1-15 Resistivity as a function of temperature for metals, semiconductors, and superconductors.

1.6.2 Thermal conductivity

The thermal conductivity describes how well a material conducts heat. Heat sinks contain materials with high thermal conductivity to effectively transfer heat away (e.g., computer cooling, frying pan), and thermal insulators contain materials with low thermal conductivity to minimize heat conduction (e.g., clothing, spacecraft insultation). An exciting application for materials with low thermal conductivity is in a thermoelectric device, which converts a temperature gradient into an electrical potential. The low

thermal conductivity is important for maintaining the temperature gradient, which would otherwise be degraded during the operation of the device.

One way to determine thermal conductivity is through the relationship $\kappa = \rho\alpha C_p$, where ρ is the density, α is the thermal diffusivity, and C_p is the heat capacity at constant pressure. Thermal diffusivity (α) is a measure of thermal inertia and describes the ability of material to conduct heat relative to the ability to store thermal energy. Thermal diffusivity and thermal conductivity differ in their physical meaning. The former one tells how fast heat can be transferred and the latter one determines how much of heat will be transferred. Heat capacity measures the amount of heat needed to change the temperature of a sample by one degree.

Thermal conductivity analysis is discussed in detail elsewhere;[31-33] herein, only a brief overview is given. In solids, heat is transferred mainly through electrons and phonons. The temperature dependence is different for metals (where main heat carriers are electrons) and nonmetals (where main carriers are phonons). According to the Wiedemann-Franz law ($\kappa = \sigma LT$, where κ is thermal conductivity, σ is electrical conductivity, L is the Lorenz number, and T is temperature), the thermal conductivity of metals is proportional to the temperature and electrical conductivity. In turn, the electrical conductivity is a function of temperature, crystal defects, grain boundaries, and phonon scattering, resulting in a complex dependence of thermal conductivity on temperature.

Thermal diffusivity was measured on annealed arc-melted ingots. Samples were first polished to be coplanar with a thickness of 1 to 2 mm and then cut into disc shapes with either 8 or 12 mm diameters via electrical discharge machining. The thermal

diffusivity of the discs was then measured using the laser flash method with a Netzsch LFA 457 instrument with a Cape-Lehman[34] pulse length and heat loss correction model. Samples were coated with graphite on both sides to promote uniform absorption and emission.

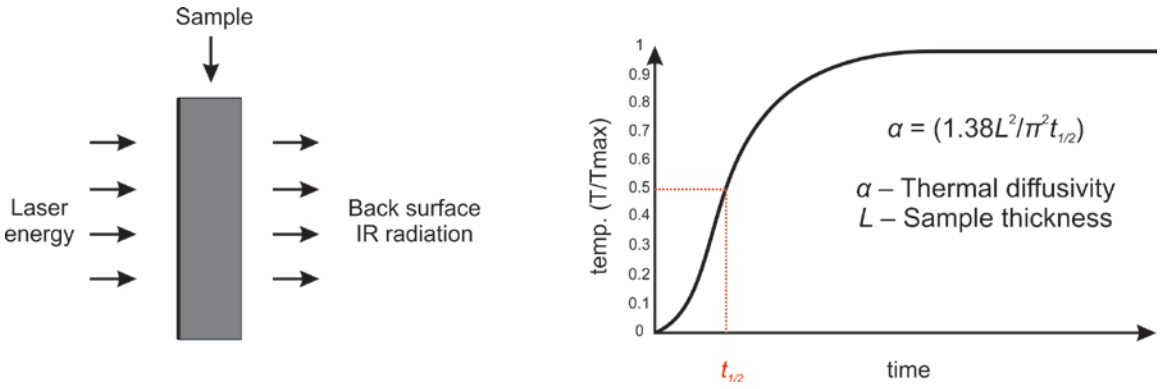

Figure 1-16 Laser flash analysis for measuring thermal diffusivity

The sample is located in a vacuum chamber or inert atmosphere. Carbon coating ensures high absorption and emission of radiation. A laser is used to give thermal energy at the front side of a sample. The time needed to reach the maximum temperature on the other side of the sample is registered. The ideal model (shown on the right side of Figure 1-16) was proposed by Parker.[32] However, some deviations may take place due to non-uniform radiation on the front face, non-uniform heating, and distortion in the curve due to two-dimensional heat flow.

Heat capacity was determined using a Netzsch Sirius 3500 temperature modulated differential scanning calorimeter (TM-DSC) or on a Perkin Elmer Pyris 1 DSC. Thermal conductivity, κ, of the samples was calculated from the standard relationship $\kappa = \rho\alpha C_p$. Figure 1-17[35] shows the possible trends in the sample (e.g., $TiRu_2Ga$ sample), typical for

metallic compounds. The thermal diffusivity increases with higher temperature, and the thermal conductivity decreases, due to phonon and electron contributions.

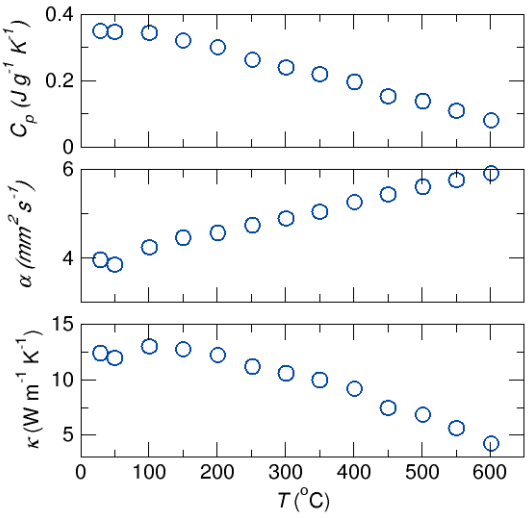

Figure 1-17 Heat capacity (C_P), thermal diffusivity (α), and thermal conductivity (κ) data from metallic $TiRu_2Ga$ sample.

1.6.3 Magnetic properties

Magnetism involves an interaction of magnetic moments of electrons within the material with an applied external magnetic field. Familiar behaviour includes paramagnetism (attraction to a magnetic field) and diamagnetism (repulsion). Paramagnetic substances contain unpaired valence electrons (e.g., isolated Cl atom), whereas diamagnetic substances contain no unpaired electrons (e.g., isolated Zn atom). Electron configurations and valence states can thus be inferred from magnetic measurements. More complex behaviour is possible.[36] Substances containing many f- and d-electrons, such as the rare-earth transition-metal germanides studied here, often exhibit interesting magnetic properties (e.g., magnetocaloric effect).

Magnetic measurements were typically made between 2 and 300 K under an applied field of 0.5 T on a Quantum Design 9T-PPMS magnetometer. Magnetization (M)

is the vector field of magnetic moments in a magnetic material that is a response of a material to an external magnetic field. Magnetic susceptibility (χ) indicates whether a material is attracted to a magnetic field or is repelled out of it. Susceptibility values were corrected for contributions from the holder and sample diamagnetism. Standard measurements were the temperature dependence (χ vs T) and the field dependence (M vs H) of a sample.

Weak diamagnetism, which is independent of temperature, is not particularly interesting for applications. Other types of magnetic behaviour show more interesting temperature dependence (Figure 1-18). Paramagnetism originates from a collection of non-interacting spins of electrons, which become increasingly aligned with the external field at lower temperatures (Curie law).[36] Ferromagnetism involves cooperatively interacting spins that are aligned in a parallel fashion and can remain aligned even when external field is removed. Antiferromagnetism also features alignment of interacting spins, but in an antiparallel fashion.

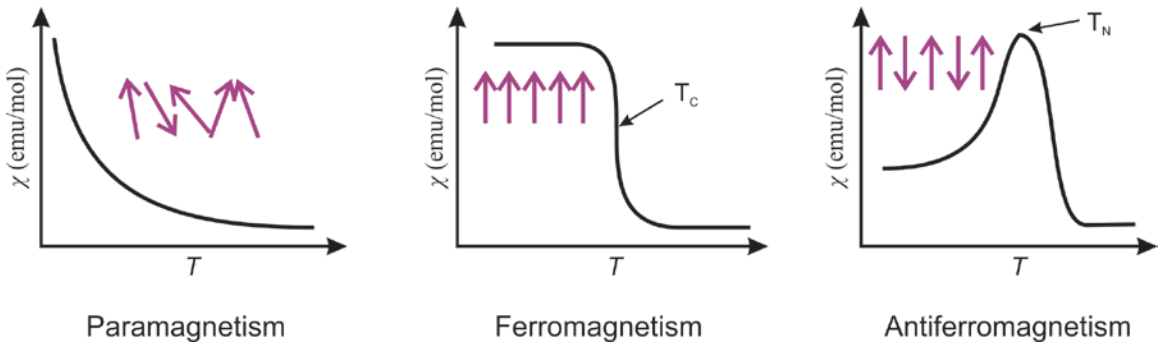

Figure 1-18 Temperature dependence curves of magnetic susceptibility (χ) in three main types of magnetism and their electron spin alignment.

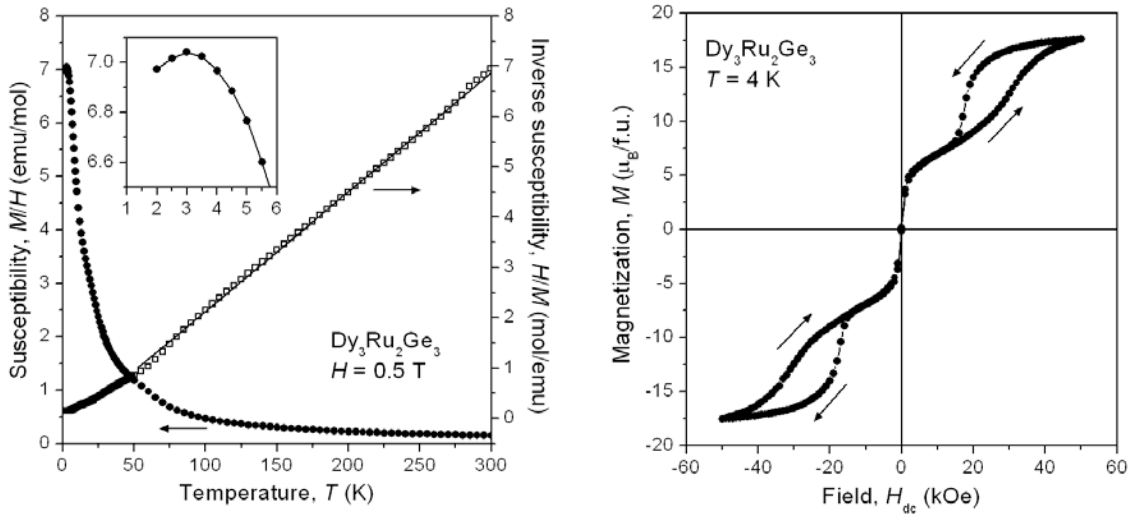

Figure 1-19 Magnetic susceptibility vs Temperature plot (left) and Magnetization vs Field dependence (right) for intermetallic germanide antiferromagnet $Dy_3Ru_2Ge_3$.

A typical analysis of antiferromagnetic substance is shown (Figure 1-19).[28] Antiferromagnetic ordering occurs below 3 K. The inverse susceptibility above this temperature can be fit to the Curie-Weiss law, and the negative *x*-intercept is consistent with antiferromagnetic exchange interactions. The magnetization curve at 4 K actually suggests more complicated behaviour than simple antiferromagnetism.

1.7 Machine learning techniques

Most scientific work builds on existing literature to yield data-driven discoveries; it is hard to find instances where a novel idea is proposed solely from intuition. However, because extracting knowledge from the literature is performed by human beings, this process may be biased, incomplete, and tedious. To overcome these problems, machine-learning may be a promising tool. Within chemistry, machine learning has been used to identify jet fuels,[37] classify gasoline components,[38-42] or discover biomarkers,[43,44] but they have not been widely applied to solid state materials.

One of the fundamental goals in chemistry is be able to foresee (based on fundamental rules) what kind of structure will form from any given combination of elements. It also is one of the "great challenges" according to the U.S. Department of Energy, where complex correlations of atomic components can determine the properties of the compound formed by these atoms. The search for new materials requires developing a detailed chemical understanding of the structures of solids. This can be done either by development of structure-property relationships through the traditional approach of systematic synthesis and property measurements, or by taking guidance from a machine-learning algorithm. Both approaches require a judicious validation by experimental confirmation, but machine-learning has the advantage of being much faster and unbiased. The work described in this thesis may have significant impact for both fundamental crystal chemistry and practical materials science.

Previous data mining machine-learning studies in solid state science include engineering semiconductor band gaps,[45] enhancing hardness of nitrides,[46] designing zeolite topologies,[47] and implementing principal component analysis (PCA) for various problems.[48,49] For my part, I participated in the experimental validation of a thermoelectric recommendation engine (http://thermoelectrics.citrination.com)[50] and combined novel approaches with a traditional structural study of germanides.[51] In this thesis, machine learning was applied to predict the crystal structures of binary and ternary intermetallics with experimental validation. The ultimate goal is to be able to predict a structure based solely on composition for all possible binary and ternary combinations of the elements, and to reveal the components important to design a material with a predicted property performance.

1.7.1 Random forest algorithm

A random forest algorithm is a method for classification based on many decision trees, each of which is trained to learn highly complicated patterns.[52] A decision tree is first built based on a training set of variables used to describe each entry, and then applied to make predictions about a new candidate. Because such a tree is specific to a unique training set, its predictions tend to be unbiased and accurate, but with high variance. To lower the variance, a "forest" is constructed from a random collection of a large number of decision trees each trained on diverse sets of data and each giving a classification answer.[53] The final decision is made through normalization by dividing by the number of trees. This method is fast, works well with large databases, and can handle thousands of variables used to describe data which may be noisy. There is no need for a separate cross-validation test, because the algorithm is already self-validated. The drawbacks include unreliable prediction for candidates lying beyond the range of a training data and possible overfitting of noisy datasets.

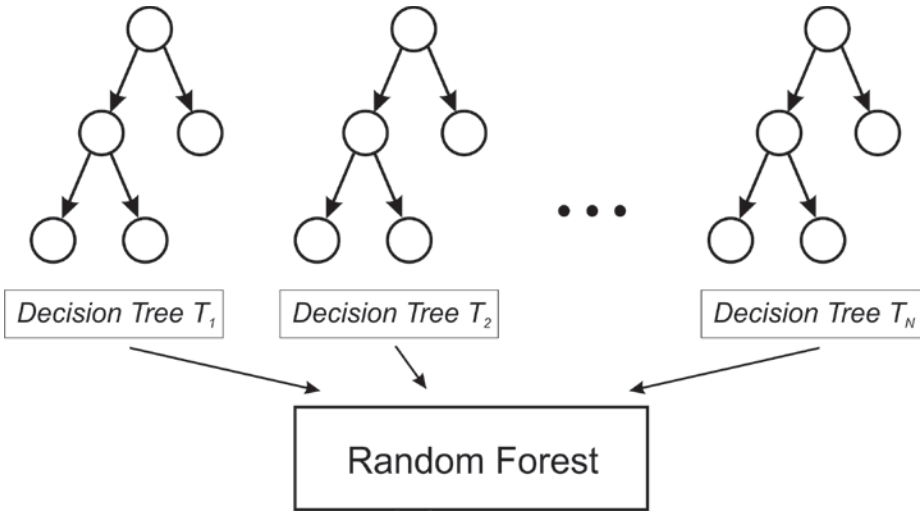

Figure 1-20 Schematic representation of random forest algorithm

1.7.2 Principal component analysis

Although it is not a classification tool, principal component analysis (PCA) refers to a statistical procedure for exploratory data analysis.[54] The idea is to reduce the dimensionality of a problem by transforming a large number of axes (each representing an experimental variable) into a small number of principal component axes.[55] When some variables convey similar information because they are correlated, they can be combined. The principal component axes are constructed as a linear combination of the original correlated variables such that the new axes lie orthogonal to each other and maximize the variance exhibited by the data. The data are centred and normalized, with component "scores" (transformed variable value) plotted along the axes. In this way, a multidimensional space can be represented in fewer dimensions. PCA thus facilitates the visualization of data, highlighting similarities and differences, and identifying hidden patterns. However, PCA only assumes that correlations are linear, which may be inapplicable for a complex problem, and that the principal component axis with the largest variance is the most important, which may not be true.

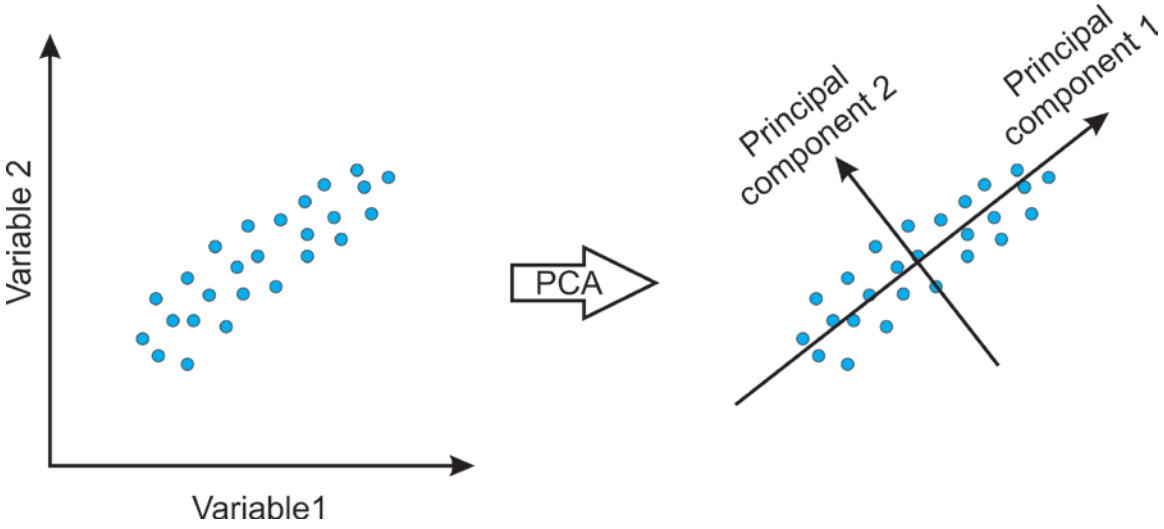

Figure 1-21 Schematic representation of principal component analysis.

1.7.3 Support vector machine

A support vector machine (SVM) is a relatively modern machine-learning algorithm that has been exceptionally successful for classification, in applications as diverse as facial expression classification and personal recommendation system for news websites.[56] SVM has never been previously applied to problems in crystallography. In SVM, data described by the large number of variables are represented in a higher-dimensional space. The goal of SVM is to separate data belonging to different classes in this space by a hyperplane which maximizes the gaps between these classes. Then, an unknown sample is evaluated to determine which class it belongs to by seeing which side of a hyperplane it falls on. A powerful advantage of SVM is that it can capture complex non-linear relationships inherent in many phenomena, and is thus well suited for classification problems. However, SVM requires that all relevant variables are included in the representation and it is not easy to gain an intuitive understanding on the relationship between parameters.

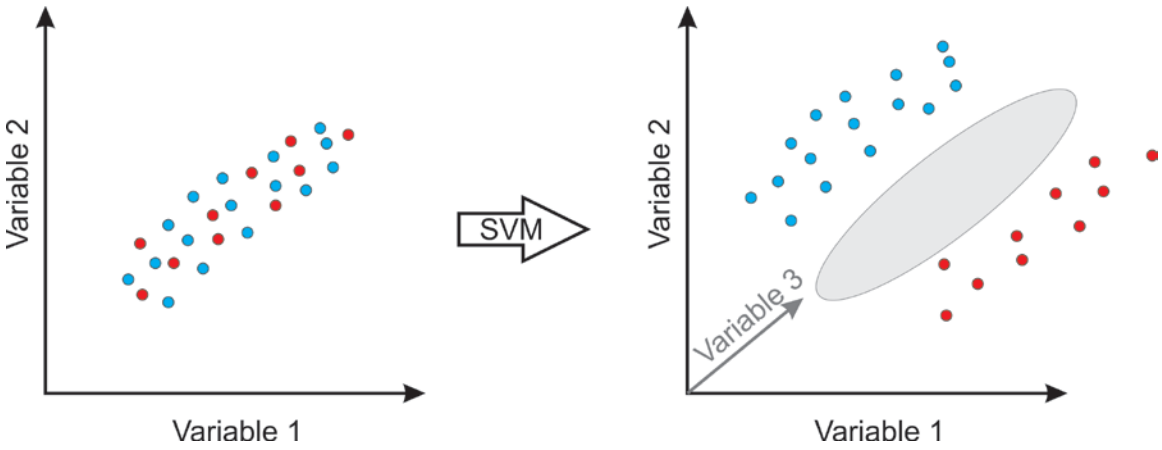

Figure 1-22 Schematic representation of support vector machine approach.

1.8 Structural chemistry of germanides

Germanides are intermetallic compounds of germanium with metals or metalloids. They are generally synthesized by sintering or melting. Although some are semiconducting (alkali and alkaline-earth germanides), most are metallic (transition-metal germanides). Germanides show many similarities to silicides, but show a tendency for greater metallic character in their bonding because Ge is a metalloid with intermediate behaviour between metals and non-metals. In fact, because the electronegativity of Ge is close to those of many transition metals, germanides can contain a complex combination of *M*–Ge, *M*–*M*, and Ge–Ge bonding.

Given that the focus of this thesis is on rare-earth transition-metal germanides, it is helpful to survey the literature, which has been reviewed up to 1999 in the Handbook on the Physics and Chemistry of Rare Earths,[57] supplemented by a search of more recent work to date through 2014.[58] Phase diagrams have been established for many *RE*–*M*–Ge systems where *M* is a transition metal, showing the existence of many phases with diverse compositions and crystal structures. (In contrast, ternary *RE*–(s-block or p-block metals or metalloids)–Ge systems contain relatively few compounds.) The *RE*–(Fe triad)–Ge systems are especially rich in phases, generally exhibiting limited solid solubility and related by complex equilibria. The Ni-containing systems are the most populated, with an average of about 11 compounds per system and the highest number (20) in the Ce–Ni–Ge system.[59] The systems containing precious metals, *RE*–(Ru, Rh, Pd, Os, Ir, Pt)–Ge, have not been well studied, with only a few isolated compounds of specific composition being identified.

Rare-earth metals can be classified into the lighter elements (La–Eu) and the heavier ones (Gd–Lu), most of which are trivalent. The divalent state is more common for Eu and Yb, and sometimes encountered for Sm. Exotic magnetic properties are frequently encountered in compounds containing Ce, Eu, and Yb, so these are often the most well studied. The most common structure types found in *RE*–*M*–Ge systems are also shared by *M*′–*M*–Ge systems where *M*′ is Zr and Hf (Table 1-1). A generalized phase diagram representing the compositions of these common structure types highlights the absence of phases with high *RE* content and the existence of some interesting Ge-rich phases (Figure 1-23).

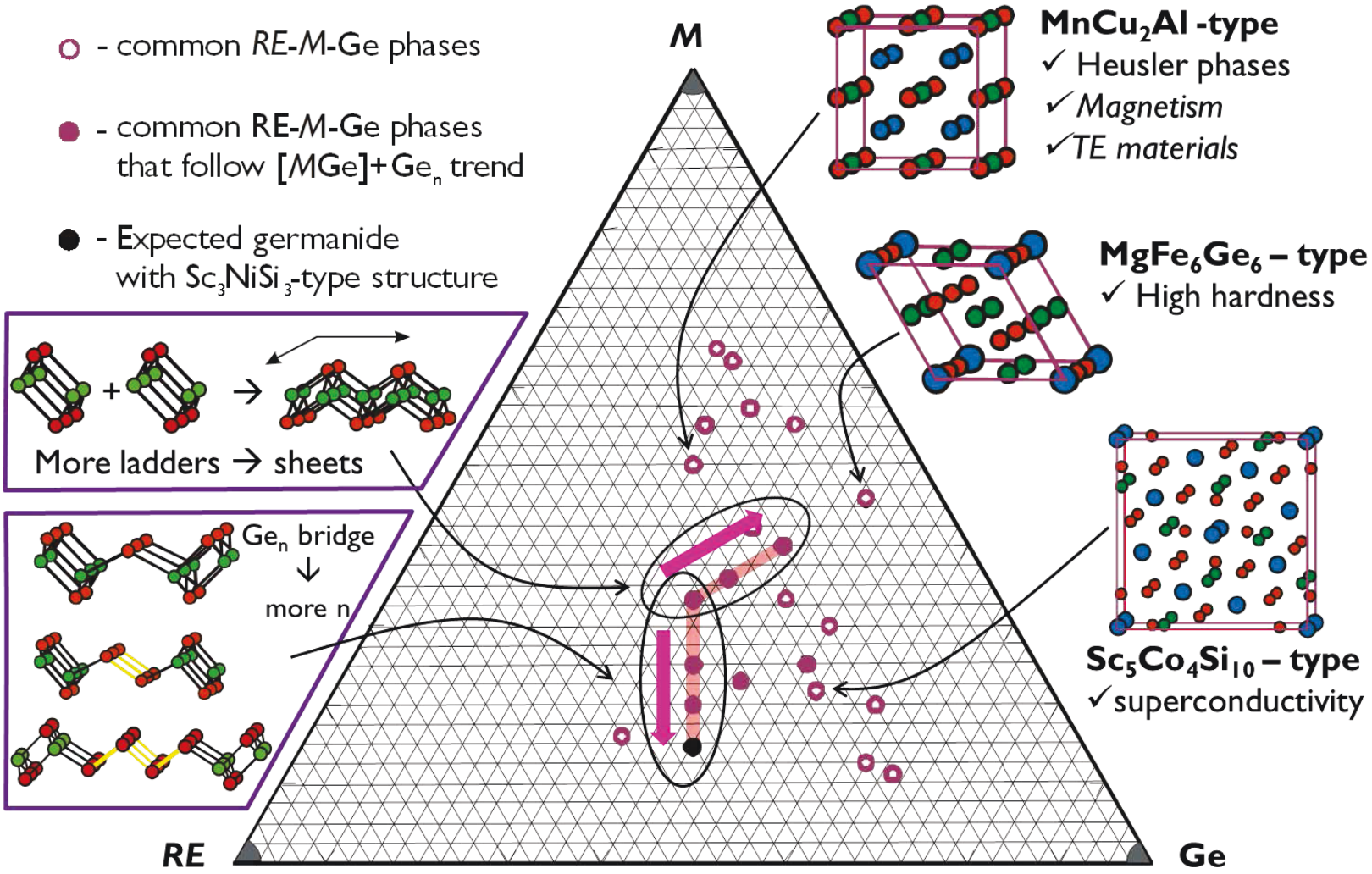

Figure 1-23 Generalized *RE–M*–Ge phase diagram with the most common phases in these systems, including structural trends and structures known for their unique properties.

Table 1-1 Common structure types in the *RE–M*–Ge and *M–M'*–Ge ternary systems

Structure type	Space group	Number of reports	Structure type	Space group	Number of reports
$CeAl_2Ga_2$	*I*4/*mmm*	129	$Hf_3Ni_2Si_3$	*Cmcm*	33
TiNiSi	*Pnma*	121	Gd_3NiSi_2	*Pnma*	30
Ce_2CuGe_6	*Amm*2	112	$ZrFe_4Si_2$	$P4_2/mnm$	30
$MgFe_6Ge_6$	*P*6/*mmm*	111	$Mg_6Cu_{16}Si_7$	*Fm*-3*m*	25
$Gd_3Cu_4Ge_4$	*Immm*	73	$Lu_2Co_3Si_5$	*C*2/*c*	20
ZrNiAl	*P*-62*m*	67	$LaPt_2Ge_2$	$P2_1$	18
$YIrGe_2$	*Immm*	58	YNi_5Si_3	*Pnma*	17
$MnCu_2Al$	*Fm*-3*m*	52	TiFeSi	*Ima*2	16
$Sc_5Co_4Si_{10}$	*P*4/*mbm*	47	$Tb_3Co_2Ge_4$	*C*2/*m*	10
Sc_2CoSi_2	*C*2/*m*	40	Y_2HfS_5	*Pnma*	10
$U_4Re_7Si_6$	*Im*-3*m*	37	$Tb_2Pt_9Ge_3$	*C*2/*c*	8
$ZrCrSi_2$	*Pbam*	37			

Many germanides contain recurring structural motifs that can be identified to help systematize the structures. One such motif is a trigonal prism with Ge at the center and *RE* and *M* atoms at the vertices, analogous to similar motifs frequently found in other intermetallics, especially phosphides and silicides.[60] These Ge-centred trigonal prisms can be connected by edge- and face-sharing in many different ways, limited only by nature's imagination (Figure 1-24). These motifs are helpful as a starting point for visualization, but bonding interactions also have to be taken into account. Usually the strongest bonds in *RE–M*–Ge structures are between *M* and Ge atoms.[51] To maximize *M*–Ge bonding, these motifs can be combined into infinite *M*Ge ladders, which in turn can be further connected to form two-dimensional sheets (Figure 1-23). In Ge-rich compounds, Ge–Ge bonding becomes important and the *M*Ge ladders are found to be connected by Ge_n bridges. From these patterns, it becomes possible to propose structures of hypothetical compounds to be targeted for synthesis.[51]

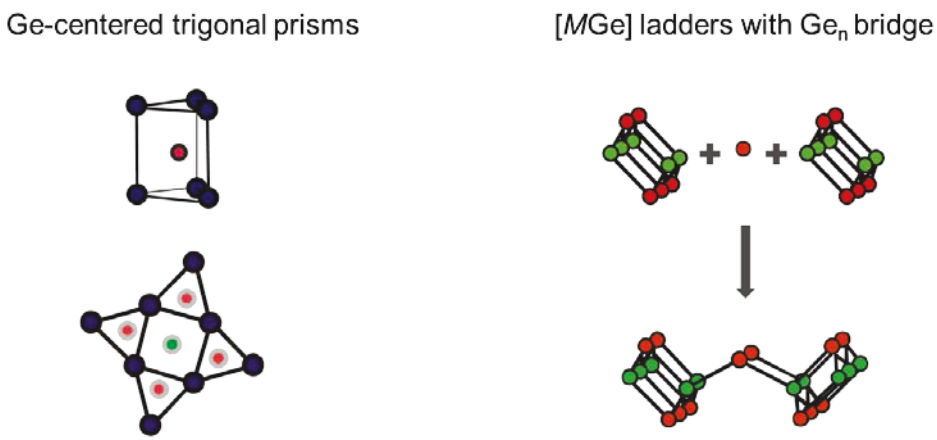

Figure 1-24 Two structural motifs (trigonal prisms and infinite ladders) summarize the basic approaches towards new structures in germanide families.

Prior to this work, there were not a lot of quaternary germanides known (246), most of which involve site disorder of metal components within a binary or ternary germanide. Quaternary germanides with ordered structures have been found in only five cases. Many more quaternary germanides can be anticipated with interesting structures.

1.9 Research Motivation

The main focus of this thesis is to attain a systematic understanding of the detailed crystal structures of ternary and quaternary germanides, to evaluate their physical properties for potential application as new materials, and to relate the structures to the properties. Introducing additional elements increases structural complexity and brings more control of properties. In particular, the combination of rare-earth and transition metals allows interplay of f- and d-electrons, which can result in a complex magnetic behaviour, and introducing large mass contrast influences phonon scattering, which can reduce thermal conductivity for thermoelectric applications. From a fundamental point of

view, germanides exhibit interesting structures (e.g., inorganic helices) with implications for novel bonding, in which the similar electronegativities of the component elements lead to a competition between homoatomic and heteroatomic bonding.

Systematization of crystal structures helps identify trends so that general principles can be developed to rationalize and predict new structures. However, I am also interested in applying machine-learning approaches to guide the search for new materials with desired properties to replace the traditional, more intuitive approach, which may have overlooked hidden or non-obvious patterns. With collaborators, I am specifically using these methods to predict the thermoelectric performance of a large number of compounds, including germanides. As an ambitious extension of this approach, I wish to test the broader idea of predicting the structures of inorganic solids in general, which has been called one of chemistry's grandest challenges. This involves creating a database containing variables that could potentially influence crystal structures, applying different evaluative methods, and experimentally validating the predictions. This work may have significant impact for both fundamental crystal chemistry as well as practical materials science to build the next generation of the state-of-art technology.

1.10 References

[1] Chatterjee, B. *Diverse Topics in Science and Technology*, AuthorHouse UK, 2013.

[2] Sauthoff, G. *Intermetallics*, VCH, Wienheim, 1995.

[3] Bardeen, J.; Brattain, W. H. *Phys. Rev.* **1948**, *74*, 230–231.

[4] Qin, G.; Yuan, H.; Qin, Y.; Seo, J.; Wang, Y.; Ma, J.; Ma, Z. *IEEE Elec. Dev. Lett.* **2013**, *34*, 160–162.

[5] Kong, H.; Shi, X.; Uher, C.; Morelli; D.T. *J. Appl. Phys.* **2007**, *102*, 023702-1–023702-5.

[6] Strydom, A. M. *J. Phys.: Condens. Matter* **2007**, *19*, 386205-1–386205-15.

[7] Tegus, O.; Duong, N. P.; Dagula, W.; Zhang, L.; Brück, E.; Buschow, K. H. J.; de Boer, F. R. *J. Appl. Phys.* **2002**, *91*, 8528–8530.

[8] Venturini, G.; Méot-Meyer, M.; Marêché, J. F.; Malaman, B.; Roques B. *Mater. Res. Bull.* **1986**, *21*, 33–39.

[9] Singh, Y.; Ramakrishnan, S. *Phys. Rev. B* **2004**, *69*, 174423-1–174423-13.

[10] Images: (a) sintering from http://www.shutterstock.com/; (b) arc-melting from https://www.youtube.com/watch?v=bH8kkxZqzhE; (c) induction from http://chaturvedimetalsolution.com/

[11] Kingery, W. D.; Bowen, H. K.; Ulmann, D. R. *Introduction to Ceramics*, 2nd ed., John Wiley & Sons, Academic Press, 1976.

[12] Yu, K.-O. *Modeling for Casting & Solidification Processing*, CRC, 2001.

[13] Rudnev, V. *Handbook of Induction Heating*, CRC, 2003.

[14] Canfield, P. C.; Fisk, Z. *Philos. Mag. B* **1992**, *65*, 1117–1123.

[15] Ferreira, S. O. *Advanced Topics on Crystal Growth*, InTech, 2013.

[16] Massa, W. *Crystal Structure Determination*, 2nd ed., Springer–Verlag: Berlin, 2004.

[17] West, A. R. *Basic Solid State Chemistry*, 2nd ed., Wiley: New York, 1999.

[18] Eckert, M. *Ann. Phys.* **2012**, *524*, A83–A85.

[19] Bragg, W. H.; Bragg W. L. *Proc. R. Soc. Lond. A* **1913**, *88*, 428–438.

[20] Oliynyk, A. O.; Mar, A. *J. Solid State Chem.* **2013**, *206*, 60–65.

[21] Rietveld, H. M. *J. Appl. Crystallogr.* **1969**, *2*, 65–71

[22] Gibbs, J. W. *Scientific Papers*, Dover, New York, 1961.

[23] Oliynyk, A. O.; Sparks, T. D.; Gaultois, M. W.; Ghadbeigi, L.; Mar, A. submitted to *Inorg. Chem.*

[24] Akselrud, L. G.; Zavalii, P. Yu.; Grin, Yu. N.; Pecharski, V. K.; Baumgartner, B.; Wölfel, E. *Mater. Sci. Forum* **1993**, *133-136*, 335-342.

[25] Russ, J. C. *Fundamentals of energy dispersive X-ray analysis*, Butterworth: London, 1984.

[26] Oliynyk, A. O.; Djama-Kayad, K.; Mar, A. *J. Alloys Compd.* **2014**, *602*, 130–134.

[27] Dronskowski, R. *Computational Chemistry of Solid State Materials*, Wiley-VCH, Weinheim, 2005.

[28] Oliynyk, A. O.; Stoyko, S. S.; Mar, A. *J. Solid State Chem.* **2013**, *202*, 241–249.

[29] Tank, R.; Jepsen, O.; Burkhardt, A.; Andersen, O. K. *TB-LMTO-ASA Program*, version 4.7, Max Plank Institut für Festkörperforschung, Stuttgart, Germany, 1998.

[30] Dronskowski, R.; Blöchl, P. E. *J. Phys. Chem.* **1993**, *97*, 8617–8624.

[31] Vozar, L.; Hohenauer, W. *High Temp. – High Pressures* **2003**, *35*, 253–264.

[32] Parker, W. J.; Jenkins, R. J.; Butler, C. P.; Abbott, G. L. *J. Appl. Phys.* **1962**, *32*, 1679–1684.

[33] Cowan, R. D. *J. Appl. Phys.* **1962**, *34*, 926–927.

[34] Cape, J. A.; Lehman, G. W. *J. Appl. Phys.* **1963**, *34*, 1909–1913.

[35] Oliynyk, A. O.; Antono, E.; Sparks, T. D., Ghadbeigi, L.; Gaultois, M. W.; Meredig, B.; Mar, A. submitted to *Chem. Mater.*

[36] Martin, D. H. *Magnetism in Solids*, M.I.T. Press, Cambridge, 1967.

[37] Johnson, K. J.; Synovec, R. E. *Chemom. Intell. Lab. Syst.* **2002**, *60*, 225–237.

[38] Doble, P.; Sandercock, M.; Du Pasquier, E.; Petocz, P.; Roux, C.; Dawson, M. *Forensic Sci. Int.* **2003**, *132*, 26–39.

[39] Sandercock, P. M. L.; Du Pasquier, E. *Forensic Sci. Int.* **2003**, *134*, 1–10.

[40] Sandercock, P. M. L.; Du Pasquier, E. *Forensic Sci. Int.* **2004**, *140*, 43–59.

[41] Sandercock, P. M. L.; Du Pasquier, E. *Forensic Sci. Int.* **2004**, *140*, 71–77.

[42] Sinkov, N. A.; Harynuk, J. J. *Talanta* **2011**, *83*, 1079–1087.

[43] Li, X.; Xu, Z.; Lu, X.; Yang, X.; Yin, P.; Kong, H.; Yu, Y.; Xu, G. *Anal. Chim. Acta* **2009**, *633*, 257–262.

[44] Beckstrom, A. C.; Humston, E. M.; Snyder, L. R.; Synovec, R. E.; Juul, S. E. *J. Chromatogr. A* **2011**, *1218*, 1899–1906.

[45] Srinivasan, S.; Rajan, K. *Materials* **2013**, *6*, 279–290.

[46] Petterson, F.; Suh, C.; Saxén, H.; Rajan, K.; Chakraborti, N. *Mater. Manuf. Processes* **2008**, *24*, 2–9.

[47] Lach-hab, M.; Yang, S.; Vaisman, I. I.; Blaisten-Barojas, E. *Mol. Inf.* **2010**, *29*, 297–301.

[48] Rajan, K. *Mater. Today* **2005**, *8*, 38–45.

[49] Broderick, S.; Rajan, K. Sci. Technol. *Adv. Mater.* **2015**, *16*, 013501-1–013501-8.

[50] Gaultois, M. W.; Oliynyk, A. O.; Mar, A.; Sparks, T. D.; Mulholland, G. J.; Meredig, B. *APL Materials*, accepted.

[51] Sparks, T. D.; Gaultois, M. W.; Oliynyk, A. O.; Brgoch, J.; Meredig, B. *Scr. Mater.* **2016**, *111*, 10–15.

[52] Ho, T. K. *IEEE Trans. Pattern Anal. Mach. Intell.* **1998**, *20*, 832–844.

[53] Hastie, T.; Tibshirani, R.; Friedman, J. *The Elements of Statistical Learning*, 2nd ed., Springer, 2008.

[54] Hotelling, H. *J. Educ. Psychol.* **1933**, *24*, 417–441.

[55] Abdi, H.; Williams, L. J. *Wiley Interdiscip. Rev. Comput. Stat.* **2010**, *2*, 433–459.

[56] Cortes, C.; Vapnik, V. *Machine Learning* **1995**, *20*, 273–297.

[57] Salamakha, P. S.; Sologub, O. L.; Bodak, O. I. Chapter 173 Ternary rare-earth-germanium systems, *Handbook on the Physics and Chemistry of Rare Earths, Volume* **1999**, *27*, 1–223.

[58] Pöttgen, R.; Johrendt, D. *Intermetallics*, Walter de Gruyter GmbH, Berlin/Boston, 2014

[59] Salamakha, P. S.; Konyk, M. B.; Sologub, O. L.; Bodak O. I. *J. Alloys Compd.* **1996**, *236*, 206–211.

[60] Parthé, E.; Chabot, B.; Hovestreydt, E. *Acta Cryst. B* **1983**, *29*, 596–6.

Chapter 2

Ternary rare-earth ruthenium and iridium germanides $RE_3M_2Ge_3$ (*RE* = Y, Gd–Tm, Lu; *M* = Ru, Ir)

A version of this chapter has been published. Oliynyk, A. O.; Stoyko, S. S.; Mar, A. J. Solid State Chem. 2013, 202, 241–249.

2.1 Introduction

A rich variety of ternary rare-earth transition-metal germanides *RE*–*M*–Ge are known. Among systems with *M* = 3d metals, the ones involving the later elements (M = Mn, Fe, Co, Ni, Cu) give rise to numerous phases, in contrast to those containing the earlier elements (*M* = V, Cr),[1] for which the new compounds $REMGe_3$ and $RECr_xGe_2$ have only been identified recently.[2-4] The same pattern emerges for systems with *M* = 4d and 5d metals, in which the ones containing the precious metals (*M* = Ru, Os, Rh, Ir, Pd, Pt) promise to show many phases, whereas those containing the earlier elements have barely been explored.[1] Much of the interest in these germanides relates to their diverse physical properties which may prove useful in materials applications. Recent reports of such germanides containing a precious metal have been motivated by the search for new magnetocaloric (e.g., $GdRu_2Ge_2$),[5] thermoelectric (e.g., $RE_3M_4Ge_{13}$),[6,7] and superconducting materials (e.g., $RE_2Ir_3Ge_5$).[8,9]

In this chapter the elucidation of the series $RE_3M_2Ge_3$ (*RE* = Y, Gd–Tm, Lu; M = Ru, Ir) is discussed. Only a few isolated members of these series have been identified

previously: $Ho_3Ru_2Ge_3$,[10-12] $Ho_3Ir_2Ge_3$,[13] and $Lu_3Ir_2Ge_3$.[14] The crystal structures for all remaining members for the $RE_3Ru_2Ge_3$ series have now been determined, as well as for $Tb_3Ir_2Ge_3$. Electrical resistivity measurements for the $RE_3Ru_2Ge_3$ series, as well as magnetic susceptibility measurements on $Dy_3Ru_2Ge_3$ is reported. The nature of bonding in these compounds has been examined through band structure calculations.

2.2 Experimental

2.2.1. Synthesis

Stoichiometric mixtures (0.2-g total mass) of freshly filed *RE* pieces (*RE* = Y, Gd–Tm, Lu, 99.9%, Hefa), Ru (99.95%, Cerac) or Ir powder (99.9%, Cerac), and Ge powder (99.9999%, Alfa-Aesar) were pressed into pellets, which were arc-melted in a Centorr 5TA tri-arc furnace on a water-cooled copper hearth under an argon atmosphere. To ensure homogeneity, the samples were melted twice, after which the weight loss was found to be less than 1%. The ingots were then sealed within fused-silica tubes and annealed at 800 °C for 12 d, followed by quenching in cold water. No attempts were made to extend the *RE* substitution to Yb, whose high volatility would pose problems in arc-melting. The products were characterized by powder X-ray diffraction (XRD) patterns, collected with Cu $K\alpha_1$ radiation on an Inel diffractometer equipped with a curved position-sensitive detector (CPS 120). The Ru-containing samples generally consisted of $RE_3Ru_2Ge_3$ as the major phase (55–100%), along with smaller amounts of RE_2RuGe_2.[15] The Ir-containing samples generally consisted of $RE_3Ir_2Ge_3$ as the major phase (45–55%), along with RE_2IrGe_2[14,16] and *RE*IrGe.[17,18] Cell parameters for the

orthorhombic $RE_3M_2Ge_3$ (M = Ru, Ir) phases were refined from the powder XRD data with use of the CSD suite of programs[19] and are listed in Table 2-1.

Table 2-1 Cell parameters for $RE_3M_2Ge_3$ (M = Ru, Ir). [a]

Compound	a (Å)	b (Å)	c (Å)	V (Å^3)	Reference
$Y_3Ru_2Ge_3$	4.2700(9)	10.754(2)	13.877(6)	637.2(5)	This work
$Gd_3Ru_2Ge_3$	4.267(1)	10.962(3)	14.071(4)	658.2(5)	This work
$Tb_3Ru_2Ge_3$	4.2551(7)	10.861(2)	13.981(2)	646.1(3)	This work
$Dy_3Ru_2Ge_3$	4.2529(7)	10.810(2)	13.898(2)	638.9(3)	This work
$Ho_3Ru_2Ge_3$	4.2263(8)	10.729(2)	13.828(2)	627.0(3)	This work
$Ho_3Ru_2Ge_3$	4.242(2)	10.731(6)	13.840(9)	630(1)	[10]
$Er_3Ru_2Ge_3$	4.2263(6)	10.701(1)	13.794(2)	623.8(2)	This work
$Tm_3Ru_2Ge_3$	4.2271(7)	10.661(2)	13.774(3)	620.7(4)	This work
$Lu_3Ru_2Ge_3$	4.2130(8)	10.577(1)	13.676(3)	609.4(3)	This work
$Y_3Ir_2Ge_3$	4.2815(9)	10.448(2)	14.190(3)	634.8(4)	This work
$Gd_3Ir_2Ge_3$	4.321(1)	10.594(2)	14.357(5)	657.2(5)	This work
$Tb_3Ir_2Ge_3$	4.2968(8)	10.521(3)	14.259(4)	644.6(5)	This work
$Dy_3Ir_2Ge_3$	4.290(1)	10.462(3)	14.281(3)	641.0(5)	This work
$Ho_3Ir_2Ge_3$	4.271(1)	10.399(2)	14.100(4)	626.2(4)	This work
$Ho_3Ir_2Ge_3$	4.2730(7)	10.403(1)	14.128(2)	628.0(3)	[13]
$Er_3Ir_2Ge_3$	4.248(1)	10.374(3)	14.179(4)	624.9(5)	This work
$Tm_3Ir_2Ge_3$	4.246(1)	10.324(4)	14.219(4)	623.3(6)	This work
$Lu_3Ir_2Ge_3$	4.2506(7)	10.241(2)	13.945(2)	607.0(3)	This work
$Lu_3Ir_2Ge_3$	4.265(1)	10.191(2)	13.989(4)	608.0(4)	[14]

[a] Cell parameters reported in this work were refined from powder X-ray diffraction data.

RE_2IrGe_2 were also identified as new phases, which adopt the monoclinic Sc_2CoSi_2-type structure (space group $C2/m$) with refined cell parameters listed in Table 2-2. (Because Ho_2IrGe_2 and Lu_2IrGe_2 were detected only in trace quantities, their cell parameters could not be refined; Tm_2IrGe_2 did not apparently form.) Small single crystals of $RE_3M_2Ge_3$ (M = Ru, Ir) could be extracted manually from the products and their chemical compositions were determined by energy-dispersive X-ray (EDX) analysis on a JEOL JSM-6010LA scanning electron microscope. The experimental compositions (35–38% *RE*, 24–28% *M*, 36–40% Ge) (Table A1-1) were in good agreement with expectations (37.5% *RE*, 25.0% *M*, 37.5% Ge).

Table 2-2 Cell parameters for RE_2IrGe_2. [a]

Compound	a (Å)	b (Å)	c (Å)	β (deg.)	V (Å^3)	Reference
Y_2IrGe_2	10.549(3)	4.223(1)	10.256(2)	117.30(1)	406.0(5)	This work
Nd_2IrGe_2	10.84(1)	4.352(1)	10.54(2)	117.23(2)	442(2)	[16]
Gd_2IrGe_2	10.705(2)	4.342(1)	10.197(3)	118.01(2)	418.4(4)	This work
Tb_2IrGe_2	10.677(2)	4.269(1)	10.153(2)	118.19(1)	407.9(3)	This work
Dy_2IrGe_2	10.583(2)	4.268(1)	10.111(2)	118.07(1)	403.0(3)	This work
Er_2IrGe_2	10.513(2)	4.230(1)	10.040(3)	118.10(1)	393.9(3)	This work
Yb_2IrGe_2	10.271(8)	4.228(2)	10.103(9)	116.64(9)	392(1)	[14]

[a] Cell parameters reported in this work were refined from powder X-ray diffraction data.

2.2.2 Structure determination

Suitable crystals of the entire $RE_3Ru_2Ge_3$ (*RE* = Y, Gd–Tm, Lu) series were available for single-crystal X-ray diffraction analysis. Crystals of the corresponding $RE_3Ir_2Ge_3$ series were also tested but generally they were too small or diffracted poorly; however, a suitable crystal of one member, $Tb_3Ir_2Ge_3$, gave acceptable results. Intensity data were collected at –100 °C on a Bruker PLATFORM diffractometer equipped with a SMART APEX II CCD area detector and a graphite-monochromated Mo *K*α radiation source, using ω scans to generate at least 5 sets of frames at different ϕ angles with a frame width of 0.3º and an exposure time of 12 s per frame. Face-indexed absorption corrections were applied. Structure solution and refinement were carried out with use of the SHELXTL (version 6.12) program package.[20] The centrosymmetric orthorhombic space group *Cmcm* was chosen on the basis of Laue symmetry, systematic absences, and intensity statistics. Direct methods led to a structural model consistent with the $Hf_3Ni_2Si_3$-type structure. Atomic positions were standardized with the program STRUCTURE TIDY.[21] Refinements proceeded in a straightforward fashion, with all atomic sites being fully occupied and having reasonable displacement parameters. Agreement factors were excellent in all cases (conventional *R*(*F*) for observed reflections less than 0.05). For two samples, there was some residual electron density in the difference map ($(\Delta\rho)_{max,min}$ = 6.14, –2.05 $e^-/Å^3$ for $Y_3Ru_2Ge_3$ and 6.63, –1.84 $e^-/Å^3$ for $Ho_3Ru_2Ge_3$); however, the peaks were too close (~1.4 Å) to *RE* atoms to be physically meaningful and are likely an artefact of inadequate absorption corrections. Crystal data and further details of the data collections are given in Table 2-3, final values of the

positional and displacement parameters are given in Table 2-4, and selected interatomic distances are given in Table 2-5.

Table 2-3 Crystallographic data for $RE_3Ru_2Ge_3$ (RE = Y, Gd–Tm, Lu) and $Tb_3Ir_2Ge_3$.

Formula	$Y_3Ru_2Ge_3$	$Gd_3Ru_2Ge_3$	$Tb_3Ru_2Ge_3$	$Dy_3Ru_2Ge_3$	$Ho_3Ru_2Ge_3$
Formula mass (amu)	686.64	891.66	896.67	907.41	914.70
a (Å)	4.2477(6)	4.2610(3)	4.2491(4)	4.2439(5)	4.2303(3)
b (Å)	10.7672(16)	10.9103(8)	10.8391(9)	10.7736(12)	10.7310(7)
c (Å)	13.894(2)	14.0263(10)	13.9361(12)	13.8666(16)	13.8237(9)
V (Å^3)	635.44(16)	652.07(8)	641.85(10)	634.01(13)	627.53(7)
Z	4	4	4	4	4
ρ_{calcd} (g cm^{-3})	7.177	9.083	9.279	9.506	9.682
T (K)	173	173	173	173	173
Crystal dimensions (mm)	0.06 × 0.03 × 0.03	0.16 × 0.03 × 0.02	0.11 × 0.03 × 0.02	0.10 × 0.04 × 0.02	0.06 × 0.04 × 0.02
Radiation	Graphite monochromated Mo $K\alpha$, λ = 0.71073 Å				
μ(Mo $K\alpha$) (mm^{-1})	45.52	48.04	50.87	53.39	56.04
Transmission factors	0.113–0.350	0.041–0.440	0.061–0.467	0.064–0.508	0.061–0.318
2θ limits	5.86–66.22°	5.80–66.44°	5.84–66.48°	5.88–66.44°	5.90–66.16°
Data collected	$-6 \le h \le 6$, $-16 \le k \le 16$, $-20 \le l \le 21$	$-6 \le h \le 6$, $-16 \le k \le 16$, $-21 \le l \le 21$	$-6 \le h \le 6$, $-16 \le k \le 16$, $-21 \le l \le 20$	$-6 \le h \le 6$, $-16 \le k \le 16$, $-21 \le l \le 21$	$-6 \le h \le 6$, $-16 \le k \le 16$, $-21 \le l \le 21$
No. of data collected	4527	4616	4441	4467	4495
No. of unique data, including $F_o^2 < 0$	697 (R_{int} = 0.046)	711 (R_{int} = 0.018)	702 (R_{int} = 0.033)	692 (R_{int} = 0.067)	687 (R_{int} = 0.030)
No. of unique data, with $F_o^2 > 2\sigma(F_o^2)$	606	686	660	581	652
No. of variables	27	28	28	28	28
$R(F)$ for $F_o^2 > 2\sigma(F_o^2)$ [a]	0.043	0.015	0.020	0.030	0.025
$R_w(F_o^2)$ [b]	0.120	0.035	0.051	0.070	0.064
Goodness of fit	1.26	1.12	1.22	1.08	1.29
$(\Delta\rho)_{max}$, $(\Delta\rho)_{min}$ (e Å^{-3})	6.14, –2.05	1.42, –1.56	4.30, –1.65	3.05, –2.20	6.63, –1.84

Formula	$Er_3Ru_2Ge_3$	$Tm_3Ru_2Ge_3$	$Lu_3Ru_2Ge_3$	$Tb_3Ir_2Ge_3$
Formula mass (amu)	921.69	926.70	944.82	1078.93
a (Å)	4.2237(9)	4.2202(8)	4.2045(8)	4.2937(3)
b (Å)	10.693(2)	10.631(2)	10.561(2)	10.4868(7)
c (Å)	13.774(3)	13.715(3)	13.639(3)	14.2373(10)
V (Å^3)	622.1(2)	615.3(2)	605.6(2)	641.07(8)
Z	4	4	4	4
ρ_{calcd} (g cm^{-3})	9.841	10.00	10.36	11.18
T (K)	173	173	173	173
Crystal dimensions (mm)	0.09 × 0.02 × 0.02	0.09 × 0.02 × 0.02	0.09 × 0.02 × 0.02	0.11 × 0.03 × 0.02
Radiation	Graphite monochromated Mo $K\alpha$, λ = 0.71073 Å			
μ(Mo $K\alpha$) (mm^{-1})	58.84	61.84	67.78	87.69
Transmission factors	0.042–0.425	0.099–0.483	0.075–0.422	0.044–0.338
2θ limits	5.92–66.34°	5.94–66.64°	5.98–66.30°	5.72–66.40°
Data collected	$-6 \le h \le 6$, $-16 \le k \le 16$, $-20 \le l \le 21$	$-6 \le h \le 6$, $-16 \le k \le 16$, $-20 \le l \le 20$	$-6 \le h \le 6$, $-16 \le k \le 15$, $-20 \le l \le 20$	$-6 \le h \le 6$, $-16 \le k \le 16$, $-21 \le l \le 21$
No. of data collected	4433	4404	4239	4600
No. of unique data, including $F_o^2 < 0$	683 (R_{int} = 0.038)	680 (R_{int} = 0.037)	664 (R_{int} = 0.113)	708 (R_{int} = 0.029)
No. of unique data, with $F_o^2 > 2\sigma(F_o^2)$	618	612	483	680
No. of variables	28	28	28	28
$R(F)$ for $F_o^2 > 2\sigma(F_o^2)$ [a]	0.017	0.022	0.037	0.019
$R_w(F_o^2)$ [b]	0.036	0.046	0.076	0.045
Goodness of fit	1.06	1.14	1.04	1.16
$(\Delta\rho)_{max}$, $(\Delta\rho)_{min}$ (e Å^{-3})	1.70, –1.68	2.68, –2.23	4.24, –3.73	2.93, –3.65

[a] $R(F) = \sum||F_o| - |F_c|| / \sum|F_o|$ for $F_o^2 > 2\sigma(F_o^2)$.

[b] $R_w(F_o^2) = [\sum[w(F_o^2 - F_c^2)^2] / \sum wF_o^4]^{1/2}$; $w^{-1} = [\sigma^2(F_o^2) + (Ap)^2 + Bp]$, where $p = [\max(F_o^2,0) + 2F_c^2] / 3$.

Table 2-4 Positional and equivalent isotropic displacement parameters (Å^2) [a] for $RE_3Ru_2Ge_3$ (RE = Y, Gd–Tm, Lu) and $Tb_3Ir_2Ge_3$.

	$Y_3Ru_2Ge_3$	$Gd_3Ru_2Ge_3$	$Tb_3Ru_2Ge_3$	$Dy_3Ru_2Ge_3$	$Ho_3Ru_2Ge_3$
*RE*1 in 8*f* (0, *y*, *z*)					
y	0.07810(11)	0.07811(2)	0.07778(3)	0.07771(4)	0.07767(3)
z	0.11301(9)	0.11353(1)	0.11350(2)	0.11343(4)	0.11343(2)
U_{eq}	0.0051(2)	0.00533(7)	0.00478(10)	0.00781(14)	0.00375(12)
*RE*2 in 4*c* (0, *y*, ¼)					
y	0.35575(17)	0.35671(3)	0.35575(4)	0.35487(7)	0.35472(5)
U_{eq}	0.0064(3)	0.00620(8)	0.00603(11)	0.00954(17)	0.00472(13)
M in 8*f* (0, *y*, *z*)					
y	0.21333(9)	0.21422(3)	0.21386(5)	0.21357(8)	0.21326(6)
z	0.58249(7)	0.58173(2)	0.58209(4)	0.58238(6)	0.58261(5)
U_{eq}	0.0053(2)	0.00527(8)	0.00474(12)	0.00767(18)	0.00375(15)
Ge1 in 8*f* (0, *y*, *z*)					
y	0.38334(13)	0.38257(4)	0.38351(7)	0.38414(10)	0.38456(8)
z	0.04027(10)	0.04001(3)	0.03992(5)	0.04020(8)	0.04011(6)
U_{eq}	0.0056(3)	0.00563(10)	0.00528(15)	0.0076(2)	0.00417(17)
Ge2 in 4*c* (0, *y*, ¼)					
y	0.66424(19)	0.66764(6)	0.66578(10)	0.66420(16)	0.66351(12)
U_{eq}	0.0062(4)	0.00620(12)	0.00595(19)	0.0093(3)	0.0047(2)
	$Er_3Ru_2Ge_3$	$Tm_3Ru_2Ge_3$	$Lu_3Ru_2Ge_3$	$Tb_3Ir_2Ge_3$	
*RE*1 in 8*f* (0, *y*, *z*)					
y	0.07749(2)	0.07728(3)	0.07716(7)	0.08377(3)	
z	0.11341(2)	0.11343(2)	0.11344(5)	0.11062(2)	
U_{eq}	0.00561(7)	0.00586(9)	0.00964(18)	0.00472(9)	
*RE*2 in 4*c* (0, *y*, ¼)					
y	0.35418(3)	0.35354(4)	0.35368(9)	0.35971(4)	
U_{eq}	0.00687(9)	0.00745(11)	0.0110(2)	0.00543(10)	
M in 8*f* (0, *y*, *z*)					
y	0.21317(4)	0.21289(5)	0.21257(13)	0.20143(2)	
z	0.58289(3)	0.58309(4)	0.58353(9)	0.60106(2)	
U_{eq}	0.00542(10)	0.00534(12)	0.0101(3)	0.00622(9)	
Ge1 in 8*f* (0, *y*, *z*)					
y	0.38521(6)	0.38548(7)	0.38602(17)	0.37589(7)	
z	0.04025(4)	0.04034(6)	0.04054(12)	0.03538(5)	
U_{eq}	0.00576(12)	0.00579(15)	0.0099(3)	0.00577(14)	
Ge2 in 4*c* (0, *y*, ¼)					
y	0.66240(8)	0.66126(11)	0.6599(2)	0.65838(10)	
U_{eq}	0.00642(16)	0.0069(2)	0.0107(5)	0.00521(17)	

[a] U_{eq} is defined as one-third of the trace of the orthogonalized U_{ij} tensor.

Table 2-5 Selected interatomic distances (Å) in $RE_3Ru_2Ge_3$ (*RE* = Y, Gd–Tm, Lu) and $Tb_3Ir_2Ge_3$.

	$Y_3Ru_2Ge_3$	$Gd_3Ru_2Ge_3$	$Tb_3Ru_2Ge_3$	$Dy_3Ru_2Ge_3$	$Ho_3Ru_2Ge_3$
*RE*1–Ge2 (×2)	2.9990(11)	3.0261(3)	3.0070(4)	2.9929(7)	2.9810(5)
*RE*1–Ge1 (×2)	3.0361(13)	3.0596(4)	3.0431(6)	3.0348(9)	3.0238(7)
*RE*1–Ge1 (×2)	3.1511(14)	3.1865(4)	3.1622(6)	3.1437(9)	3.1297(7)
*RE*1–Ge1	3.4384(19)	3.4782(6)	3.4688(8)	3.4540(13)	3.4457(9)
*RE*1–*M*	3.0818(16)	3.1155(4)	3.0992(6)	3.0846(10)	3.0758(7)
*RE*1–*M* (×2)	3.1199(12)	3.1419(3)	3.1314(5)	3.1216(7)	3.1127(5)
*RE*1–*M*	3.1664(16)	3.2204(4)	3.1913(7)	3.1675(10)	3.1508(7)
*RE*2–Ge1 (×2)	2.9290(15)	2.9589(5)	2.9432(8)	2.9262(12)	2.9190(9)
*RE*2–Ge2 (×2)	2.9601(19)	2.9656(5)	2.9587(8)	2.9534(13)	2.9469(9)
*RE*2–Ge2	3.322(3)	3.3923(8)	3.3604(12)	3.3326(18)	3.3136(14)
*RE*2–*M* (×4)	3.2373(9)	3.2724(3)	3.2494(5)	3.2325(7)	3.2188(5)
M–Ge1 (×2)	2.4368(9)	2.4488(3)	2.4440(5)	2.4399(7)	2.4333(5)
M–Ge1	2.5020(17)	2.5078(6)	2.5045(9)	2.5033(14)	2.5015(11)
M–Ge2	2.6747(14)	2.6892(5)	2.6791(8)	2.6715(12)	2.6652(9)
Ge1–Ge1	2.750(3)	2.7974(10)	2.7595(15)	2.734(2)	2.7144(17)
	$Er_3Ru_2Ge_3$	$Tm_3Ru_2Ge_3$	$Lu_3Ru_2Ge_3$	$Tb_3Ir_2Ge_3$	
*RE*1–Ge2 (×2)	2.9706(5)	2.9593(6)	2.9414(10)	3.0264(4)	
*RE*1–Ge1 (×2)	3.0164(6)	3.0095(7)	2.9968(13)	3.0180(5)	
*RE*1–Ge1 (×2)	3.1149(6)	3.1009(7)	3.0795(14)	3.2418(6)	
*RE*1–Ge1	3.5063(7)	3.4264(10)	3.410(2)	3.2453(8)	
*RE*1–*M*	3.0686(7)	3.0566(8)	3.0434(15)	3.2566(4)	
*RE*1–*M* (×2)	3.1061(6)	3.0987(6)	3.0850(12)	3.1147(3)	
*RE*1–*M*	3.1363(8)	3.1129(9)	3.0869(16)	2.9939(4)	
*RE*2–Ge1 (×2)	2.9082(9)	2.8953(10)	2.8772(18)	3.0604(7)	
*RE*2–Ge2 (×2)	2.9437(8)	2.9379(10)	2.934(2)	3.0111(8)	
*RE*2–Ge2	3.2958(12)	3.2714(14)	3.234(3)	3.1321(11)	
*RE*2–*M* (×4)	3.2057(6)	3.1924(6)	3.1723(11)	3.0849(2)	
M–Ge1 (×2)	2.4314(6)	2.4269(6)	2.4182(11)	2.4781(4)	
M–Ge1	2.5024(9)	2.4964(11)	2.494(2)	2.6684(8)	
M–Ge2	2.6587(8)	2.6514(9)	2.6399(18)	2.5803(7)	
Ge1–Ge1	2.6937(13)	2.6747(17)	2.649(4)	2.7912(14)	

Further data, in CIF format, have been sent to Fachinformationszentrum Karlsruhe, Abt. PROKA, 76344 Eggenstein-Leopoldshafen, Germany, as supplementary material No. CSD-425769 to -425777 and can be obtained by contacting FIZ (quoting the article details and the corresponding CSD numbers).

2.2.3. Band structure calculations

Tight-binding linear muffin tin orbital band structure calculations were performed on $Y_3Ru_2Ge_3$ within the local density and atomic spheres approximation with use of the Stuttgart TB-LMTO program.[22] The basis set consisted of Y 5s/5p/4d, Ru 5s/5p/4d, and Ge 4s/4p/4d orbitals, with the Y 5p and Ge 4d orbitals being downfolded. Integrations in reciprocal space were carried out with an improved tetrahedron method over 129 irreducible *k* points within the first Brillouin zone.

2.2.4. Electrical resistivity and magnetic susceptibility measurements

The identities of selected single crystals or aggregates of crystals of $RE_3Ru_2Ge_3$ (*RE* = Y, Gd–Tm, Lu) were confirmed by EDX analysis. Although these samples sometimes exhibited striations that made them unsuitable for X-ray diffraction experiments, they were sufficiently large to permit standard four-probe electrical resistivity measurements to be made between 2 and 300 K on a Quantum Design Physical Property Measurement System (PPMS) equipped with an ac transport controller (Model 7100). The current was 100 μA and the frequency was 16 Hz. Measurements were repeated at least twice for each member.

The powder sample of $Dy_3Ru_2Ge_3$ contained no other phases, so that its bulk magnetic properties could be determined reliably. Measurements of dc magnetic susceptibility were made between 2 and 300 K under an applied field of 0.5 T on a Quantum Design 9T-PPMS magnetometer. Susceptibility values were corrected for contributions from the holder and sample diamagnetism.

2.2.5. Thermal conductivity measurements

Thermal conductivity, κ, of the samples was calculated from the standard relationship $\kappa = \rho\alpha C_p$ where ρ is the density, α is the thermal diffusivity and C_p is the heat capacity at constant pressure. Density values were taken from Pearson's Crystal Database estimated by single crystal diffraction report. Heat capacity was determined at the University of Utah using a Netzsch Sirius 3500 temperature modulated differential scanning calorimeter (TM-DSC) and additionally on a Perkin Elmer Pyris 1 DSC at the University of Alberta. Small fragments were cut from the annealed arc-melted ingots and calorimetry was performed from room temperature up to 600^{o}C. Thermal diffusivity was measured on annealed arc-melted ingots. Samples were first polished to be coplanar with a thickness of 1 to 2 mm and then cut into disc shapes with either 8 or 12 mm diameters via electrical discharge machining. Samples were coated with graphite on both sides to promote uniform absorption and emission. Measurements were taken from room temperature up to 600^{o}C in 100^{o}C increments.

2.3. Results and discussion

The ternary germanides $RE_3M_2Ge_3$ (RE = Y, Gd–Tm, Lu; M = Ru, Ir) have been obtained by arc-melting reactions and determined by X-ray diffraction studies to adopt the orthorhombic $Hf_3Ni_2Si_3$-type structure.[23] This structure type is a relative rare one formed mostly by silicides $Zr_3M_2Si_3$ (M = Fe, Co),[23] $Hf_3M_2Si_3$ (M = Fe, Co, Ni),[23] $RE_3Fe_2Si_3$ (RE = Gd–Tm, Lu, Y, Sc),[24,25] $RE_3Co_2Si_3$ (RE = Tb–Tm, Lu, Y, Sc),[24-26] $Sc_3Ni_2Si_3$,[27] and $Y_3M_2Si_3$ (M = Rh, Pd);[28] and germanides $Gd_3Mn_2Ge_3$,[29] $RE_3Fe_2Ge_3$ (RE = Er, Tm),[30] $RE_3Co_2Ge_3$ (RE = Sm–Tm, Y, Sc),[31-34] $Ho_3M_2Ge_3$ (M = Ru, Rh, Ir),[10-13,35] $Lu_3M_2Ge_3$ (M = Ni, Ir),[14,36] and $RE_3Li_2Ge_3$ (RE = Tm, Lu).[37] It may also be considered to be an ordered variant of the binary phases Ca_3Ga_5 and Sr_3In_5,[38] from which can be derived ternary triel-containing representatives $A_3M'_xM''_{5-x}$ (A = Ca, Sr; M', M'' = Al, Ga, In) and Sr_3In_4Pb.[39] Whereas the $RE_3Ru_2Ge_3$ series was relatively straightforward to synthesize, the $RE_3Ir_2Ge_3$ samples were generally formed together with RE_2IrGe_2 and REIrGe phases. The RE_2IrGe_2 series was previously limited to only two known members (RE = Nd, Yb) but has now been considerably expanded (RE = Y, Gd–Dy, Er); these compounds adopt the monoclinic Sc_2CoSi_2-type structure,[26] which is closely related to the $Hf_3Ni_2Si_3$-type structure, as explained further below. The unit cell volumes decrease regularly through the lanthanide members in $RE_3M_2Ge_3$ (M = Ru, Ir) and RE_2IrGe_2 (Figure 2-1). The cell volumes are similar for $RE_3Ru_2Ge_3$ and $RE_3Ir_2Ge_3$, reflecting the nearly identical metallic radii of Ru (1.25 Å) and Ir (1.26 Å).[40]

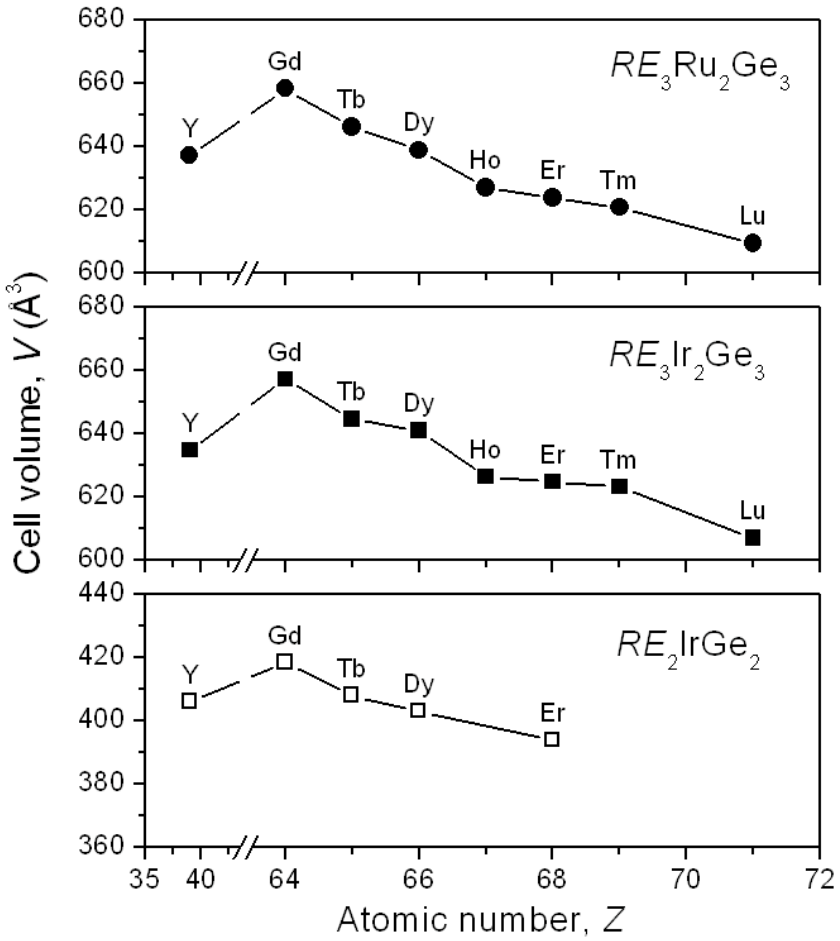

Figure 2-1 Plot of cell volumes vs. *RE* in $RE_3Ru_2Ge_3$, $RE_3Ir_2Ge_3$, and RE_2IrGe_2 phases obtained in this work.

The $Hf_3Ni_2Si_3$-type structure has been described in several ways in the literature.[10,14,23-28] Here, we make the assumption that the *RE* atoms in $RE_3M_2Ge_3$ participate in more ionic bonding and focus on the covalent framework [M_2Ge_3], which consists of layers that are built up of MGe_4 tetrahedra and lie parallel to the *ac*-plane (Figure 2-2). Double-chains of edge-sharing tetrahedra propagate along the *a*-direction; in turn, these chains are connected by corner-sharing along the *c*-direction. The MGe_4 tetrahedra are highly distorted. Three of the *M*–Ge bonds are close to the sum of the

metallic radii (Ru–Ge, 2.49 Å; Ir–Ge, 2.51 Å)[40] whereas the fourth is markedly longer; for example, the $RuGe_4$ tetrahedra in $Gd_3Ru_2Ge_3$ have Ru–Ge distances of 2.4488(3)–2.5078(6) Å to three Ge1 atoms vs. 2.6892(5) Å to the fourth Ge2 atom. Moreover, the angles within these tetrahedra deviate significantly from the ideal values; for example, the Ge–Ru–Ge angles lie in the range 98.81(2)–120.92(2)° for $Gd_3Ru_2Ge_3$. The [M_2Ge_3] layers are separated from each other by intervening *RE* atoms, but there appear to be weak Ge1–Ge1 interactions that bridge these layers together. These Ge1–Ge1 distances become as short as 2.649(4) Å in $Lu_3Ru_2Ge_3$, which can be compared to distances found in Ge_2 dimers in Gd_2MgGe_2 (2.525(3) Å)[41] or Ge_3 trimers in *RE*$CrGe_3$ (2.604(1)–2.575(3) Å).[2] Whether the Ge1–Ge1 distances correspond to true bonding interactions is a question that can be addressed by evaluation of the band structure, presented later. The occurrence of similar bridges or "dumbbells" that connect these covalent layers has also been noted in other $Hf_3Ni_2Si_3$-type compounds such as $Lu_3Ir_2Ge_3$[14] and Sr_3In_4Pb.[39]

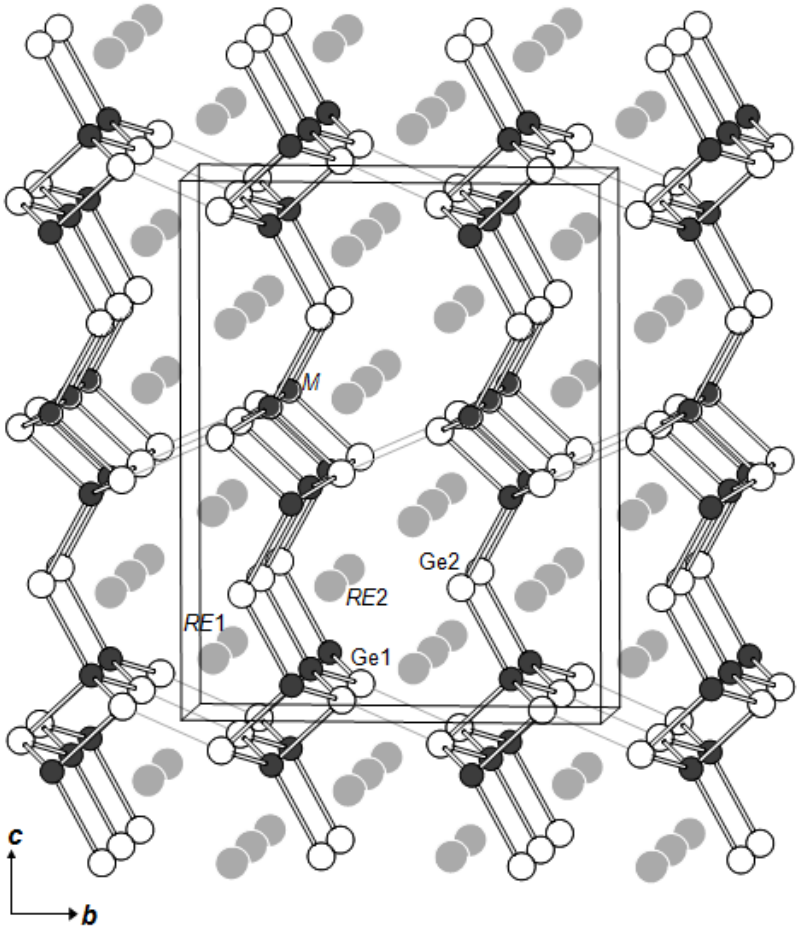

Figurre 2-2 Structure of $RE_3M_2Ge_3$ (M = Ru, Ir) highlighting [M_2Ge_3] layers separated by *RE* atoms. The large shaded circles are *RE* atoms, the small solid circles are *M* atoms, and the medium open circles are Ge atoms.

The more conventional way to describe $Hf_3Ni_2Si_3$-type compounds draws attention to the connectivity of trigonal prisms centred by the p-block element. This approach has the advantage of revealing close relationships to other structures. In particular, $RE_3M_2Ge_3$ (M = Ru, Ir) ($Hf_3Ni_2Si_3$-type) and RE_2IrGe_2 (Sc_2CoSi_2-type) can now be clearly seen to be members of a structural family (Figure 2-3). There are two types of centred trigonal prisms: RE_4M_2 prisms centred by Ge1 atoms and RE_6 prisms centred by Ge2 atoms. The RE_4M_2 prisms share a common quadrilateral RE_4 face

straddled across by the Ge1–Ge1 pairs. Both types of prisms extend as columns along the short-axis direction (*a*-axis in $RE_3M_2Ge_3$ and *b*-axis in RE_2IrGe_2) by sharing opposite triangular faces, and in turn, these columns extend as sheets by sharing common prism edges. These sheets are displaced by half the short-axis parameter with respect to each other. The $Hf_3Ni_2Si_3$-type structure has also been described in terms of intergrown slabs cut either from $MgCuAl_2$ and α-TlI structures,[23] or from CrB-, $ThCr_2Si_2$-, and W-type structures,[27] depending on what structural evolution one wants to emphasize. In the progression from $RE_3M_2Ge_3$ (*M* = Ru, Ir) to RE_2IrGe_2, it is sufficient to identify the presence of CrB- and $ThCr_2Si_2$-type slabs which alternate as they stack together. The general formula $RE_{2+n}M_2Ge_{2+n}$ then applies,[27] with *n* indicating the thickness of the CrB-type slabs in $RE_3M_2Ge_3$ (*n* = 1) and RE_2IrGe_2 (*n* = 2).

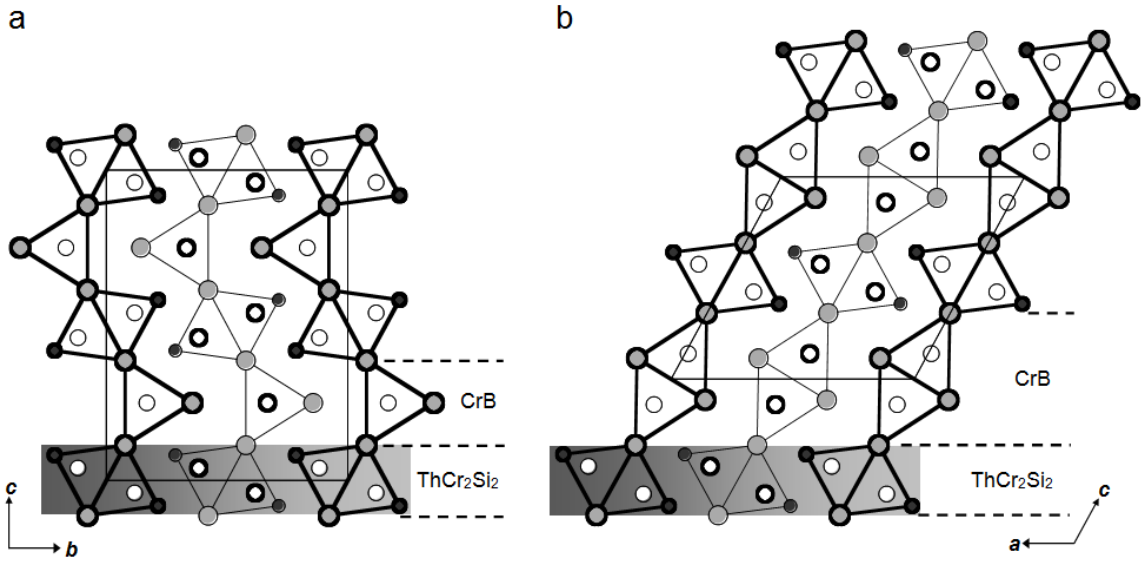

Figure 2-3. Comparison of $RE_3M_2Ge_3$ (*M* = Ru, Ir) ($Hf_3Ni_2Si_3$-type structure) and RE_2IrGe_2 (Sc_2CoSi_2-type structure), built up of Ge-centred trigonal prisms that are arranged in CrB- and $ThCr_2Si_2$-type slabs. Thick and thin lines distinguish atoms displaced by half the short-axis parameter.

The band structure was calculated for $Y_3Ru_2Ge_3$, a member of the $RE_3Ru_2Ge_3$ series free of the complications introduced by f-electrons in the *RE* component. Consistent with the high metal content, the density of states (DOS) curve features a wide manifold extending from –5 eV upwards that is derived from substantial mixing of Y 4d, Ru 4d, and Ge 4p states (Figure 2-4a). This mixing implies that despite the electron transfer that would be expected to occur from Y to Ru and Ge atoms (cf. Pauling electronegativities of 1.2 for Y, 2.2 for Ru, and 2.0 for Ge),[40] there is a significant covalent component to the bonding of Y to these other atoms. Metallic behaviour is predicted, although it should be noted that the Fermi level is close to a pseudogap. The narrower bands lying much deeper in energy, from –11 to –8 eV, are primarily based on Ge 4s states. The crystal orbital Hamilton population (COHP) curves reveal that the major bonding interactions come from Y–Ge, Y–Ru, and Ru–Ge contacts (Figure 2-4b). The electron count corresponds to a compromise between underfilling bonding levels still available for Y–Ge and Y–Ru interactions and overfilling antibonding levels for Ru–Ge interactions. Intrinsically, the Ru–Ge interactions are much stronger than the Y–Ge and Y–Ru interactions (cf. integrated COHP, or –ICOHP values, of 1.8 eV/bond for Ru–Ge, 0.5 eV/bond for Y–Ge and 0.5 eV/bond for Y–Ru), supporting the picture of [M_2Ge_3] layers sandwiched by *RE* atoms, presented above. However, there are a greater number of contacts to the Y atoms such that the Y–Ge and Y–Ru interactions together contribute more (57%) than the Ru–Ge interactions (41%) to the overall covalent bonding stability of the compound. Interestingly, the Ge1–Ge1 bridge (2.7 Å) provides only very weak bonding (–ICOHP of 0.3 eV/bond), much less significant than the other contributions, as

a result of ineffective orbital overlap and the nearly equal occupation of bonding and antibonding levels, as seen in the COHP curve.

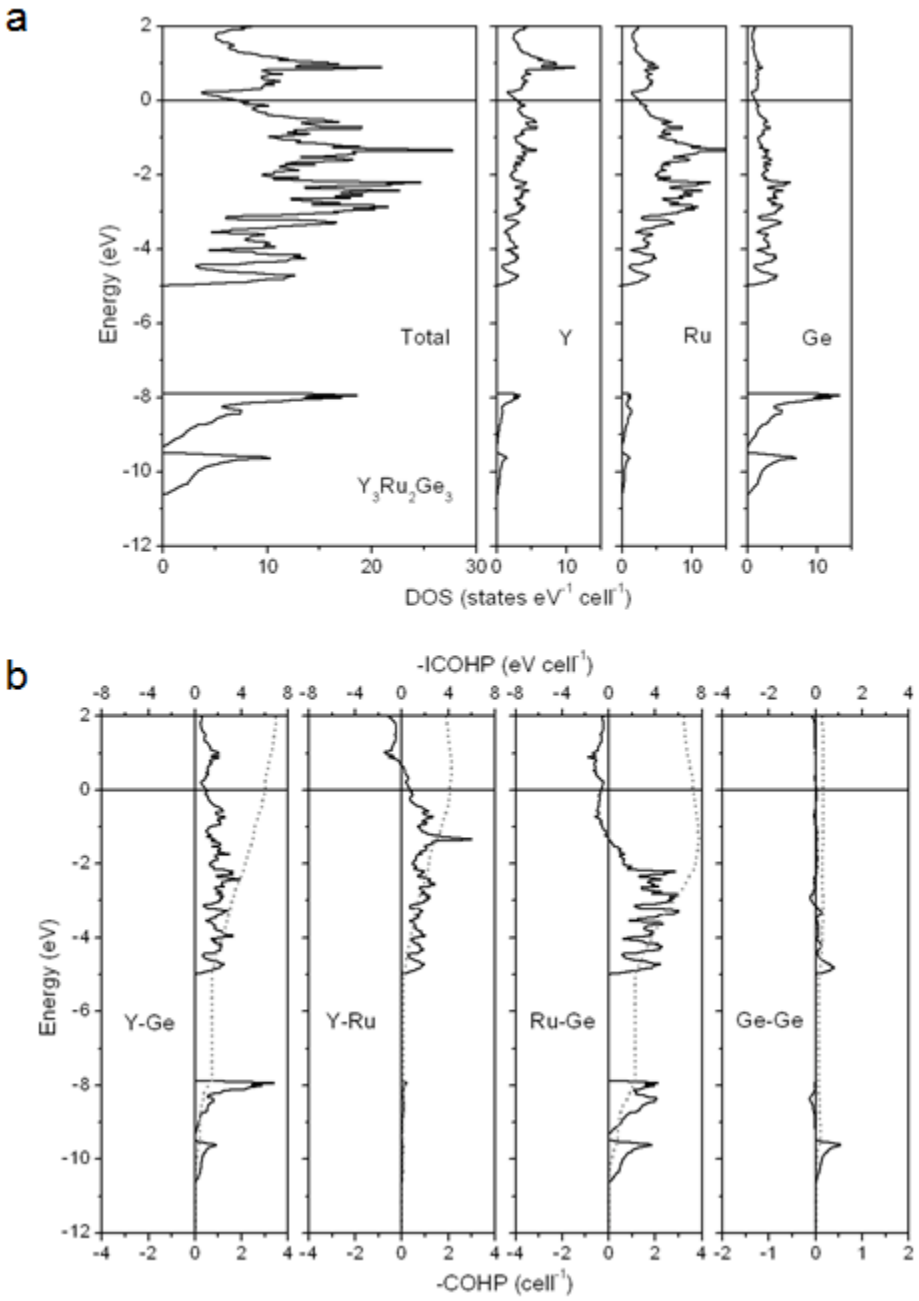

Figure 2-4. (a) Density of states (DOS) and its atomic projections for $Y_3Ru_2Ge_3$. (b) Crystal orbital Hamilton population (–COHP) curves for Y–Ge, Y–Ru, Ru–Ge, and Ge–Ge contacts. The Fermi level is at 0 eV.

From the electronic structure calculated for $Y_3Ru_2Ge_3$, it is anticipated that $RE_3Ru_2Ge_3$ compounds should exhibit metallic behaviour. The temperature dependence of the electrical resistivity does confirm this expectation for most members of $RE_3Ru_2Ge_3$ except for $Y_3Ru_2Ge_3$ itself (Figure 2-5). For *RE* = Gd, Tb, Ho, Er, Tm, Lu, the low absolute resistivities (ρ_{2K} = 10–60 μΩ·cm), the relative resistivity ratios (RRR = ρ_{300K}/ρ_{2K} = 3–10), and the positive temperature coefficient are typical of many intermetallic compounds. The Dy member behaves similarly but shows somewhat higher resistivity, probably because of variations in grain boundary effects. Prominent transitions take place at low temperature for $Gd_3Ru_2Ge_3$ and $Tb_3Ru_2Ge_3$. There is a sudden decrease in resistivity below 20 K in $Gd_3Ru_2Ge_3$, suggestive of a loss of spin-disorder scattering, on the assumption that magnetic ordering takes place at this temperature. On the other hand, $Tb_3Ru_2Ge_3$ undergoes an upturn in resistivity at 15 K, followed quickly by a plateau. Although the changes in resistivity are smaller, $Dy_3Ru_2Ge_3$ exhibits both an upturn at 12 K and a downturn at 8 K, possibly followed by a leveling off near 3 K. Similar anomalies observed in other materials are typically attributed to the Kondo effect or spin localization,[7,9] but further measurements are required to understand the origin of this upturn. Remarkably, the resistivity for $Y_3Ru_2Ge_3$ increases continuously as the temperature is lowered from 300 to 2 K, reminiscent of a highly degenerate semiconductor (with a small energy gap) or a semimetal (with a zero energy gap). The measurement is reproducible over several specimens. As noted in the examination of the band structure above, there is a pseudogap in the DOS curve that lies only 0.2 eV above the Fermi level. The phenomenon of a rare-

earth intermetallic series exhibiting metallic or semiconducting behaviour depending on the *RE* component is unusual, but has been observed in related germanide systems such as $RE_3Ru_4Ge_{13}$[6,42] and $RE_2Ir_3Ge_5$.[9] As well, $Y_3Ir_4Ge_{13}$ has been shown to display activated behaviour with a saturation regime in its resistivity.[7]

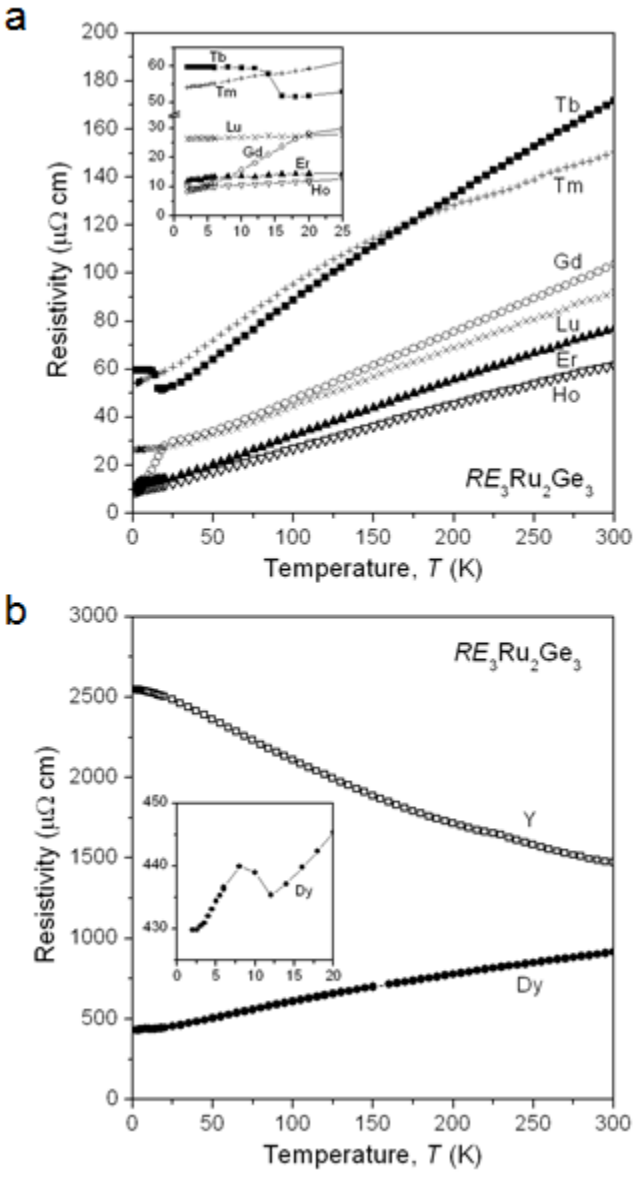

Figure 2-5 Plots of electrical resistivity for $RE_3Ru_2Ge_3$: (a) *RE* = Gd, Tb, Ho, Er, Tm, Lu. (b) *RE* = Y, Dy. The insets highlight the low-temperature behaviour.

Six members of $RE_3Ru_2Ge_3$ series (RE = Y, Gd–Tm) were synthesized in a form of large ingots and shaped into cylinders with diameter 12.7 mm and thickness 2–4 mm for thermal conductivity measurements. Thermal diffusivity values were collected at room temperature, 50, 100, 150, 200 °C and every 100 degrees up to 600 °C. Thermal conductivity, κ, was calculated from the standard relationship $\kappa = \rho\alpha C_p$ where ρ is the density, α is the thermal diffusivity and C_p is the heat. The thermal conductivity of the samples varies from 26 to 12 W m^{-1} K^{-1} depending on the sample, however the values at high temperatures tend to stay constant (Figure 2-6). For $Y_3Ru_2Ge_3$ compound thermal conductivity has a decreasing trend (from 13 to 2 W m^{-1} K^{-1}) with increasing temperatures, which is typical for metallic compounds.

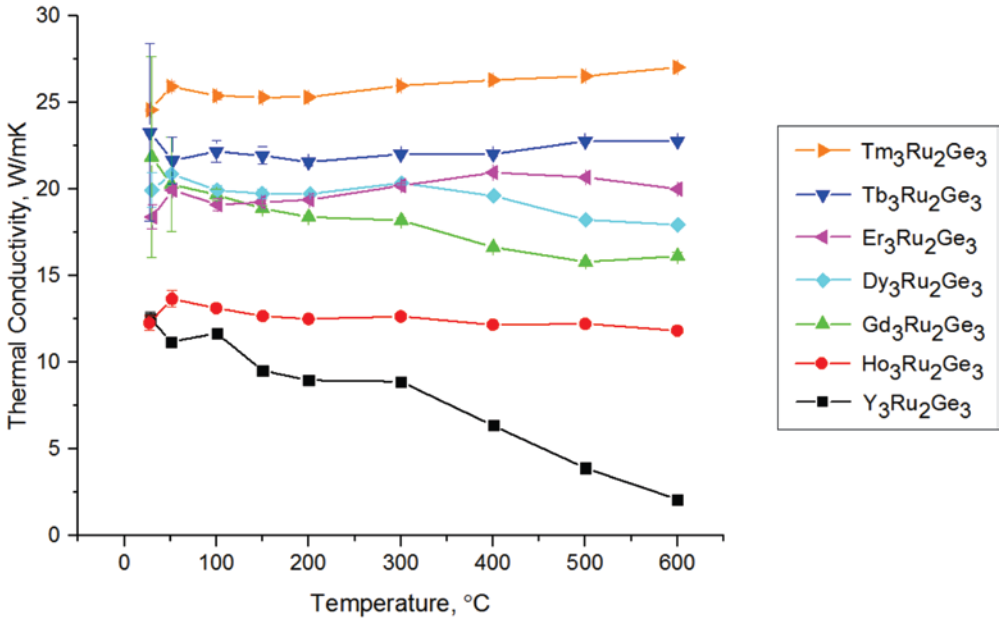

Figure 2-6 Thermal conductivity of the $RE_3Ru_2Ge_3$ series (RE = Y, Gd–Tm) compounds.

The magnetic properties of $Dy_3Ru_2Ge_3$, which could be prepared free from other phases, were examined. The temperature dependence of the magnetic susceptibility,

measured under an applied field of 0.5 T, indicates paramagnetic behaviour above 50 K but subtle kinks are evident at lower temperature, including a maximum suggesting antiferromagnetic ordering below a Néel temperature of 3 K (Figure 2-6a). The inverse magnetic susceptibility is linear at high temperature (50 to 300 K) and can be fit to the Curie-Weiss law, $\chi = C / (T - \theta_p)$. The resulting effective magnetic moment μ_{eff} is 18.4(1) μ_B per formula unit, or 10.6(1) μ_B per Dy atom, which agrees well with the theoretical free-ion value of 10.64 μ_B for Dy^{3+}. This agreement implies that the Ru atoms do not contribute to the magnetic moment, a common situation for many f-d intermetallics in which the d-orbitals of the transition-metal component are strongly delocalized. The Weiss constant θ_p is –10(1) K, the negative value being consistent with antiferromagnetic coupling of the Dy^{3+} moments. Magnetic measurements made on most members, but not the Dy one, of the corresponding cobalt-containing series $RE_3Co_2Ge_3$ generally also show antiferromagnetic ordering; a complex non-collinear spiral magnetic structure that undergoes field-dependent transitions has been proposed from neutron diffraction studies on $Tb_3Co_2Ge_3$.[34] Similarly, the magnetization of $Dy_3Ru_2Ge_3$ at 4 K reveals at least two transitions as the applied field is increased, a sharp one at 2 kOe and a more subtle inflection near 25 kOe (Figure 2-6b). The magnetization is hysteretic as the field is decreased but the loop closes below 15 kOe. The most interesting feature is a sudden jump observed at 38 kOe (upon increasing field) when the isothermal magnetization measurements are conducted at 2.0 and 2.5 K, below the Néel temperature (Figure 2-6c). These multiple metamagnetic transitions likely originate from spin reorientation (spin flips) in the antiferromagnetic arrangement, if the magnetic structure is

assumed to be similar to $Tb_3Co_2Ge_3$,[34] but detailed interpretation will require further measurements through neutron diffraction experiments.

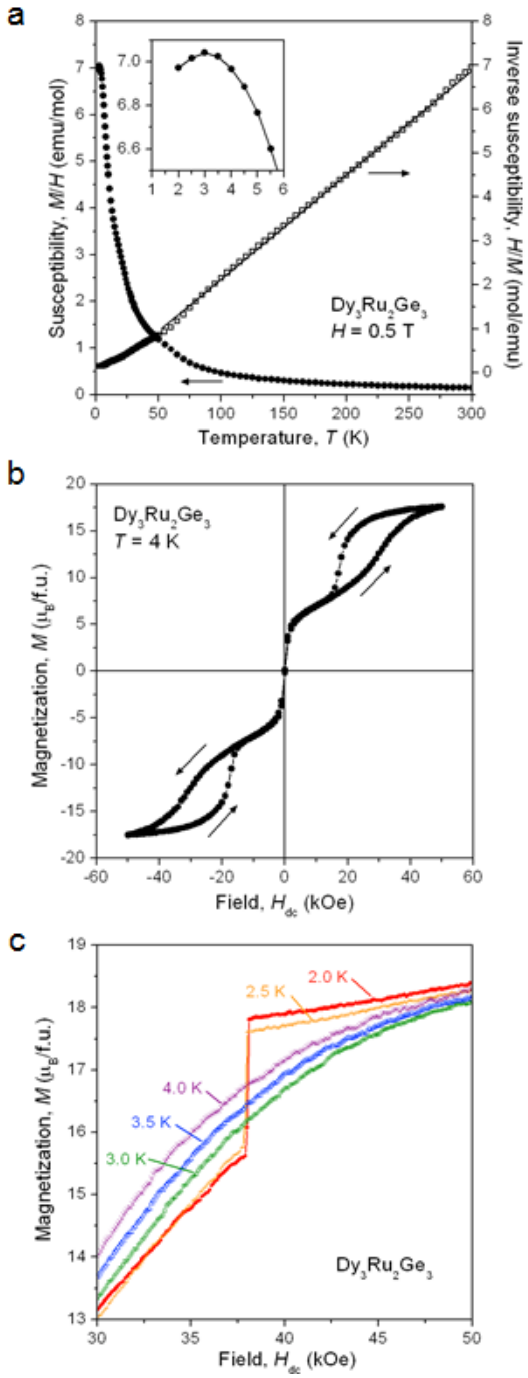

Figure 2-6 $Dy_3Ru_2Ge_3$: (a) Magnetic susceptibility and its inverse as a function of temperature. (b) Magnetization at 4 K under applied fields from –50 to +50 kOe. (c) Magnetization vs. field at different temperatures.

2.4. Conclusions

Ternary rare-earth germanides $RE_3M_2Ge_3$ with the $Hf_3Ni_2Si_3$-type structure have been established for M = Ru, Ir, and it will be worthwhile to attempt the preparation of the analogous series with M = Os, Rh. Although the conventional description in terms of Ge-centred RE_4M_2 and RE_6 trigonal prisms is helpful in clarifying relationships to other structures, the alternative description that emphasizes the presence of $[M_2Ge_3]$ layers is more accurate in portraying the strong covalent M–Ge bonding interactions that occur in this structure, as confirmed by band structure calculations on $Y_3Ru_2Ge_3$. However, the Ge1–Ge1 bridges that appear to connect these layers are insignificant and, instead, there are important contributions from Y–Ge and Y–Ru covalent interactions. The electrical resistivity for most members of $RE_3Ru_2Ge_3$ reveals metallic behaviour but $Y_3Ru_2Ge_3$ itself is anomalous in displaying semiconductor-like behaviour, which may be related to the presence of a pseudogap near the Fermi level. $Y_3Ru_2Ge_3$ exhibits low thermal conductivity and further measurements of other physical properties are in progress to evaluate the feasibility of this potential thermoelectric material. $Dy_3Ru_2Ge_3$ undergoes antiferromagnetic ordering and complex field-dependent transitions that portend diverse magnetic behaviour for the other $RE_3Ru_2Ge_3$ members.

2.5 References

[1] Salamakha, P. S.; Sologub, O. L.; Bodak, O. I.; in: Gschneidner Jr., K. A.; Eyring L. (Eds.), *Handbook on the Physics and Chemistry of Rare Earths*, vol. 27, Elsevier, Amsterdam, 1999, pp. 1–223.

[2] Bie, H.; Zelinska, O. Ya.; Tkachuk, A. V.; Mar, A. *Chem. Mater.* **2007**, *19*, 4613–4620.

[3] Bie, H.; Mar, A. J. *Mater. Chem.* **2009**, *19*, 6225–6230.

[4] Bie, H.; Tkachuk, A. V.; Mar, A. *J. Solid State Chem.* **2009**, *182*, 122–128.

[5] Tegus, O.; Duong, N. P.; Dagula, W.; Zhang, L.; Brück, E.; Buschow, K. H. J.; de Boer, F. R. *J. Appl. Phys.* **2002**, *91*, 8528–8530.

[6] Kong, H.; Shi, X.; Uher, C.; Morelli, D. T. *J. Appl. Phys.* **2007**, *102*, 023702-1–023702-5.

[7] Strydom, A. M. *J. Phys.: Condens. Matter* **2007**, *19*, 386205-1–386205-15.

[8] Venturini, G.; Méot-Meyer, M.; Marêché, J. F.; Malaman, B.; Roques, B. *Mater. Res. Bull.* **1986**, *21*, 33–39.

[9] Singh, Y.; Ramakrishnan, S. *Phys. Rev. B* **2004**, *69*, 174423-1–174423-13.

[10] Sologub, O. L.; Prots', Yu. M.; Salamakha, P. S.; Bodak, O. I. *J. Alloys Compd.* **1994**, *209*, 107–109.

[11] Sologub, O. L.; Prots', Yu. M.; Salamakha, P. S.; Bodak, O. I. Stępień-Damm, J. *Pol. J. Chem.* **1995**, *69*, 423–426.

[12] Sologub, O. L.; Hiebl, K.; Rogl, P.; Noël, H. *J. Alloys Compd.* **1996**, *245*, L13–L17.

[13] Salamakha, P.; Sologub, O.; Stępień-Damm, J.; Stash, A. *Kristallografiya* **1996**, *41*, 1135–1136.

[14] Rodewald, U. Ch.; Pöttgen, R. *Solid State Sci.* **2003**, *5*, 487–493.

[15] Boulet, P.; Weitzer, F.; Hiebl, K.; Noël, H. *Physica B* **2000**, *292*, 302–319.

[16] Salamakha, P. S.; Bodak, O. I.; Pecharskii, V. K.; Bel'skii, V. K. *Izv. Akad. Nauk SSSR, Metally* (**1989**) 206–208.

[17] Hovestreydt, E.; Engel, N.; Klepp, K.; Chabot, B.; Parthé, E. *J. Less-Common Met.* **1982**, *85*, 247–274.

[18] Penc, B.; Hofmann, M.; Leciejewicz, J.; Ślaski, M.; Szytuła, A. *J. Alloys Compd.* **1999**, *287*, 18–24.

[19] Akselrud, L. G.; Zavalii, P. Yu.; Grin, Yu. N. Pecharski, V. K.; Baumgartner, B.; Wölfel, E. *Mater. Sci. Forum* **1993**, *133–136*, 335–342.

[20] Sheldrick, G. M. SHELXTL, version 6.12, Bruker AXS Inc., Madison, WI, 2001.

[21] Gelato, L. M.; Parthé, E. *J. Appl. Crystallogr.* **1987**, *20*, 139–143.

[22] Tank, R.; Jepsen, O.; Burkhardt, A.; Andersen, O. K. TB-LMTO-ASA Program, version 4.7, Max Planck Institut für Festkörperforschung, Stuttgart, Germany, 1998.

[23] Yarmolyuk, Ya. P.; Grin', Yu. N.; Gladyshevskii, E. I. *Kristallografiya* **1977**, *22*, 726–730.

[24] Welter, R.; Ijjalli, I.; Venturini, G.; Malaman, B. *J. Alloys Compd.* **1997**, *257*, 196–200.

[25] Chabot, B.; Engel, N.; Parthé, E. *J. Less-Common Met.* **1984**, *96*, 331–340.

[26] Gladyshevskii, E. I.; Kotur, B. Ya. *Kristallografiya* **1987**, *23*, 946–950.

[27] Zhao, J. T.; Parthé, E. *Acta Crystallogr., Sect. C* **1989**, *45*, 1853–1856.

[28] Paccard, D.; Le Roy, J.; Moreau, J. M. *Acta Crystallogr., Sect. B* **1982**, *38*, 2448–2449.

[29] Markiv, V. Ya.; Beloborodova, E. A.; Belyavina, N. N.; Alekseeva, N. V. *Dopov. Akad. Nauk Ukr.* (**1993**) 70–73.

[30] Bodak, O. I.; Oleksin, O. Ya.; Fedyna, M. F.; Pecharskii, V. K. *Neorg. Mater.* **1992**, *28*, 493–497.

[31] Kotur, B. Ya.; Andrusyak, R. I. *Neorg. Mater.* **1991**, *27*, 1433–1439.

[32] Morozkin, A. V.; Yao, J.; Mozharivskyj, Yu. *Intermetallics* **2012**, *21*, 115–120.

[33] Morozkin, A. V. *Intermetallics* **2012**, *25*, 136–138.

[34] Morozkin, A. V.; Nirmala, R.; Yao, J.; Mozharivskyj, Y.; Isnard, O. *J. Solid State Chem.* **2012**, *196*, 93–99.

[35] Sologub, O. L.; Stash, A.; Zavodnik, V. E.; Salamakha, P. S.; Bodak, O. I. *Coll. Abs. 6th Int. Conf. Crystal Chem. Intermet. Compd.* (Lvov) (**1995**) 96.

[36] Koterlyn, G. M.; Bodak, O. I.; Pavlyuk, V. V.; Stępień-Damm, J.; Pietraszko, A. *J. Alloys Compd.* **1999**, *291*, 110–116.

[37] Pavlyuk, V. V.; Bodak, O. I. *Neorg. Mater.* **1992**, *28*, 1119–1121.

[38] Seo, D.-K.; Corbett, J. D. *J. Am. Chem. Soc.* **2001**, *123*, 4512–4518.

[39] Rhode, M.; Wendorff, M.; Röhr, C. *Z. Anorg. Allg. Chem.* **2006**, *632*, 1195–1205.

[40] Pauling, L. *The Nature of the Chemical Bond*, 3rd ed., Cornell University Press, Ithaca, NY, 1960.

[41] Choe, W.; Miller, G. J.; Levin, E. M. *J. Alloys Compd.* **2001**, *329*, 121–130.

[42] Ghosh, K.; Ramakrishnan, S.; Chandra, G. *Phys. Rev. B* **1993**, *48*, 10435–10439.

Chapter 3

Ternary rare-earth manganese germanides $RE_3Mn_2Ge_3$ (*RE* = Ce–Nd) and a possible oxygen-interstitial derivative $Nd_4Mn_2Ge_5O_{0.6}$

A version of this chapter has been published. Oliynyk, A. O.; Djama-Kayad, K.; Mar, A. J. Alloys Compd. 2014, 602, 130–134.

3.1. Introduction

Ternary rare-earth transition-metal germanium systems *RE*–*M*–Ge reveal many phases with diverse structures;[1,2] they often exhibit complicated electrical and magnetic behaviour as a result of interactions between the localized f-electrons on the *RE* atoms with the delocalized d-electrons on the *M* atoms. Among these, $RE_3M_2Ge_3$ phases with the $Hf_3Ni_2Si_3$-type structure were previously known mostly for later first-row transition-metal components and a few isolated members containing precious metals, generally in combination with smaller rare-earth components: $RE_3Fe_2Ge_3$ (*RE* = Er, Tm),[3] $RE_3Co_2Ge_3$ (*RE* = Sm–Tm, Y, Sc),[4-7] $Ho_3M_2Ge_3$ (*M* = Ru, Rh, Ir),[8-12] and $Lu_3M_2Ge_3$ (*M* = Ni, Ir).[13,14] The Mn-containing compound $Gd_3Mn_2Ge_3$ has been reported at a conference but no crystallographic details have been forthcoming.[15] Recently we have extended the $RE_3Ru_2Ge_3$ and $RE_3Ir_2Ge_3$ series considerably to *RE* = Y, Gd–Tm, Lu.[16] Related Li-containing members $RE_3Li_2Ge_3$ (*RE* = Tm, Lu) have also been prepared.[17]

In the course of investigating the Ce–Mn–Ge system at 800 °C, it was noted that the formation of a ternary phase with approximate composition "$Ce_{40}Mn_{25}Ge_{35}$",[18] which

does not appear in the phase diagram at 400 °C,[1] and suspected that it corresponds to a $Hf_3Ni_2Si_3$-type phase. Herein the existence of the series $RE_3Mn_2Ge_3$ (*RE* = Ce, Pr, Nd) phases adopting the $Hf_3Ni_2Si_3$-type structure has been confirmed and magnetic data on these compounds has been reported. The structure of an oxygen-interstitial derivative $Nd_4Mn_2Ge_5O_{0.6}$ obtained as an unexpected minor oxidation product in the reaction involving Nd has been described.

3.2. Experimental

3.2.1. Synthesis

Starting materials were *RE* pieces (*RE* = La–Nd, Sm, Gd–Tm, Lu, 99.9%, Hefa) which were freshly filed to remove surface oxide layers, Mn powder (99.96%, Cerac), and Ge powder (99.9999%, Alfa-Aesar). Mixtures in a total mass of 0.3 g and with various loading compositions within 1% of "$RE_3Mn_2Ge_3$" were pressed into pellets and arc-melted twice in a Centorr 5TA tri-arc furnace on a water-cooled copper hearth under an argon atmosphere. Weight losses after arc-melting never exceeded 1%. To improve homogeneity, the ingots were sealed within fused-silica tubes and annealed at 800 °C for 1 week, followed by quenching in cold water. Powder X-ray diffraction (XRD) patterns, collected with Cu $K\alpha_1$ radiation on an Inel diffractometer equipped with a curved position-sensitive detector (CPS 120), were examined to detect the formation of the desired ternary phase. The $RE_3Mn_2Ge_3$ series was found to be limited to *RE* = Ce–Nd; attempts to prepare analogous compounds with other *RE* metals were unsuccessful under these conditions. Cell parameters for these orthorhombic phases were refined from the powder XRD data with use of the CSD suite of programs[19] and are listed in Table 3-1.

Energy-dispersive X-ray (EDX) analysis on a JEOL JSM-6010LA scanning electron microscope confirmed the expected chemical composition (e.g., 39(3)% Nd, 27(2)% Mn, 34(3)% Ge for the $Nd_3Mn_2Ge_3$ sample).

Table 3-1 Cell parameters for $RE_3Mn_2Ge_3$. [a]

Compound	*a* (Å)	*b* (Å)	*c* (Å)	*V* (Å^3)
$Ce_3Mn_2Ge_3$	4.3255(8)	11.621(2)	14.660(2)	736.9(4)
$Pr_3Mn_2Ge_3$	4.3157(8)	11.525(2)	14.564(2)	724.4(4)
$Nd_3Mn_2Ge_3$	4.2929(8)	11.524(3)	14.473(3)	716.0(5)

[a] Refined from powder X-ray diffraction data.

3.2.2. Structure determination

The samples of $RE_3Mn_2Ge_3$ (*RE* = Ce, Pr, Nd) were inspected to select single crystals for X-ray diffraction analysis but suitably sized and well-diffracting crystals were available only for $Ce_3Mn_2Ge_3$. Intensity data were collected on a Bruker PLATFORM diffractometer equipped with a SMART APEX II CCD area detector and a graphite-monochromated Mo $K\alpha$ radiation source, using ω scans to generate 8 sets of frames at different ϕ angles with a frame width of 0.3º and an exposure time of 12 s per frame. Face-indexed absorption corrections were applied. Structure solution and refinement were carried out with use of the SHELXTL (version 6.12) program package.[20] The centrosymmetric orthorhombic space group *Cmcm* was chosen on the basis of Laue symmetry, systematic absences, and intensity statistics. A model based on the $Hf_3Ni_2Si_3$-type structure was suggested by direct methods. Atomic positions were standardized with the program STRUCTURE TIDY.[21] Refinements proceeded without complications, leading to good agreement factors and a featureless difference map.

On close examination, the surface of the $Nd_3Mn_2Ge_3$ ingot was found to contain about a dozen very small crystals (~20 μm in their longest dimension). It is evident that these crystals are not representative of the bulk sample (for which powder X-ray diffraction clearly indicates a $Hf_3Ni_2Si_3$-type phase). Out of curiosity, one of these crystals was selected and found to diffract surprisingly well. Data collection parameters were the same as described above but now the centrosymmetric monoclinic space group *C*2/*m* was chosen and an initial model "$Nd_4Mn_2Ge_5$" apparently based on the structure of $Yb_4Mn_2Sn_5$ (a ternary ordered derivative of the Mg_5Si_6-type structure)[22] was suggested by direct methods. Refinements led to good agreement factors ($R(F)$ for $F_o^2 > 2\sigma(F_o^2)$ of 0.041) and all sites were fully occupied with reasonable displacement parameters. However, the difference map revealed some residual electron density (~8 $e^-/Å^3$) located at the centre of an octahedron at distances of 2.7 Å to four Nd atoms and 2.2 Å to two Ge atoms. This is similar to the situation in $Yb_2Zn_3Ge_{3.1}$ in which an interstitial Ge atom partially fills an octahedral site at low occupancy (0.19).[23] The distances in the case of "$Nd_4Mn_2Ge_5$" preclude the occupation of this extra site with interstitial Ge atoms but seem to be compatible with ranges of literature Nd–O (2.2–2.9 Å) and Ge–O distances (1.5–2.2 Å).[24] The fact that this crystal was found in trace quantities on the surface of the ingot suggests that it may have resulted from a minor surface oxidation reaction, perhaps occuring during the arc-melting process. EDX analysis of the same crystal used for data collection does reveal the presence of an O *K*α peak at 0.52 eV, which overlaps slightly with the Mn *L*α peak at 0.64 eV (Figure A2-1), but we caution that adventitious oxygen (and carbon) surface species are often present even in non-oxygen-containing samples and that analysis of such light elements is unreliable. In the absence of more definitive

evidence, we allowed the interstitial site to be partially occupied with oxygen atoms in the structure refinement. This led to meaningfully improved agreement factors ($R(F)$ for $F_o^2 > 2\sigma(F_o^2)$ of 0.030) and a now featureless difference map ($(\Delta\rho)_{max}$, $(\Delta\rho)_{min}$ = 2.70, –2.48 $e^-/Å^3$) for the structural model "$Nd_4Mn_2Ge_5O_{0.6}$".

Crystal data and further details of the data collections are given in Table 3-2, final values of the positional and displacement parameters are given in Table 3-3, and selected interatomic distances are given in Table 3-4. Further data, in CIF format, have been sent to Fachinformationszentrum Karlsruhe, Abt. PROKA, 76344 Eggenstein-Leopoldshafen, Germany, as supplementary material No. CSD-427218 and -427219 and can be obtained by contacting FIZ (quoting the article details and the corresponding CSD numbers).

3.2.3. Magnetic susceptibility measurements

Magnetic susceptibility measurements on powder samples of $RE_3Mn_2Ge_3$ (*RE* = Ce, Pr, Nd) were made from 2 to 300 K (zero-field-cooled) under an applied field of 0.5 T on a Quantum Design 9T-PPMS magnetometer. Susceptibility values were corrected for contributions from the holder and sample diamagnetism.

Table 3-2 Crystallographic data for $Ce_3Mn_2Ge_3$ and $Nd_4Mn_2Ge_5O_{0.6}$.

Formula	$Ce_3Mn_2Ge_3$	$Nd_4Mn_2Ge_5O_{0.57(4)}$
Formula mass (amu)	748.01	1058.75
Space group	*Cmcm* (No. 63)	*C*2/*m* (No. 12)
a (Å)	4.3340(3)	16.275(3)
b (Å)	11.6069(9)	4.3779(8)
c (Å)	14.6717(12)	7.3783(14)
β (deg)	90	107.372(2)
V (Å^3)	738.05(10)	501.73(16)
Z	4	2
ρ_{calcd} (g cm^{-3})	6.732	7.008
T (K)	296	296
Crystal dimensions (mm)	0.04 × 0.03 × 0.02	0.07 × 0.02 × 0.02
Radiation	Graphite monochromated Mo *K*α, λ = 0.71073 Å	
μ(Mo *K*α) (mm^{-1})	33.32	37.37
Transmission factors	0.365–0.602	0.238–0.624
2θ limits	5.56–66.36°	5.24–66.40°
Data collected	$-6 \le h \le 6$, $-17 \le k \le 17$, $-22 \le l \le 22$	$-24 \le h \le 24$, $-6 \le k \le 6$, $-11 \le l \le 11$
No. of data collected	5302	3662
No. of unique data, including $F_o^2 < 0$	813 (R_{int} = 0.070)	1057 (R_{int} = 0.044)
No. of unique data, with $F_o^2 > 2\sigma(F_o^2)$	626	836
No. of variables	28	41
$R(F)$ for $F_o^2 > 2\sigma(F_o^2)$ [a]	0.031	0.030
$R_w(F_o^2)$ [b]	0.064	0.063
Goodness of fit	1.13	1.07
$(\Delta\rho)_{max}$, $(\Delta\rho)_{min}$ (e Å^{-3})	3.12, –1.79	2.70, –2.48

[a] $R(F) = \sum||F_o| - |F_c|| / \sum|F_o|$ for $F_o^2 > 2\sigma(F_o^2)$.

[b] $R_w(F_o^2) = [\sum[w(F_o^2 - F_c^2)^2] / \sum wF_o^4]^{1/2}$; $w^{-1} = [\sigma^2(F_o^2) + (Ap)^2 + Bp]$, where $p = [\max(F_o^2,0) + 2F_c^2] / 3$.

Table 3-3 Positional and equivalent isotropic displacement parameters (Å^2) for $Ce_3Mn_2Ge_3$ and $Nd_4Mn_2Ge_5O_{0.6}$.

Atom	Wyckoff position	*x*	*y*	*z*	U_{eq} (Å^2) [a]
$Ce_3Mn_2Ge_3$					
Ce1	8*f*	0	0.07077(4)	0.11522(3)	0.01049(13)
Ce2	4*c*	0	0.36059(6)	¼	0.01186(16)
Mn	8*f*	0	0.22280(12)	0.58153(10)	0.0133(3)
Ge1	8*f*	0	0.38722(8)	0.04217(6)	0.0120(2)
Ge2	4*c*	0	0.66482(13)	¼	0.0140(3)
$Nd_4Mn_2Ge_5O_{0.6}$					
Nd1	4*i*	0.34767(3)	0	0.07220(7)	0.01295(13)
Nd2	4*i*	0.58141(3)	0	0.37015(7)	0.01262(13)
Mn	4*i*	0.21878(9)	0	0.6216(2)	0.0125(3)
Ge1	4*i*	0.06232(6)	0	0.65630(14)	0.0122(2)
Ge2	4*i*	0.19551(6)	0	0.24829(14)	0.0124(2)
Ge3	2*a*	0	0	0	0.0104(3)
O [b]	2*b*	0	½	0	0.031(7)

[a] U_{eq} is defined as one-third of the trace of the orthogonalized U_{ij} tensor. [b] Occupancy of 0.57(4).

Table 3-4 Selected interatomic distances (Å) in $Ce_3Mn_2Ge_3$ and $Nd_4Mn_2Ge_5O_{0.6}$.

$Ce_3Mn_2Ge_3$			
Ce1–Ge2 (×2)	3.1301(6)	Ce2–Ge2 (×2)	3.1399(12)
Ce1–Ge1 (×2)	3.2042(8)	Ce2–Ge2	3.5313(16)
Ce1–Ge1 (×2)	3.2223(8)	Ce2–Mn (×4)	3.4267(11)
Ce1–Mn (×2)	3.2682(11)	Mn–Ge1 (×2)	2.5807(9)
Ce1–Mn	3.3833(15)	Mn–Ge1	2.6336(17)
Ce1–Mn	3.4431(15)	Mn–Ge2	2.7948(16)
Ce2–Ge1 (×2)	3.0648(10)	Ge1–Ge1	2.8958(19)
$Nd_4Mn_2Ge_5O_{0.6}$			
Nd1–Ge1 (×2)	3.0328(8)	Nd2–Mn	3.2344(16)
Nd1–Ge2	3.1212(12)	Nd2–Mn (×2)	3.2796(12)
Nd1–Ge2 (×2)	3.1440(9)	Nd2–O	2.6558(7)
Nd1–Ge3 (×2)	3.4656(6)	Mn–Ge2 (×2)	2.6190(10)
Nd1–Mn	3.3598(16)	Mn–Ge1	2.6341(18)
Nd1–Mn (×2)	3.5389(12)	Mn–Ge2	2.6661(18)
Nd1–O	2.6868(7)	Ge1–Ge1	2.577(2)
Nd2–Ge1 (×2)	3.1205(9)	Ge3–Ge1 (×2)	2.999(1)
Nd2–Ge1 (×2)	3.1669(9)	Ge3–Ge2 (×2)	3.162(1)
Nd2–Ge2 (×2)	3.1695(8)	Ge3–O (×2)	2.1890(4)
Nd2–Ge3 (×2)	3.4416(6)		

3.3. Results and discussion

The compounds $RE_3Mn_2Ge_3$ (RE = Ce–Nd) were obtained by arc-melting and annealing at 800 °C. These phases do not occur in the isothermal sections of the ternary phase diagrams previously elucidated for the Ce–Mn–Ge system at 400 °C and the Nd–Mn–Ge system at 600 °C,[1] so it can be assumed that they are stable only at higher temperatures. An earlier report suggested the existence of $Gd_3Mn_2Ge_3$, prepared at 700 °C, but no structural details were available;[15] it was not formed under our synthetic conditions at 800 °C.

Structural analysis reveals that these compounds adopt the orthorhombic $Hf_3Ni_2Si_3$-type structure,[25,26] the first Mn-containing examples to be confirmed among ternary germanides $RE_3M_2Ge_3$ previously known for M = Fe, Co, Ni, Ru, Rh, Ir, and Li.[3-17] Interestingly, the $RE_3Mn_2Ge_3$ series is limited to only larger RE components (Ce–Nd), in contrast to the other series which are formed generally with smaller RE components (Sm–Lu). It might be thought that size effects play a role, but in most scales of atomic radii, Mn has nearly the same size as Fe (e.g., Pauling R_1 values of 1.18 Å for Mn, 1.17 Å for Fe;[27] Slater radii of 1.40 Å for both Mn and Fe[28]) and the radius ratio r_M/r_{RE} is unsuccessful in providing a clear segregation.

The $Hf_3Ni_2Si_3$-type structure of $RE_3Mn_2Ge_3$ consists of layers, lying parallel to the *ac*-plane, that are built up of double-chains of edge-sharing $MnGe_4$ tetrahedra and are separated by RE atoms (Figure 3-1a). An alternative description based on Ge-centred trigonal prisms can also be made.[16] Relative to other $RE_3M_2Ge_3$ series, the structure is considerably expanded in $RE_3Mn_2Ge_3$. This results not only from the presence of larger RE components, but also longer Mn–Ge distances within the tetrahedra (2.6–2.8 Å in

$Ce_3Mn_2Ge_3$, compared to 2.4–2.6 Å in most other $RE_3M_2Ge_3$ compounds). The Ge1–Ge1 contacts straddling the layers also become very long (2.9 Å in $Ce_3Mn_2Ge_3$) to the point that they are probably nonbonding.

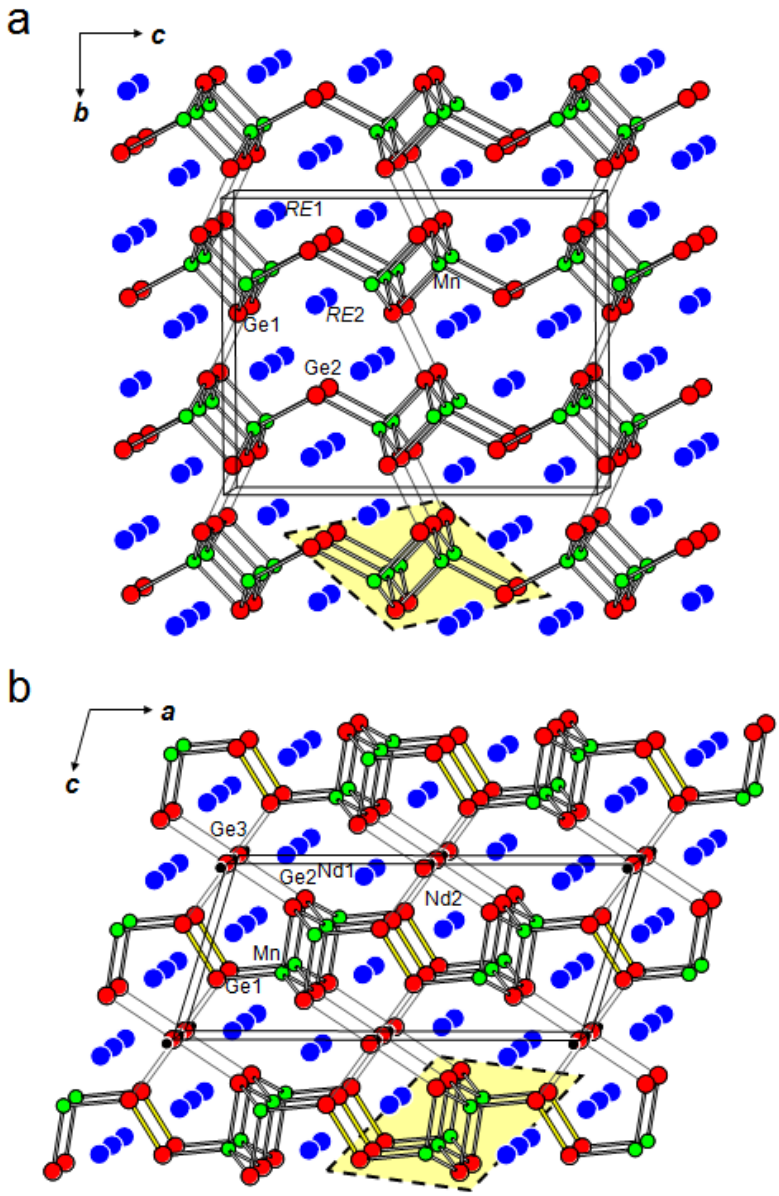

Figure 3-1 Structure of (a) $RE_3Mn_2Ge_3$ (*RE* = Ce, Pr, Nd) and (b) $Nd_4Mn_2Ge_5O_{0.6}$, built up of double-chains of $MnGe_4$ tetrahedra (highlighted by the yellow parallelograms). The large blue circles are *RE* atoms, the small green circles are Mn atoms, and the medium red circles are Ge atoms. The O atoms in (b) are shown as small black circles.

A minor oxidation product that was formed in conjunction with $Nd_3Mn_2Ge_3$ was tentatively identified to be an oxygen-interstitial germanide $Nd_4Mn_2Ge_5O_{0.6}$. The host monoclinic structure (space group $C2/m$) corresponds to that of the $Yb_4Mn_2Sn_5$-type, a ternary ordered variant of Mg_5Si_6-type.[22] Quaternary germanides $RE_4M_2InGe_4$ (M = Mn, Ni) adopt the $Ho_4Ni_2InGe_4$-type structure with a more complex site distribution.[29,30] The structure of $Nd_4Mn_2Ge_5O_{0.6}$ consists of layers, lying parallel to the *ab*-plane, that are also built up of double-chains of edge-sharing $MnGe_4$ tetrahedra but now they are connected through Ge_2 dimers (2.58 Å) (Figure 3-1b). Between the layers, there are not only Nd atoms, but also isolated Ge3 atoms that are coordinated in a square planar geometry by the surrounding Ge1 and Ge2 atoms at very long distances (3.00–3.16 Å). There are octahedral voids (Wyckoff position 2*b*) located between pairs of Ge3 atoms that are suitable to be partially occupied with interstitial oxygen atoms. The only other example of a compound crystallizing in this space group with Wyckoff sequence i^5ba is La_4PdO_7, which also has octahedral voids filled with oxygen atoms in 2*b*, but the connectivity of structural elements is otherwise quite different.[31] Test reactions with the composition "$Nd_4Mn_2Ge_5O_{1-x}$" are in progress to determine if the interstitial oxygen atoms are intrinsic to the stabilization of this structure. The occurrence of isolated Ge atoms in the host structure is certainly unusual, and contrasts with other cases in which occupation of larger atoms in the same site at similar distances of 3.0 Å to surrounding atoms implies weak bonding ($SnSn_4$ square planes in $Yb_4Mn_2Sn_5$[22] or $InGe_4$ square planes in $RE_4M_2InGe_4$ (M = Mn, Ni).[29,30]

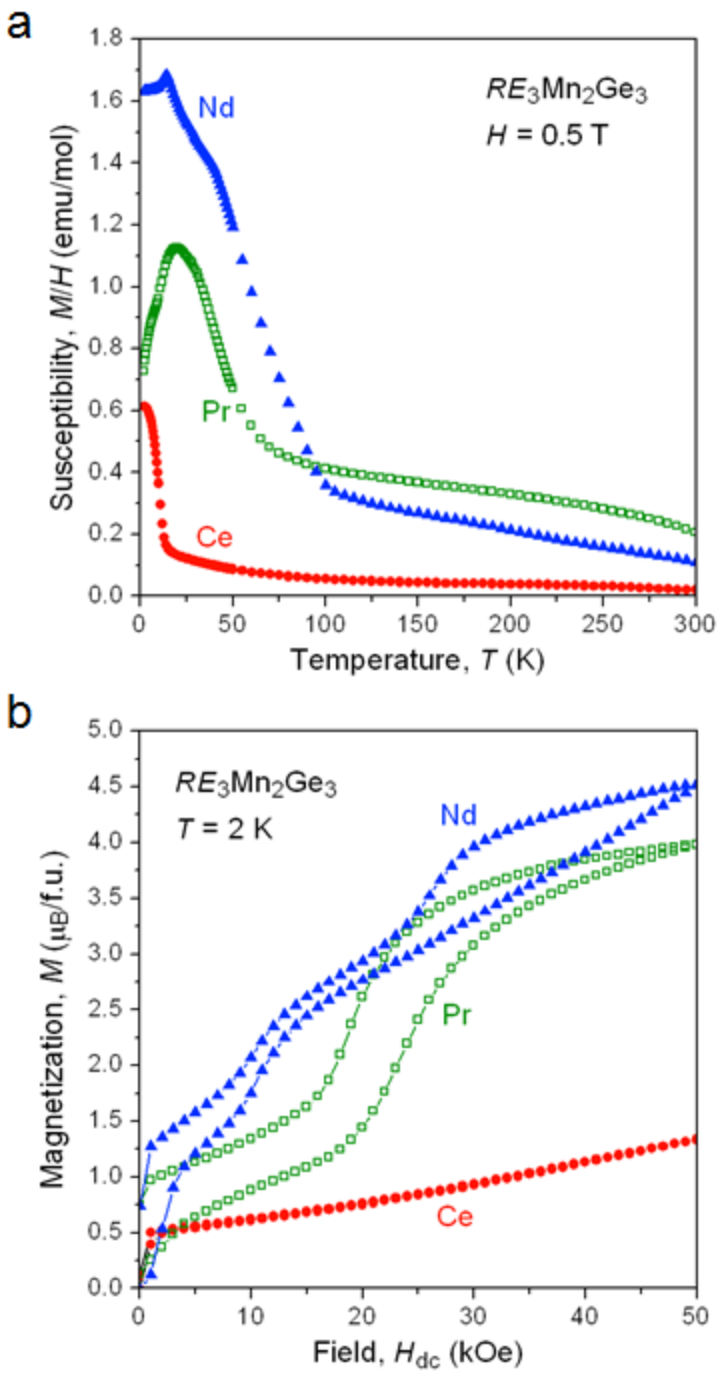

Figure 3-2 Plots of (a) magnetic susceptibility as a function of temperature at 0.5 T and (b) magnetization as a function of field at 2 K for $RE_3Mn_2Ge_3$ (RE = Ce, Pr, Nd).

The magnetic properties of $RE_3Mn_2Ge_3$ (RE = Ce–Nd) are quite complex, with multiple transitions seen in the temperature dependence of the magnetic susceptibility (Figure 3-2a). The high-temperature regions of the magnetic susceptibility could not be fit to the Curie-Weiss law. All eventually undergo downturns in the magnetic susceptibility at low temperature (near 2 K for $Ce_3Mn_2Ge_3$, 25 K for $Pr_3Mn_2Ge_3$, and 20 K for $Nd_3Mn_2Ge_3$), suggesting antiferromagnetic ordering. Magnetization curves measured at 2 K reveal several field-dependent transitions and significant hysteresis for $Pr_3Mn_2Ge_3$ and $Nd_3Mn_2Ge_3$ (Figure 3-2b). The magnetizations at the highest field (50 kOe) are well below the theoretical saturation values expected for the trivalent RE species alone (2.1 μ_B/Ce^{3+}, 3.2 μ_B/Pr^{3+}, 3.3 μ_B/Nd^{3+}). Further interpretation is difficult at this point but it is worthwhile noting that a neutron diffraction study on $Tb_3Co_2Ge_3$ shows various spiral antiferromagnetic orderings associated with field-dependent transitions.[7] Similar spin-reorientation processes are likely occurring in $RE_3Mn_2Ge_3$.

3.4. Conclusions

The preparation of $RE_3Mn_2Ge_3$ suggests that ternary germanides $RE_3M_2Ge_3$ with the $Hf_3Ni_2Si_3$-type structure containing other earlier transition-metal components M may be worthwhile targeting. The very long interlayer Ge–Ge distance found in $Ce_3Mn_2Ge_3$ implies that this contact is probably not essential for the stability of this structure type. The minor oxidation product $Nd_4Mn_2Ge_5O_{0.6}$ identified in the course of this investigation illustrates the potential for the $Yb_4Mn_2Sn_5$-type and related structures like $Ho_4Mn_2InGe_4$ to accommodate small interstitial atoms like oxygen.

3.5 References

[1] Salamakha, P. S.; Sologub, O. L.; Bodak, O. I.; in: Gschneidner Jr., K. A.; Eyring L. (Eds.), *Handbook on the Physics and Chemistry of Rare Earths*, vol. 27, Elsevier, Amsterdam, 1999, pp. 1–223.

[2] Salamakha, P. S.; in: Gschneidner Jr., K. A.; Eyring L. (Eds.), *Handbook on the Physics and Chemistry of Rare Earths*, vol. 27, Elsevier, Amsterdam, 1999, pp. 225–338.

[3] Bodak, O. I.; Oleksin, O. Ya. Fedyna, M. F.; Pecharskii, V. K. *Neorg. Mater.* **1992**, *28*, 493–497.

[4] Kotur, B. Ya.; Andrusyak, R. I. *Neorg. Mater.* **1991**, *27*, 1433–1439.

[5] Morozkin, A. V.; Yao, J.; Mozharivskyj, Yu. *Intermetallics* **2012**, *21*, 115–120.

[6] Morozkin, A. V. *Intermetallics* **2012**, *25*, 136–138.

[7] Morozkin, A. V.; Nirmala, R.; Yao, J.; Mozharivskyj, Y.; Isnard, O. *J. Solid State Chem.* **2012**, *196*, 93–99.

[8] Sologub, O. L.; Prots', Yu. M.; Salamakha, P. S.; Bodak, O.I. *J. Alloys Compd.* **1994**, *209*, 107–109.

[9] Sologub, O. L.; Prots', Yu. M.; Salamakha, P. S.; Bodak, O. I.; Stępień-Damm, J. *Pol. J. Chem*. **1995**, *69*, 423–426.

[10] Sologub, O. L.; Hiebl, K.; Rogl, P.; Noël, H. *J. Alloys Compd.* **1996**, *245*, L13–L17.

[11] Salamakha, P.; Sologub, O.; Stępień-Damm, J.; Stash, A. *Kristallografiya* **1996**, *41*, 1135–1136.

[12] Sologub, O. L.; Stash, A.; Zavodnik, V. E.; Salamakha, P. S.; Bodak, O. I. *Coll. Abs. 6th Int. Conf. Crystal Chem. Intermet. Compd.* (Lvov) (**1995**) 96.

[13] Rodewald, U. Ch.; Pöttgen, R. *Solid State Sci.* **2003**, *5*, 487–493.

[14] Koterlyn, G. M.; Bodak, O. I.; Pavlyuk, V. V.; Stępień-Damm, J.; Pietraszko, A. *J. Alloys Compd.* **1999**, *291*, 110–116.

[15] Markiv, V. Ya.; Beloborodova, E. A.; Belyavina, N. N.; Alekseeva, N. V. *Dopov. Akad. Nauk Ukr.* (**1993**) 70–73.

[16] Oliynyk, A. O.; Stoyko, S. S.; Mar, A. *J. Solid State Chem.* **2013**, *202*, 241–249.

[17] Pavlyuk, V. V.; Bodak, O. I. *Neorg. Mater.* **1992**, *28*, 1119–1121.

[18] Oliynyk, A. O.; Mar, A. *J. Solid State Chem.* **2013**, *206*, 60–65.

[19] Akselrud, L. G.; Zavalii, P. Yu.; Grin, Yu. N.; Pecharski, V. K.; Baumgartner, B.; Wölfel, E. *Mater. Sci. Forum* **1993**, *133–136*, 335–342.

[20] Sheldrick, G. M. SHELXTL, version 6.12, Bruker AXS Inc., Madison, WI, 2001.

[21] Gelato, L. M.; Parthé, E. *J. Appl. Crystallogr*. **1987**, *20*, 139–143.

[22] Lei, X.-W.; Zhong, G.-H.; Li, M.-J.; Mao, J.-G. *J. Solid State Chem.* **2008**, *181*, 2448–2455.

[23] Grytsiv, A.; Kaczorowski, D.; Rogl, P.; Tran, V.; Godart, C.; Gofryk, K.; Giester, G. *J. Phys.: Condens. Matter* **2005**, *17*, 385–397.

[24] Villars, P.; Cenzual, K. *Pearson's Crystal Data – Crystal Structure Database for Inorganic Compounds*, release 2010/11, ASM International, Materials Park, OH, 2010.

[25] Yarmolyuk, Ya. P.; Grin', Yu. N.; Gladyshevskii, E. I. *Kristallografiya* **1977**, *22*, 726–730.

[26] Zhao, J. T.; Parthé, E. *Acta Crystallogr., Sect. C* **1989**, *45*, 1853–1856.

[27] Pauling, L. *The Nature of the Chemical Bond*, 3rd ed., Cornell University Press, Ithaca, NY, 1960.

[28] Slater, J. C.; *J. Chem. Phys.* **1964**, *41*, 3199–3205.

[29] Oliynyk, A. O.; Stoyko, S. S.; Mar, A. *Inorg. Chem.* **2013**, *52*, 8264–8271.

[30] Salvador, J. R.; Kanatzidis, M. G. *Inorg. Chem.* **2006**, *45*, 7091–7099.

[31] Attfield, J. P.; Férey, G. *J. Solid State Chem.* **1989**, *80*, 286–298.

Chapter 4

Rare-earth manganese germanides $RE_{2+x}MnGe_{2+y}$ (*RE* = La, Ce) built from four-membered rings and *stellae quadrangulae* of Mn-centred tetrahedral

A version of this chapter has been published. Oliynyk, A. O.; Mar, A. J. Solid State Chem. 2013, 206, 60–65.

4.1. Introduction

Among ternary rare-earth manganese germanides, the most commonly encountered phases are $REMn_6Ge_6$ ($HfFe_6Ge_6$-type and related structures),[1,2] $REMn_2Ge_2$ ($CeGa_2Al_2$-type),[3-5] *RE*MnGe (PbFCl- or TiNiSi-type),[6-7] and $REMn_xGe_2$ ($CeNiGe_2$-type).[8] The temperature and synthetic method can strongly influence the formation of such ternary phases. For example, the equiatomic compound CeMnGe can be prepared either by arc-melting and annealing at 400 °C[9] or by induction-melting and annealing at 800 °C,[6] whereas NdMnGe fails to form by arc-melting and annealing at 600 °C[10] but does form by induction-melting and annealing at 800 °C.[6] Many of these compounds exhibit interesting magnetic properties, such as ferromagnetic or ferrimagnetic ordering at relatively high temperatures for $REMn_6Ge_6$,[1,11-13] $REMn_2Ge_2$,[14-16] and *RE*MnGe.[6,7] Systematic investigations of phase equilibria have been conducted for only a few *RE*–Mn–Ge systems (*RE* = Ce, Nd, Gd, Tb, Yb), typically at temperatures ranging from 400 to 900 °C;[17] for example, the isothermal section of Ce–Mn–Ge at 400 °C indicates the occurrence of $CeMn_2Ge_2$, Ce_2MnGe_6, Ce_2MnGe_5, and CeMnGe.[9]

The close relationship of the quaternary germanides $RE_4Mn_2InGe_4$ ($Ho_4Ni_2InGe_4$-type) to the ternary indium-containing germanides RE_2InGe_2 (Mo_2FeB_2-type) has been highlighted.[18] In the course of this investigation, we wondered if the corresponding ternary manganese-containing germanides "RE_2MnGe_2" could be prepared, given that RE_2MGe_2 (Sc_2CoSi_2-type) is known for M = Co, Ru, Rh, Os, Ir.[19-28] Targeting this composition has led instead to the germanides $RE_{2+x}MnGe_{2+y}$ (RE = La, Ce) adopting a new structure type. The crystal structure and physical properties of the La member are presented here.

4.2. Experimental

4.2.1. Synthesis

Mixtures with various loading compositions within 1% of "$RE_{40}Mn_{20}Ge_{40}$" in the RE–Mn–Ge phase diagram in a total mass of 0.3 g were prepared from freshly filed RE pieces (RE = La–Nd, Sm, Gd–Tm, Lu, 99.9%, Hefa), Mn powder (99.96%, Alfa-Aesar), and Ge powder (99.9999%, Alfa-Aesar). They were pressed into pellets, which were arc-melted twice on a Centorr 5TA tri-arc furnace on a water-cooled copper hearth under an argon atmosphere. The weight loss after arc-melting was less than 1%. The arc-melted ingots were then sealed within fused-silica tubes and annealed at 800 °C for two weeks, followed by quenching in cold water. Powder X-ray diffraction (XRD) patterns were collected with Cu $K\alpha_1$ radiation on an Inel diffractometer equipped with a curved position-sensitive detector (CPS 120) (Figure A3-1). Attempts were made to prepare the title compounds for many RE components (from La to Lu), but the syntheses were successful only for RE = La and Ce. The highest yield (99%) of the La-containing ternary phase was obtained from the loading composition "$La_{40}Mn_{20}Ge_{40}$", whereas small

amounts of other phases (e.g., Ce–Ge binaries) were generally found in the Ce-containing samples. The tetragonal cell parameters refined from the powder XRD patterns with use of the CSD suite of programs[29] were a = 16.061(2) Å, c = 8.169(1) Å, V = 2107.2(8) Å^3 for $La_{2+x}MnGe_{2+y}$, and a = 15.769(3) Å, c = 8.048(2) Å, V = 2001(1) Å^3 for $Ce_{2+x}MnGe_{2+y}$. The chemical compositions were determined from energy-dispersive X-ray (EDX) analysis on a JEOL JSM-6010LA scanning electron microscope (Figure A3-2). Small single crystals of $La_{2+x}MnGe_{2+y}$ extracted from the La-containing sample showed a composition (43(2)% La, 18(1)% Mn, 39(2)% Ge) close to the loading composition (40% La, 20% Mn, 40% Ge). Polished surfaces of the Ce-containing samples revealed the presence of up to three phases, including $Ce_{2+x}MnGe_{2+y}$ (43(2)% Ce, 18(1)% Mn, 39(2)% Ge), Ce_3Ge, and another ternary phase with a different composition (40(2)% Ce, 25(1)% Mn, 35(2)% Ge). Although the compounds $RE_{2+x}MnGe_{2+y}$ only form for RE = La and Ce, this other ternary phase with approximate composition "$RE_{40}Mn_{25}Ge_{35}$" was observed for a wide range of rare-earth metals (RE = Ce–Nd, Sm, Gd–Dy). Efforts are underway to further characterize "$RE_{40}Mn_{25}Ge_{35}$".

4.2.2. Structure determination

Intensity data for two single crystals of $La_{2+x}MnGe_{2+y}$ were collected at room temperature on a Bruker PLATFORM diffractometer equipped with a SMART APEX II CCD area detector and a graphite-monochromated Mo $K\alpha$ radiation source, using ω scans at 7–8 different ϕ angles with a frame width of 0.3º and an exposure time of 12 s per frame. Face-indexed absorption corrections were applied. Structure solution and refinement were carried out with use of the SHELXTL (version 6.12) program package.[30]

The centrosymmetric tetragonal space group *P*4/*nmm* was chosen on the basis of Laue symmetry, systematic absences, and intensity statistics. Initial positions for most atoms were revealed by direct methods. However, significant electron density remained at five sites all lying on the line ¼, ¼, *z* located within large tunnels in the structural model. These sites were assigned as La or Ge atoms (labeled La5, La6, Ge5, Ge6, and Ge7), with consideration taken on the coordination environment provided by surrounding atoms in the tunnels and reasonable interatomic distances. To avoid unphysically short distances (La5–La6, 0.5 Å; Ge5–Ge6, 0.9 Å), these sites must be partially occupied. Constraints were applied such that: (i) the occupancies sum to unity for La5 and La6, and similarly for Ge5 and Ge6; (ii) the occupancies are equal for La5 and Ge6, and they are equal for La6, Ge5, and Ge7; (iii) the displacement parameters are equal for La5 and La6, and they are equal for Ge5, Ge6, and Ge7. The interpretation of this structural model is that there are two possible local orderings (La5–Ge6–La5… and La6–Ge5–Ge7–La6…) to account for the disorder manifested as a string of five sites within the tunnels. When refinements were performed subject to these constraints, the resulting compositions for the two crystals examined were $La_{2.12(1)}MnGe_{2.16(1)}$ and $La_{2.13(1)}MnGe_{2.17(1)}$. These compositions (40% La, 19% Mn, 41% Ge) are consistent with the loaded reaction composition as well as the EDX analysis. Atomic positions were standardized with the program STRUCTURE TIDY.[31] For brevity, the results for only one of these crystals are tabulated. Table 4-1 lists crystal data and details of the data collection, Table 4-2 lists positional and displacement parameters, and Table 4-3 lists selected interatomic distances. Further data, in CIF format, have been sent to Fachinformationszentrum Karlsruhe, Abt. PROKA, 76344 Eggenstein-Leopoldshafen, Germany, as supplementary

material No. CSD-426272 and can be obtained by contacting FIZ (quoting the article details and the corresponding CSD numbers).

Table 4-1 Crystallographic data for $La_{2+x}MnGe_{2+y}$.

Formula	$La_{2.12(1)}MnGe_{2.16(1)}$
Formula mass (amu)	507.10
Space group	*P*4/*nmm* (No. 129)
a (Å)	16.0491(4)
c (Å)	8.1587(2)
V (Å^3)	2101.47(9)
Z	16
ρ_{calcd} (g cm^{-3})	6.411
T (K)	296
Crystal dimensions (mm)	0.09 × 0.05 × 0.04
Radiation	Graphite monochromated Mo *K*α, λ = 0.71073 Å
μ(Mo *K*α) (mm^{-1})	31.28
Transmission factors	0.233–0.463
2θ limits	3.58–66.36°
Data collected	$-24 \le h \le 24$, $-24 \le k \le 24$, $-12 \le l \le 12$
No. of data collected	29480
No. of unique data, including $F_o^2 < 0$	2227 (R_{int} = 0.065)
No. of unique data, with $F_o^2 > 2\sigma(F_o^2)$	1880
No. of variables	70
$R(F)$ for $F_o^2 > 2\sigma(F_o^2)$ [a]	0.022
$R_w(F_o^2)$ [b]	0.044
Goodness of fit	1.07
$(\Delta\rho)_{max}$, $(\Delta\rho)_{min}$ (e Å^{-3})	5.66, –5.73

[a] $R(F) = \sum||F_o| - |F_c|| / \sum|F_o|$ for $F_o^2 > 2\sigma(F_o^2)$.

[b] $R_w(F_o^2) = [\sum[w(F_o^2 - F_c^2)^2] / \sum wF_o^4]^{1/2}$; $w^{-1} = [\sigma^2(F_o^2) + (Ap)^2 + Bp]$, where $p = [\max(F_o^2,0) + 2F_c^2] / 3$.

Table 4-2 Positional and equivalent isotropic displacement parameters (Å^2) for $La_{2+x}MnGe_{2+y}$.

Atom	Wyckoff position	Occupancy	*x*	*y*	*z*	U_{eq} or U_{iso} (Å^2) [a]
La1	8*j*	1	0.11027(2)	0.11027(2)	0.69469(4)	0.0103(1)
La2	8*i*	1	¼	0.06483(2)	0.34409(4)	0.0099(1)
La3	8*h*	1	0.37493(2)	0.62507(2)	½	0.0091(1)
La4	8*g*	1	0.42052(1)	0.57948(1)	0	0.0090(1)
La5	2*c*	0.729(4) [b]	¼	¼	0.0003(2)	0.0186(4)
La6	2*c*	0.279(3) [b]	¼	¼	0.0628(6)	0.0186(4)
Mn1	8*i*	1	¼	0.03398(6)	0.97817(11)	0.0120(2)
Mn2	8*i*	1	¼	0.66533(6)	0.86516(11)	0.0101(2)
Ge1	8*j*	1	0.04218(3)	0.04218(3)	0.33255(8)	0.0102(1)
Ge2	8*j*	1	0.11313(3)	0.11313(3)	0.07537(8)	0.0090(1)
Ge3	8*i*	1	¼	0.52695(4)	0.70039(8)	0.0105(1)
Ge4	8*i*	1	¼	0.61051(4)	0.18301(8)	0.0090(1)
Ge5	2*c*	0.279(3) [b]	¼	¼	0.4289(7)	0.0182(4)
Ge6	2*c*	0.729(4) [b]	¼	¼	0.5403(3)	0.0182(4)
Ge7	2*c*	0.279(3) [b]	¼	¼	0.7196(7)	0.0182(4)

[a] U_{eq} is defined as one-third of the trace of the orthogonalized U_{ij} tensor. [b] Occupancies were constrained to be equal for La5 and Ge6, and equal for La6, Ge5, and Ge7.

Table 4-3 Selected interatomic distances (Å) in $La_{2+x}MnGe_{2+y}$.

La1–Ge2	3.1065(7)	La5–Ge2 (×4)	3.1664(7)
La1–Ge3 (×2)	3.1435(5)	La5–Ge5	3.498(6)
La1–Ge7/Ge6	3.1780(5)/3.4126(9)	La5–Ge6	3.753(7)
La1–Ge1	3.3344(7)	La6–Ge2 (×4)	3.1083(6)
La1–Ge1	3.4673(7)	La6–Ge7	2.800(7)
La2–Ge5/Ge6	3.0513(14)/3.3754(11)	La6–Ge5	2.987(8)
La2–Ge4	3.1057(7)	Mn1–Ge3	2.4683(11)
La2–Ge2 (×2)	3.1988(5)	Mn1–Ge2 (×2)	2.6585(6)
La2–Ge3	3.2590(7)	Mn1–Ge4	2.8584(12)
La2–Ge1 (×2)	3.3564(5)	Mn2–Ge3	2.5960(11)
La3–Ge3 (×2)	3.0286(5)	Mn2–Ge4 (×2)	2.6482(7)
La3–Ge4 (×2)	3.2807(5)	Mn2–Ge4	2.7385(11)
La3–Ge1 (×2)	3.2926(4)	Mn2–Mn2	2.718(2)
La4–Ge4 (×2)	3.1570(4)	Mn2–Mn2 (×2)	2.921(2)
La4–Ge2 (×2)	3.1977(5)	Ge1–Ge2	2.6449(9)
La4–Ge1 (×2)	3.3959(6)	Ge5–Ge7	2.372(8)

4.2.3. Electrical resistivity and magnetic susceptibility measurements

The sample prepared from the loading composition "$La_{40}Mn_{20}Ge_{40}$" contained suitable crystals and high purity (99%) of the ternary phase $La_{2+x}MnGe_{2+y}$. Standard four-probe electrical resistivity measurements between 2 and 300 K were made on single crystals of $La_{2+x}MnGe_{2+y}$, whose identities were confirmed by EDX analysis, on a Quantum Design Physical Property Measurement System (PPMS) equipped with an ac transport controller (Model 7100). The current was 100 μA and the frequency was 16 Hz. Measurements of dc magnetic susceptibility were made between 2 and 300 K under

an applied field of 0.5 T on a Quantum Design 9T-PPMS magnetometer. Isothermal magnetization curves were measured at various temperatures from 0 to 50 kOe. Susceptibility values were corrected for contributions from the holder and sample diamagnetism.

4.3. Results and discussion

The ternary germanides $RE_{2+x}MnGe_{2+y}$ (*RE* = La, Ce), prepared by arc-melting and annealing at 800 °C, are new phases in the La–Mn–Ge and Ce–Mn–Ge systems. The formula is close to "RE_2MnGe_2" but with a slight excess of *RE* and Ge, as suggested by the composition obtained from crystal structure refinements on the La member, ~$La_{2.1}MnGe_{2.2}$. This composition differs slightly from RE_2MGe_2 (*M* = Co, Ru, Rh, Os, Ir),[19-28] but is close to $RE_{117}Cr_{52}Ge_{112}$ and $RE_{117}Fe_{52}Ge_{112}$ (or ~$RE_{2.2}MGe_{2.2}$)[10,32,33] as well as the stannide $Dy_{117}Co_{57}Sn_{112}$ (or ~$Dy_{2.1}CoSn_{2.0}$).[34] Notwithstanding the nearly identical compositions, the tetragonal structure of $La_{2.1}MnGe_{2.2}$ is unrelated to the monoclinic structure of RE_2MGe_2 (Sc_2CoSi_2-type), which is built up of Ge-centred trigonal prisms, and bears only a remote resemblance to the cubic structures of $RE_{117}M_{52}Ge_{112}$ ($Tb_{117}Fe_{52}Ge_{112}$-type)[32] and $Dy_{117}Co_{57}Sn_{112}$ (own type)[34] to the extent that these also contain densely packed atoms arranged in complex clusters within very large unit cells.

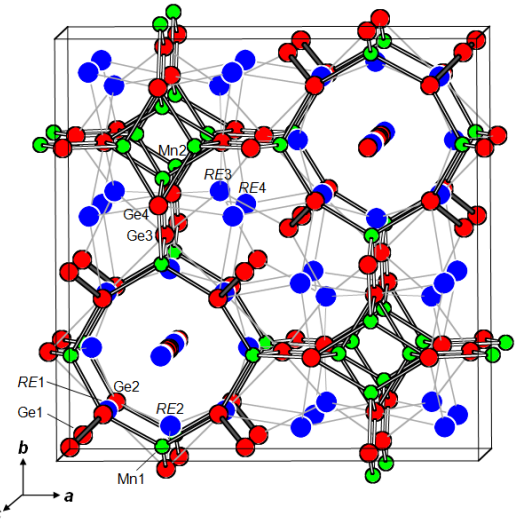

Figure 4-1 Structure of $RE_{2+x}MnGe_{2+y}$ (*RE* = La, Ce) viewed down the *c*-direction. The large blue circles are *RE* atoms, the small green circles are Mn atoms, and the medium red circles are Ge atoms.

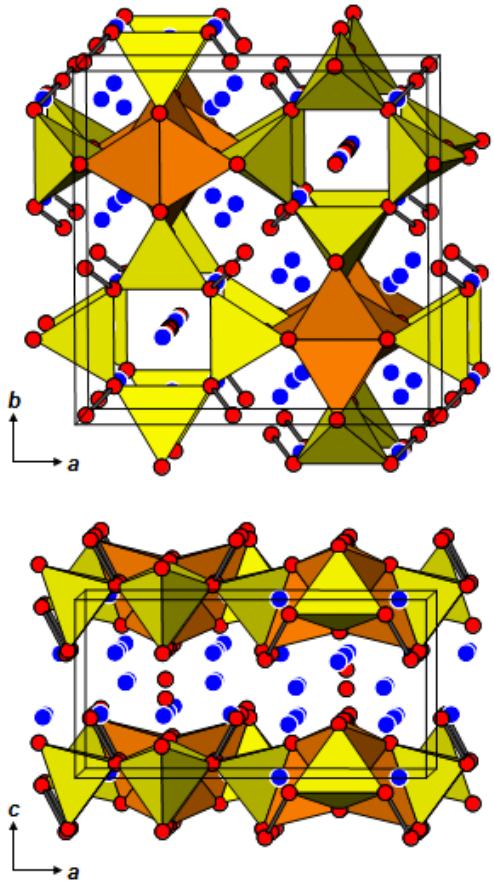

Figure 4-2 Polyhedral representation of $RE_{2+x}MnGe_{2+y}$ highlighting the Mn1- (yellow) and Mn2-centred tetrahedra (orange), viewed

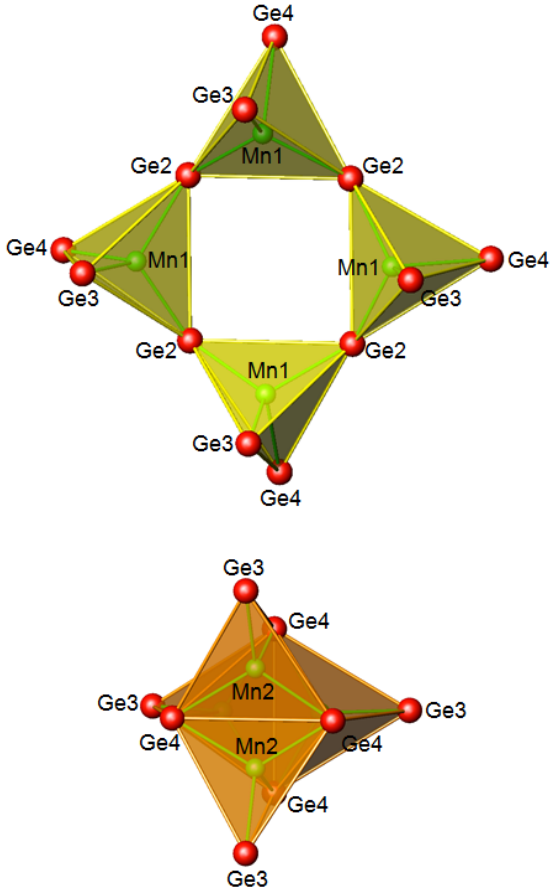

Figure 4-3 Arrangements of Mn1-centred tetrahedra in a four-membered ring (top) and of Mn2-centred tetrahedra in a

down the *c*- (top) or *b*-direction (bottom). *stella quadrangula* (bottom).

The most straightforward way to describe the structure of $La_{2.1}MnGe_{2.2}$ is in terms of a Mn–Ge framework, built up of Mn-centred tetrahedra, that outlines tunnels within which are located La atoms and additional Ge atoms (Figure 4-1). The tetrahedra are condensed to form layers parallel to the *ab*-plane (Figure 4-2) and are found in two types of arrangements (Figure 4-3). The Mn1-centred tetrahedra share corners to form a four-membered ring, an unusual arrangement analogous to cyclosilicates $[Si_4O_{12}]^{8-}$ found in $BaCuSi_2O_6$ (renowned as an ancient pigment, "Han purple"[35], as well as a model spin system for Bose-Einstein condensation[36]). These four-membered rings are decorated by additional Ge1 atoms that bond with the bridging Ge2 atoms to form Ge_2 dimers (2.645 Å). The Mn2-centred tetrahedra share edges to form a *stella quadrangula*, which can be viewed as tetracapped tetrahedron, or four filled tetrahedra surrounding an empty one. Both types of tetrahedra are distorted, with Mn–Ge distances (2.468–2.858 Å around Mn1, 2.596–2.738 Å around Mn2) that are greater than the sum of the Pauling metallic radii R_1 (Mn–Ge, 2.42 Å)[37] and comparable to those found in $La_4Mn_2InGe_2$ (2.611–2.654 Å).[18] The edge-sharing of the Mn2-centred tetrahedra leads to shortened Mn–Mn contacts (2.718–2.921 Å). The four-membered rings and the *stellae quadrangulae* are connected together through edge-sharing, four of one type around the other, and vice versa.

The most complicated part of the structure arises from disorder of La and Ge atoms occupying five closely spaced split sites located along ¼, ¼, *z* (and ¾, ¾, *z*) within the tunnels centred within the interior of the four-membered rings of tetrahedra. These sites are all in Wyckoff position 2*c* and are partially occupied, with one set (La5, Ge6) at

roughly 70% and the other set (La6, Ge5, Ge7) at roughly 30%. (An earlier precedent for split Ge sites within similar types of tunnels can be found in $Li_5Ce_{26}Ge_{22+x}$.[38]) A local ordering arrangement can be proposed in which the La atoms are octahedrally coordinated by Ge atoms, while the Ge atoms are either isolated (Ge6) or form Ge_2 dimers (Ge5–Ge7) (Figure 4-4). Two of the distances verge on being inappropriately short (cf. La6–Ge7, 2.800 Å and Ge5–Ge7, 2.372 Å with the sums of Pauling metallic radii, La–Ge, 2.93 Å and Ge–Ge, 2.48 Å),[37] but they may be an artefact of taking an average of a more irregular site occupation than proposed in the simplified picture shown in the figure.

Electrical resistivity measurements confirm the metallic behaviour expected for $La_{2.1}MnGe_{2.2}$, but the temperature dependence is rather weak, as shown for a representative sample (Figure 4-5a). For four crystals tested, the absolute resistivity values are high (ρ_{2K} = 750–950 μΩ·cm) and the relative resistivity ratios are small (ρ_{300K}/ρ_{2K} = ~1.2), consistent with the disorder present in the crystal structure. The appearance of the magnetic susceptibility vs. temperature curve, which does not follow the Curie-Weiss law (Figure 4-5b), and the approach to saturation observed in the magnetization vs. field curves at 2 and 300 K (Figure 4-5c) both suggest that $La_{2.1}MnGe_{2.2}$ undergoes ferro- or ferrimagnetic ordering with a Curie temperature above 300 K. In this compound containing a nonmagnetic *RE* component, it is assumed that only the Mn moments contribute to the overall magnetization. As noted above, there are close Mn–Mn separations (2.7–2.9 Å) found within the *stellae quadrangulae* that are likely the source of magnetic coupling interactions. The ternary germanides *RE*MnGe and $REMn_2Ge_2$ also exhibit similar Mn–Mn distances and undergo complex magnetic

ordering with transition temperatures typically well above 300 K (e.g., LaMnGe, 420 K; $LaMn_2Ge_2$, 310 and 410 K).[6] Detailed interpretation of the magnetic behaviour of $La_{2.1}MnGe_{2.2}$ will require further measurements at higher temperature and neutron diffraction experiments.

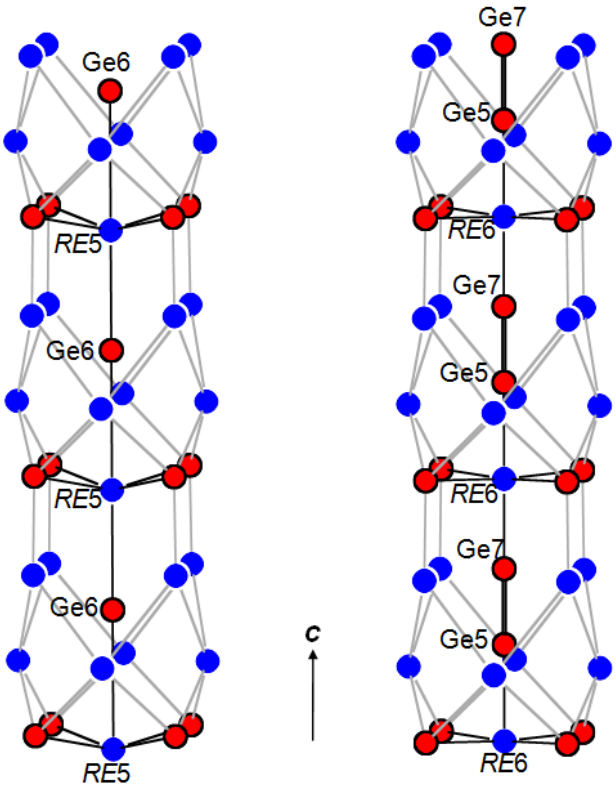

Figure 4-4 Proposed local ordering arrangements within tunnels in $RE_{2+x}MnGe_{2+y}$, consisting of strings of *RE*5–Ge6–*RE*5… atoms (left) or of *RE*6–Ge5–Ge7–*RE*6… atoms (right).

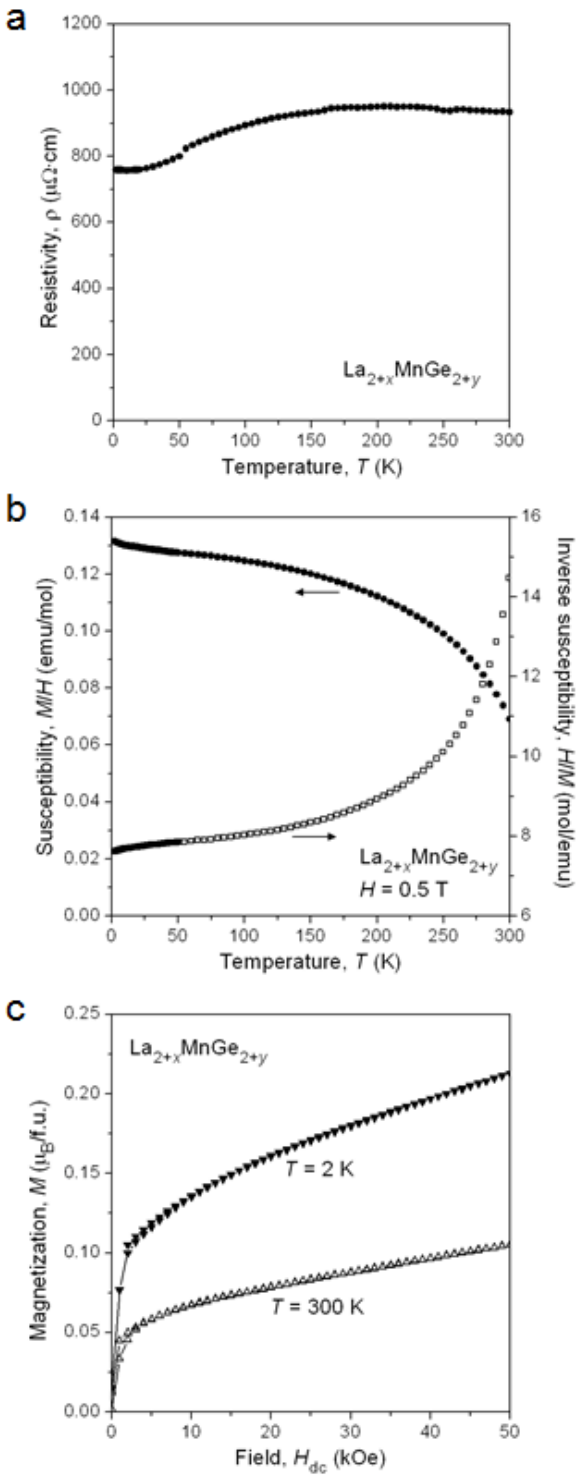

Figure 4-5 Plots of (a) electrical resistivity, (b) magnetic susceptibility and its inverse as a function of temperature, and (c) magnetization as a function of field at 2 and 300 K for $La_{2.1}MnGe_{2.2}$.

4.4 Conclusions

Although the originally targeted compounds "RE_2MnGe_2" were not formed at 800 °C, new phases $RE_{2+x}MnGe_{2+y}$ with nearly this composition and adopting a surprisingly complex structure were found in the *RE*–Mn–Ge (*RE* = La, Ce) systems. The region near the RE_2MnGe_2–$RE_3Mn_2Ge_3$ line in the phase diagrams appears to be rich with additional ternary compounds yet to be identified. In particular, the Ce–Mn–Ge system also contains $Ce_3Mn_2Ge_3$ ($Hf_3Ni_2Si_3$-type) and ~$Ce_{40}Mn_{25}Ge_{35}$ (unknown structure), for which characterization is in progress.

4.5 References

[1] Venturini, G.; Welter, R.; Malaman, B. *J. Alloys Compd.* **1992**, *185*, 99–107.

[2] Lefèvre, C.; Venturini, G.; Malaman, B. *J. Alloys Compd.* **2003**, *354*, 47–53.

[3] Rossi, D.; Marazza, R.; Mazzone, D.; Ferro, R. *J. Less-Common Met.* **1978**, *59*, 79–83.

[4] Venturini, G.; Malaman, B.; Roques, B. *J. Solid State Chem.* **1989**, *79*, 136–145.

[5] Morozkin, A. V.; Seropegin, Yu. D.; Gribanov, A. V.; Barakatova, J. M. *J. Alloys Compd.* **1997**, *256*, 175–191.

[6] Welter, R.; Venturini, G.; Ressouche, E.; Malaman, B. *J. Alloys Compd.* **1995**, *228*, 59–74.

[7] Klosek, V.; Vernière, A.; Ouladdiaf, B.; Malaman, B. *J. Magn. Magn. Mater.* **2003**, *256*, 69–92.

[8] François, M.; Venturini, G.; Malaman, B.; Roques, B. *J. Less-Common Met.* **1990**, *160*, 197–213.

[9] Konyk, M. B.; Bodak, O. I. *J. Alloys Compd.* **2005**, *387*, 243–245.

[10] Salamakha, P. S.; Prots', Yu. M.; Sologub, O. L.; Bodak, O. I. *J. Alloys Compd.* **1994**, *215*, 51–54.

[11] Brabers, J. H. V. J.; Duijn, V. H. M.; de Boer, F. R.; Buschow, K. H. J. *J. Alloys Compd.* **1993**, *198*, 127–132.

[12] Chafik El Idrissi, B.; Venturini, G.; Malaman, B.; Ressouche, E. *J. Alloys Compd.* **1994**, *215*, 187–193.

[13] Kelemen, M. T.; Rösch, P.; Dormann, E.; Buschow, K. H. J. *J. Magn. Magn. Mater.* **2001**, *223*, 253–260.

[14] Narasimhan, K. S. V. L.; Rao, V. U. S.; Bergner, R. L.; Wallace, W. E. *J. Appl. Phys.* **1975**, *46*, 4957–4960.

[15] Szytuła, A.; Szott, I. *Solid State Commun.* **1981**, *40*, 199–202.

[16] Kolmakova, N. P.; Sidorenko, A. A.; Levitin, R. Z. *Low Temp. Phys.* (Transl. Fiz. Nizk. Temp. (Kiev)) **2002**, *28*, 653–668.

[17] Salamakha, P. S.; Sologub, O. L.; Bodak, O. I.; in: Gschneidner Jr., K. A.; Eyring L. (Eds.), *Handbook on the Physics and Chemistry of Rare Earths*, vol. 27, Elsevier, Amsterdam, 1999, pp. 1–223.

[18] Oliynyk, A. O.; Stoyko, S. S.; Mar, A. *Inorg. Chem.* **2013**, *52*, 8264–8271.

[19] Bodak, O. I.; Pecharskii, V. K.; Starodub, P. K.; Salamakha, P. S.; Mruz, O. Ya.; Bruskov, V. A. *Izv. Akad. Nauk SSSR, Metally* (**1986**) 214–216.

[20] Salamakha, P. S.; Bodak, O. I.; Pecharskii, V. K.; Bel'skii, V. K. *Izv. Akad. Nauk SSSR, Metally* (**1989**) 206–208.

[21] Gladyshevskii, R. E.; Sologub, O. L.; Parthé, E. *J. Alloys Compd.* **1991**, *176*, 329–335.

[22] Morozkin, A. V.; Seropegin, Yu. D.; Bodak, O. I. *J. Alloys Compd.* **1986**, *234*, 143–150.

[23] Hiebl, K.; Sologub, O. *J. Magn. Magn. Mater.* **1998**, *186*, 56–64.

[24] Salamakha, P. S.; Sologub, O. L. *J. Alloys Compd.* **1999**, *287*, L1–L3.

[25] Boulet, P.; Weitzer, F.; Hiebl, K.; Noël, H. *Physica B* **2000**, *292*, 302–319.

[26] Rodewald, U. Ch.; Pöttgen, R. *Solid State Sci.* **2003**, *5*, 487–493.

[27] Morozkin, A. V.; Yao, J.; Mozharivskyj, Yu. *Intermetallics* **2012**, *21*, 115–120.

[28] Oliynyk, A. O.; Stoyko, S. S.; Mar, A. *J. Solid State Chem.* **2013**, *202*, 241–249.

[29] Akselrud, L. G.; Zavalii, P. Yu.; Grin, Yu. N.; Pecharski, V. K.; Baumgartner, B.; Wölfel, E. *Mater. Sci. Forum* **1993**, *133–136*, 335–342.

[30] Sheldrick, G. M. SHELXTL, version 6.12, Bruker AXS Inc., Madison, WI, 2001.

[31] Gelato, L. M.; Parthé, E. *J. Appl. Crystallogr.* **1987**, *20*, 139–143.

[32] Pecharskii, V. K.; Bodak, O. I.; Bel'skii, V. K.; Starodub, P. K.; Mokra, I. R.; Gladyshevskii, E. I. *Kristallografiya* **1987**, *32*, 334–338.

[33] Morozkin, A. V.; Seropegin, Yu. D.; Portnoy, V. K.; Sviridov, I. A.; Leonov, A. V. *Mater. Res. Bull.* **1998**, *33*, 903–908.

[34] Salamakha, P.; Sologub, O.; Bocelli, G.; Otani, S.; Takabatake, T. *J. Alloys Compd.* **2001**, *314*, 177–180.

[35] Berke, H. *Angew. Chem. Int. Ed.* **2002**, *41*, 2483–2487.

[36] Sebastian, S. E.; Harrison, N.; Batista, C. D.; Balicas, L.; Jaime, M.; Sharma, P. A.; Kawashima, N.; Fisher, I. R. *Nature (London, U.K.)* **2006,** *441*, 617–620.

[37] Pauling, L. *The Nature of the Chemical Bond*, 3rd ed., Cornell University Press, Ithaca, NY, 1960.

[38] Pavlyuk, V. V.; Pecharskii, V. K.; Bodak, O. I.; Bruskov, V. A. *Kristallografiya* **1987**, *32*, 70–73.

Chapter 5

Investigation of the quaternary Ce–Mn–In–Ge phase diagram and isothermal sections of the boundary ternary systems at 800 °C

A version of this chapter has been published. Oliynyk, A. O.; Djama-Kayad, K.; Mar, A. J. Alloys Compd. 2015, 622, 837–841.

5.1. Introduction

In contrast to ternary rare-earth transition-metal germanides *RE*–*M*–Ge, which are numerous and valued for their diverse physical properties, quaternary germanides containing a p-block metalloid component are still relatively uncommon. For example, despite the potentially large number of element permutations, quaternary phases within the *RE*–*M*–In–Ge systems have so far been limited to $RE_4M_2InGe_4$ (*M* = Mn,[1] Ni[2]), $RE_7Co_4InGe_{12}$,[3] $RE_7Ni_{5-x}In_6Ge_{3+x}$,[4,5] and $Yb_3AuIn_3Ge_2$.[6] The combination of In and Ge is interesting because their similar electronegativities lead to a competition between heteroatomic (In–Ge) and homoatomic (Ge–Ge) bonding arrangements. Many of these quaternary phases were discovered, probably serendipitously, in the course of flux-growth reactions.[2,3,6] To date, there has been no systematic study of the phase equilibria within the quaternary phase diagrams to determine whether these are truly thermodynamically stable phases. As a step towards greater understanding of these quaternary systems, which are experimentally more difficult to investigate, we wish to undertake a study of the boundary ternary systems. I would want to focus your attention

on the Ce–Mn–In–Ge system, particularly on clarifying the existence of any missing ternary phases because this is an essential prerequisite for characterization before the formation of more complex quaternary phases can be examined.

Within the Ce–Mn–In system, only one ternary compound, $CeMn_{0.67}In_{1.33}$, has been established.[7] Within the Mn–In–Ge system, no ternary compounds are known. Within the Ce–In–Ge system, previously studied at 600 °C, five ternary compounds have been reported, but not all of them have been well characterized.[8] The Ce–Mn–Ge system is perhaps the most noteworthy. Isothermal sections of phase diagrams for many rare-earth manganese germanium systems *RE*–Mn–Ge have been previously investigated at various temperatures for *RE* = Ce (400 °C),[9] Nd (600 °C),[10] Gd (700 °C),[11] Tb (600 °C),[12] Er (600 °),[13] and Yb (400 °C),[14] revealing the existence of many ternary phases. Ternary Ce–Mn–Ge phases display a wide variety of magnetic behaviour (e.g., antiferromagnetism in CeMnGe;[15] ferromagnetism in $CeMn_2Ge_2$[16-18] and Ce_2MnGe_6[19]) that depend sensitively on Mn–Mn distances. Moreover, recently reported two new ternary phases prepared at 800 °C, $Ce_{2+x}MnGe_{2+y}$[20] and $Ce_3Mn_2Ge_3$,[21] that do not appear in the phase diagram at 400 °C.[9] To elucidate the phase equilibria and corroborate the formation of ternary phases, we present here detailed determinations of the isothermal sections of all four boundary ternary systems at 800 °C, a more challenging endeavour given that melting and decomposition processes are more likely to take place near this higher temperature. Reactions were also conducted to probe the existence of quaternary Ce–Mn–In–Ge phases.

5.2. Experimental

Freshly filed Ce pieces (99.9%, Hefa), Mn powder (99.96%, Cerac), In shot (99.999%, Cerac), and Ge powder (99.9999%, Alfa-Aesar) were combined in various loading compositions, each with a total mass of 0.3 g. The mixtures were pressed into pellets and arc-melted twice in a Centorr 5TA tri-arc furnace or an Edmund Bühler MAM-1 arc-melter on a water-cooled copper hearth under an argon atmosphere. Weight losses after arc-melting were negligible. The ingots were sealed in evacuated fused-silica tubes and annealed at 800 °C for one week, after which they were quenched in cold water. Calibration against the melting point of Ce (798 °C), which is close to the annealing tempeature of 800 °C, indicated that the high-temperature furnaces used for these annealing experiments typically have a precision of 2–3 degrees within the temperature setpoint. This is particularly important to establish in this investigation because literature data indicates that Ce_3Ge decomposes at 790 °C, Mn_2Ge begins to form at 790 °C, and $Mn_{11}Ge_8$ decomposes at ~796 °C.[22] Ground samples were examined by powder X-ray diffraction (XRD), performed with Cu $K\alpha_1$ radiation on an Inel diffractometer equipped with a curved position-sensitive detector (CPS 120). Cell parameters were refined from the powder XRD patterns with use of the CSD suite of programs.[23] Polished samples embedded in resin were examined by energy-dispersive X-ray (EDX) analysis, performed on a JEOL JSM-6010LA scanning electron microscope.

5.3. Results and discussion

About 20–30 samples within each of the ternary Ce–Mn–In, Ce–In–Ge, and Mn–In–Ge systems and about 40 samples within the more complex Ce–Mn–Ge system were prepared with various loading compositions. Over 80 four-component samples within the quaternary Ce–Mn–In–Ge system were prepared in increments of 10 at.% for each component, to an upper limit of 70% in the content of In because of its high solubility with the other three components. The overall chemical composition of each sample (quaternary and ternary) was confirmed through EDX analysis of a global SEM image viewed at low magnification; in general, the observed compositions agree well with the nominal loading compositions. Chemical compositions of individual phases were obtained through EDX point analyses. The identity and number of phases present in each sample were determined by XRD analysis and the corresponding points on the phase diagrams were located at the observed compositions as determined by EDX analysis (Tables A4-1–A4-2 and Figures A4-1–A4-2). Table 5-1 summarizes the binary, ternary, and quaternary phases formed at 800 °C, including their refined cell parameters, and Figures 5-1–5-4 show the isothermal sections of Ce–Mn–In, Mn–In–Ge, Ce–In–Ge, and Ce–Mn–Ge phase diagrams.

Table 5-1 Binary, ternary, and quaternary phases in the Ce–Mn–In–Ge system at 800 °C.

Phase	Structure type	Space group	*a* (Å)	*b* (Å)	*c* (Å)
Binary phases					
Ce_5Ge_3 (up to 5% Mn solubility)	Mn_5Si_3	$P6_3/mcm$	8.842(4)–8.937(2)		6.602(5)–6.668(2)
Ce_4Ge_3	Th_3P_4	$I\bar{4}3d$	9.205(1)		
Ce_5Ge_4	Sm_5Ge_4	*Pnma*	7.954(4)	15.235(5)	8.044(3)
CeGe	FeB	*Pnma*	8.301(4)	4.082(1)	6.009(1)
β-$CeGe_{2-x}$	$GdSi_{1.4}$	*Imma*	4.215(1)	4.271(1)	14.083(4)
Ce_3In	Cu_3Au	$Pm\bar{3}m$	4.978(1)		
Ce_2In	$Co_{1.75}Ge$	$P6_3/mmc$	5.551(4)		6.884(3)
Ce_5In_4 (up to 5% Mn solubility)	*No data*				
Ce_3In_5	Pu_3Pd_5	*Cmcm*	10.220(3)	8.308(4)	10.529(4)
$CeIn_2$	KHg_2	*Imma*	4.724(4)	7.606(3)	9.002(2)
$CeIn_3$	Cu_3Au	$Pm\bar{3}m$	4.683(1)		
$Mn_{3.4}Ge$	Mg_3Cd	$P6_3/mmc$	5.367(5)		4.139(3)
Mn_5Ge_2	Mn_5Ge_2	$P3c1$	7.188(2)		13.059(4)
Mn_2Ge	$Co_{1.75}Ge$	$P6_3/mmc$	4.174(8)		5.272(6)
Mn_5Ge_3	Mn_5Si_3	$P6_3/mcm$	7.187(1)		5.058(2)
$Mn_{11}Ge_8$	$Cr_{11}Ge_8$	*Pnma*	13.211(2)	5.0863(9)	15.875(4)

$Mn_{9.75}In_{3.25}$	Cu_9Al_4	$P\bar{4}3m$	9.428(2)		
Ternary phases					
$CeIn_{1.33}Mn_{0.67}$	AlB_2	*P*6/*mmm*	4.919(3)		3.768(4)
Ce_2InGe_2	Mo_2FeB_2	*P*4/*mbm*	7.565(2)		4.379(1)
$Ce_{11}In_6Ge_4$	$Sm_{11}In_6Ge_4$	*I*4/*mmm*	12.003(4)		16.609(3)
$Ce_3In_{0.89}Ge_{1.11}$	Gd_3Ga_2	*I*4/*mcm*	12.139(2)		15.905(2)
$Ce_3In_{4.33}Ge_{0.67}$ [a]	Tl_4PbTe_3	*I*4/*mcm*	8.482(3)		11.515(2)
$CeMn_2Ge_2$	$CeAl_2Ga_2$	*I*4/*mmm*	4.126(1)		10.914(4)
Ce_2MnGe_6	Ce_2CuGe_6	*Amm*2	4.302(2)	4.1616(8)	21.125(3)
CeMnGe	PbClF	*P*4/*nmm*	4.190(1)		7.362(1)
$Ce_3Mn_2Ge_3$ [b]	$Hf_3Ni_2Si_3$	*Cmcm*	4.3255(8)–4.3149(5)	11.621(2)–11.587(5)	14.660(2)–14.632(3)
$Ce_{43}Mn_{18}Ge_{39}$	$La_{2+x}MnGe_{2+y}$	*P*4/*nmm*	15.729(5)		7.978(4)
Quaternary phases					
$Ce_4Mn_2InGe_4$	$Ho_4Ni_2InGe_4$	*C*2/*m*	16.468(5)	4.3722(4) β = 106.728(5)°	7.3903(5)
$Ce_2Mn_2InGe_2$	*No data*				

[a] This ternary phase has a small homogeneity range, $Ce_{38}In_{46}Ge_{16}$–$Ce_{38}In_{52}Ge_{10}$, with cell parameters for this solid solution deviating up to 0.01 Å. [b] This ternary phase has a small homogeneity range, $Ce_{37.5}Mn_{25}Ge_{37.5}$–$Ce_{40}Mn_{25}Ge_{35}$, with cell parameters for the Ge-rich limit taken from the single-crystal structure [21].

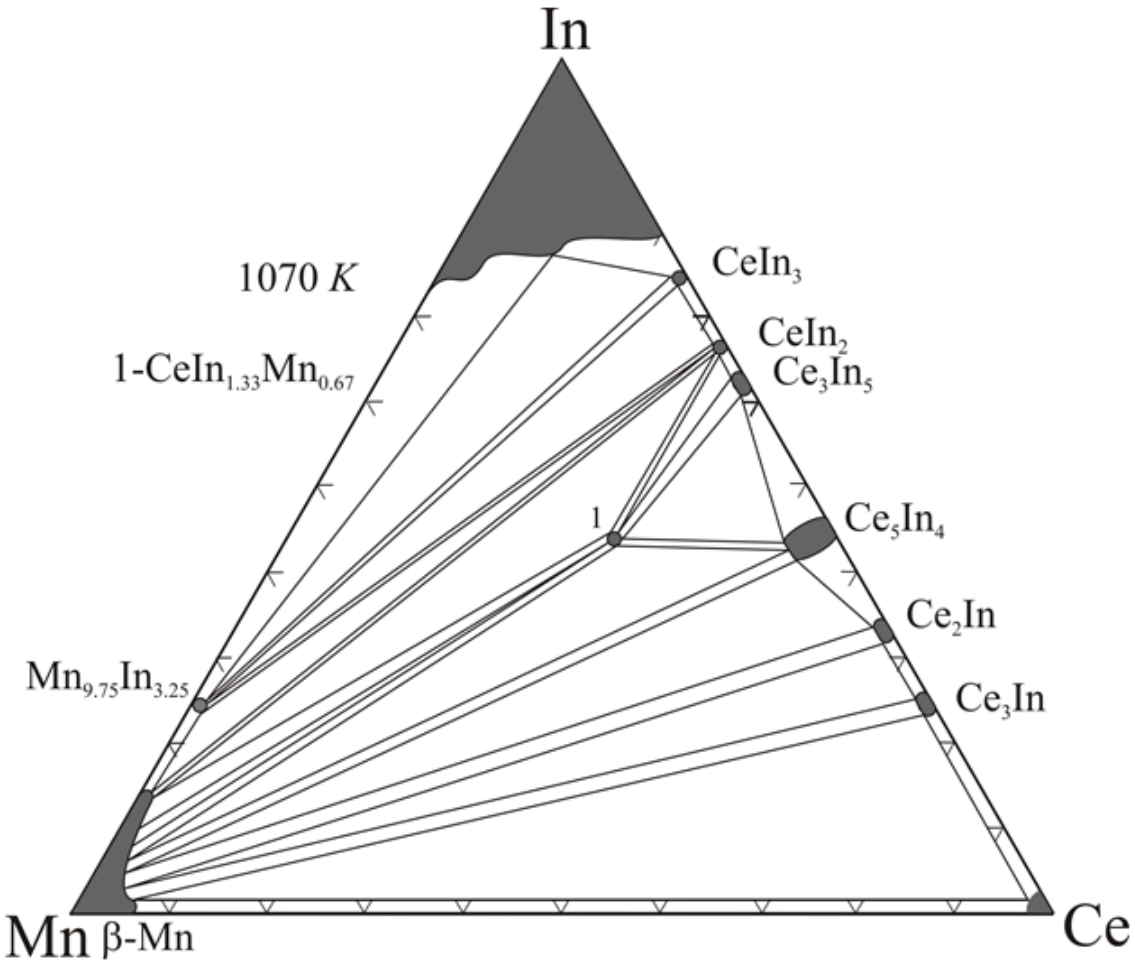

Figure 5-1 Isothermal section of the Ce–Mn–In system at 800 °C

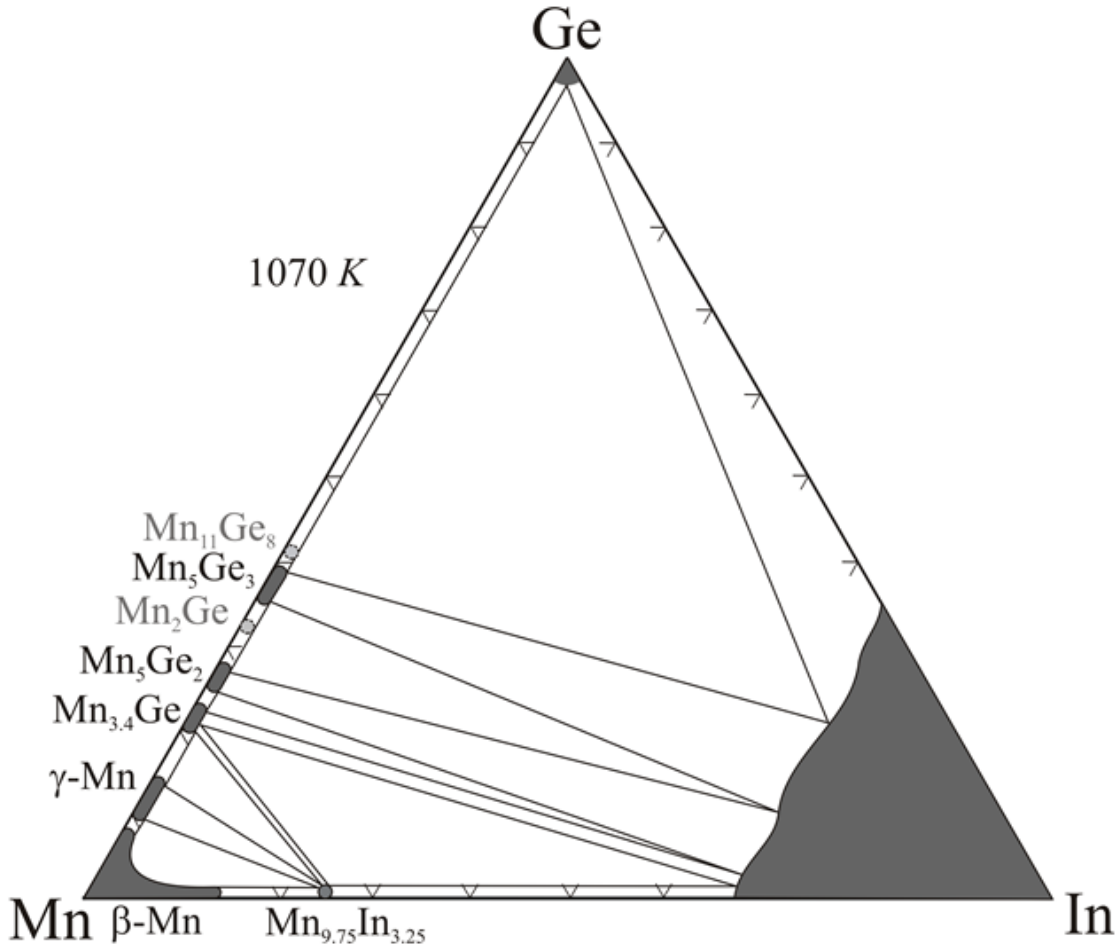

Figure 5-2 Isothermal section of the Mn–In–Ge system at 800 °C

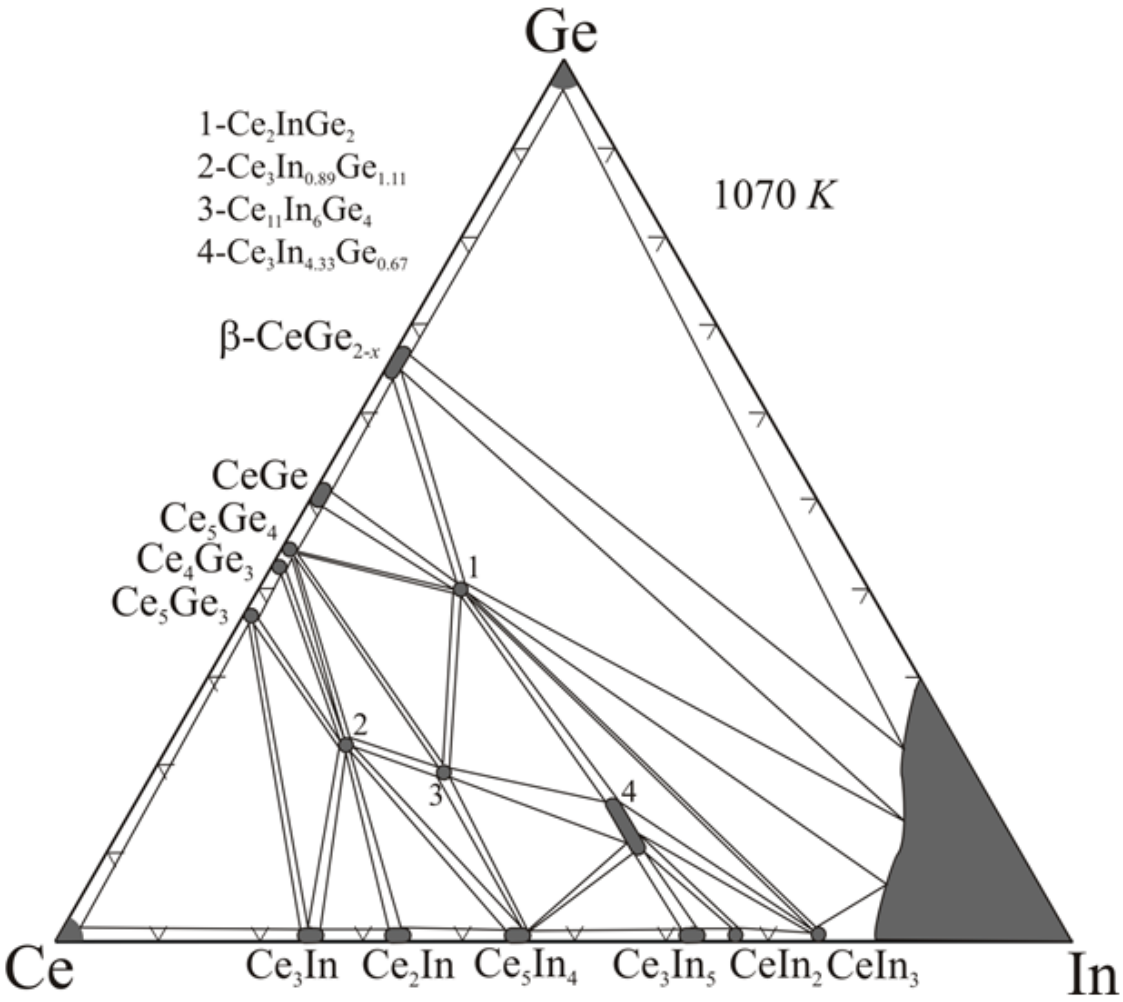

Figure 5-3 Isothermal section of the Ce–In–Ge system at 800 °C

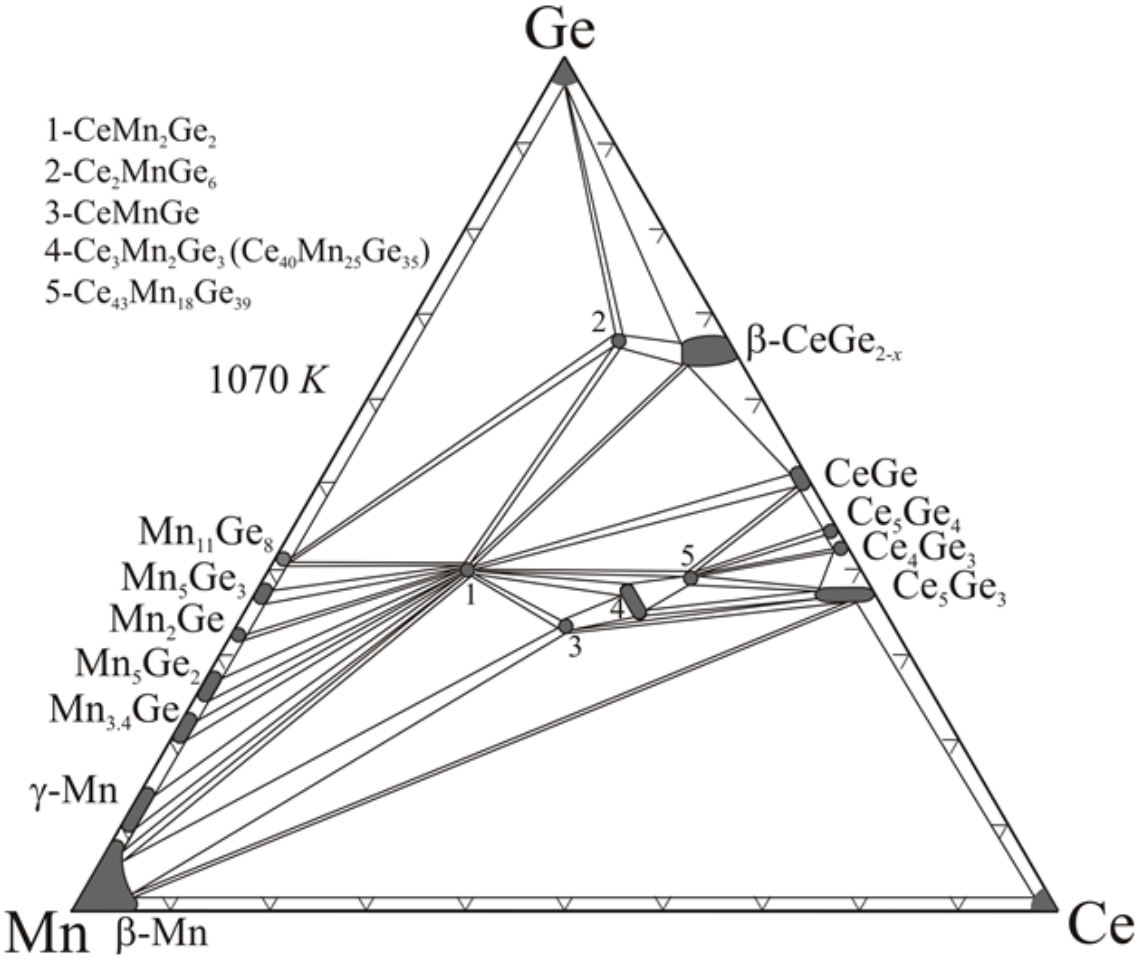

Figure 5-4 Isothermal section of the Ce–Mn–Ge system at 800 °C

Within the six boundary binary systems, no Ce–Mn or Ge–In phases are known, and the existence of all expected binary phases was confirmed:

(1) Ce–Ge. Among the five binary Ce–Ge phases, none exhibits any solubility of In, but two of them undergo up to ~5% solubility of Mn. First, Ce_5Ge_3 can accommodate Mn, likely through a substitutional solid solution given that Ce_5Ge_3 and Mn_5Ge_3 both adopt the Mn_5Si_3-type structure,[24,25] even though Ce and Mn differ significantly in size.[26] Evidence for this solubility comes from variations in cell parameters and from the presence of Mn within the Ce_5Ge_3 phase through EDX analysis. Second, β-$CeGe_{2-x}$ already exhibits deviations in composition in the form of Ge deficiencies within partially occupied sites;[27] introduction of Mn adds one more compositional degree of freedom, probably through Mn inclusions within voids in the parent structure. This proposal is supported by the observation that the cell parameters remain nearly unchanged upon solubilizing Mn within β-$CeGe_{2-x}$.

(2) Ce–In. Among the six binary Ce–In phases, none exhibits any solubility of Ge, but Ce_5In_4 undergoes up to ~5% solubility of Mn. Ce_5In_4 has an unknown structure but it appears in all previously reported Ce–In phase diagrams.[22] Evidence for the formation of Ce_5In_4 was provided only through EDX analysis. Our attempts to determine the structure of Ce_5In_4 have been thwarted so far by the poor quality of all crystals examined on a single-crystal X-ray diffractometer.

(3) Mn–Ge. All five binary Mn–Ge phases were confirmed, but two of them have been reported to undergo transitions at temperatures close to 800 °C: Mn_2Ge (forms above 790 °C) and $Mn_{11}Ge_8$ (decomposes above ~796 °C).[22] These two phases were observed in the Ce–Mn–Ge system but not in the Mn–In–Ge system (where they are marked with

dashed circles in Figure 5-2). This inconsistency is likely attributed to the use of different furnaces for annealing samples within these systems, as well as to slight temperature inhomogeneities within the furnaces. It is also possible that there may be small inaccuracies in the reported transition temperatures. None of these binary germanides show any significant solubility of the other components (Ce or In). Mn_5Ge_2, $Mn_{3.4}Ge$, and γ-Mn show only rather small homogeneity ranges (<3%) of the binary components.

(4) Mn–In. Only one binary phase, $Mn_{9.75}In_{3.25}$, was found, with no solubility of the other components (Ce or Ge).

Within the four boundary ternary systems, no Mn–In–Ge phases are known but a variety of ternary phases were found in the other systems:

(1) Ce–Mn–In. Only one ternary phase, $CeIn_{1.33}Mn_{0.67}$, forms. It adopts the hexagonal AlB_2-type structure in which In and Mn atoms are disordered within the same site.

(2) Ce–In–Ge. Four ternary phases (Ce_2InGe_2, $Ce_3In_{0.89}Ge_{1.11}$, $Ce_{11}In_6Ge_4$, and $Ce_3In_{4.33}Ge_{0.67}$) were found at 800 °C; in contrast, a fifth ternary phase ($Ce_3In_3Ge_4$) previously found at 600 °C[8] does not form and is thus a low-temperature phase only. $Ce_3In_{4.33}Ge_{0.67}$ exhibits a slight solid solubility range of 5 at.% on the In–Ge section (at constant Ce content), the same as at 600 °C;[8] the change in cell parameters is small, within 0.01 Å.

(3) Ce–Mn–Ge. Five ternary phases are formed at 800 °C: $CeMn_2Ge_2$, Ce_2MnGe_6, CeMnGe, $Ce_3Mn_2Ge_3$, and $Ce_{43}Mn_{18}Ge_{39}$. In contrast, at 400 °C, the ternary phases formed are $CeMn_2Ge_2$, Ce_2MnGe_6, Ce_2MnGe_5, and CeMnGe.[9] Thus, Ce_2MnGe_5 is a low-temperature phase, whereas $Ce_3Mn_2Ge_3$ and $Ce_{43}Mn_{18}Ge_{39}$ are confirmed to be new

high-temperature phases. These two high-temperature phases are very close in composition but can be distinguished in SEM micrographs (Figure A4-5). The first high-temperature phase, $Ce_3Mn_2Ge_3$, exhibits a small homogeneity range (~2%), from the ideal composition $Ce_{37.5}Mn_{25}Ge_{37.5}$ to a slightly germanium-poorer composition $Ce_{40}Mn_{25}Ge_{35}$. The powder XRD patterns of these two limiting compositions are very similar and give nearly identical cell parameters (deviating by 0.01–0.03 Å) corresponding to the orthorhombic $Hf_3Ni_2Si_3$-type structure.[28] Analogous to β-$CeGe_{2-x}$, we propose that slight Ge deficiencies in the structure may account for the compositional deviation, $Ce_3Mn_2(Ge_{1-x})_3$ (x = 0–0.1). In fact, this Ge-deficient phase was probably what was first observed when it was detected in a separate investigation.[20] It is certain that $RE_3Mn_2Ge_3$ with the $Hf_3Ni_2Si_3$-type structure forms for early *RE* components (Ce, Pr, Nd).[21] However, although the composition $RE_{40}Mn_{25}Ge_{35}$ was also observed for later *RE* components (Sm, Gd, Tb, Dy), it does not appear to correspond to a $Hf_3Ni_2Si_3$-type phase.[20] The second high-temperature phase, $Ce_{43}Mn_{18}Ge_{39}$, can also be reformulated approximately as $Ce_{2.3}MnGe_{2.1}$, to better reflect the tetragonal $La_{2+x}MnGe_{2+y}$-type structure that it adopts.[20] Notwithstanding the formula of this structure type, the homogeneity range is negligible. The nonstoichiometry originates from a complicated disorder of *RE* atoms, Ge atoms, and Ge_2 dimers within tunnels in the structure.

Within the quaternary Ce–Mn–In–Ge system, the existence of $Ce_4Mn_2InGe_4$ has been confirmed. In $RE_4M_2InGe_4$ (M = Mn,[1] Ni[2]) compounds for which crystal structures have been refined, the In site is found to be slightly deficient (~90% occupancy), but it has not been clear if a homogeneity range is possible. EDX analysis of all samples containing $Ce_4Mn_2InGe_4$ showed that the composition of this phase remains fixed with an

In content of 92.5–93.4%. This observation indicates that the In substoichiometry is intrinsic and does not arise from formation of a solid solution within the quaternary system. A second quaternary phase with the nominal composition $Ce_2Mn_2InGe_2$ was also discovered. Despite many attempts to select single crystals for X-ray diffraction experiments and to change synthetic conditions to obtain larger crystals, the structure determination of this phase remains elusive. Efforts to improve crystal growth of this phase are ongoing.

5.4 References

[1] Olinyk, A. O.; Stoyko, S. S.; Mar, A. *Inorg. Chem.* **2013**, *52*, 8264–8271.

[2] Salvador, J. R.; Kanatzidis, M. G. *Inorg. Chem.* **2006**, *45*, 7091–7099.

[3] Chondroudi, M.; Balasubramanian, M.; Welp, U.; Kwok, W.-K.; Kanatzidis, M. G. *Chem. Mater.* **2007**, *19*, 4769–4775.

[4] Chumalo, N.; Nychyporuk, G. P.; Pavlyuk, V. V.; Pöttgen, R.; Kaczorowski, D.; Zaremba, V. I. *J. Solid State Chem.* **2010**, *183*, 2963–2967.

[5] Dominyuk, N.; Zaremba, V. I.; Pöttgen, R.; Naturforsch. Z. *B: J. Chem. Sci.* **2011**, *66*, 433–436.

[6] Chondroudi, M.; Peter, S. C.; Malliakas, C. D.; Balasubramanian, M.; Li, Q. A.; Kanatzidis, M. G. *Inorg. Chem.* **2011**, *50*, 1184–1193.

[7] Dzevenko, M. V.; Galadzhun, Ya. V.; Zaremba, V. I.; Kalychak, Ya. M. *J. Alloys Compd.* **2005**, *397*, 161–164.

[8] Nychyporuk, G.; Zaremba, V.; Kalychak, Ya. *Visn. L'viv. Univ., Ser. Khim.* 2003, 43, 9–14.

[9] Konyk, M. B.; Bodak, O. I. *J. Alloys Compd.* **2005**, *387*, 243–245.

[10] Salamakha, P. *J. Alloys Compd.* **1997**, *225*, 209–220.

[11] Markiv, V. Ya.; Beloborodova, E. A.; Belyavina, N. N.; Alekseeva, N. V. *Dopov. Akad. Nauk Ukr.* **1993**, *7*, 70–73.

[12] Starodub, P. K.; Zapotots'ka, L. M.; Bodak, O. I. *Visn. L'viv. Univ., Ser. Khim.* **1996**, *36*, 57–59.

[13] Konyk, M. B.; Romaka, L. P.; Romaka, V. V.; Serkiz, R. Ya. *Fiz. Khim. Tverd. Tila* **2012**, *13*, 956–962.

[14] Salamakha, P. S.; Sologub, O. L.; Bodak O. I.; in: Gschneidner Jr., K. A.; Eyring L. (Eds.), *Handbook on the Physics and Chemistry of Rare Earths*, vol. 27, Elsevier, Amsterdam, 1999, pp. 1–223.

[15] Welter, R.; Venturini, G.; Ressouche, E.; Malaman, B. *J. Alloys Compd.* **1995**, *228*, 59–74.

[16] Leciejewicz, J.; Szytuła, A.; Bażela, W.; Siek, S. *J. Magn. Magn. Mater.* **1990**, *89*, 29–32.

[17] Welter, R.; Venturini, G.; Ressouche, E.; Malaman, B. *J. Alloys Compd.* **1995**, *218*, 204–215.

[18] Nowik, I.; Levi, Y.; Felner, I.; Bauminger, E. R. *J. Magn. Magn. Mater.* **1995**, *147*, 373–384.

[19] Duraj, R.; Konyk, M.; Przewoźnik, J.; Romaka, L.; Szytuła, A. *Solid State Sci.* **2013**, *25*, 11–14.

[20] Oliynyk, A. O.; Mar, A.; *J. Solid State Chem.* **2013**, *206*, 60–65.

[21] Oliynyk, A. O.; Djama-Kayad, K.; Mar, A. *J. Alloys Compd.* **2014**, *602*, 130–134.

[22] Villars, P. (editor-in-chief); Okamoto, H.; Cenzual K. (section editors), *ASM Alloy Phase Diagrams Center* (www1.asminternational.org/asmenterprise/apd), ASM International, Materials Park, OH, 2006.

[23] Akselrud, L. G.; Zavalii, P. Yu.; Grin, Yu. N.; Pecharski, V. K.; Baumgartner, B.; Wölfel, E. *Mater. Sci. Forum* **1993**, *133–136*, 335–342.

[24] Arbuckle, J.; Parthé, E. *Acta Crystallogr.* **1962**, *15*, 1205–1207.

[25] Forsyth, J. B.; Brown, P. J. *J. Phys.: Condens. Matter* **1990**, *2*, 2713–2720.

[26] Pauling, L. *The Nature of the Chemical Bond*, 3rd ed., Cornell University Press, Ithaca, NY, 1960.

[27] Gladyshevskii, E. I. *Zh. Strukt. Khim.* **1964**, *5*, 568–575.

[28] Yarmolyuk, Ya. P.; Grin', Yu. N.; Gladyshevskii, E. I. *Kristallografiya* **1977**, *22*, 726–730.

Chapter 6

Quaternary germanides $RE_4Mn_2InGe_4$ (*RE* = La–Nd, Sm, Gd–Tm, Lu)

A version of this chapter has been published. Oliynyk, A. O.; Stoyko, S. S.; Mar, A. Inorg. Chem. 2013, 52, 8264–8271.

6.1. Introduction

Ternary rare-earth transition-metal germanides *RE–M*–Ge form a large class of compounds that exhibit a rich variety of structures and physical properties; they have been especially well investigated for systems containing a first-row or later d-block element.[1,2] Ternary germanides are also known in which the *M* component is extended to include p-block metalloids from groups 13 and 14. Within the *RE*–In–Ge system, there exist several ternary phases,[3–11] the most common being RE_2InGe_2 which forms for many *RE* members.[3–6] The presence of two metalloids with similar electronegativities in these compounds leads to interesting heteroatomic and homoatomic bonding networks in their structures. Some of these compounds were initially discovered in the course of experiments intended to promote the crystal growth of ternary rare-earth transition-metal germanides. Through the use of a molten metal (such as Al, Ga, or In) behaving as a reactive flux, however, ternary metalloid-containing germanides as well as quaternary phases containing both a d-block and p-block component were obtained instead. In this way, the series $RE_4Ni_2InGe_4$ (*RE* = Dy, Ho, Er, Tm),[12] $RE_7Co_4InGe_{12}$ (*RE* = Dy, Ho, Yb),[13] and $Yb_3AuIn_3Ge_2$ [14] were identified as new quaternary phases in the *RE–M*–In–Ge

system (where *M* = d-block element). On the other hand, a fourth series, $RE_7Ni_{5-x}In_6Ge_{3+x}$ (*RE* = La–Nd, Sm), has been prepared simply through arc-melting of the elements.[15,16] The combination of magnetically active species (from both the rare-earth and transition-metal components) and relatively complex crystal structures leads to potentially diverse physical properties for these quaternary germanides. There has also been some discussion in the literature on whether the flux-formed germanides represent thermodynamically stable phases in their phase diagrams.[6]

In this chapter the study describes synthesis of the quaternary germanides $RE_4Mn_2InGe_4$, which are manganese-containing analogues of the $RE_4Ni_2InGe_4$ series, and their structural characterization by powder and single-crystal X-ray diffraction. The large range of *RE* substitution permits elucidation of structural trends within this series. The close structural relationship between $RE_4M_2InGe_4$ (*M* = Mn, Ni) and RE_2InGe_2 is highlighted, which apparently has not been explicitly described previously. Band structure calculations were performed to evaluate the bonding in $RE_4Mn_2InGe_4$.

6.2 Experimental

6.2.1 Synthesis

Starting materials were freshly filed *RE* pieces (*RE* = La–Nd, Sm, Gd–Tm, Lu; 99.9%, Hefa), Mn powder (99.96%, Alfa-Aesar), In shot (99.999%, Cerac), and Ge pieces (99.9999%, Alfa-Aesar). Mixtures with the nominal composition "$RE_4Mn_2InGe_4$" were prepared from these elements, cold-pressed into pellets, and melted three times in a Centorr 5TA tri-arc furnace on a water-cooled copper hearth under an argon atmosphere. The weight loss after arc-melting was less than 1%. The arc-melted ingots were then

sealed within evacuated fused-silica tubes and annealed at 800 °C for 12 d, followed by quenching in cold water. The products were characterized by powder X-ray diffraction (XRD) patterns, collected with Cu $K\alpha_1$ radiation on an Inel diffractometer equipped with a curved position-sensitive detector (CPS 120). Qualitative analysis of the XRD patterns, with use of the program Powder Cell to compare with theoretical patterns,[17] revealed that the title compounds were formed in conjunction with RE_2InGe_2, $REMn_2Ge_2$, *RE*MnGe, and $RE_{11}Ge_{10}$ as the most common accompanying phases (Table A5-1). Cell parameters were refined with use of the CSD suite of programs [18] and are listed in Table 1. Energy-dispersive X-ray (EDX) analysis was performed on selected crystals on a JEOL JSM-6010LA scanning electron microscope, operated with an accelerating voltage of 20 kV and an acquisition time of 70 s. For four of the members of the $RE_4Mn_2InGe_4$ series (*RE* = La, Ce, Pr, Tm, Lu), these analyses gave experimental compositions (38–39% *RE*, 18–19% Mn, 7–8% In, 35–36% Ge) that agree reasonably well with the fully stoichiometric formula (36.4% *RE*, 18.2% Mn, 9.1% In, 36.4% Ge). As discussed below, there is evidence for a slight substoichiometry in indium, corresponding to the formula $RE_4Mn_2In_{0.9}Ge_4$, but the expected composition (36.7% *RE*, 18.3% Mn, 8.2% In, 36.7% Ge) does not deviate sufficiently to permit the EDX analysis, which is typically precise to only a few percent, to provide definitive support. For the remaining samples, overlap of *RE* with Mn or Ge peaks in the EDX spectra precluded quantitative analysis.

Table 6-1 Cell Parameters for $RE_4Mn_2InGe_4$ (*RE* = La–Nd, Sm, Gd–Lu) [a]

compound	*a* (Å)	*b* (Å)	*c* (Å)	β (°)	*V* (Å^3)
$La_4Mn_2InGe_4$	16.666(1)	4.4252(5)	7.5023(6)	106.958(4)	529.2(1)
$Ce_4Mn_2InGe_4$	16.464(2)	4.3724(6)	7.3899(6)	106.743(4)	509.4(2)
$Pr_4Mn_2InGe_4$	16.367(1)	4.3472(5)	7.3523(6)	106.876(5)	500.6(1)
$Nd_4Mn_2InGe_4$	16.299(4)	4.333(1)	7.335(2)	106.848(7)	495.8(4)
$Sm_4Mn_2InGe_4$	16.112(2)	4.2739(9)	7.229(1)	106.536(6)	477.2(2)
$Gd_4Mn_2InGe_4$	16.018(2)	4.2427(7)	7.1732(6)	106.358(4)	467.8(5)
$Tb_4Mn_2InGe_4$	15.921(4)	4.203(2)	7.120(2)	106.154(6)	457.6(5)
$Dy_4Mn_2InGe_4$	15.857(2)	4.1900(6)	7.0938(5)	106.146(7)	452.7(2)
$Ho_4Mn_2InGe_4$	15.773(2)	4.1661(5)	7.0549(6)	106.103(5)	445.4(2)
$Er_4Mn_2InGe_4$	15.720(2)	4.1488(7)	7.0345(8)	106.027(4)	441.0(2)
$Tm_4Mn_2InGe_4$	15.648(2)	4.1296(6)	6.9990(8)	105.996(6)	434.8(2)
$Lu_4Mn_2InGe_4$	15.578(3)	4.101(1)	6.959(1)	105.974(6)	427.4(3)

[a] Refined from powder diffraction data.

6.2.2 Structure determination

Sufficiently large single crystals of $RE_4Mn_2InGe_4$, which were grey and irregularly shaped, were available for *RE* = La–Nd, Sm, and Gd. Intensity data were collected on a Bruker D8 diffractometer equipped with a SMART APEX II CCD area detector and a Mo *K*α radiation source, using ω scans at 6–8 different ϕ angles with a frame width of 0.3° and an exposure time of 12 s per frame. Face-indexed numerical absorption corrections were applied. Structure solution and refinement were carried out with use of the SHELXTL (version 6.12) program package.[19] The centrosymmetric

monoclinic space group *C*2/*m* was chosen on the basis of Laue symmetry, systematic absences, and intensity statistics. Direct methods revealed initial atomic positions corresponding to the $Ho_4Ni_2InGe_4$-type structure.[12] Atomic coordinates were standardized with use of the program STRUCTURE TIDY.[20] Structure refinements were straightforward except that the displacement parameters for the In site were consistently elevated compared to the other sites. Successive refinements indicated partial occupancy for the In site (ranging from 0.944(3) in the La member to 0.864(7) in the Gd member), in contrast to full occupancies for all remaining sites (0.99(1)–1.02(1)). Similar observations were previously made for the $RE_4Ni_2InGe_4$ series, for which the occupancy of the In site was 0.96 or greater.[12] For brevity, the idealized formula $RE_4Mn_2InGe_4$ is used in subsequent discussion but the nonstoichiometric formula $RE_4Mn_2In_{1-x}Ge_4$ is retained in the crystallographic tables. Crystal data and further experimental details are given in Table 6-2. Final values of the positional and displacement parameters are given in Table 6-3 and selected interatomic distances are given in Table 6-4. Further data in the form of crystallographic information files (CIFs) are available as Supporting Information or may be obtained from Fachinformationszentrum Karlsruhe, Abt. PROKA, 76344 Eggenstein-Leopoldshafen, Germany (CSD-426119 to 426124).

Table 6-2 Crystallographic Data for $RE_4Mn_2InGe_4$ (*RE* = La–Nd, Sm, Gd)

formula	$La_4Mn_2In_{0.945(2)}Ge_4$	$Ce_4Mn_2In_{0.927(2)}Ge_4$	$Pr_4Mn_2In_{0.921(2)}Ge_4$	$Nd_4Mn_2In_{0.881(4)}Ge_4$	$Sm_4Mn_2In_{0.904(3)}Ge_4$	$Gd_4Mn_2In_{0.866(3)}Ge_4$
formula mass (amu)	1064.38	1066.93	1068.94	1078.24	1104.98	1128.56
space group	*C*2/*m* (No. 12)	*C*2/*m* (No. 12)	*C*2/*m* (No. 12)	*C*2/*m* (No. 12)	*C*2/*m* (No. 12)	*C*2/*m* (No. 12)
a (Å)	16.646(2)	16.4357(6)	16.3401(11)	16.249(3)	16.093(2)	15.9808(9)
b (Å)	4.4190(6)	4.3652(2)	4.3470(3)	4.3313(7)	4.2718(6)	4.2363(2)
c (Å)	7.4834(10)	7.3742(3)	7.3425(5)	7.3185(12)	7.2124(10)	7.1590(4)
β (°)	106.893(2)	106.6390(10)	106.7210(10)	106.813(2)	106.458(2)	106.3040(10)
V (Å^3)	526.72(12)	506.91(4)	499.49(6)	493.05(14)	475.51(11)	465.17(4)
Z	2	2	2	2	2	2
ρ_{calcd} (g cm^{-3})	6.711	6.990	7.107	7.263	7.717	8.057
T (K)	173(2)	173(2)	173(2)	173(2)	173(2)	173(2)
crystal dimensions (mm)	0.09 × 0.06 × 0.03	0.14 × 0.05 × 0.05	0.09 × 0.03 × 0.03	0.11 × 0.04 × 0.03	0.07 × 0.04 × 0.04	0.09 × 0.05 × 0.02
radiation	graphite monochromated Mo $K\alpha$, λ = 0.71073 Å					
μ(Mo $K\alpha$) (mm^{-1})	31.32	33.60	35.36	37.04	41.31	45.42
transmission factors	0.167–0.484	0.067–0.309	0.179–0.580	0.123–0.454	0.175–0.379	0.088–0.438
2θ limits	5.12–66.48°	5.18–66.36°	5.20–66.40°	5.24–66.40°	5.28–66.30°	5.32–66.46°
data collected	$-25 \le h \le 25$, $-6 \le k \le 6$, $-11 \le l \le 11$	$-24 \le h \le 25$, $-6 \le k \le 6$, $-11 \le l \le 11$	$-24 \le h \le 24$, $-6 \le k \le 6$, $-11 \le l \le 11$	$-24 \le h \le 24$, $-6 \le k \le 6$, $-10 \le l \le 11$	$-24 \le h \le 24$, $-6 \le k \le 6$, $-10 \le l \le 10$	$-24 \le h \le 24$, $-6 \le k \le 6$, $-10 \le l \le 11$
no. of data collected	3733	3628	3612	3642	3390	3319
no. of unique data,	1099 (R_{int} = 0.028)	1063 (R_{int} = 0.018)	1052 (R_{int} = 0.025)	1029 (R_{int} = 0.029)	994 (R_{int} = 0.033)	978 (R_{int} = 0.026)

including $F_o^2 < 0$						
no. of unique data, with $F_o^2 > 2\sigma(F_o^2)$	989	1028	942	912	896	887
no. of variables	37	37	37	37	37	37
$R(F)$ for $F_o^2 > 2\sigma(F_o^2)$ [a]	0.020	0.017	0.020	0.026	0.022	0.018
$R_w(F_o^2)$ [b]	0.042	0.038	0.047	0.066	0.052	0.037
goodness of fit	1.05	1.16	1.07	1.07	1.07	1.10
$(\Delta\rho)_{max}$, $(\Delta\rho)_{min}$ (e Å^{-3})	1.93, –1.12	1.68, –1.25	2.62, –1.09	3.97, –1.40	3.34, –1.40	1.82, –1.11

[a] $R(F) = \sum||F_o| - |F_c|| / \sum|F_o|$. [b] $R_w(F_o^2) = [\sum[w(F_o^2 - F_c^2)^2] / \sum wF_o^4]^{1/2}$; $w^{-1} = [\sigma^2(F_o^2) + (Ap)^2 + Bp]$, where $p = [\max(F_o^2,0) + 2F_c^2] / 3$.

Table 6-3 Atomic Coordinates and Equivalent Isotropic Displacement Parameters for $RE_4Mn_2InGe_4$ (*RE* = La–Nd, Sm, Gd)

	$La_4Mn_2In_{0.945(2)}Ge_4$	$Ce_4Mn_2In_{0.927(2)}Ge_4$	$Pr_4Mn_2In_{0.921(2)}Ge_4$	$Nd_4Mn_2In_{0.881(4)}Ge_4$	$Sm_4Mn_2In_{0.904(3)}Ge_4$	$Gd_4Mn_2In_{0.866(3)}Ge_4$
*RE*1 in 4*i* (*x*, 0, *z*)						
x	0.34869(2)	0.34856(1)	0.34779(2)	0.34837(2)	0.34697(2)	0.34642(2)
z	0.07052(4)	0.07032(3)	0.07133(4)	0.07190(5)	0.07277(4)	0.07408(4)
U_{eq}	0.0074(1)	0.0065(1)	0.0067(1)	0.0071(1)	0.0061(1)	0.0064(1)
*RE*2 in 4*i* (*x*, 0, *z*)						
x	0.58252(2)	0.58211(1)	0.58169(2)	0.58085(2)	0.58089(2)	0.58057(2)
z	0.36528(4)	0.36473(3)	0.36612(4)	0.36504(5)	0.36627(4)	0.36699(4)
U_{eq}	0.0073(1)	0.0066(1)	0.0066(1)	0.0067(1)	0.0062(1)	0.0064(1)
Mn in 4*i* (*x*, 0, *z*)						
x	0.21679(4)	0.21744(4)	0.21840(5)	0.21888(7)	0.21956(6)	0.22018(5)
z	0.62018(10)	0.61982(8)	0.61982(11)	0.61892(15)	0.61928(13)	0.61883(12)
U_{eq}	0.0083(1)	0.0071(1)	0.0074(2)	0.0069(2)	0.0067(2)	0.0069(2)
In in 2*a* (0, 0, 0)						
occupancy	0.945(2)	0.927(2)	0.921(2)	0.881(4)	0.904(3)	0.866(3)
U_{eq}	0.0107(2)	0.0092(1)	0.0099(2)	0.0103(2)	0.0087(2)	0.0092(2)
Ge1 in 4*i* (*x*, 0, *z*)						
x	0.06228(3)	0.06276(2)	0.06309(3)	0.06336(5)	0.06377(4)	0.06384(4)
z	0.64873(7)	0.65019(6)	0.65145(8)	0.65175(10)	0.65308(9)	0.65464(8)
U_{eq}	0.0079(1)	0.0067(1)	0.0069(1)	0.0068(2)	0.0064(1)	0.0068(1)
Ge2 in 4*i* (*x*, 0, *z*)						
x	0.20235(3)	0.20111(3)	0.19878(4)	0.19749(5)	0.19588(4)	0.19381(4)
z	0.25755(8)	0.25494(6)	0.25157(8)	0.24909(11)	0.24653(9)	0.24366(8)
U_{eq}	0.0089(1)	0.0082(1)	0.0080(1)	0.0075(2)	0.0073(1)	0.0074(1)

Table 6-4 Interatomic Distances (Å) in $RE_4Mn_2InGe_4$ (*RE* = La–Nd, Sm, Gd)

	$La_4Mn_2In_{0.945(2)}Ge_4$	$Ce_4Mn_2In_{0.927(2)}Ge_4$	$Pr_4Mn_2In_{0.921(2)}Ge_4$	$Nd_4Mn_2In_{0.881(4)}Ge_4$	$Sm_4Mn_2In_{0.904(3)}Ge_4$	$Gd_4Mn_2In_{0.866(3)}Ge_4$
*RE*1–Ge1 (×2)	3.1117(5)	3.0685(3)	3.0467(4)	3.0265(6)	2.9876(5)	2.9582(4)
*RE*1–Ge2	3.1423(7)	3.1010(5)	3.0877(6)	3.0872(9)	3.0346(8)	3.0140(6)
*RE*1–Ge2 (×2)	3.2278(5)	3.1720(3)	3.1442(5)	3.1227(7)	3.0727(6)	3.0418(4)
*RE*1–Mn	3.4465(9)	3.4030(6)	3.3805(9)	3.3738(12)	3.3320(11)	3.3167(9)
*RE*1–In (×2)	3.5038(4)	3.4594(2)	3.4546(3)	3.4333(5)	3.4110(4)	3.3944(2)
*RE*1–Mn (×2)	3.5907(7)	3.5469(5)	3.5281(7)	3.5262(9)	3.4625(8)	3.4302(6)
*RE*2–Ge1 (×2)	3.1481(5)	3.1112(3)	3.0939(5)	3.0852(7)	3.0397(6)	3.0179(4)
*RE*2–Ge2 (×2)	3.2320(5)	3.1861(4)	3.1651(5)	3.1517(7)	3.1044(6)	3.0723(4)
*RE*2–Ge1 (×2)	3.2489(5)	3.2087(3)	3.1877(5)	3.1669(7)	3.1333(6)	3.1041(5)
*RE*2–Mn	3.3109(9)	3.2637(6)	3.2384(8)	3.2222(12)	3.1833(11)	3.1573(9)
*RE*2–Mn (×2)	3.3223(6)	3.2944(5)	3.2848(6)	3.2805(9)	3.2504(8)	3.2336(7)
*RE*2–In (×2)	3.4726(4)	3.4264(2)	3.4158(3)	3.3945(5)	3.3596(4)	3.3388(2)
Mn–Ge2 (×2)	2.6106(6)	2.5886(4)	2.5908(5)	2.5904(8)	2.5699(7)	2.5662(6)
Mn–Ge1	2.6420(9)	2.6151(7)	2.6141(9)	2.6067(13)	2.5868(12)	2.5822(10)
Mn–Ge1	2.6539(10)	2.6265(7)	2.6296(10)	2.6272(14)	2.6062(11)	2.5992(10)
In–Ge1 (×2)	3.0933(6)	3.0401(4)	3.0217(6)	3.0123(8)	2.9613(7)	2.9274(6)
In–Ge2 (×2)	3.3597(7)	3.3017(4)	3.2418(6)	3.1995(9)	3.1500(8)	3.0988(6)
Ge1–Ge1	2.5636(10)	2.5585(8)	2.5609(10)	2.5549(15)	2.5536(13)	2.5552(11)

6.2.3 Band structure calculations

Tight-binding linear muffin tin orbital band structure calculations were performed on a fully stoichiometric $La_4Mn_2InGe_4$ model within the local density and atomic spheres approximation with use of the Stuttgart TB-LMTO-ASA program (version 4.7).[21] The basis set consisted of La 6s/6p/5d/4f, Mn 4s/4p/3d, In 5s/5p/5d/4f, and Ge 4s/4p/4d orbitals, with the La 6p, In 5d/4f, and Ge 4d orbitals being downfolded. Integrations in reciprocal space were carried out with an improved tetrahedron method over 554 irreducible *k* points within the first Brillouin zone.

6.2.4 Electrical resistivity measurement.

A block-shaped crystal of $Pr_4Mn_2InGe_4$, whose identity was confirmed by EDX analysis, was mounted for standard four-probe electrical resistivity measurements between 2 and 300 K on a Quantum Design Physical Property Measurement System (PPMS) equipped with an ac transport controller (Model 7100). The current was 100 μA and the frequency was 16 Hz.

6.3 Results and discussion

Quaternary germanides $RE_4M_2InGe_4$ were previously known only for M = Ni,[12] and have been extended here to include M = Mn. The *RE* substitution is limited to the later members for $RE_4Ni_2InGe_4$ (*RE* = Dy–Tm) but spans through all the typically trivalent members in $RE_4Mn_2InGe_4$ (*RE* = La–Nd, Sm, Gd–Tm, Lu), with the unit cell volumes steadily decreasing as expected following the lanthanide contraction (Figure 6-1). This contrast is probably attributable to the different synthetic conditions used. The

Ni-containing compounds were prepared through off-stoichiometric reactions with substantial excess of In at temperatures no higher than 1000 °C; they could not be obtained in reactions with stoichiometric amounts of *RE*, Ni, and Ge in excess In.[12] On the other hand, the Mn-containing compounds were prepared by arc-melting stoichiometric mixtures of the elements followed by annealing at 800 °C. The arc-melting process assures that the melting points are exceeded and compound formation takes place upon cooling. The presence of considerable amounts of secondary phases after annealing implies that decomposition has probably occurred during equilibration, although we cannot rule out experimental errors such as loss of small amounts of Mn during the cold-pressing of pellets. It seems likely that the $RE_4Ni_2InGe_4$ series can be extended to more *RE* members, perhaps through use of arc-melting instead of a flux technique, and that further $RE_4M_2InGe_4$ series can be prepared for other transition metal components *M*.

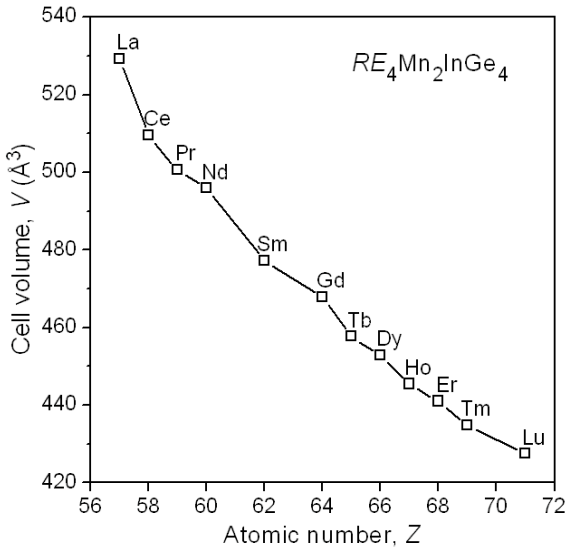

Figure 6-1 Plot of unit cell volumes in $RE_4Mn_2InGe_4$

The germanides $RE_4Mn_2InGe_4$ adopt the monoclinic $Ho_4Ni_2InGe_4$-type structure.[12] If the *RE* atoms are assumed to participate in ionic interactions only, the remaining atoms form a covalent bonding network built from $MnGe_4$ tetrahedra, $InGe_4$ square planes, and Ge_2 dimers (Figure 6-2). The Mn-centred tetrahedra share edges to form double chains $[Mn_2Ge_{4/2}]$ extending down the *b*-direction; in turn, these chains are connected by the Ge_2 dimers along the *a*-direction to form $[Mn_2Ge_4]$ layers that lie parallel to the *ab*-plane. The In atoms in square planar coordination serve to bridge these $[Mn_2Ge_4]$ layers together to form the three-dimensional network. The resulting framework delimits tunnels extending along the *b*- and *c*-directions within which the *RE* atoms are located. There are similarities to other germanides, such as $Yb_2Zn_3Ge_3$,[22] $La_4Mg_7Ge_6$,[23] and $(Sr_{1-x}Ca_x)_5In_3Ge_6$,[24] which are built from the same structural units but connected in different ways.

It is helpful to examine the coordination polyhedra of each site (Figure 6-3) to clarify the relationship of the quaternary $Ho_4Ni_2InGe_4$-type structure adopted by $RE_4M_2InGe_4$ (*M* = Mn, Ni) to the binary Mg_5Si_6-type structure [25,26] from which it is derived as well as to the ternary or pseudoternary variants $Yb_4Mn_2Sn_5$ [27] and $(Eu_{1-x}Ca_x)_4In_3Ge_4$ (Table 6-5).[28] The ordered occupation of the six different sites within the parent Mg_5Si_6-type structure can be rationalized to a first approximation by size effects. The large electropositive components (alkaline-earth and rare-earth atoms) in these structures enter the sites with the highest CN, at the centres of pentagonal prisms. These prisms, which are augmented by additional capping atoms (not shown), figure prominently in Mg_5Si_6 and they are preserved in related binary Mg–Si and ternary Mg–Si–Al alloys.[29–31] The transition-metal components (Mn atoms in $Yb_4Mn_2Sn_5$; Mn or Ni

atoms in $RE_4M_2InGe_4$) are generally the smallest and thus fill the tetrahedral sites, with the lowest CN. A noteworthy feature is the square planar coordination of the metalloid components (Sn atoms in $Yb_4Mn_2Sn_5$; In atoms in $(Eu_{1-x}Ca_x)_4In_3Ge_4$ and $RE_4M_2InGe_4$). The four surrounding atoms can be considered to cap the waists of a tetragonal prism (nearly a cube), reminiscent of what is found within the more prevalent Mo_2FeB_2-type structure.[32] The close relationship to these structures becomes apparent when the coordination around the group-14 components is highlighted. As is common in many intermetallic germanides, the Ge atoms in $RE_4M_2InGe_4$ centre trigonal prisms. If the $RE_4M_2InGe_4$ structure is portrayed in terms of these trigonal prisms (RE_6 around Ge1 and RE_4M_2 around Ge2), it is clearly seen to contain fragments of the tetragonal Mo_2FeB_2-type structure, adopted by ternary germanides RE_2InGe_2, for example (Figure 6-4).[3–6] In RE_2InGe_2, 3^2434 nets of *RE* atoms are stacked along the *c*-direction, to form trigonal prisms occupied by Ge atoms and tetragonal prisms occupied by In atoms. In $RE_4M_2InGe_4$, the 3^2434 nets are severed and the *RE* atoms in one of the corners of the trigonal prisms are replaced by *M* atoms, to generate alternating slabs that are displaced by half the repeat parameter along the stacking direction, with the notches of each slab fitting into the grooves of the adjacent slabs.

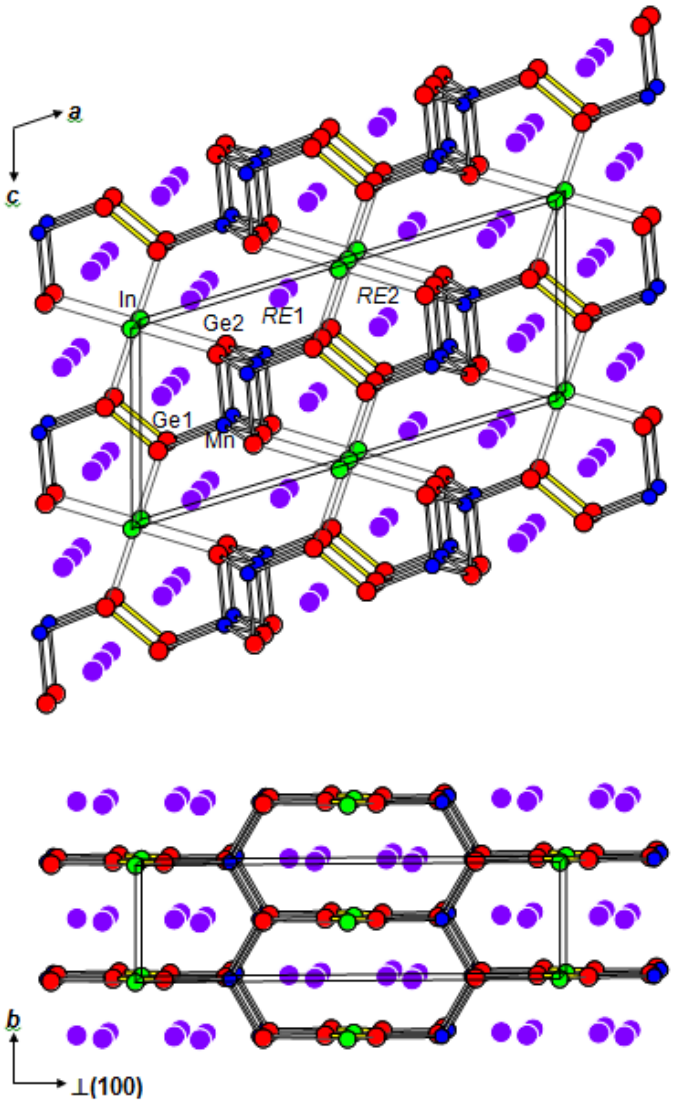

Figure 6-2 Structure of $RE_4Mn_2InGe_4$ highlighting the [Mn_2InGe_4] covalent bonding network, viewed down the *b*- (top) and *c*-directions (bottom). The large purple circles are *RE* atoms, the small blue circles are Mn atoms, the medium green circles are In atoms, and the medium red circles are Ge atoms

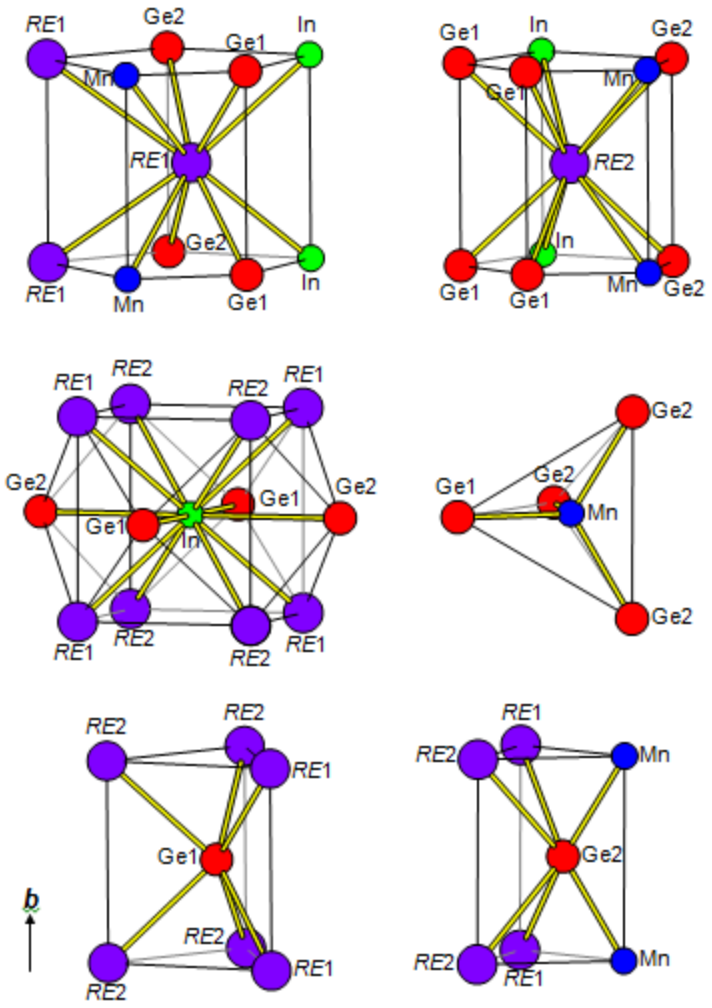

Figure 6-3 Coordination polyhedra in $RE_4Mn_2InGe_4$

Table 6-5 Comparison of Unit Cell Contents in Mg_5Si_6-Derived Structures

sites	Mg_5Si_6	$Yb_4Mn_2Sn_5$	$(Eu_{1-x}Ca_x)_4In_3Ge_4$	$RE_2M_2InGe_4$
pentagonal prisms (4*i*, 4*i*)	8 Mg	8 Yb	8 $(Eu_{1-x}Ca_x)$	8 *RE*
tetrahedra (4*i*)	4 Si	4 Mn	4 In	4 *M*
tetragonal prisms (2*a*)	2 Mg	2 Sn	2 In	2 In
trigonal prisms (4*i*, 4*i*)	8 Si	8 Sn	8 Ge	8 Ge

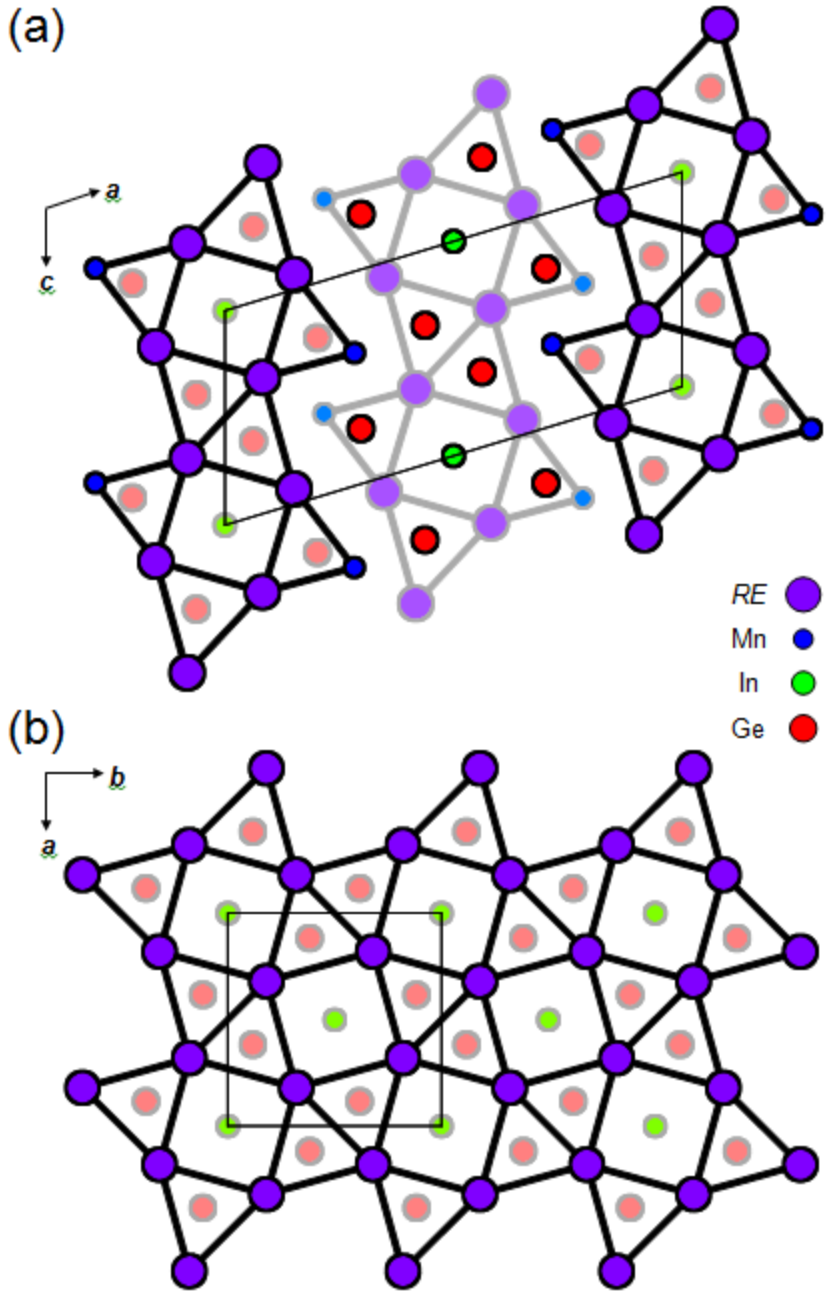

Figure 6-4 Comparison of (a) $RE_4Mn_2InGe_4$ ($Ho_4Ni_2InGe_4$-type) and (b) RE_2InGe_2 (Mo_2FeB_2-type) structures, represented in terms of Ge-centred square prisms and In-centred tetragonal prisms. Dark and light lines distinguish between atoms displaced by half the cell parameter along the viewing direction

The availability of single-crystal diffraction data for $RE_4Mn_2InGe_4$ (*RE* = La–Nd, Sm, Gd) allows structural trends to be examined more closely (Table 6-4). For reference, the sums of Pauling metallic radii (R_1) are: La–Ge, 2.93 Å; Gd–Ge, 2.86 Å; Mn–Ge, 2.42 Å; In–Ge, 2.66 Å; and Ge–Ge, 2.48 Å.[33] The observed *RE*–Ge distances are within 0.1–0.2 Å of expected values and decrease systematically with smaller *RE*. Concurrent with this contraction, the average Mn–Ge distance within the $MnGe_4$ tetrahedra does not vary much (2.58–2.63 Å) and the Ge1–Ge1 distance within the Ge_2 dimers is practically unchanged (2.56 Å), while the In–Ge distances shorten dramatically (from 3.09–3.36 Å in the La member to 2.93–3.10 Å in the Gd member) (Figure 6-5). The implication is that the Mn and Ge atoms define a relatively rigid framework, supporting the picture presented earlier of covalently bonded $[Mn_2Ge_2]$ layers bridged together via weaker bonds to In atoms. The bond length in the Ge_2 dimers in $RE_4Mn_2InGe_4$ is similar as found in other polygermanides (typically 2.5–2.6 Å),[34–37] but the most relevant comparison is with $RE_4Ni_2InGe_4$, where it is also invariant (2.49 Å) with *RE* substitution.[12] The strengthening of the Ge–Ge bond as *M* is substituted with a later transition metal in $RE_4M_2InGe_4$ resembles the bond-making and bond-breaking effects seen in AB_2X_2 compounds with the $ThCr_2Si_2$-type structure.[38,39] The In–Ge distances, which separate into two inequivalent sets in $RE_4Mn_2InGe_4$, can be compared with those in RE_2InGe_2, where the In coordination is rigorously square planar; for a fixed *RE*, they are always longer in $RE_4Mn_2InGe_4$ (cf., 3.02–3.24 Å in $Pr_4Mn_2InGe_4$ vs. 3.01 Å in Pr_2InGe_2).[3–6]

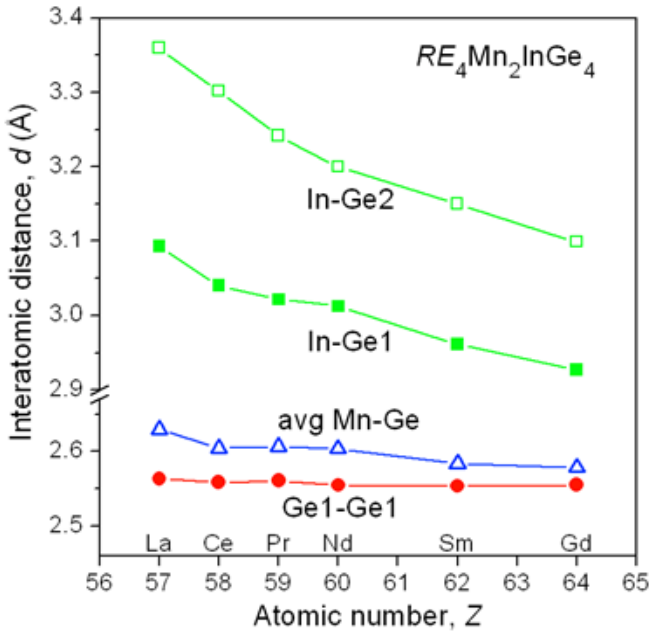

Figure 6-5 Plots of Mn–Ge, In–Ge, and Ge–Ge distances in $RE_4Mn_2InGe_4$

To evaluate the bonding in $RE_4Mn_2InGe_4$ in more detail, the electronic band structure has been calculated for the La member (Figure 6-6). From considerations of relative electronegativities (Pauling values of 1.1 for La, 1.6 for Mn, 1.8 for In, and 2.0 for Ge)[33] and directions of electron transfer, we expect to find mostly empty La states, partially filled Mn and In states, and mostly filled Ge states, as corroborated in the density of states (DOS) curve and its atomic projections. The three narrow bands lying lowest in energy (–10 to –7 eV) correspond essentially to Ge 4s states, and another narrow band at higher energy (centred at –5 eV) to In 5s states. The broad manifold from –4 eV upwards results from strong mixing of La 5d, Mn 3d, and Ge 4p states, with small contributions of In 5p states. Empty La 5d states are found well above the Fermi level (0

eV). The DOS curve for $La_4Mn_2InGe_4$ resembles that for $Eu_2Ca_2In_3Ge_4$ except that Mn 3d states are much more dominant near the Fermi level.[28] Consistent with the earlier discussion of bond distances, the crystal orbital Hamilton population (COHP) curves confirm the presence of La–Ge, Mn–Ge, and Ge–Ge bonding interactions resulting from the filling most of the bonding states and few of the antibonding states up to the Fermi level. The integrated COHP values (–ICOHP) are 0.9 eV/bond for La–Ge, 2.2 eV/bond for Mn–Ge, and 2.2 eV/bond for Ge–Ge contacts. The profile of the Ge–Ge COHP curve, which originates from the Ge_2 dimer in the crystal structure, captures the familiar pattern of molecular orbitals for a diatomic molecule: σ_s and σ_s^* (–9.5 and –7.5 eV, respectively), σ_p and π_p (–4 to –1.5 eV), and π_p^* and σ_p^* levels (–1.5 eV upwards). The Fermi level cuts the merged π_p^*/σ_p^* states, consistent with a $(Ge_2)^{6-}$ species that is isoelectronic to a diatomic halogen molecule like Br_2 in which all but the σ_p^* states are occupied. The In–Ge interactions around the unusual In environment are found to be weakly bonding, notwithstanding the long distances (–ICOHP values of 0.92 eV/bond for the 3.09 Å contacts and 0.58 eV/bond for the 3.36 Å contacts), similar to the situation in $Eu_2Ca_2In_3Ge_4$.[28] There is some evidence for In substoichiometry from the crystal structure determinations, but the decrease in electron count would be small (from 45 e^-/f.u. in $La_4Mn_2InGe_4$ to 44.7 e^-/f.u. in $La_4Mn_2In_{0.9}Ge_4$) and the Fermi level would only be negligibly lowered by 0.02 eV.

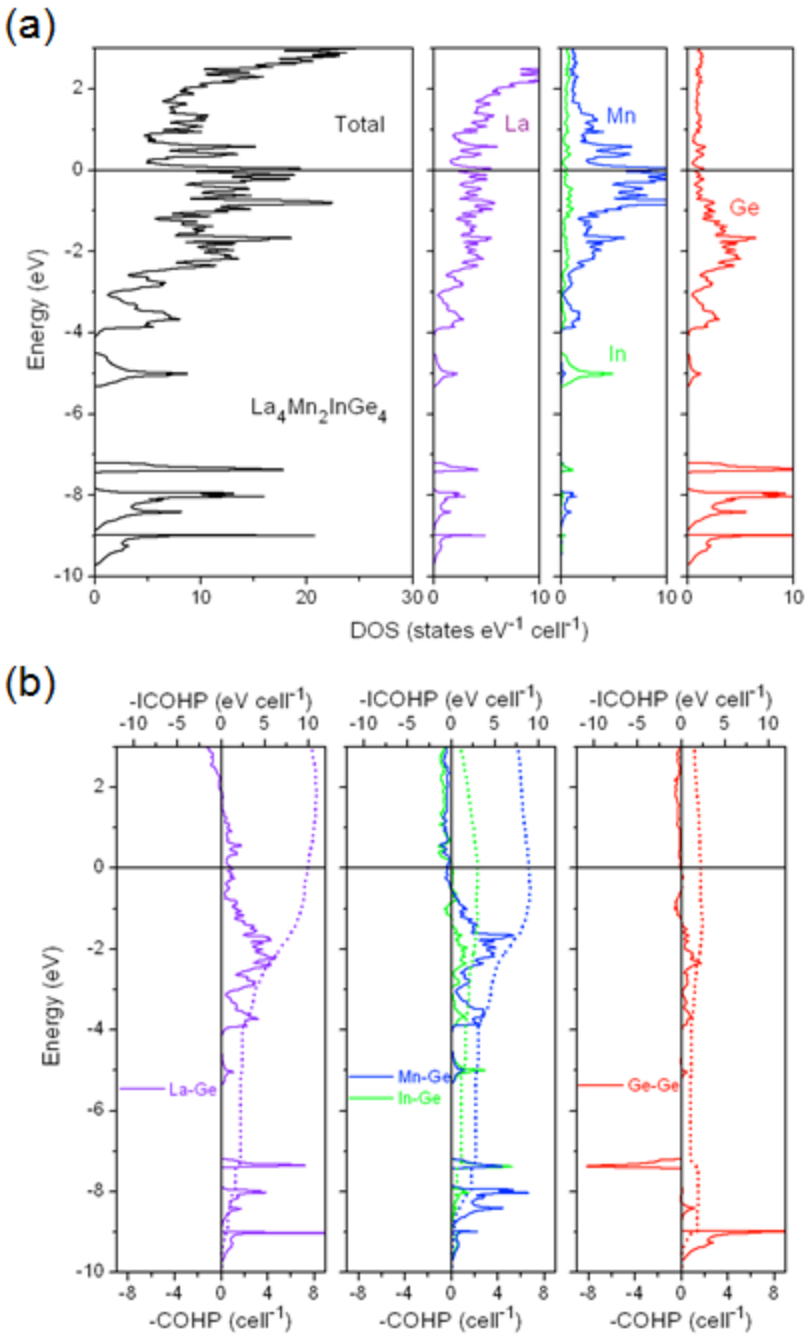

Figure 6-6 (a) Density of states (DOS) and its atomic projections for $La_4Mn_2InGe_4$. (b) Crystal orbital Hamilton population (COHP) curves for La–Ge, Mn–Ge, In–Ge, and Ge–Ge contacts. The Fermi level is at 0 eV

The prediction of metallic behaviour from the band structure of $La_4Mn_2InGe_4$, which can be assumed to be similar for other members of $RE_4Mn_2InGe_4$, is verified by electrical resistivity measurements on $Pr_4Mn_2InGe_4$ (Figure 6-7). The temperature dependence exhibits distinct curvature, with two changes in slope near 130 and 15 K. Similar kinks observed in the resistivity for RE_2InGe_2 (*RE* = Ce–Nd, Sm, Gd) are related to the development of long-range magnetic ordering, typically antiferromagnetism.[4,6] Given that the magnetic susceptibility of Pr_2InGe_2 undergoes an upturn near 15 K,[4] we speculate that the resistivity transition in $Pr_4Mn_2InGe_4$ at this same temperature originates from magnetic ordering of the Pr moments whereas the transition at 130 K involves coupling with the Mn moments. Unfortunately the arc-melting process did not yield single-phase samples required for magnetic measurements. It would be worthwhile attempting use of a flux, as was done for $RE_4Ni_2InGe_4$, even if it does not afford single-phase samples, as magnetic measurements could still be made on selected large crystals of the desired compound.

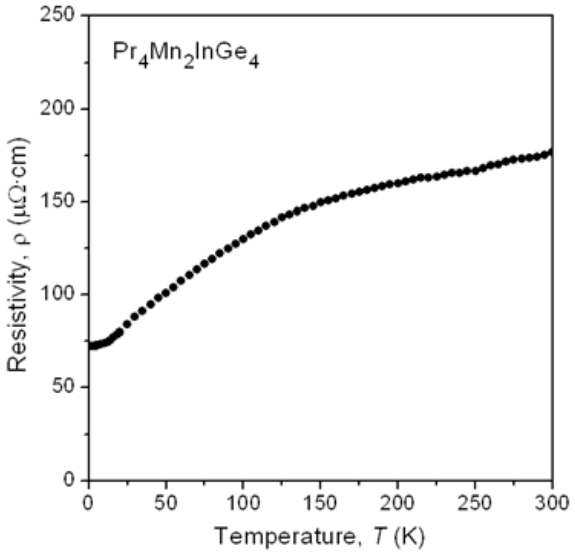

Figure 6-7 Electrical resistivity of $Pr_4Mn_2InGe_4$

6.4 Conclusions

The $RE_4M_2InGe_4$ series, previously known only for M = Ni,[12] has now been extended to include M = Mn. It is probable that the isostructural series containing the intervening transition-metals (M = Fe, Co) exist, and efforts are underway in our laboratory to prepare them. Analysis of the bonding favours a structural description involving $[Mn_2Ge_4]$ layers held weakly together by the In atoms, with *RE* atoms entering tunnels. However, we demonstrate that the structure of $RE_4M_2InGe_4$ can also be derived in a conceptually simple way from RE_2InGe_2 in which introduction of M atoms into one of the *RE* sites in RE_2InGe_2 and cleavage of the 3^2434 nets results in segregated slabs that are shifted with respect to each other. This alternative approach may prove helpful in the eventual interpretation of physical properties for $RE_4M_2InGe_4$ compounds, which are expected to be similar to those for RE_2InGe_2.

6.5 References

[1] Salamakha, P. S.; Sologub, O. L.; Bodak, O. I. In *Handbook on the Physics and Chemistry of Rare Earths*; Gschneidner, K. A., Jr., Eyring, L., Eds.; Elsevier: Amsterdam, 1999; Vol. 27, pp 1–223.

[2] Salamakha, P. S. In *Handbook on the Physics and Chemistry of Rare Earths*; Gschneidner, K. A., Jr., Eyring, L., Eds.; Elsevier: Amsterdam, 1999; Vol. 27, pp 223–338.

[3] Zaremba, V. I.; Stępień-Damm, A.; Nichiporuk, G. P.; Tyvanchuk, Yu. B.; Kalychak, Ya. M. *Kristallografiya* **1998**, *43*, 13–16.

[4] Zaremba, V. I.; Kaczorowski, D.; Nychyporuk, G. P.; Rodewald, U. Ch.; Pöttgen, R. *Solid State Sci.* **2004**, *6*, 1301–1306.

[5] Zaremba, V. I.; Johrendt, D.; Rodewald, U. Ch.; Nychyporuk, G. P.; Pöttgen, R. *Solid State Sci.* **2005**, *7*, 998–1002.

[6] Tobash, P. H.; Lins, D.; Bobev, S.; Lima, A.; Hundley, M. F.; Thompson, J. D.; Sarrao, J. L. *Chem. Mater.* **2005**, *17*, 5567–5573.

[7] Guloy, A. M.; Corbett, J. D. *Inorg. Chem.* **1996**, *35*, 2616–2622.

[8] Nychyporuk, G.; Zaremba, V.; Kalychak, Ya.; Stępień-Damm, A.; Pietraszko, A. *J. Alloys Compd.* **2000**, *312*, 154–157.

[9] Mao, J.; Guloy, A. M. *J. Alloys Compd.* **2001**, *322*, 135–142.

[10] Mao, J.-G.; Goodey, J.; Guloy, A. M. *Inorg. Chem.* **2002**, *41*, 931–937.

[11] Zaremba, V. I.; Kaczorowski, D.; Nychyporuk, G. P.; Rodewald, U. Ch.; Heying, B.; Pöttgen, R. *Z. Anorg. Allg. Chem.* **2006**, *632*, 975–980.

[12] Salvador, J. R.; Kanatzidis, M. G. *Inorg. Chem.* **2006**, *45*, 7091–7099.

[13] Chondroudi, M.; Balasubramanian, M.; Welp, U.; Kwok, W.-K.; Kanatzidis, M. G. *Chem. Mater.* **2007**, *19*, 4769–4775.

[14] Chondroudi, M.; Peter, S. C.; Malliakas, C. D.; Balasubramanian, M.; Li, Q. A.; Kanatzidis, M. G. *Inorg. Chem.* **2011**, *50*, 1184–1193.

[15] Chumalo, N.; Nychyporuk, G. P.; Pavlyuk, V. V.; Pöttgen, R.; Kaczorowski, D.; Zaremba, V. I. *J. Solid State Chem.* **2010**, *183*, 2963–2967.

[16] Dominyuk, N.; Zaremba, V. I.; Pöttgen, R. *Z. Naturforsch., B.: J. Chem. Sci.* **2011**, *66*, 433–436.

[17] Kraus, W.; Nolze, G. *J. Appl. Crystallogr.* **1996**, *29*, 301–303.

[18] Akselrud, L. G.; Grin, Yu. N.; Zavalij, P. Yu.; Pecharsky, V. K.; Fundamenskii, V. S. *Abstracts of Papers*, 12th European Crystallographic Meeting, Moscow, USSR, Aug 20–29, 1989.

[19] Sheldrick, G. M. *SHELXTL*, version 6.12; Bruker AXS Inc.: Madison, WI, 2001.

[20] Gelato, L. M.; Parthé, E. *J. Appl. Crystallogr.* **1987**, *20*, 139–143.

[21] Tank, R.; Jepsen, O.; Burkhardt, A.; Andersen, O. K. *TB-LMTO-ASA Program*, version 4.7; Max Planck Institut für Festkörperforschung: Stuttgart, Germany, 1998.

[22] Grystiv, A.; Kaczorowski, D.; Rogl, P.; Tran, V.; Godart, C.; Gofryk, K.; Giester, G. *J. Phys.: Condens. Matter* **2005**, *17*, 385–397.

[23] Solokha, P.; De Negri, S.; Skrobanska, M.; Saccone, A.; Pavlyuk, V.; Proserpio, D. M. *Inorg. Chem.* **2012**, *51*, 207–214.

[24] You, T.-S.; Bobev, S. *J. Solid State Chem.* **2010**, *183*, 1258–1265.

[25] Zandbergen, H. W.; Andersen, S. J.; Jansen, J. *Science* **1997**, *277*, 1221–1225.

[26] Andersen, S. J.; Zandbergen, H. W.; Jansen, J.; Træholt, C.; Tundal, U.; Reiso, O. *Acta Mater.* **1998**, *46*, 3283–3298.

[27] Lei, X.-W.; Zhong, G.-H.; Li, M.-J.; Mao, J.-G. *J. Solid State Chem.* **2008**, *181*, 2448–2455.

[28] You, T.-S.; Tobash, P. H.; Bobev, S. *Inorg. Chem.* **2010**, *49*, 1773–1783.

[29] Andersen, S. J.; Marioara, C. D.; Frøseth, A.; Vissers, R.; Zandbergen, H. W. *Mater. Sci. Eng., A* **2005**, *390*, 127–138.

[30] van Huis, M. A.; Chen, J. H.; Zandbergen, H. W.; Sluiter, M. H. F. *Acta Mater.* **2006**, *54*, 2945–2955.

[31] van Huis, M. A.; Chen, J. H.; Sluiter, M. H. F.; Zandbergen, H. W. *Acta Mater.* **2007**, *55*, 2183–2199.

[32] Lukachuk, M.; Pöttgen, R. *Z. Kristallogr.* **2003**, *218*, 767–787.

[33] Pauling, L. *The Nature of the Chemical Bond*, 3rd ed.; Cornell University Press: Ithaca, NY, 1960.

[34] Choe, W.; Miller, G. J.; Levin, E. M. *J. Alloys Compd.* **2001**, *329*, 121–130.

[35] You, T.-S.; Bobev, S. *J. Solid State Chem.* **2010**, *183*, 2895–2902.

[36] Siggelkow, L.; Hlukhyy, V.; Fässler, T. F. *J. Solid State Chem.* **2012**, *191*, 76–89.

[37] Guo, S.-P.; Meyers, J. J.; Tobash, P. H.; Bobev, S. *J. Solid State Chem.* **2012**, *192*, 16–22.

[38] Hoffmann, R.; Zheng, C. *J. Phys. Chem.* **1985**, *89*, 4175–4181.

[39] Johrendt, D.; Felser, C.; Jepsen, O.; Andersen, O. K.; Mewis, A.; Rouxel, J. *J. Solid State Chem.* **1997**, *130*, 254–265.

Chapter 7

Many metals make the cut: quaternary rare-earth germanides $RE_4M_2InGe_4$ (M = Fe, Co, Ni, Ru, Rh, Ir) and $RE_4RhInGe_4$ derived from excision of slabs in RE_2InGe_2

A version of this chapter has been published. Oliynyk, A. O.; Stoyko, S. S.; Mar, A. Inorg. Chem. 2015, 54, 2780–2792.

7.1. Introduction

Ternary rare-earth germanides *RE*–*M*–Ge are known for a wide variety of metal or metalloid components *M*, encompassing representatives from the s-block (Li, Mg), d-block (mostly first-row transition-metals from Mn to Cu, as well as some precious metals Ru–Ag and Os–Au), and p-block (Al, Ga, In, Si).[1] These intermetallic compounds are of interest for their rich structural chemistry and diverse physical properties, including complex magnetic ordering (e.g., $RECrGe_3$),[2] magnetocaloric effects (e.g., $Gd_5(Si_xGe_{1-x})_4$),[3] and superconductivity (e.g., $RE_2Pt_3Ge_5$).[4] Among the examples containing a p-block metalloid, the RE_2InGe_2 phases are prevalent, forming for many *RE* components.[5–8] They adopt the tetragonal Mo_2FeB_2-type structure (an ordered variant of the U_3Si_2-type),[9] which exhibits some unusual features, the most remarkable of which are four-coordinate In atoms in rare square-planar geometry and Ge_2 dimers with strong bonds that are little affected by *RE* substitution. Some of the *RE* members can be prepared by stoichiometric reactions of the elements at high temperatures,[6,7] whereas others appear to require use of excess In acting as a flux.[8] Indeed, among the few known quaternary rare-earth

germanides containing In, namely $RE_4Ni_2InGe_4$ (RE = Dy, Ho, Er, Tm),[10] $RE_7Co_4InGe_{12}$ (RE = Dy, Ho, Yb),[11] and $Yb_3AuIn_3Ge_2$,[12] most were obtained, apparently serendipitously, from In flux reactions. It is unclear whether use of a flux is essential for the formation of these compounds, given that $RE_4Mn_2InGe_4$ (RE = La–Nd, Sm, Gd–Tm, Lu), reported recently by us,[13] and $RE_7Ni_{5-x}In_6Ge_{3+x}$ (RE = La–Nd, Sm) can be obtained by conventional methods.[14,15]

There is a close structural relationship between RE_2InGe_2 and $RE_4M_2InGe_4$ (M = Mn, Ni): the substitution within one of the RE sites by a transition-metal atom M in the structure of RE_2InGe_2, along with removal of some of the In atoms, leads to a cleavage of the three-dimensional framework into two-dimensional slabs found in the structure of $RE_4M_2InGe_4$. In this study, three hypotheses were investigated. First, we assert that all quaternary germanides $RE_4M_2InGe_4$ are thermodynamically stable phases that can be prepared through direct reactions of the elements. Second, we predict that new series of germanides $RE_4M_2InGe_4$ can be extended to many other transition-metal components M besides Mn and Ni. Third, we propose that new structures of quaternary germanides can be derived from cutting the framework of RE_2InGe_2 in different ways. After systematic synthetic experiments and structure determinations are carried out, we seek to understand the bonding interactions in these series with the aid of band structure calculations.

7.1 Experimental

7.1.1 Synthesis

Starting materials were freshly filed pieces of all the normally trivalent rare-earth metals (RE = La–Nd, Sm, Gd–Tm, Lu; 99.9%, Hefa), powders of various transition

metals from groups 6 to 10 (*M* = Cr, Mo, W; Mn, Re; Fe, Ru, Os; Co, Rh, Ir; Ni, Pd, Pt; all greater than 99.9% purity, from Alfa-Aesar, Cerac, Spex, or Terochem), In shot (99.999%, Cerac), and Ge pieces (99.9999%, Alfa-Aesar). Mixtures of the elements with the nominal composition "$RE_4M_2InGe_4$" were prepared with a total mass of 3.0 g for samples containing the cheaper transition metals or 2.0 g for those containing the precious metals. In initial experiments, only a few representative *RE* members (*RE* = La, Nd, Tb, Ho) were selected, and if the syntheses were successful for a given series, they were extended to other *RE* members. The samples were cold-pressed into pellets and arc-melted twice in a Centorr 5TA tri-arc furnace or an Edmund Bühler MAM-1 arc-melter on a water-cooled copper hearth under an argon atmosphere. Weight losses after arc-melting were less than 1%. The ingots were sealed in evacuated fused-silica tubes and annealed at 800 °C for one week, after which they were quenched in cold water. The products were ground and analyzed by powder X-ray diffraction (XRD), carried out with Cu $K\alpha_1$ radiation on an Inel diffractometer equipped with a curved position-sensitive detector (CPS 120). Table 7-1 summarizes the results of the reactions, indicating whether or not the synthesis of a given $RE_4M_2InGe_4$ member was successful. In the course of these reactions, a different Rh-containing series $RE_4RhInGe_4$ was found for some later *RE* members. Cell parameters for the quaternary phases were refined with use of the CSD suite of programs[16] and are listed in Table 7-2. Chemical compositions of selected crystals were determined by energy-dispersive X-ray (EDX) analysis on a JEOL JSM-6010LA InTouchScope scanning electron microscope, operated with an accelerating voltage of 20 kV and acquisition times of 70 s. All samples had compositions within 2% of values expected from the chemical formulas.

Table 7-1 Formation of Quaternary Germanides $RE_4M_2InGe_4$ [a]

compound	La	Ce	Pr	Nd	Sm	Gd	Tb	Dy	Ho	Er	Tm	Lu
$RE_4Cr_2InGe_4$	–			–			–		–			
$RE_4Mo_2InGe_4$	–			–			–		–			
$RE_4W_2InGe_4$	–			–			–		–			
$RE_4Mn_2InGe_4$	+	+	+	+	+	+	+	+	+	+	+	+
$RE_4Re_2InGe_4$	–			–			–		–			
$RE_4Fe_2InGe_4$	–	+	+	+	+	+	+	+	+	+	+	+
$RE_4Ru_2InGe_4$	–	+	+	+	+	+	+	+	+	+	+	+
$RE_4Os_2InGe_4$	–			–			–		–			
$RE_4Co_2InGe_4$	–	+	+	+	+	+	+	+	+	+	+	+
$RE_4Rh_2InGe_4$	–	+	+	+	+	+	*	*	*	*	–	–
$RE_4Ir_2InGe_4$	+	+	+	+	–	–	–		–			
$RE_4Ni_2InGe_4$	–	–	–	–	+	+	+	+	+	+	+	–
$RE_4Pd_2InGe_4$					–	–	–	–	–	–	–	–
$RE_4Pt_2InGe_4$				–			–		–			

[a] Legend: known (+), unknown (–), alternative phase $RE_4M InGe_4$ forms (*), reaction not performed (blank entries), single-crystal structures determined (shaded in yellow). Except for $RE_4Mn_2InGe_4$ (all members)[13] and $RE_4Ni_2InGe_4$ (RE = Dy–Tm),[10] all results presented are from this work.

Table 7-2 Cell Parameters for $RE_4M_2InGe_4$ (M = Fe, Co, Ru, Rh, Ir) and $RE_4RhInGe_4$ [a]

compound	a (Å)	b (Å)	c (Å)	β (°)	V (Å^3)
***RE*$_4$Fe$_2$InGe$_4$**					
$Ce_4Fe_2InGe_4$	16.078(1)	4.376(1)	7.305(1)	107.151(8)	491.2(2)
$Pr_4Fe_2InGe_4$	16.0469(6)	4.3386(6)	7.2495(4)	106.954(7)	482.8(1)
$Nd_4Fe_2InGe_4$	15.967(2)	4.3176(8)	7.2351(8)	107.17(1)	476.6(2)
$Sm_4Fe_2InGe_4$	15.781(1)	4.2725(7)	7.1240(6)	107.050(8)	459.2(2)
$Gd_4Fe_2InGe_4$	15.706(2)	4.250(2)	7.081(4)	106.97(3)	452.1(4)
$Tb_4Fe_2InGe_4$	15.623(1)	4.2311(8)	7.0412(5)	107.129(8)	444.8(2)
$Dy_4Fe_2InGe_4$	15.538(2)	4.2125(6)	6.9956(9)	106.976(8)	437.9(2)
$Ho_4Fe_2InGe_4$	15.519(2)	4.200(1)	6.9785(6)	107.13(1)	434.7(2)
$Er_4Fe_2InGe_4$	15.449(2)	4.1783(9)	6.945(1)	107.02(1)	428.7(2)
$Tm_4Fe_2InGe_4$	15.406(2)	4.1734(6)	6.9220(8)	107.146(8)	425.3(2)
$Lu_4Fe_2InGe_4$	15.342(3)	4.150(1)	6.8868(7)	107.233(6)	418.8(2)
***RE*$_4$Co$_2$InGe$_4$**					
$Ce_4Co_2InGe_4$	15.990(1)	4.3504(6)	7.288(1)	107.66(1)	483.1(2)
$Pr_4Co_2InGe_4$	15.847(4)	4.3415(9)	7.2376(8)	107.425(8)	475.1(3)
$Nd_4Co_2InGe_4$	15.8443(6)	4.3167(4)	7.2065(4)	107.603(8)	469.8(1)
$Sm_4Co_2InGe_4$	15.692(1)	4.2823(7)	7.1341(7)	107.714(5)	456.7(2)
$Gd_4Co_2InGe_4$	15.563(2)	4.241(1)	7.061(1)	107.74(1)	443.9(2)
$Tb_4Co_2InGe_4$	15.4676(7)	4.2350(9)	7.0240(5)	107.66(2)	438.4(2)
$Dy_4Co_2InGe_4$	15.406(3)	4.213(1)	6.9904(4)	107.653(9)	432.4(2)
$Ho_4Co_2InGe_4$	15.364(2)	4.1979(7)	6.9698(4)	107.663(5)	428.3(2)
$Er_4Co_2InGe_4$	15.321(2)	4.1834(6)	6.9491(4)	107.67(1)	424.4(2)
$Tm_4Co_2InGe_4$	15.256(2)	4.181(1)	6.9215(7)	107.694(7)	420.6(2)
$Lu_4Co_2InGe_4$	15.193(1)	4.154(1)	6.8851(8)	107.712(7)	413.9(2)
***RE*$_4$Ni$_2$InGe$_4$**					
$Sm_4Ni_2InGe_4$	15.685(3)	4.281(1)	7.133(1)	107.68(2)	456.3(3)
$Gd_4Ni_2InGe_4$	15.532(1)	4.2662(8)	7.111(2)	107.73(1)	448.8(3)
$Tb_4Ni_2InGe_4$	15.4471(9)	4.232(1)	7.069(1)	107.75(3)	440.1(3)
$Dy_4Ni_2InGe_4$	15.410(1)	4.2177(9)	7.0170(4)	108.62(1)	432.2(2)
$Ho_4Ni_2InGe_4$	15.388(2)	4.2074(9)	6.9976(9)	108.542(4)	429.5(2)
$Er_4Ni_2InGe_4$	15.346(1)	4.1936(7)	6.9786(5)	108.511(8)	425.9(1)
$Tm_4Ni_2InGe_4$	15.316(3)	4.1730(9)	6.9618(9)	108.51(1)	421.9(3)
***RE*$_4$Ru$_2$InGe$_4$**					
$Ce_4Ru_2InGe_4$	16.194(1)	4.3821(9)	7.2449(3)	106.239(9)	493.6(2)
$Pr_4Ru_2InGe_4$	16.1110(9)	4.3678(7)	7.2024(4)	106.286(8)	486.5(2)
$Nd_4Ru_2InGe_4$	16.029(2)	4.351(1)	7.1691(4)	106.366(9)	479.7(2)
$Sm_4Ru_2InGe_4$	15.900(1)	4.3175(4)	7.1022(4)	106.546(5)	467.4(1)
$Gd_4Ru_2InGe_4$	15.794(1)	4.291(1)	7.0447(5)	106.608(7)	457.5(2)
$Tb_4Ru_2InGe_4$	15.676(1)	4.2681(9)	6.9902(5)	106.666(5)	448.0(2)
$Dy_4Ru_2InGe_4$	15.638(1)	4.2600(8)	6.9732(5)	106.765(9)	444.8(2)
$Ho_4Ru_2InGe_4$	15.581(1)	4.2385(7)	6.9472(4)	106.766(5)	439.3(1)
$Er_4Ru_2InGe_4$	15.552(2)	4.2286(7)	6.9205(5)	106.843(6)	435.6(2)

$Tm_4Ru_2InGe_4$	15.492(1)	4.2257(8)	6.9053(6)	106.890(8)	432.6(2)
$Lu_4Ru_2InGe_4$	15.458(1)	4.2033(7)	6.8721(4)	107.01(1)	427.0(1)
***RE*$_4$Rh$_2$InGe$_4$**					
$Ce_4Rh_2InGe_4$	16.192(1)	4.3897(7)	7.2480(6)	106.829(7)	493.1(2)
$Pr_4Rh_2InGe_4$	16.146(1)	4.378(1)	7.2236(5)	106.856(9)	488.7(2)
$Nd_4Rh_2InGe_4$	16.0389(8)	4.3549(9)	7.1800(6)	106.91(1)	479.8(2)
$Sm_4Rh_2InGe_4$	15.910(1)	4.3226(8)	7.1131(3)	107.000(8)	467.8(2)
$Gd_4Rh_2InGe_4$	15.793(2)	4.3167(8)	7.0665(4)	107.10(1)	460.5(2)
***RE*$_4$Ir$_2$InGe$_4$**					
$La_4Ir_2InGe_4$	16.548(2)	4.4152(8)	7.3445(6)	106.798(8)	513.7(2)
$Ce_4Ir_2InGe_4$	16.269(2)	4.3643(7)	7.2217(8)	106.953(8)	490.5(2)
$Pr_4Ir_2InGe_4$	16.166(1)	4.3464(6)	7.195(2)	106.92(2)	483.7(3)
$Nd_4Ir_2InGe_4$	16.156(2)	4.3428(6)	7.1839(7)	107.034(8)	481.9(2)
***RE*$_4$RhInGe$_4$**					
$Tb_4RhInGe_4$	20.221(3)	4.251(1)	10.227(2)	105.01(2)	849.1(6)
$Dy_4RhInGe_4$	20.181(2)	4.238(2)	10.225(1)	105.11(1)	844.3(6)
$Ho_4RhInGe_4$	20.110(2)	4.2162(7)	10.220(1)	105.21(1)	836.2(3)
$Er_4RhInGe_4$	20.029(2)	4.2109(9)	10.161(1)	105.29(1)	826.6(4)

[a] Refined from powder diffraction data.

7.2.2 Structure determination

Suitable single crystals, which were grey and irregularly shaped, were found for many members of the $RE_4M_2InGe_4$ (M = Fe, Co, Ru, Rh) series. Intensity data were collected on a Bruker PLATFORM diffractometer equipped with a SMART APEX II CCD detector and a graphite-monochromated Mo $K\alpha$ radiation source, using ω scans at 6–8 different ϕ angles with a frame width of 0.3° and an exposure time of 12–30 s per frame. Face-indexed numerical absorption corrections were applied. Structure solution and refinement were carried out with use of the SHELXTL (version 6.12) program package.[17] The Laue symmetry, systematic absences, and intensity statistics established the centrosymmetric monoclinic space group $C2/m$; direct methods suggested models consistent with the $Ho_4Ni_2InGe_4$-type structure. Atomic coordinates were standardized with use of the program STRUCTURE TIDY.[18] Given previous reports of a small In substoichiometry in related compounds,[10,13] the occupancies of all sites were successively freed in later stages of refinement. The occupancy of the In site ranged from 0.93(2) to 0.99(2), whereas the occupancies for all other sites did not deviate significantly from unity, 1.00(2). In most cases, the occupancy of the In site is quite close to unity and it is difficult to judge whether the slight substoichiometry is physically meaningful or an artefact (e.g., from inadequate absorption correction). The displacement parameters for the In site are always slightly greater than those of the other atoms, but this feature probably reflects the unusually low coordination of this site. Nevertheless, to ensure consistency among all structure determinations, the In occupancy was treated as a variable parameter.

Within the different $RE_4RhInGe_4$ series, a suitable crystal could be found for the Tb member for data collection. $Tb_4RhInGe_4$ also crystallizes in the monoclinic space group $C2/m$; its cell parameters a and c are different from those in $RE_4M_2InGe_4$ but b is similar (~4 Å), suggesting that their structures are related. Direct methods revealed locations of all atoms and refinements proceeded in a straightforward manner. Here there was no evidence of an In substoichiometry and the ideal formula $Tb_4RhInGe_4$ was retained.

Table 7-3 lists abbreviated crystal data and experimental details and Table 7-4 lists ranges of interatomic distances. Full crystallographic data for all structures, including all atomic coordinates and individual interatomic distances, are provided in Tables A6-1–A6-12 as Supporting Information.

7.2.3 Band structure calculations

Tight-binding linear muffin tin orbital band structure calculations were performed within the local density and atomic spheres approximation with use of the Stuttgart TB-LMTO-ASA program (version 4.7).[19] To avoid computational difficulties associated with 4f orbitals of *RE* atoms, the model compounds $La_4M_2InGe_4$ (M = Mn, Fe, Co, Ru) and $Y_4RhInGe_4$ containing nonmagnetic *RE* components were considered. Cell parameters and atomic positions for $La_4M_2InGe_4$ were taken from the corresponding Ce members because the La members are unknown except for the Mn-containing series; similarly, structural parameters for $Y_4RhInGe_4$ were taken from those of the crystallographically characterized Tb member. For $La_4M_2InGe_4$, the basis sets consisted of La 6s/6p/5d/4f, *M* 4s/4p/3d (for Mn, Fe, Co) or 5s/5p/4d/4f (for Ru), In 5s/5p/5d/4f,

and Ge 4s/4p/4d orbitals, with the La 6p/4f, In 5d/4f, and Ge 4d orbitals being downfolded; for $Y_4RhInGe_4$, the basis set consisted of Y 5s/5p/4d/4f, Rh 5s/5p/4d/4f, In 5s/5p/5d/4f, and Ge 4s/4p/4d orbitals, with the Y 5p/4f, Rh 4f, In 5d/4f, and Ge 4d orbitals being downfolded. Integrations in reciprocal space were carried out with an improved tetrahedron method over 554 irreducible k points (from a 16 × 16 × 8 mesh) within the first Brillouin zone. To understand the effect of distortion on the $InGe_4$ square plane, hypothetical structures were examined for $La_4Fe_2InGe_4$ in which the atomic coordinates of Ge1 and Ge2 were adjusted such that the In–Ge1 distances contract while the In–Ge2 distances expand in increments (Δx) of 0.05 Å from an idealized square plane with equal In–Ge distances, while the bond angles around the In atom were fixed (close to 90°).

7.2.4 Magnetic susceptibility measurement

The Sm-containing samples, $Sm_4M_2InGe_4$ (M = Fe, Co, Ru, Rh) were found to be free of impurity phases and were suitable for magnetic susceptibility measurements. The dc magnetic susceptibility was measured under an applied field of 0.5 T between 2 and 300 K on a Quantum Design 9T-PPMS magnetometer. Susceptibility values were corrected for contributions from the holder and sample diamagnetism.

Table 7-3 Crystallographic Data for $RE_4M_2InGe_4$ (M = Fe, Co, Ru, Rh) and $Tb_4RhInGe_4$ [a]

formula	fw (amu)	a (Å)	b (Å)	c (Å)	β (°)	V (Å^3)	ρ_c (g cm^{-3})	μ (mm^{-1})	$R(F)$ [b]	$R_w(F_o^2)$ [c]
$Ce_4Fe_2In_{0.969(2)}Ge_4$	1077.36	16.071(4)	4.3480(10)	7.2757(17)	106.945(3)	486.34(19)	7.357	35.58	0.017	0.039
$Pr_4Fe_2In_{0.974(3)}Ge_4$	1080.52	16.0089(12)	4.3242(3)	7.2282(5)	106.8770(10)	478.83(6)	7.494	37.48	0.020	0.039
$Nd_4Fe_2In_{0.987(2)}Ge_4$	1093.84	15.9354(10)	4.3102(3)	7.2004(5)	107.0650(9)	472.78(6)	7.684	39.31	0.017	0.037
$Sm_4Fe_2In_{0.964(3)}Ge_4$	1118.28	15.770(4)	4.2745(11)	7.1211(17)	107.011(3)	459.0(2)	8.091	43.45	0.020	0.041
$Gd_4Fe_2In_{0.983(5)}Ge_4$	1145.88	15.672(3)	4.2436(8)	7.0643(13)	107.068(3)	449.12(14)	8.473	47.80	0.031	0.069
$Ce_4Co_2In_{0.986(3)}Ge_4$	1083.52	15.9351(14)	4.3361(4)	7.2602(6)	107.5309(12)	478.35(7)	7.523	36.61	0.022	0.045
$Pr_4Co_2In_{0.985(2)}Ge_4$	1086.68	15.8705(6)	4.3247(2)	7.2264(3)	107.5111(5)	473.00(3)	7.630	38.38	0.016	0.034
$Nd_4Co_2In_{0.965(2)}Ge_4$	1100.00	15.7845(9)	4.3028(3)	7.1824(4)	107.5115(8)	465.20(5)	7.853	40.40	0.018	0.037
$Sm_4Co_2In_{0.973(2)}Ge_4$	1124.44	15.6336(12)	4.2723(3)	7.1131(6)	107.6415(10)	452.75(6)	8.248	44.52	0.016	0.033
$Gd_4Co_2In_{0.970(4)}Ge_4$	1152.04	15.548(6)	4.2483(16)	7.058(3)	107.618(5)	444.3(5)	8.610	48.78	0.026	0.054
$Ce_4Ru_2In_{0.962(3)}Ge_4$	1167.80	16.174(4)	4.3794(10)	7.2321(17)	106.144(3)	492.1(2)	7.882	35.29	0.022	0.051
$Pr_4Ru_2In_{0.959(5)}Ge_4$	1170.96	16.083(5)	4.3605(13)	7.190(2)	106.254(4)	484.1(2)	8.033	37.20	0.035	0.081
$Nd_4Ru_2In_{0.954(3)}Ge_4$	1184.28	16.014(6)	4.3463(16)	7.160(3)	106.353(5)	478.2(3)	8.225	38.99	0.024	0.053
$Sm_4Ru_2In_{0.965(3)}Ge_4$	1208.72	15.877(3)	4.3178(7)	7.0936(12)	106.517(2)	466.23(13)	8.610	42.91	0.022	0.044
$Gd_4Ru_2In_{0.962(3)}Ge_4$	1236.32	15.773(4)	4.2875(11)	7.0393(18)	106.635(4)	456.1(2)	9.002	47.20	0.024	0.044

$Tb_4Ru_2In_{0.932(3)}Ge_4$	1243.00	15.6651(9)	4.2639(2)	6.9895(4)	106.672(1)	447.23(4)	9.230	50.10	0.019	0.043
$Dy_4Ru_2In_{0.961(4)}Ge_4$	1257.32	15.612(3)	4.2519(9)	6.9641(15)	106.728(3)	442.73(16)	9.432	52.42	0.024	0.051
$Ho_4Ru_2In_{0.962(4)}Ge_4$	1267.04	15.550(4)	4.2349(12)	6.9425(19)	106.842(4)	437.6(2)	9.617	55.05	0.023	0.054
$Er_4Ru_2In_{0.980(5)}Ge_4$	1276.36	15.526(5)	4.2254(14)	6.916(2)	106.850(4)	434.2(2)	9.762	57.68	0.030	0.069
$Sm_4Rh_2In_{0.973(3)}Ge_4$	1212.40	15.857(3)	4.3147(8)	7.0971(14)	106.878(3)	464.65(16)	8.666	43.36	0.020	0.039
$Tb_4RhInGe_4$	1143.77	20.2575(12)	4.2641(3)	10.2434(6)	104.9984(9)	854.68(9)	8.889	50.89	0.024	0.058

[a] For all structures, $\lambda = 0.71073$ Å, space group $C2/m$ (No. 12). For $RE_4M_2InGe_4$ (M = Fe, Co, Ru, Rh), $T = 173(2)$ K and $Z = 2$; for $Tb_4RhInGe_4$, $T = 296(2)$ K and $Z = 4$. [b] $R(F) = \sum||F_o| - |F_c|| / \sum|F_o|$ for $F_o^2 > 2\sigma(F_o^2)$. [c] $R_w(F_o^2) = [\sum[w(F_o^2 - F_c^2)^2] / \sum wF_o^4]^{1/2}$; $w^{-1} = [\sigma^2(F_o^2) + (Ap)^2 + Bp]$, where $p = [\max(F_o^2,0) + 2F_c^2] / 3$.

Table 7-4 Ranges of Interatomic Distances (Å) for $RE_4M_2InGe_4$ (M = Fe, Co, Ru, Rh) and $Tb_4RhInGe_4$

compound	*RE*–Ge	*RE*–*M*	*RE*–In	*M*–Ge	In–Ge	Ge–Ge
$Ce_4Fe_2In_{0.969(2)}Ge_4$	3.0543(6)–3.4490(8)	3.1351(11)–3.5205(8)	3.3951(6)–3.4591(6)	2.4612(6)–2.4996(10)	3.0088(8)–3.4185(9)	2.5834(10)
$Pr_4Fe_2In_{0.974(3)}Ge_4$	3.0311(5)–3.4545(7)	3.1244(9)–3.4933(7)	3.3810(3)–3.4413(3)	2.4529(5)–2.4944(10)	2.9854(6)–3.3887(7)	2.5803(12)
$Nd_4Fe_2In_{0.987(2)}Ge_4$	3.0108(4)–3.4511(6)	3.1068(7)–3.4749(6)	3.3742(3)–3.4349(3)	2.4524(4)–2.4980(9)	2.9726(5)–3.3412(6)	2.5701(10)
$Sm_4Fe_2In_{0.964(3)}Ge_4$	2.9742(7)–3.4470(9)	3.0692(11)–3.4409(9)	3.3404(6)–3.4048(6)	2.4392(7)–2.4924(12)	2.9333(8)–3.2790(9)	2.5615(13)
$Gd_4Fe_2In_{0.983(5)}Ge_4$	2.9445(9)–3.4429(14)	3.0479(18)–3.4076(13)	3.3257(6)–3.3849(6)	2.4312(11)–2.484(2)	2.9099(12)–3.2302(13)	2.547(2)
$Ce_4Co_2In_{0.986(3)}Ge_4$	3.0399(6)–3.3859(8)	3.0855(10)–3.5304(8)	3.3957(3)–3.4571(3)	2.4439(5)–2.4800(11)	3.0056(7)–3.3725(8)	2.5884(13)
$Pr_4Co_2In_{0.985(2)}Ge_4$	3.0258(4)–3.3858(5)	3.0701(6)–3.5153(5)	3.3822(2)–3.4499(2)	2.4405(3)–2.4790(7)	2.9870(5)–3.3425(6)	2.5810(9)
$Nd_4Co_2In_{0.965(2)}Ge_4$	3.0017(4)–3.3852(6)	3.0536(8)–3.4955(6)	3.3608(3)–3.4317(3)	2.4338(4)–2.4699(9)	2.9657(6)–3.3075(7)	2.5731(10)
$Sm_4Co_2In_{0.973(2)}Ge_4$	2.9680(4)–3.3785(6)	3.0168(7)–3.4674(5)	3.3360(2)–3.4075(3)	2.4262(4)–2.4656(8)	2.9335(5)–3.2372(6)	2.5570(9)
$Gd_4Co_2In_{0.970(4)}Ge_4$	2.9400(10)–3.3814(14)	2.9995(17)–3.4338(12)	3.3209(9)–3.3924(9)	2.4234(10)–2.4683(17)	2.9044(13)–3.1907(14)	2.5493(19)
$Ce_4Ru_2In_{0.962(3)}Ge_4$	3.0495(7)–3.4922(10)	3.1433(9)–3.5311(7)	3.3929(6)–3.4867(6)	2.4792(6)–2.5273(10)	2.9789(9)–3.4512(10)	2.6063(14)
$Pr_4Ru_2In_{0.959(5)}Ge_4$	3.0319(12)–3.4880(16)	3.1249(14)–3.5054(11)	3.3800(8)–3.4736(8)	2.4740(9)–2.5243(16)	2.9552(14)–3.4039(15)	2.594(2)
$Nd_4Ru_2In_{0.954(3)}Ge_4$	3.0178(9)–3.4890(13)	3.1141(13)–3.4863(10)	3.3686(9)–3.4614(9)	2.4728(9)–2.5184(13)	2.9401(12)–3.3660(13)	2.5796(17)
$Sm_4Ru_2In_{0.965(3)}Ge_4$	2.9849(6)–3.4890(9)	3.0846(8)–3.4472(6)	3.3533(5)–3.4389(5)	2.4685(5)–2.5112(9)	2.9051(8)–3.2896(9)	2.5609(15)
$Gd_4Ru_2In_{0.962(3)}Ge_4$	2.9536(8)–3.4947(12)	3.0685(11)–3.4113(8)	3.3370(7)–3.4123(7)	2.4626(7)–2.5078(13)	2.8757(10)–3.2324(11)	2.5463(18)
$Tb_4Ru_2In_{0.932(3)}Ge_4$	2.9289(4)–3.5055(6)	3.0494(6)–3.3829(4)	3.3192(2)–3.3874(2)	2.4582(4)–2.5100(8)	2.8429(6)–3.1781(7)	2.5380(12)

$Dy_4Ru_2In_{0.961(4)}Ge_4$	2.9182(8)–3.4955(9)	3.0343(9)–3.3687(7)	3.3138(6)–3.3828(6)	2.4545(7)–2.5107(13)	2.8341(10)–3.1540(11)	2.5284(18)
$Ho_4Ru_2In_{0.962(4)}Ge_4$	2.9011(8)–3.5013(11)	3.0263(11)–3.3514(8)	3.3044(7)–3.3654(7)	2.4520(8)–2.5123(13)	2.8187(10)–3.1202(11)	2.5245(17)
$Er_4Ru_2In_{0.980(5)}Ge_4$	2.8931(11)–3.5009(14)	3.0196(14)–3.3355(10)	3.3025(8)–3.3612(8)	2.4518(10)–2.5120(17)	2.8076(14)–3.1001(15)	2.513(3)
$Sm_4Rh_2In_{0.973(3)}Ge_4$	2.9777(6)–3.5543(9)	3.0788(8)–3.4434(6)	3.3891(5)–3.4219(5)	2.4964(5)–2.5342(9)	2.9013(8)–3.2141(8)	2.5569(13)
$Tb_4RhInGe_4$	2.9166(9)–3.4498(9)	3.0761(7)–3.3288(5)	3.3673(3)–3.4358(3)	2.4703(5)–2.5524(10)	2.8177(9)–3.0700(9)	2.5958(12)–2.6192(12)

Table 7-5 Integrated Crystal Orbital Hamilton Populations for $La_4M_2InGe_4$ (M = Mn, Fe, Co, Ru) and $Y_4RhInGe_4$ Models

	distances (Å)	–ICOHP (eV/bond)	–ICOHP (eV/cell)	contribution (%)
$La_4Mn_2InGe_4$				
Mn–Ge	2.589 (×2), 2.615, 2.626	2.32 (×2), 2.34, 2.05	9.04	63.0
In–Ge	3.040 (×2), 3.302 (×2)	0.98 (×2), 0.61 (×2)	3.18	22.2
Ge–Ge	2.558	2.12	2.12	14.8
$La_4Fe_2InGe_4$				
Fe–Ge	2.461 (×2), 2.490, 2.500	2.58 (×2), 2.48, 2.27	9.91	66.5
In–Ge	3.009 (×2), 3.418 (×2)	1.04 (×2), 0.47 (×2)	3.02	20.2
Ge–Ge	2.583	1.99	1.99	13.3
$La_4Co_2InGe_4$				
Co–Ge	2.444 (×2), 2.480, 2.473	2.46 (×2), 2.33, 2.20	9.46	64.9
In–Ge	3.006 (×2), 3.372 (×2)	1.05 (×2), 0.52 (×2)	3.14	21.6
Ge–Ge	2.588	1.97	1.97	13.5
$La_4Ru_2InGe_4$				
Ru–Ge	2.479 (×2), 2.527, 2.504	2.77 (×2), 2.55, 2.52	10.61	68.4
In–Ge	2.979(×2), 3.451 (×2)	1.09 (×2), 0.42 (×2)	3.02	19.5
Ge–Ge	2.606	1.87	1.87	12.1
$Y_4RhInGe_4$				
Rh–Ge	2.470 (×2), 2.542, 2.552	1.69 (×2), 1.59, 1.95	6.92	41.5
In–Ge	2.870 (×2), 3.070 (×2), 2.818 (×2), 2.870 (×2)	1.12 (×2), 0.37 (×2) 1.00 (×2), 0.58 (×2)	6.14	36.8
Ge–Ge	2.596, 2.619	1.95, 1.68	3.63	21.7

7.3 Results and discussion

To investigate the formation of quaternary germanides $RE_4M_2InGe_4$, a total of 115 samples were prepared by arc-melting mixtures of the elements followed by annealing at 800 °C for one week. Given that the previously known series were limited to *M* = Mn and Ni,[10,13] attempts were made to substitute all other transition-metal elements from groups 6 to 10 (except Tc). For a fixed *M*, the *RE* components were initially restricted to La, Nd, Tb, and Ho, and then extended to other trivalent *RE* metals if the syntheses were successful. The existence of $RE_4M_2InGe_4$ phases was confirmed for a wide variety of metals from groups 7 (Mn), 8 (Fe, Ru), 9 (Co, Rh, Ir), and 10 (Ni) (Table 7-1). The extent of *RE* substitution varies depending on the identity of *M*. The Mn-containing series is the most extensive, forming for all lanthanides from La to Lu (except Eu and Yb, which are too volatile to be suitable for arc-melting reactions, and Pm, which is radioactive). The Fe-, Ru-, and Co-containing series are almost as extensive except that the La members do not form. In the progression down the Co-triad metals, the extent of *RE* substitution gradually becomes narrower until only the largest members (La–Nd) are found for $RE_4Ir_2InGe_4$. An unexpected result of these synthetic experiments is that although $RE_4Rh_2InGe_4$ forms for *RE* = La–Nd, Sm, Gd, a different series $RE_4RhInGe_4$ was discovered for *RE* = Tb–Er. The Ni-containing series was previously known for *RE* = Dy–Tm; it was suggested that this series could only be prepared through use of an In flux but not through arc-melting or induction-melting reactions.[10] However, the present investigation indicates that not only can this series be formed through arc-melting and annealing, it can also be extended to include *RE* = Sm, Gd, and Tb.

Cell parameters determined from powder XRD data (Table 7-2) generally follow expected trends. Within any series of fixed *M*, the cell volume decreases in accordance with the lanthanide contraction (Figure 7-1). Among the series containing the 3d-metals Mn, Fe, Co, and Ni, the cell volume curves shift downwards, reflecting the trend in decreasing metallic radii of these elements on proceeding across the periodic table. The cell volume curves for $RE_4Ni_2InGe_4$ and $RE_4Co_2InGe_4$ are nearly coincident, suggesting that perhaps with appropriate changes in synthetic conditions, it may be possible to extend the Ni-containing series to further *RE* members. Among the series containing the 4d- and 5d-metals Ru, Rh, and Ir, the cell volume curves almost overlap; the trend in increasing metallic radii in this progression is reflected instead in the compatibility with larger *RE* components. These observations suggest that both size factors involving well-matched combinations of *RE* and *M* components and electronic factors restricting the *M* component to groups 7–10 are important in the stability of these compounds. If group 6 metals are excluded from consideration (given that none were found to form $RE_4M_2InGe_4$ phases in the synthetic experiments, presumably because the electron count is too low), then a structure map created by plotting the Pauling metallic radii[20] of *RE* and *M* is reasonably effective in delimiting the regions in which $RE_4M_2InGe_4$ forms (Figure 7-2). At the boundary defining the upper limit of the radius of *M* (near 1.25 Å), the alternative phase $RE_4RhInGe_4$ forms within only a very narrow region. Substitution of the *M* component in structurally related ternary rare-earth germanides such as RE_2MGe_2 (Sc_2CoSi_2-type) and REM_2Ge_2 ($CeAl_2Ga_2$-type) also appear to be restricted to later transition metals;[21] it would be interesting to develop a more generalized structure map applicable to a broader set of such phases.

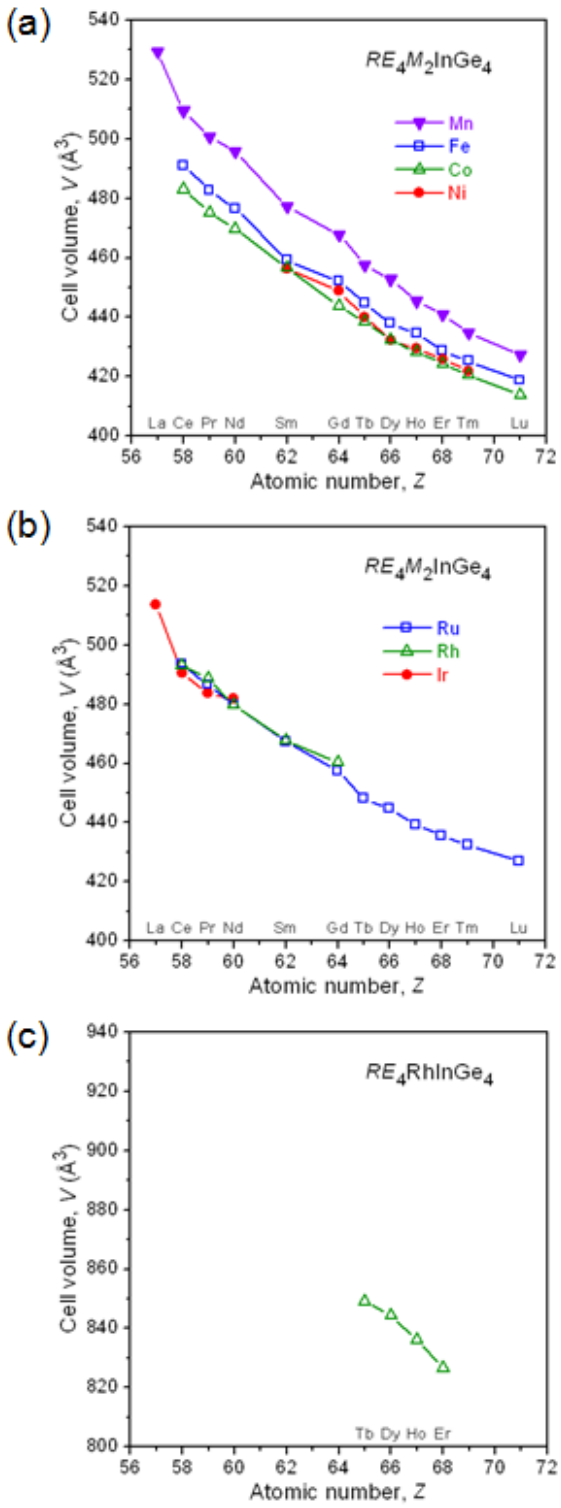

Figure 7-1 Plots of unit cell volumes for (a) $RE_4M_2InGe_4$ (M = Mn, Fe, Co, Ni), (b) $RE_4M_2InGe_4$ (M = Ru, Rh, Ir), and (c) $RE_4RhInGe_4$. Data for $RE_4Mn_2InGe_4$ are taken from Ref. 13

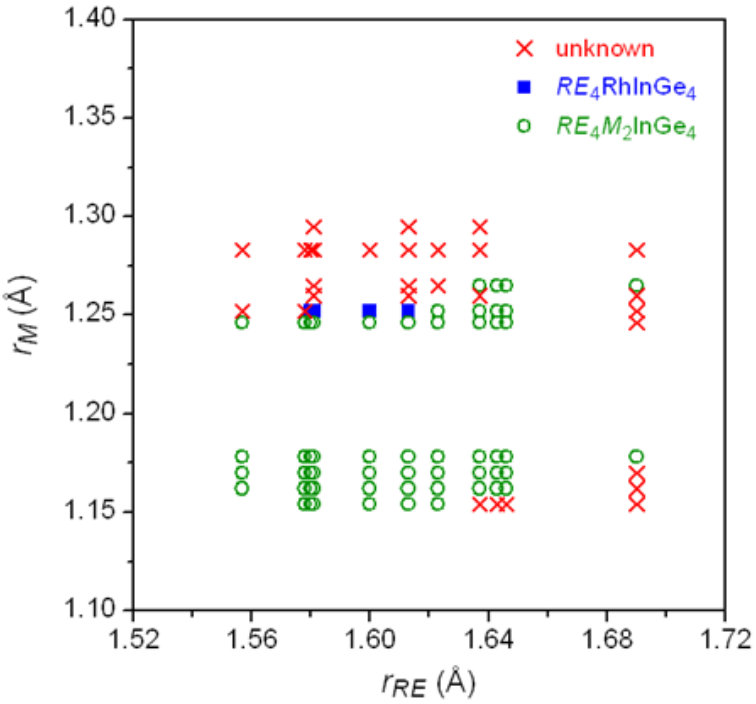

Figure 7-2 Structure map defined by Pauling metallic radii of *RE* and *M* components

To the best of our ability, we evaluated as many single crystals as possible for their suitability for further X-ray diffraction experiments. Within the four RE_4M_2InGe$_4$ series containing *M* = Fe, Co, Ni, and Ru, 20 structure determinations were carried out; unfortunately, suitable crystals could not be found for any of the Ir-containing members. Within the new RE_4RhInGe$_4$ series, the crystal structure was determined solely for the Tb member. Both RE_4M_2InGe$_4$ ($Ho_4Ni_2InGe_4$-type) and RE_4RhInGe$_4$ (new type) adopt monoclinic structures with similar values of the short-axis parameter (*b* = ~4.3 Å). In terms of a conventional description focused on the covalent framework, both structures contain the same building blocks of MGe$_4$ tetrahedra, InGe$_4$ square planes, and Ge$_2$ dimers (Figure 7-3). The MGe$_4$ tetrahedra are connected through edges and corners to

form infinite double chains extending along the *b*-direction. (These double chains could also be described as ladders made up of *M*–Ge rungs or ribbons made up of M_2Ge_2 rhombi.) In $RE_4M_2InGe_4$, one of the four Ge atoms surrounding each tetrahedrally coordinated *M* atom belongs to a Ge_2 dimer, which acts to connect adjacent double chains along the *a*-direction to generate [M_2Ge_4] layers parallel to the *ab*-plane. In atoms in square planar coordination then connect these layers together, delimiting two types of tunnels: a smaller pentagonal one filled by *RE*2 atoms and a larger oblique one (outlined by an 8-membered ring) filled by *RE*1 atoms. In $RE_4RhInGe_4$, all four Ge atoms surrounding each Rh atom belong to Ge_2 dimers, which are not connected directly to adjacent double chains but rather through the intermediary of the In atoms. Two types of pentagonal tunnels are separately filled by the *RE*2 and *RE*4 atoms, and a large irregular-shaped (12-membered ring) one is filled by the *RE*1 and *RE*3 atoms. The double chains of tetrahedra appear to be a common motif in other germanide structures, such as $RE_3M_2Ge_3$,[22] $Yb_2Zn_3Ge_3$,[23] $La_4Mg_7Ge_6$,[24] and $(Sr_{1-x}Ca_x)_5In_3Ge_6$.[25] The complete coordination environment around the In atoms includes eight *RE* atoms at the vertices of a tetragonal prism, augmented by four Ge atoms capping the waist. This twelve-coordinate geometry is reduced in symmetry from an ideal cuboctahedron; while unusual, it is also encountered around the metalloid atoms in other structures (e.g., In in RE_2InGe_2;[5–8] Sn in $Yb_4Mn_2Sn_5$).[26]

Many intermetallic structures are often usefully described in terms of stackings of nets.[27] Although this approach may seem less appealing because it neglects consideration of bonding interactions, it provides other advantages in systematizing a large number of structures and drawing out the relationships between them. Previously we had shown

that $RE_4M_2InGe_4$ can be derived from RE_2InGe_2.[13] The tetragonal (Mo_2FeB_2-type) structure of RE_2InGe_2 consists of a stacking of 3^2434 nets of *RE* atoms interleaved with $5^3 + 5^4$ (3:2) nets of In and Ge atoms.[8] (The Schläfli symbols indicate the types and numbers of polygons surrounding the nodes in a net of atoms.[27]) The In atoms lie over the squares and the Ge atoms over the triangles of the *RE* nets, so that the structure of RE_2InGe_2 may be equally well described in terms of In-centred tetragonal prisms and Ge-centred trigonal prisms. The structures of $RE_4M_2InGe_4$ and $RE_4RhInGe_4$ can now be generated through the identical procedure of excising slabs from RE_2InGe_2, separating these slabs and replacing the terminal *RE* atoms by *M* atoms, removing the intervening In atoms over cut squares, and translating these slabs parallel and perpendicular to the stacking direction so that the *M* atoms protruding from one slab rest in the notches of adjacent slabs to attain tetrahedral coordination by Ge atoms (Figure 7-4). The difference is that $RE_4M_2InGe_4$ is derived by cutting slabs parallel to (100), whereas $RE_4RhInGe_4$ is derived by cutting slabs parallel to (110). The derivation of complex structures through repetition by symmetry operations of parts of a simpler structure is, of course, a powerful systematizing principle in crystal chemistry.[28] The procedure of excising RE_2InGe_2-type slabs appears to have broader generality. For example, the structure of $(Eu_{1-x}Ca_x)_3In_2Ge_3$ [29] can be derived by cutting slabs parallel to (100) that are thicker than in $RE_4M_2InGe_4$ (Figure A6-1). It is also possible to imagine new target structures of hypothetical compounds that can be obtained by this procedure. This is not the only way to cut slabs and other approaches are possible.

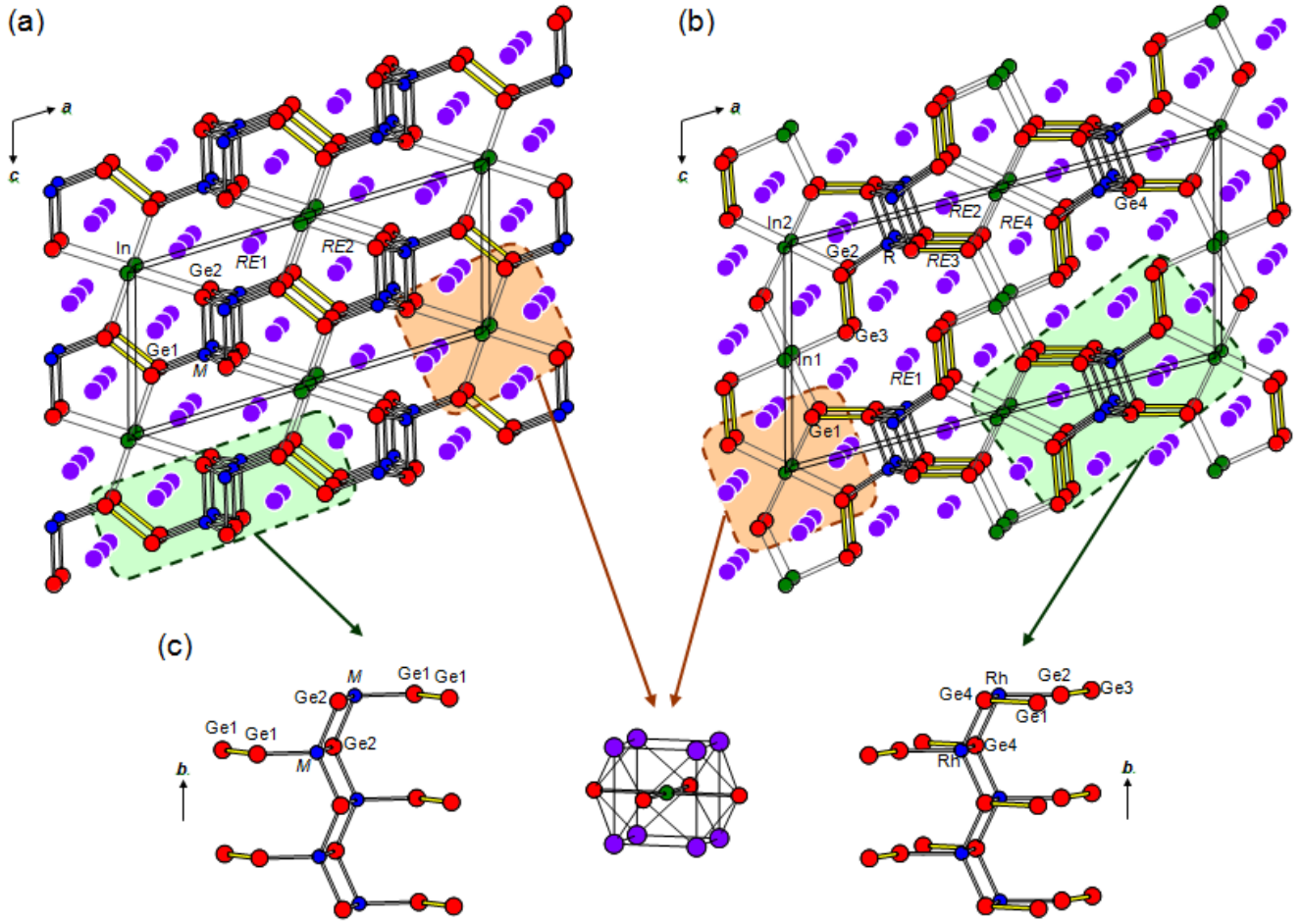

Figure 7-3 Structures of (a) $RE_4M_2InGe_4$ and (b) $RE_4RhInGe_4$ in terms of covalent frameworks built from (c) double chains of MGe_4 tetrahedra decorated with Ge_2 pairs, and In square planes embedded within tetragonal prisms of *RE* atoms. The large purple circles are *RE* atoms, the small blue circles are *M* atoms, the medium green circles are In atoms, and the medium red circles are Ge atoms

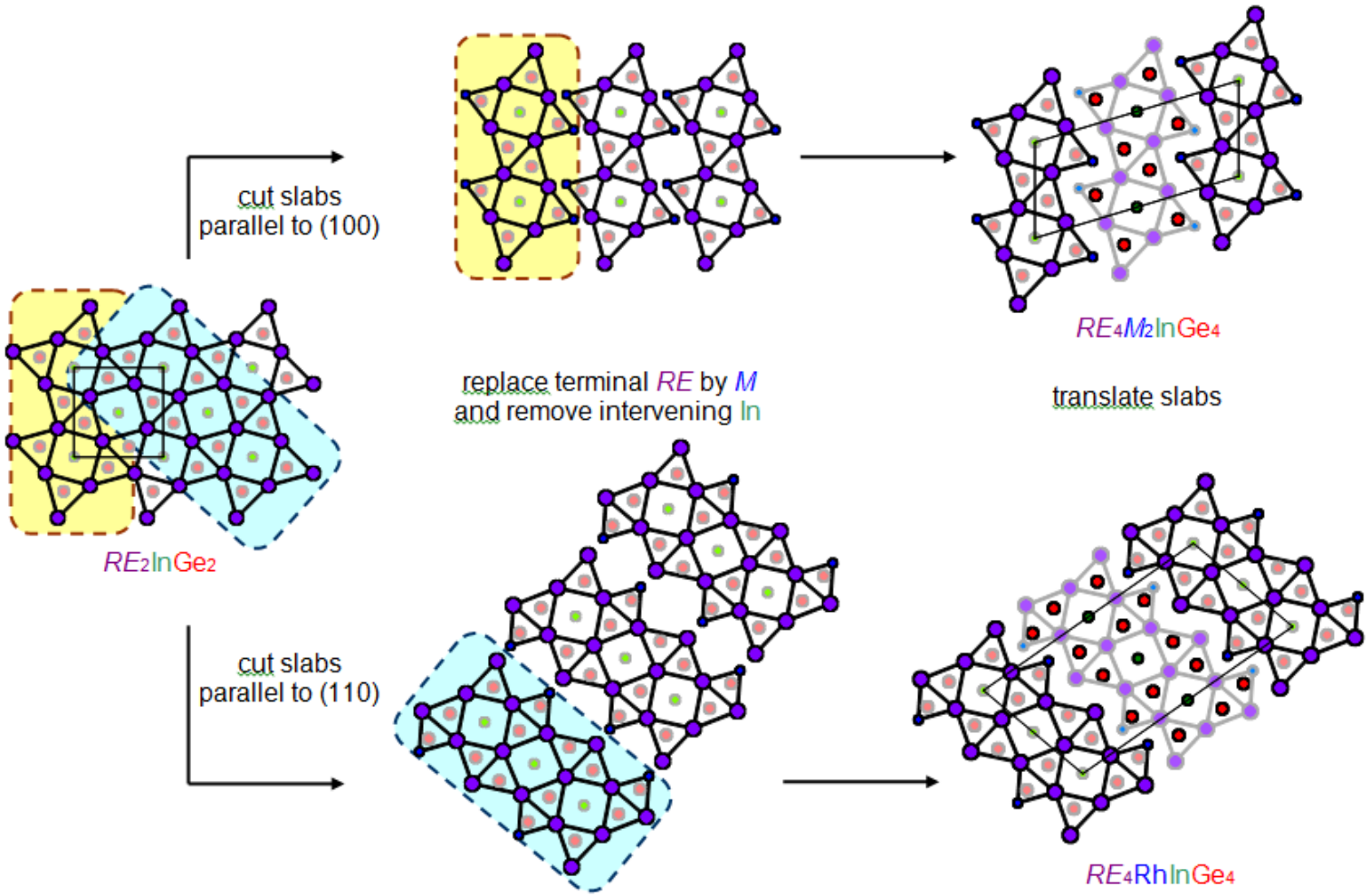

Figure 7-4 Derivation of $RE_4M_2InGe_4$ and $RE_4RhInGe_4$ from RE_2InGe_2, highlighting In-centred tetragonal prisms and Ge-centred trigonal prisms. Dark and light lines distinguish between atoms displaced by half the cell parameter along the viewing direction.

Analysis of bonding interactions suggests that the structure of $RE_4M_2InGe_4$ is dominated by strong covalent *M*–Ge and Ge–Ge bonds, which build up rigid [M_2Ge_2] layers held together by weaker covalent bonds to In atoms and mostly ionic interactions to *RE* atoms. Inspection of interatomic distances (Table 7-4) confirms that *M*–Ge bonds change little upon substitution with smaller *RE* components (Fe–Ge, 2.431–2.500 Å; Co–Ge, 2.423–2.480 Å; Ru–Ge, 2.452–2.527 Å; Rh–Ge, 2.496–2.534) and are close to the sums of Pauling metallic radii (Fe–Ge, 2.41 Å; Co–Ge, 2.40 Å; Ru–Ge, 2.49 Å; Rh–Ge, 2.49 Å).[20] The significant distinction between the nearly constant Ge1–Ge1 distances within the Ge_2 dimers and the highly variable In–Ge distances within the $InGe_4$ squares is highlighted graphically (Figure 7-5). The Ge_2 dimers are only modestly affected by *RE* or *M* substitution, containing 2.5–2.6 Å distances that are close to the sum of metallic radii (2.48 Å) and similar to those found in many polygermanides. In contrast, the $InGe_4$ squares are actually highly distorted, with a pair of shorter In–Ge1 distances (2.9–3.1 Å) and a pair of longer In–Ge2 distances (3.2–3.4 Å). As *M* is substituted with Mn, Fe, Co, and Ru in this progression, the distances within these In–Ge pairs become more disparate such that the geometry around the In atoms could perhaps be better described as linear (CN2), as in the extreme case of $Ce_4Ru_2InGe_4$ (In–Ge1, 2.979 Å; In–Ge2, 3.451 Å). These distances are much longer than the sum of metallic radii (2.66 Å); relative to other situations of four-coordinate In atoms bonded to Ge atoms, they are longer than in those in tetrahedral geometry (e.g., 2.672–2.877 Å in $(Sr_{1-x}Ca_x)_5In_3Ge_6$)[25] but typical of those in square planar (e.g., 2.967–3.211 Å in $(Eu_{1-x}Ca_x)_4In_3Ge_4$)[29] or seesaw geometry (e.g., 2.823–2.942 Å in Ca_4InGe_4).[30]

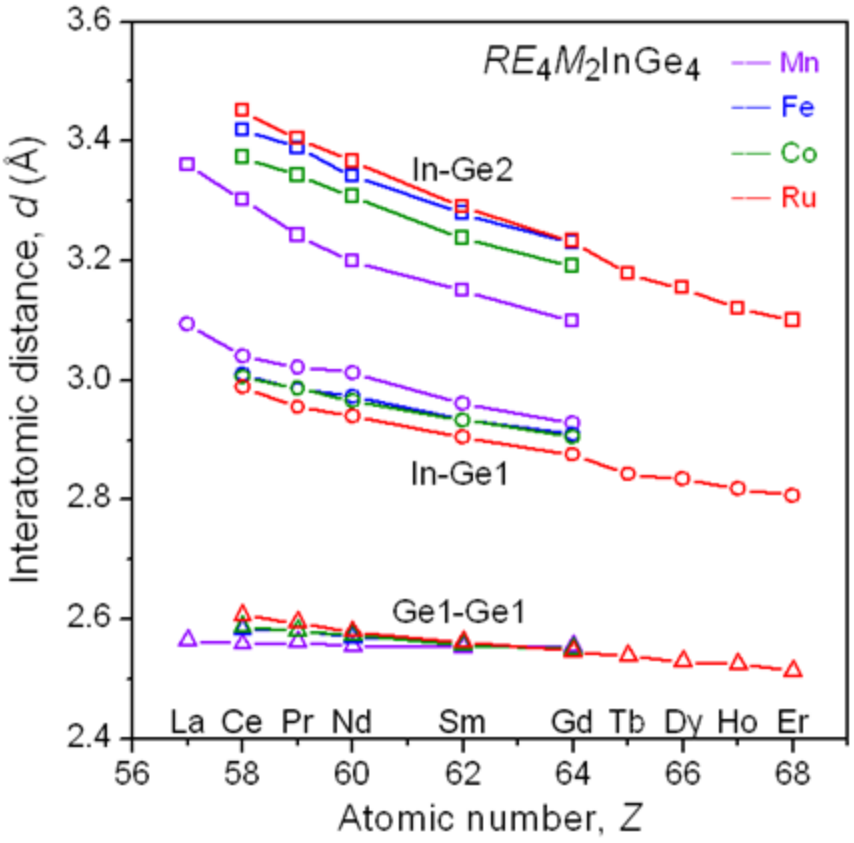

Figure 7-5 Plots of In–Ge1, In–Ge2, and Ge1–Ge1 distances in $RE_4M_2InGe_4$ (M = Mn, Fe, Co, Ru). Data for $RE_4Mn_2InGe_4$ are taken from Ref. 13

It is tempting to account for the electronic structures of these quaternary germanides by applying a rudimentary Zintl formalism, as has been done for RE_2InGe_2 previously.[8] To a good approximation, the electropositive RE atoms transfer their valence electrons entirely to form RE^{3+} cations. For RE_2InGe_2, the assumption of fully ionic character within the In–Ge bonds results in the oxidation state assignment of +3 for the In atoms within the square planes and –3 for the Ge atoms within the Ge_2 pairs, giving the formulation $(RE^{3+})_2(In^{3+})(Ge^{3-})_2(e^-)_3$, in which three excess electrons per formula unit enter the conduction band. Given the similar electronegativities of In (1.8)

and Ge (2.0),[31] the more realistic assumption of fully covalent character within the In–Ge bonds results in the formal charge assignment of 1– for the four-bonded In atoms and 1– for the three-bonded Ge atoms, giving the alternative formulation $(RE^{3+})_2(In^{1-})(Ge^{1-})_2(e^-)_3$ with the same conclusion of an electron excess. For $RE_4M_2InGe_4$, the extension of these arguments leads to the formulations $(RE^{3+})_4(M^{2+})_2(In^{3+})(Ge^{3-})_2(Ge^{4-})_2(e^-)_5$ or $(RE^{3+})_4(M^{2+})_2(In^{1-})(Ge^{2-})_2(Ge^{3-})_2(e^-)_5$, if divalent *M* atoms are assumed. For $RE_4RhInGe_4$, these formulations are $(RE^{3+})_4(Rh^{3+})(In^{3+})(Ge^{3-})_4(e^-)_6$ or $(RE^{3+})_4(Rh^{3+})(In^{1-})(Ge^{1-})(Ge^{2-})_2(Ge^{3-})(e^-)_6$, if trivalent Rh atoms are assumed.

The electronic structure of $La_4Fe_2InGe_4$ (a hypothetical model based on the structure of $Ce_4Fe_2InGe_4$ but containing a nonmagnetic *RE* component) serves as a useful point of reference to examine the effects of substitution with a transition metal on progressing across a period (*M* = Mn, Fe, Co) or down a group (*M* = Fe, Ru). The Fermi level cuts through a substantial density of states (DOS) at the Fermi level and there is no energy gap or deep pseudogap nearby that would be indicative of a Zintl phase (Figure 7-6a). Nevertheless, the formal charge assignments presented above are generally confirmed by the atomic projections, which show that the DOS is dominated by partly filled Fe, In, and Ge states up to the Fermi level, and mostly empty La states above the Fermi level. The Fe 3d band extends from –4 to +2 eV; it is more than half-filled up to the Fermi level, consistent with a simple assignment of Fe^{2+}. The In 5s states are largely localized in a narrow band near –5 eV and the In 5p states are dispersed widely from –4 eV upwards. The distinction between Ge states belonging to the Ge1–Ge1 pair and the isolated Ge2 atoms can be clearly seen. The Ge1 states follow the recognizable energy ordering for the MOs of a diatomic molecule, with the σ_s and σ_s^* levels found near –9

and –7 eV, the σ_p and π_p levels from –5 to –1 eV, and the π_p* and σ_p* levels from –1 eV upwards. In contrast, the Ge2 states do not show any splitting of the 4s states, being localized near –8.5 eV, while the 4p states are found in the manifold at higher energy (–4 eV upwards).

A more detailed analysis of the bonding can be evaluated from the crystal orbital Hamilton population curves (Figure 7-6b). In agreement with the description of the crystal structure in terms of rigid [M_2Ge_2] layers, Fe–Ge and Ge–Ge contacts constitute the strongest type of bonding interactions. The Fe–Ge interactions are nearly optimized, with only weakly antibonding levels being present at the Fermi level; roughly, this situation corresponds to occupation of the *e* and some of the t_2 levels in an isolated $FeGe_4$ tetrahedral complex. The Ge–Ge interactions (originating from the Ge1–Ge1 pair) are net bonding, resulting from the occupation of the σ_s and σ_s* levels (which cancel each other out), the σ_p and π_p levels, and some of the π_p* levels. Given the relatively poor π-overlap of Ge 4p orbitals, it is not surprising that the π_p and π_p* levels represent weak (but nonneglible) interactions. In fact, the π_p* levels, which continue to extend well above the Fermi level (up to +10 eV), are barely occupied. In an isolated $(Ge^{3-})_2$ dimer, the π_p* levels would be completely filled, similar to the isoelectronic Br_2 molecule. It is worthwhile to understand why these π_p* levels have been depopulated within the solid. The reasons are related to the formation of the weak In–Ge bonds within the $InGe_4$ square planes.

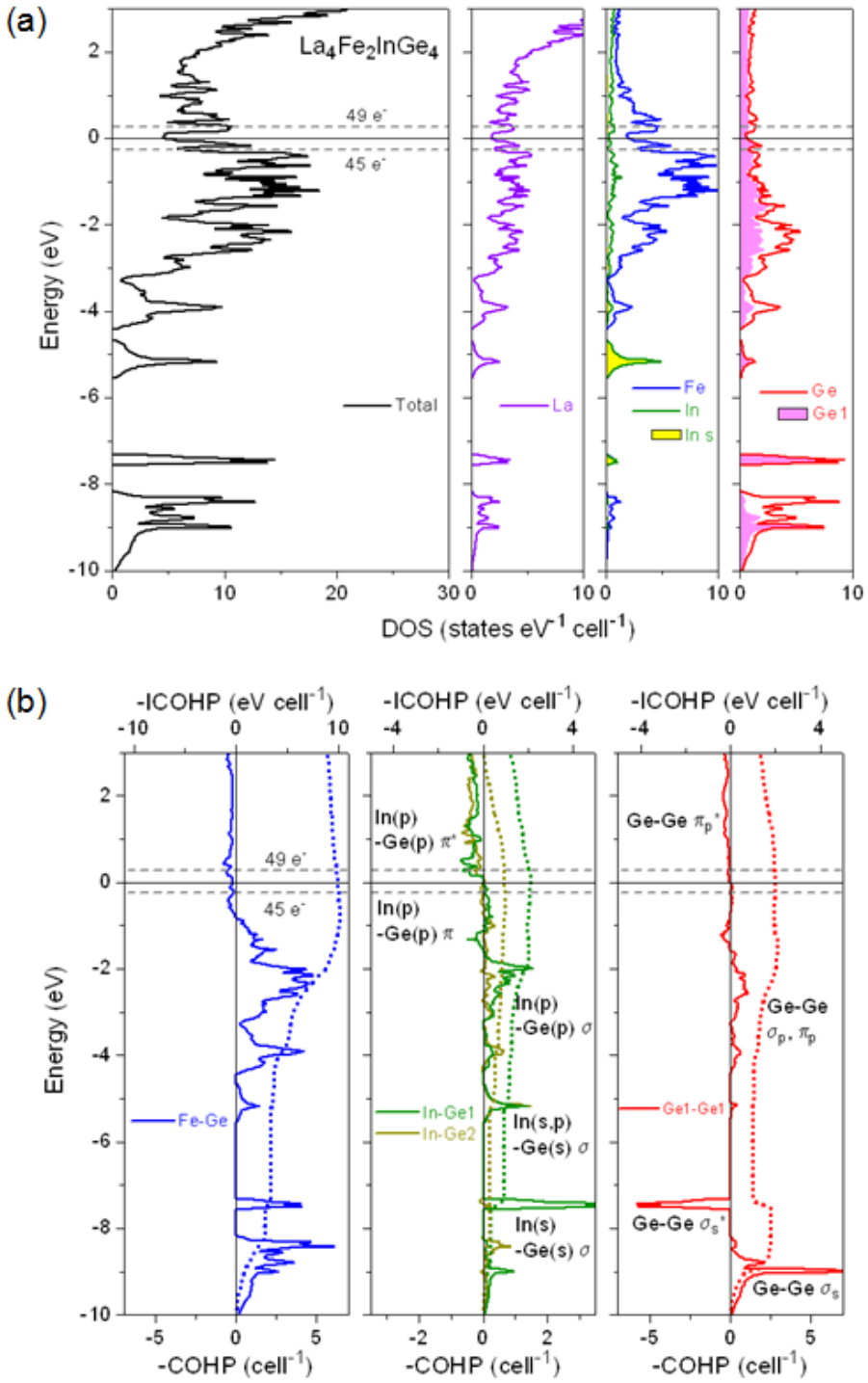

Figure 7-6 (a) Density of states (DOS) and its atomic projections for $La_4Fe_2InGe_4$. The Fermi level is at 0 eV for 47 e^-/f.u. The yellow shaded region in the third panel highlights the contribution of the In 5s states; the magenta shaded region in the last panel highlights the contribution of the Ge1 states involved in Ge1–Ge1 bonding. (b) Crystal orbital Hamilton population (COHP) curves for Fe–Ge, In–Ge, and Ge–Ge contacts.

In $RE_4M_2InGe_4$, the In–Ge distances are highly sensitive to substitution of the *M* component, and to a lesser extent, the *RE* component. All members of $RE_4M_2InGe_4$ exhibit distortion of this $InGe_4$ square plane, with the distance to the Ge1 atoms (belonging to the Ge1–Ge1 pair) being shorter than to the isolated Ge2 atoms (Figure 7-7a). The stabilizing orbital interactions responsible for these In–Ge bonds can be traced to σ-overlap of In s with Ge s orbitals (–9 to –7 eV) and of In s/p with Ge s/p orbitals (–5 to –1 eV), as seen in the COHP curves. For example, the bonding peak in the In–Ge1 COHP curve at –2 eV can be attributed to Bloch functions in which the lobes of one set of the Ge1–Ge1 π_p orbitals (lying parallel to the $InGe_4$ plane) are directed towards the p-orbitals on In atom in a σ-fashion. At higher energies, weak π-overlap of In p with Ge p orbitals becomes operative; these interactions are nearly nonbonding just below the Fermi level (–2 to 0 eV) and become antibonding above. Similarly, the Ge–Ge interactions are nearly nonbonding in this region. Thus, $La_4Fe_2InGe_4$ attains a structure in which both In–Ge and Ge–Ge distances are adjusted to avoid the occupation of the antibonding levels, including the Ge–Ge π_p^* levels mentioned above. To understand the origin of the distortion in the $InGe_4$ square plane, calculations were performed on models in which the In–Ge1 distances are contracted while the In–Ge2 distances are expanded by the same increment of Δx relative to an idealized square plane with equal distances. The total energy decreases when these distortions are introduced and is minimized when Δx is 0.2 Å (Figure 7-8a), consistent with observations for the $RE_4Fe_2InGe_4$ series (Figure 7-5). A plot of the integrated COHP values (–ICOHP) for the different interactions is instructive (Figure 7-8b). The distortion of the $InGe_4$ square plane also affects the distances of the Ge1 and Ge2 atoms to the Fe atoms to which they are bonded. A key driving force is the

need to satisfy good Fe–Ge contacts, which strengthen upon distortion of the $InGe_4$ square plane. Each Ge2 atom is bonded to three Fe atoms, whereas the Ge1 atom is only bonded to one Fe atom. Thus it is favourable for the Ge2 atoms to sacrifice what little weak bonding they have to the In atoms to optimize their stronger bonding to the Fe atoms. Put another way, because the Ge2 atoms have already saturated their bonding capacity through their contacts with the Fe atoms, they have little incentive to bond to the In atoms.

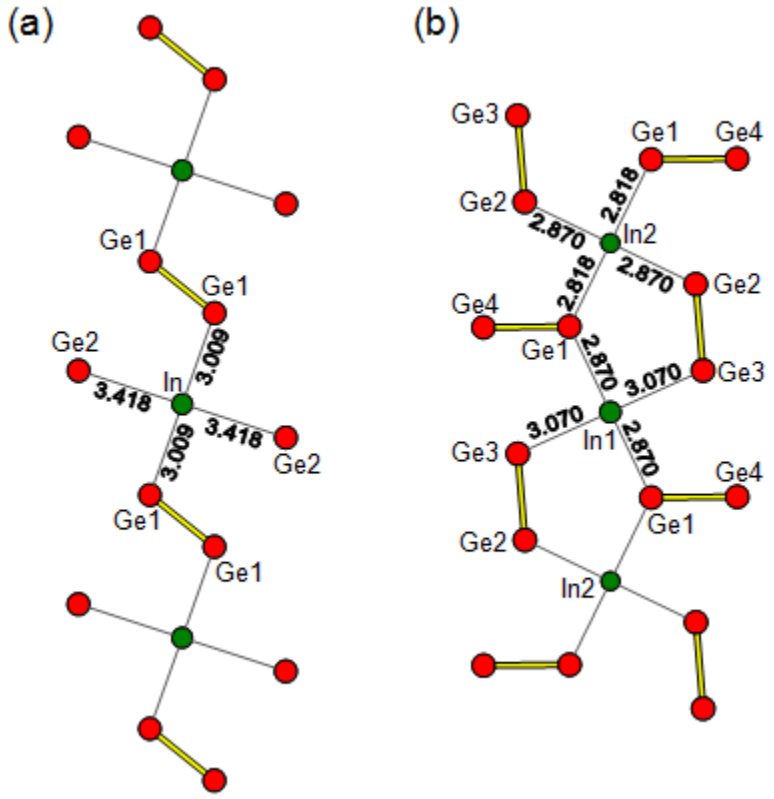

Figure 7-7 Connection of $InGe_4$ square planes in (a) $RE_4M_2InGe_4$ through Ge1–Ge1 pairs and Ge2 atoms and (b) $RE_4RhInGe_4$ through Ge1–Ge4 and Ge2–Ge3 pairs. The distances shown (in Å) refer to those found in the crystal structures of $Ce_4Fe_2InGe_4$ and $Tb_4RhInGe_4$, respectively.

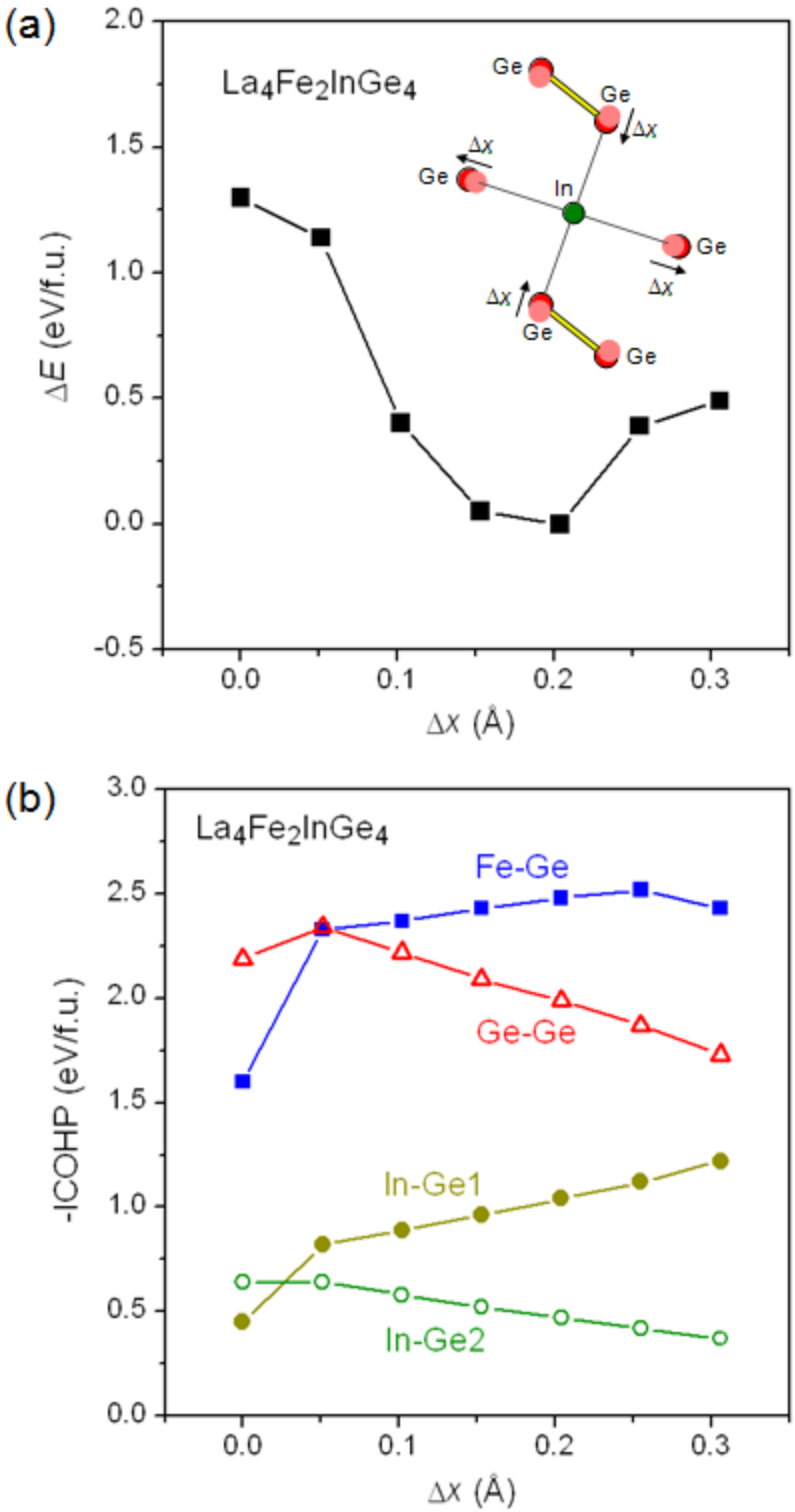

Figure 7-8 (a) Relative energy and (b) integrated COHP values (–ICOHP) for various contacts in $La_4Fe_2InGe_4$ models as the $InGe_4$ square plane is distorted from idealized equal In–Ge distances.

From Figure 7-5, we recall that the general trend in the progression of M = Mn, Fe, Co in $RE_4M_2InGe_4$ is that the distortion of the $InGe_4$ square plane tends to become more pronounced. If a rigid band approximation is applied, starting from the band structure of $La_4Fe_2InGe_4$, increasing the electron count would lead to greater occupation of antibonding levels for all types of bonds (Figure 7-6b). At the same time, the d-band of the transition metal would drop down in energy and become more filled, as confirmed in the actual DOS curves for $La_4M_2InGe_4$ (M = Mn, Fe, Co), compared in Figure 7-9. In reality, what happens is that the M–Ge interactions are always optimized, because they are the most important. To counteract the population of antibonding levels if the electron count is increased, the effect of distorting the $InGe_4$ square plane further is to stabilize In–Ge bonding levels and raise In–Ge antibonding ones, such that the states near the Fermi level are always close to being nonbonding. Note, for example, that the In 5s peak is located at –5.0 eV in $La_4Mn_2InGe_4$ and is lowered slightly to –5.2 eV in $La_4Co_2InGe_4$. Comparing $La_4Fe_2InGe_4$ and $La_4Ru_2InGe_4$ illustrates the replacement of the transition-metal component going down a group. The d-band in $La_4Ru_2InGe_4$ is more disperse than in $La_4Fe_2InGe_4$; the net effect is equivalent to a greater filling of the d-band, which would also lead to more distortion of the $InGe_4$ square plane.

With the insight gained by analyzing the electronic structure of the $La_4M_2InGe_4$ models above, we can proceed to examine $Y_4RhInGe_4$ (as a model for $Tb_4RhInGe_4$ but containing a nonmagnetic RE component) and see if the same conclusions hold. The DOS and COHP curves (Figure 7-10) show the same general features found for $La_4M_2InGe_4$ except that there are now two types of Ge_2 pairs, reflected by the appearance of two sets of σ_s and σ_s* levels (located near –9.5 eV and –7.9 eV for Ge2–Ge3, or –9.9

eV and –8.2 eV for Ge1–Ge4). The $InGe_4$ square planes are linked via these Ge_2 pairs acting as bridging ligands between the In1 and In2 atoms to form a chain (Figure 7-7b). Both atoms in the Ge2–Ge3 pairs, which are aligned parallel to the chain, are bonded to the In atom, but only the Ge1 atom in the Ge1–Ge4 pairs, which are oriented perpendicular to the chain, is bonded to the In atom. Among the Ge atoms bonded directly to the In atom, only Ge2 is also bonded to one Rh atom. In contrast to $La_4M_2InGe_4$, the orbitals on all these Ge atoms are little or not used for Rh–Ge bonding and instead can interact strongly with the In atoms. Thus the In–Ge distances are much less disparate within the $InGe_4$ square planes.

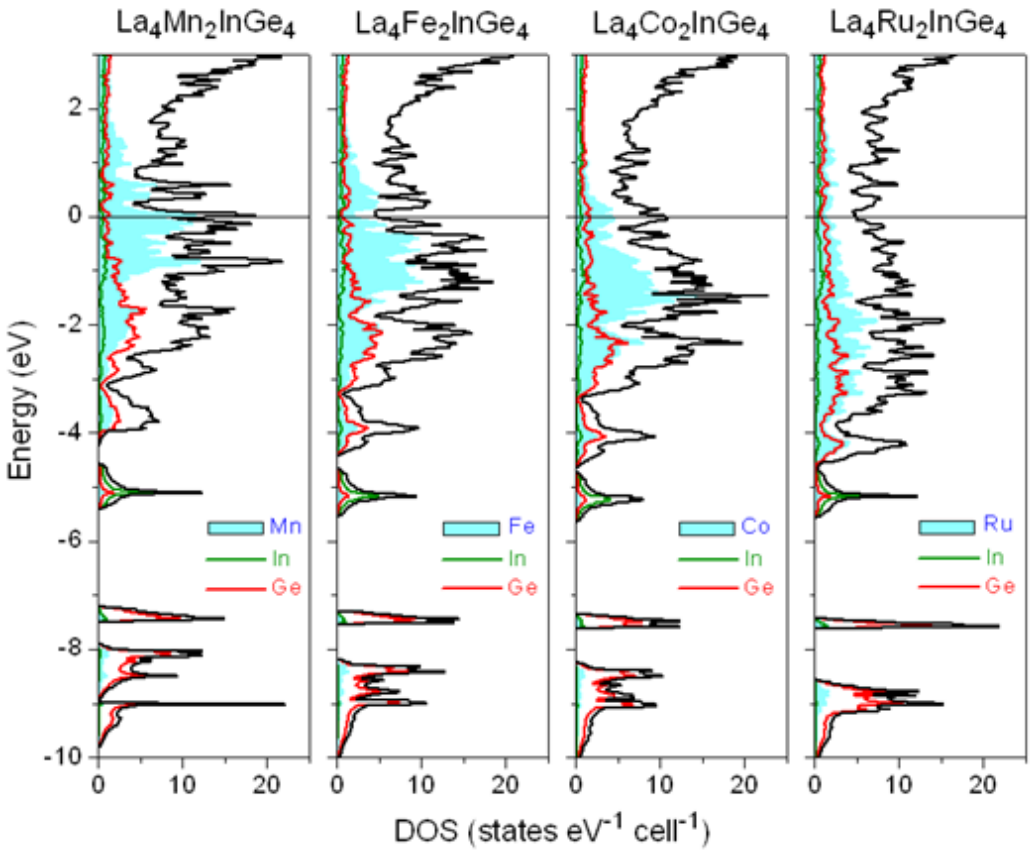

Figure 7-9 DOS and atomic projections for $La_4M_2InGe_4$ (M = Mn, Fe, Co, Ru).

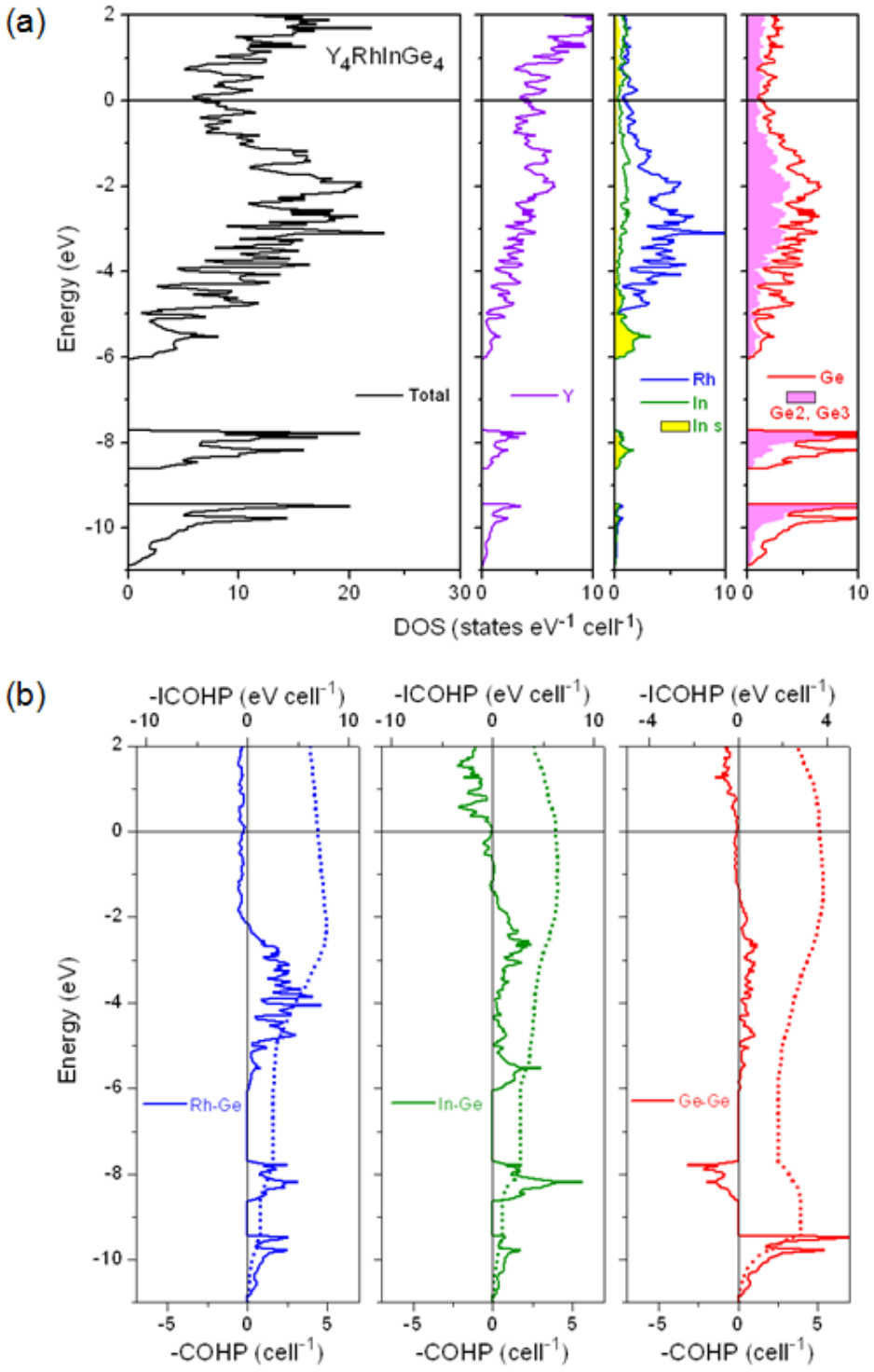

Figure 7-10 (a) DOS and atomic projections for $Y_4RhInGe_4$. In the last panel, the magenta shaded region highlights the contribution of states involved in Ge2–Ge3 bonding; what remains belongs to states involved in Ge1–Ge4 bonding. (b) COHP curves for Rh–Ge, In–Ge, and Ge–Ge bonding.

Inspection of –ICOHP values in $La_4M_2InGe_4$ and $Y_4RhInGe_4$ structures confirms that the strongest types of covalent bonds are *M*–Ge, followed by Ge–Ge and then In–Ge interactions (Table 7-5). However, when multiplied by the number of contacts present in the structure, In–Ge interactions contribute a greater proportion than Ge–Ge interactions to the bonding stability per unit cell. Moreover, in $Y_4RhInGe_4$, there are more $InGe_4$ squares and Ge_2 pairs than in $La_4M_2InGe_4$; correspondingly, In–Ge and Ge–Ge interactions contribute significantly more to the bonding stability relative to $La_4M_2InGe_4$. Within the distorted $InGe_4$ square plane in $La_4M_2InGe_4$, the shorter In–Ge contacts (3.0 A; –ICOHP of 1.0 eV/bond) are nearly twice as strong as the longer In–Ge contacts (3.3–3.4 Å; –ICOHP of 0.5–0.6 eV/bond). Interestingly, within the much less distorted $InGe_4$ square plane in $Y_4RhInGe_4$, this difference in –ICOHP values is still retained even though the two sets of In–Ge contacts differ by only 0.1–0.2 Å. In fact, even though they have the same length of 2.870 Å, the shorter set of contacts within the In1-centred square is twice as strong (In1–Ge1; –ICOHP of 1.12 eV/bond) than the longer set of contacts within the In2-centred square (In2–Ge2; –ICOHP of 0.58 eV/bond). As noted above, the Ge2 atom also participates in orbital interactions to the Rh atom; the weakness of the In2–Ge2 bond despite its "short" distance reflects a matrix effect rather than robust bonding.

Relatively little is known about the magnetic properties of $RE_4M_2InGe_4$ compounds; only a few members of the Ni-containing series have been previously analyzed (*RE* = Dy, Ho, Er, Tm) and these were found to undergo antiferromagnetic ordering at low temperatures.[10] To examine the effect of substitution of the *M* component, magnetic susceptibility measurements were made for several Sm-containing

members $Sm_4M_2InGe_4$ (M = Fe, Co, Ru, Rh), which were also the only samples that could be prepared free of other phases (Figure 7-11). The magnetic susceptibility curves obtained under zero-field-cooled and field-cooled conditions are superimposable. Typical of many Sm-containing intermetallic compounds, the magnetic susceptibility is low and cannot be fit to the Curie-Weiss law (as indicated by strong curvature in the inverse susceptibility curves, not shown); the effective magnetic moment can deviate significantly from the expected value for a free Sm^{3+} ion because of the occupation of low-lying excited states above the ground state (J = 5/2) multiplet and the influence of crystal field effects. There are two peaks in the magnetic susceptibility curves near 30 K and 10 K for M = Fe, Ru, and Rh, and possibly more complicated transitions for M = Co. Similar peaks are observed in the low-temperature behaviour for $Dy_4Ni_2InGe_4$ (30 K and 11 K) and $Ho_4Ni_2InGe_4$ (10 K and 4 K), for which spin reorientation processes are the most likely origin.[10] The magnetic behaviour of all these compounds is dominated by the *RE* component but little influenced by the *M* component, implying strong delocalization of the d-electrons of the transition-metal atoms. This is consistent with the relatively low contribution of d-states to the DOS at the Fermi level in the band structures for $La_4M_2InGe_4$ (M = Fe, Co, Ru) seen earlier (Figure 7-9). RKKY interactions in which the magnetic moments of the *RE* atoms are coupled through the mediation of conduction electrons are the likely mechanism for the magnetic behaviour. In contrast, the contribution of d-states to the DOS at the Fermi level for $La_4Mn_2InGe_4$ is markedly greater, so spin polarization of the d-band can potentially take place. It would thus be interesting to examine the magnetic properties of the Mn-containing series in future investigations.

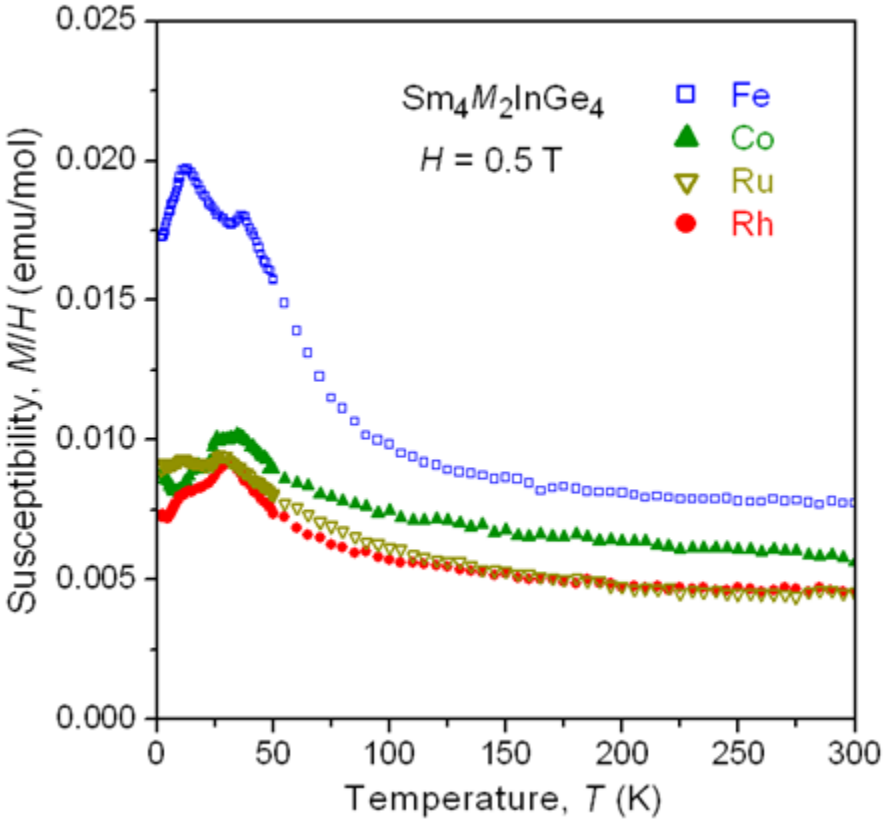

Figure 7-11 Magnetic susceptibility for $Sm_4M_2InGe_4$ (M = Fe, Co, Ru, Rh).

7.4 Conclusions

A large number of quaternary germanides $RE_4M_2InGe_4$ can be prepared through arc-melting and annealing reactions at 800 °C, without requiring the use of an In flux, indicating that these are thermodynamically stable phases. Their diversity has been considerably expanded through the substitution of the M component, which can range from the mid-to-late transition metals (M = Mn, Fe, Co, Ni, Ru, Rh, Ir). A related series $RE_4RhInGe_4$ was identified in the course of this investigation. The monoclinic structures

of both $RE_4M_2InGe_4$ and $RE_4RhInGe_4$ can be elegantly derived from the more symmetrical tetragonal RE_2InGe_2 structure by excision of slabs in different directions and translating these slabs. New target structures may be envisioned from this approach by cutting slabs in other directions. Size effects contribute to the range of *RE* substitution possible in a given $RE_4M_2InGe_4$ series, through appropriate matching of *RE* and *M* radii, and narrowly restrict the limits of formation of $RE_4RhInGe_4$. Electronic effects account for trends seen in the characteristic $InGe_4$ square planes in $RE_4M_2InGe_4$, which undergo distortions to balance the competition between the strong *M*–Ge bonds within MGe_4 tetrahedra and the weaker but more responsive In–Ge bonds within the square planes. The Ge–Ge bonds within the Ge_2 dimers are little affected by substitutions in *M* because their interactions are largely nonbonding near the Fermi level, a consequence of poor π-overlap between p orbitals on the Ge atoms. To probe the interplay between *M*–Ge, In–Ge, and Ge–Ge bonding, it will be interesting to attempt replacement of the In atoms by other atoms (perhaps Cd) in the square planar sites or Ge atoms by other p-block elements (perhaps Si) that may be prone to form dimers. The physical properties of these series are deserve further investigation.

7.5 References

[1] Salamakha, P. S.; Sologub, O. L.; Bodak, O. I. In *Handbook on the Physics and Chemistry of Rare Earths*; Gschneidner, K. A., Jr., Eyring, L., Eds.; Elsevier: Amsterdam, 1999; Vol. 27, pp 1–223.

[2] Bie, H.; Zelinska, O. Ya.; Tkachuk, A. V.; Mar, A. *Chem. Mater.* **2007**, *19*, 4613–4620.

[3] Mudryk, Y.; Pecharsky, V. K.; Gschneidner, K. A., Jr. *Z. Anorg. Allg. Chem.* **2011**, *637*, 1948–1956.

[4] Sung, N. H.; Roh, C. J.; Kim, K. S.; Cho, B. K. *Phys. Rev. B* **2012**, *86*, 224507-1–224507-6.

[5] Zaremba, V. I.; Stępień-Damm, A.; Nichiporuk, G. P.; Tyvanchuk, Yu. B.; Kalychak, Ya. M. *Kristallografiya* **1998**, *43*, 13–16.

[6] Zaremba, V. I.; Kaczorowski, D.; Nychyporuk, G. P.; Rodewald, U. Ch.; Pöttgen, R. *Solid State Sci.* **2004**, *6*, 1301–1306.

[7] Zaremba, V. I.; Johrendt, D.; Rodewald, U. Ch.; Nychyporuk, G. P.; Pöttgen, R. *Solid State Sci.* **2005**, *7*, 998–1002.

[8] Tobash, P. H.; Lins, D.; Bobev, S.; Lima, A.; Hundley, M. F.; Thompson, J. D.; Sarrao, J. L. *Chem. Mater.* **2005**, *17*, 5567–5573.

[9] Rieger, W.; Nowotny, H.; Benesovsky, F. *Monatsh. Chem.* **1964**, *95*, 1502–1503.

[10] Salvador, J. R.; Kanatzidis, M. G. *Inorg. Chem.* **2006**, *45*, 7091–7099.

[11] Chondroudi, M.; Balasubramanian, M.; Welp, U.; Kwok, W.-K.; Kanatzidis, M. G. *Chem. Mater.* **2007**, *19*, 4769–4775.

[12] Chondroudi, M.; Peter, S. C.; Malliakas, C. D.; Balasubramanian, M.; Li, Q. A.; Kanatzidis, M. G. *Inorg. Chem.* **2011**, *50*, 1184–1193.

[13] Oliynyk, A. O.; Stoyko, S. S.; Mar, A. *Inorg. Chem.* **2013**, *52*, 8264–8271.

[14] Chumalo, N.; Nychyporuk, G. P.; Pavlyuk, V. V.; Pöttgen, R.; Kaczorowski, D.; Zaremba, V. I. *J. Solid State Chem.* **2010**, *183*, 2963–2967.

[15] Dominyuk, N.; Zaremba, V. I.; Pöttgen, R. *Z. Naturforsch., B.: J. Chem. Sci.* **2011**, *66*, 433–436.

[16] Akselrud, L. G.; Zavalii, P. Yu.; Grin, Yu. N.; Pecharski, V. K.; Baumgartner, B.; Wölfel, E. *Mater. Sci. Forum* **1993**, *133–136*, 335–342.

[17] Sheldrick, G. M. *SHELXTL*, version 6.12; Bruker AXS Inc.: Madison, WI, 2001.

[18] Gelato, L. M.; Parthé, E. *J. Appl. Crystallogr.* **1987**, *20*, 139–143.

[19] Tank, R.; Jepsen, O.; Burkhardt, A.; Andersen, O. K. *TB-LMTO-ASA Program*, version 4.7; Max Planck Institut für Festkörperforschung: Stuttgart, Germany, 1998.

[20] Pauling, L. *The Nature of the Chemical Bond*, 3rd ed.; Cornell University Press: Ithaca, NY, 1960.

[21] Salamakha, P. S. In *Handbook on the Physics and Chemistry of Rare Earths*; Gschneidner, K. A., Jr., Eyring, L., Eds.; Elsevier: Amsterdam, 1999; Vol. 27, pp 223–338.

[22] Oliynyk, A. O.; Stoyko, S. S.; Mar, A. *J. Solid State Chem.* **2013**, *202*, 241–249.

[23] Grytsiv, A.; Kaczorowski, D.; Rogl, P.; Tran, V.; Godart, C.; Gofryk, K.; Giester, G. *J. Phys.: Condens. Matter* **2005**, *17*, 385–397.

[24] Solokha, P.; De Negri, S.; Skrobanska, M.; Saccone, A.; Pavlyuk, V.; Proserpio, D. M. *Inorg. Chem.* **2012**, *51*, 207–214.

[25] You, T.-S.; Bobev, S. *J. Solid State Chem.* **2010**, *183*, 1258–1265.

[26] Lei, X.-W.; Zhong, G.-H.; Li, M.-J.; Mao, J.-G. *J. Solid State Chem.* **2008**, *181*, 2448–2455.

[27] Pearson, W. B. *The Crystal Chemistry and Physics of Metals and Alloys*; Wiley: New York, 1972.

[28] Hyde, B. G.; Andersson, S. *Inorganic Crystal Structures*; Wiley: New York, 1989.

[29] You, T.-S.; Tobash, P. H.; Bobev, S. *Inorg. Chem.* **2010**, *49*, 1773–1783.

[30] You, T.-S.; Jung, Y.; Bobev, S. *Dalton Trans.* **2012**, *41*, 12446–12451.

[31] Allred, A. L. *J. Inorg. Nucl. Chem.* **1961**, *17*, 215–221.

Chapter 8

A recommendation for suggesting potential thermoelectric materials

A version of this chapter has been published. Sparks, T. D.; Gaultois, M. W.; Oliynyk, A. O.; Brgoch, J.; Meredig, B. Scr. Mater. 2016, 111, 10-15.

A part of this chapter has been uploaded to open e-print archive: arXiv.org. Gaultois, M. W.; Oliynyk, A. O; Mulholland, G. J.; Mar, A.; Sparks, T. D.; Meredig, B. arXiv:1502.07635v1. The manuscript has been accepted to APL Materials.

7.1. Introduction

Predicting thermoelectric properties from first principles (such as DFT calculations) remains a challenging endeavor[1] and experimental researchers generally do not directly use computation to drive their own synthesis efforts. To bridge this practical gap between experimental needs and computational tools, an open machine learning-based recommendation engine (http://thermoelectrics.citrination.com) for materials researchers has been reported. The recommendation engine can suggest promising new thermoelectric compositions based on pre-screening about 25,000 known materials, and also evaluate the feasibility of user-designed compounds. Suggested by the recommendation engine, a set of compounds $RE_{12}Co_5Bi$ has been tested experimentally to confirm the prediction. The $RE_{12}Co_5Bi$ series have an unusual chemical composition

for thermoelectric materials (Figure 8-1, 8-2) and are counter-intuitive candidates which in fact make a machine suggestion a guide towards unexpected chemistries.

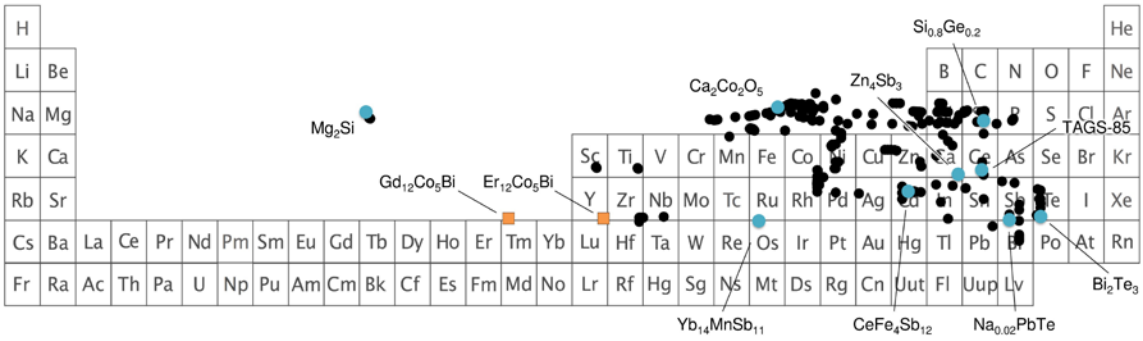

Figure 8-1 Composition-weighted diagram, where most of known thermoelectric materials lie in a tight cluster in composition space.

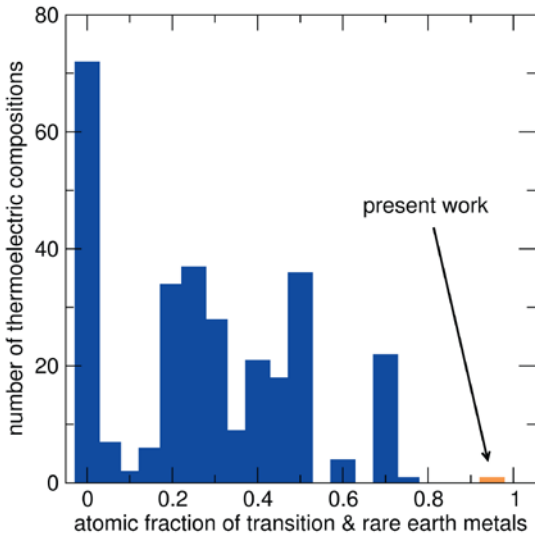

Figure 8-2 $RE_{12}Co_5Bi$ series represent the highest content of rare-earth and transition metals among thermoelectric materials reported making these intermetallic candidates an unusual suggestion.

8.2 A materials recommendation engine

The recommendation engine is a machine learning-based approach[2,3] for efficiently driving synthetic efforts toward promising new chemistries. A machine learning model has been trained to make a confidence level prediction of whether the (1) Seebeck coefficient, (2) electrical resistivity, (3) thermal conductivity, and (4) band gap of input materials are within acceptable ranges for thermoelectric applications. We define these ranges as follows: (1) $|S| > 100$ μV K−1; (2) $\rho < 10^{-2}$ Ω cm; (3) $\kappa < 10$ W m−1 K−1; and (4) $E_g > 0$ eV, all at room temperature. For each range of thermoelectric property, the engine gives a confidence score between 0% and 100% that a given material's measured value for that property at room temperature will fall within the targeted range. The recommendation engine does not make a quantitative prediction, the main purpose of thermoelectric recommendations is to augment the chemical intuition and guide researchers towards unexpected discoveries. Machine learning models described in this differ considerably from atomistic simulation approaches as density functional theory calculations (DFT). The present machine learning-based recommendation engine looks for empirical, chemically meaningful patterns in experimentally reported data on known thermoelectric compounds to make statistical predictions for the performance of new materials. The work is available as a web application (http://thermoelectrics.citrination.com) that contains ~25,000 known compounds with thermoelectric performance predicted, and requests for real-time predictions of thermoelectric candidates are available.

8.3 Experimental

To confirm the predictions $RE_{12}Co_5Bi$ (*RE* = Gd, Er) compounds were synthesized. The samples were made by arc-melting freshly filed Er or Gd pieces (99.9%, Hefa), Co powder (99.8%, Cerac), and Bi powder (99.999%, Alfa Aesar). Stoichiometric mixtures (0.5g total mass) with 5 to 7% excess Bi were pressed into pellets and melted twice in an arc-melter (Edmund Bühler Compact Arc Melter MAM-1) under argon atmosphere sealed in silica tubes and annealed at 1070 K for one week, then quenched in cold water. Pure samples were combined by melting into a single ingot and sanded to yield the appropriate geometry (either a rectangular bar, or a cylinder).

Powder X-ray diffraction patterns were collected using an INEL CPS 120 diffractometer with Cu Kα1 radiation at room temperature. Backscatter electron microscopy and elemental analysis via energy dispersive X-ray spectroscopy (EDX) were performed with a JEOL JSM-6010LA In-TouchScope scanning electron microscope. Backscatter micrographs reveal the samples are largely compositionally homogeneous. Quantitative elemental analysis on several polished pieces found an atomic composition of $Gd_{69(2)}Co_{26(2)}Bi_{5(2)}$ which is in a good agreement with expected $RE_{12}Co_5Bi$ composition. $Er_{12}Co_5Bi$ samples were not appropriate for quantitative analysis because of overlapping Co Kα (6.924 keV) and Er Lα (6.947 keV) lines.

High-temperature thermoelectric properties (electrical resistivity and Seebeck coefficient) were measured with an ULVAC Technologies ZEM-3. Sample bars had approximate dimensions of 9 mm × 4 mm × 4 mm. Measurements were performed with a helium under-pressure, and data was collected from 300 K to 800 K through three heating and cooling cycles over 18 hours to ensure sample stability and reproducibility.

8.4 New $RE_{12}Co_5Bi$ materials and their properties

Thermoelectic property measurements were performed to demonstrate that the recommendation engine can indeed guide researchers toward interesting experimental discoveries. $RE_{12}Co_5Bi$ series is a chemically distinct family of compounds (Figure 8-1 and 8-2), the crystal structure, low-temperature electric and magnetic properties have been reported previously.[4] Interestingly, the crystal structure of our candidate thermoelectric exhibits notable similarity to the structures of known thermoelectrics, in spite of the fact that crystal structure was not an input feature for our recommendation engine.

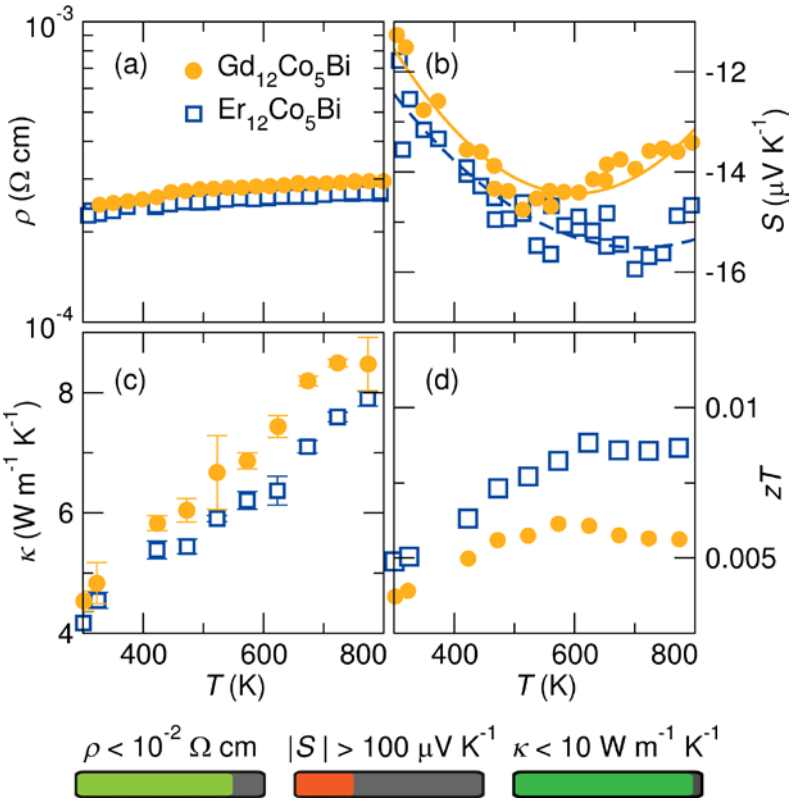

Figure 8-3 Thermoelectric characterization of $RE_{12}Co_5Bi$ (RE = Gd, Er). (a) Electrical resistivity, (b) Seebeck coefficient, (c) thermal conductivity, and (d) thermoelectric figure of merit zT as a function of temperature. Recommendation engine's confidence is indicated at the bottom of the figure with the confidence bars.

A full thermoelectic characterization of $Gd_{12}Co_5Bi$ and $Er_{12}Co_5Bi$ is presented on Figure 8-3. This class of materials remains completely unoptimized pure bulk material and thus lends itself to further study. Notably, the material falls far outside the usual search space for thermoelectrics and was neither the result of simple interpolation between known compounds nor obvious from a strict chemical intuition standpoint.

8.5 Directing the exploration of intermetallic phase space

In this section I will propose some ideas how we can use the thermoelectric recommendation engine described above, to focused on the exploration of new compounds with (1) known structures with good performance (based on isostructural series), (2) predicted high thermoelectric performance without regard for structural preference, and (3) both expected structures and potential high performance. The most promising intermetallics for thermoelectric performance are Heusler and half-Heusler compounds.[5] First, we searched through the recommendation engine's output for the most promising candidates among a large set of known crystalline compounds. From top of this list, six gallide and indide Heusler phases that have never been tested as thermoelectric materials previously were selected for further experiments (see Figure8-4). Although they are predicted to have excellent Seebeck coefficient, electrical resistivity, and thermal conductivity, their band gap is not ideal (in fact, they are predicted to very likely have no gap). Fortunately, not all Heusler gallides and indides have been discovered. We hypothesized that three compounds – $TiRu_2Ga$, $TiRu_2In$, $MnRu_2In$ – should form as Heusler phases since isostructural analogs exist for other representatives of group 8, 9, 10 elements; the recommendation engine predicted that they should not

only score high on the Seebeck, resistivity, and thermal conductivity dimensions, but also improve on the band gap. Reassuringly, the Heusler stability conjecture was confirmed by the successful preparation of these phases. Measurements of their physical properties are in progress, but thus far, the thermal diffusivity data look promising.

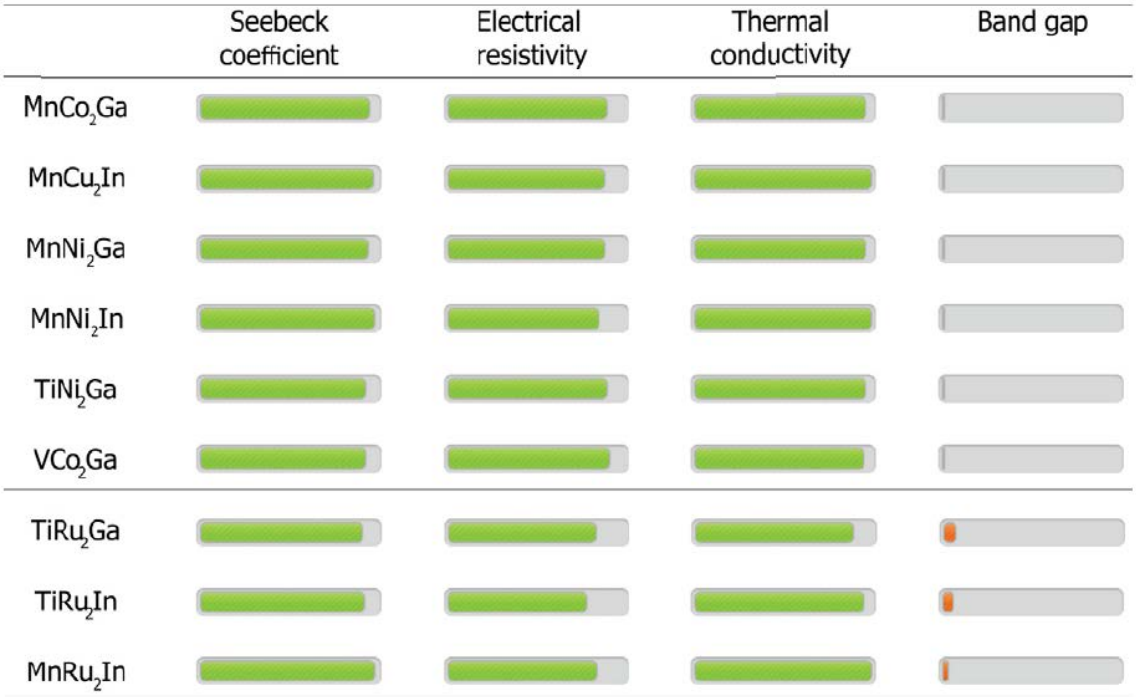

Figure 8-4 Visualization of properties for nine Heusler compounds predicted by recommendation engine.[6] The prediction represents the model's confidence that a given material will exhibit high Seebeck coefficient, low resistivity, low thermal conductivity, and finite band gap.

Another way to search for new compounds can be used to quickly evaluate given composition even if no compound with such a stoichiometry exists. The recommendation engine was used, in a brute force manner, to identify possible

compositions (with a 10 at.% increment) among all binary and ternary combinations of elements (excluding noble gas and high-*Z* elements) among 105,653 ternary systems. These compositions can then be evaluated for any property (or combination thereof). In our case, we ranked the compositions in terms of low thermal conductivity. Unexpectedly, transition-metal germanides were found near the top of this list of low thermal conductivity predictions. This is an interesting prediction because germanides are normally metallic and would not have been intuitively chosen to be potentially good thermoelectric materials.

A visualization tool is used to quickly skim through ternary phase diagrams to pinpoint the most promising composition regions that score high on the prediction of low thermal conductivity. Since our goal is to search for entirely new phases, we also applied the criteria that: (a) the system has not been previously investigated systematically and no ternary compounds have yet been reported, (b) the solubility of a second component is small in the phase diagrams of binary metal–metal and metal–germanium systems (to avoid simply forming binary solid solutions of the third component), and (c) the promising compositions should lie in the region of nearly equiatomic ratios. As a test of these ideas, the Mn–Ru–Ge system was selected. Figure 8-5 shows a map of compositions where it is most likely to find phases with low thermal conductivity.

We attempted synthesis corresponding to the composition ($Mn_{55}Ru_{15}Ge_{30}$) marked by the small black star in Figure 8-5, located in a region where the probability of low thermal conductivity is > 90%. A new compound, $Mn(Ru_{0.4}Ge_{0.6})$, was formed. It adopts the CsCl-type structure but it is not a solid solution of the known binary phases in the Mn–Ru, Ru–Ge, or Mn–Ru systems.

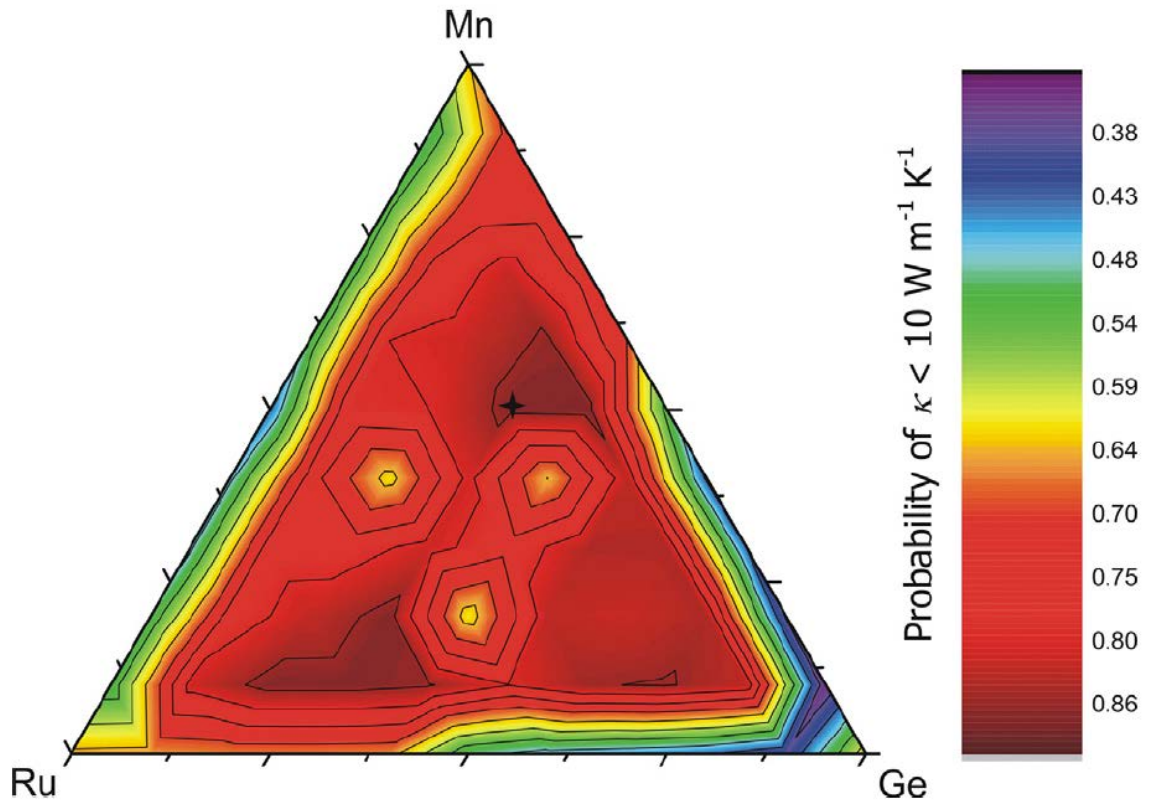

Figure 8-5 Probability of low thermal conductivity ($\kappa < 10 \mathrm{Wm^{-1}K^{-1}}$) as a function of theoretical composition.

The calculations within the recommendation engine are not costly and can be performed quickly — within fractions of a second for each composition — making it easy to perform numerous predictions. However, the accompanying synthetic experiments are time-consuming. By combining the two approaches of predicting properties and making use of crystal chemical ideas to identify potential new structures, we can accelerate the discovery process. Within a ternary composition diagram, certain phases with common structure types recur. For example, within germanide systems containing a rare-earth and a transition metal (*RE*–*M*–Ge), many ternary phases occur with the same compositions. In Figure 8-6, the most common compositions are marked.

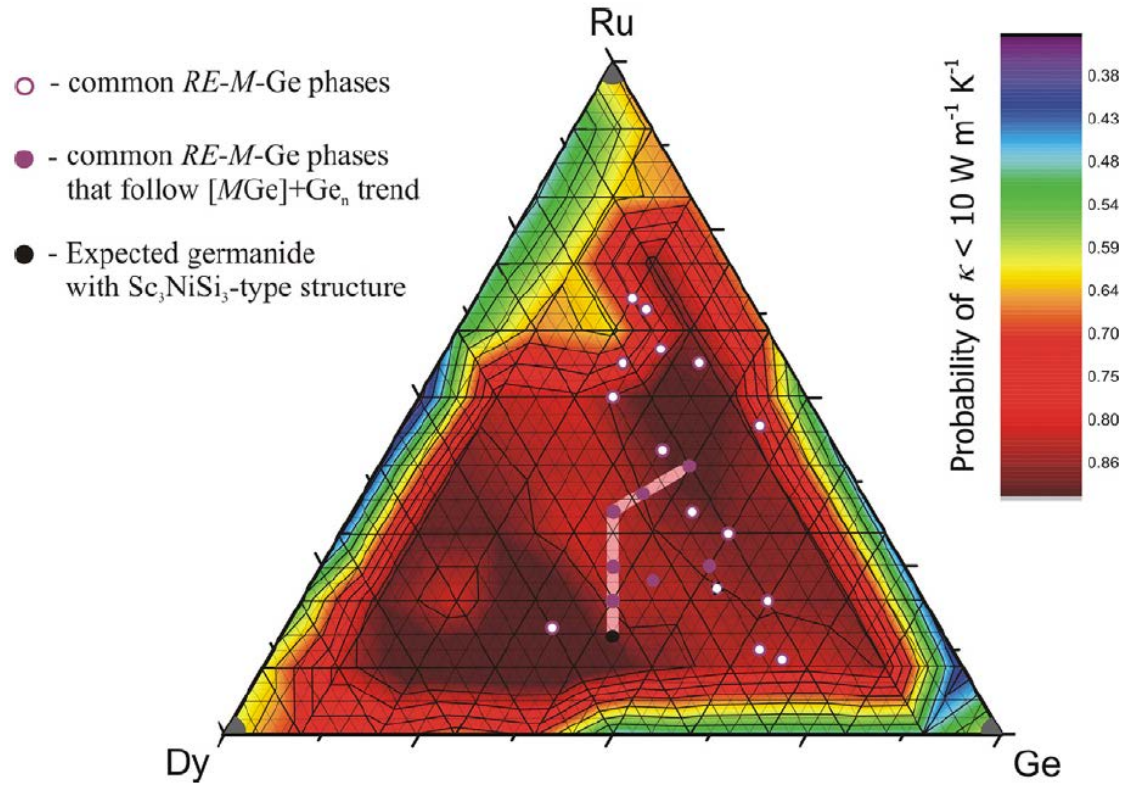

Figure 8-6 *RE–M*–Ge composition diagram with common ternary structure types and predicted thermal conductivity mapped on the Dy–Ru–Ge diagram.

A frequent motif found in these structures is an infinite ladder [*M*Ge] built up of a zigzag double chain of alternating *M* and Ge atoms.[7-10] The bonds within this ladder are very strong and dominate the electronic structure.[7] These ladders can be connected to each other through polyatomic Ge$_n$ bridges containing homoatomic Ge–Ge bonds, forming a three-dimensional network whose voids are filled with *RE* atoms. Within different structures, the ladders are slightly tilted to maximize orbital overlap. The degree of tilting of the [*M*Ge] ladders and the number of atoms *n* in the Ge$_n$ bridges determine the symmetry: if the ladders are tilted in the same direction and *n* is odd, the

structure is monoclinic (e.g., ternary $LaPt_2Ga_2$, YbFeGe, Sc_2CoSi_2, and even quaternary Ho_4Ni_2- $InGe_4$ structure types); if the ladders are related by mirror symmetry and n is even, the structure is orthorhombic (e.g., ternary $Gd_3Cu_4Ge_4$, $Hf_3Ni_2Si_3$, $YIrGe_2$ structure types). By extrapolation, we can target new structures containing an [*M*Ge] ladder and a Ge_2 bridge, which should result in the formula RE_xMGe_3 (where x is unknown at this stage, since we cannot know how the *RE* atoms will be situated).

The existing compounds *REM*Ge, $RE3M_2Ge_3$, and RE_2MGe_2 fall in a straight line in the diagram (Figure 8-6), so we might expect that the predicted structure will follow this trend and attain a composition of RE_3MGe_3. Synthesis at this composition confirmed that RE_3MGe_3 exists (for *RE* = Er, Dy, Tm; *M* = Ru). At this stage, regions of low thermal conductivity can be mapped on the same diagram (Figure 8-6), for the Dy–Ru–Ge system as an example. By itself, the thermal conductivity map cannot guarantee if any phase exists in reality, but by combining it with the structure map, we can pick the best compounds that are likely to be good thermoelectric materials. This combined map shows that RE_3RuGe_3 is a good candidate, and physical properties are currently under investigation. Though *RE*–Ru–Ge phases are not practical for thermoelectric applications due to resource considerations, our goal here is to show how we can combine the concept of a recommendation engine and well understood structural chemistry.

Intermetallic compounds typically have large Seebeck coefficients and low electrical resistivities, which are good for thermo- electric materials; however, they tend to have high thermal conductivities as well as no band gap, which limits zT.[11] Thus, for an intermetallic compound to be a good thermoelectric material, the challenge is primarily to find a candidate that has a low thermal conductivity. Surprisingly, the

germanides presented here may be good candidates because they exhibit complex crystal structures and they are amenable to doping with introduction of one or more elements. Introducing semiconductor-like behavior in these germanides appears to be a greater problem, but with careful selection of the *RE* component, it is possible to obtain good candidates. For example, although $RE_3Ru_2Ge_3$ generally shows metallic behavior, the Y-containing member has a semiconductor-like electrical resistivity behavior.[7]

8.6 Conclusions

The recommendation engine can take into account variations in compositions and estimate thermoelectric performance at different compositions. Our goal in these investigations is not necessarily to obtain materials with high *zT* but to explore new phase-space with the aid of machine learning. The examples presented above suggest that this approach shows promise in identifying new candidates and future work will determine the thermoelectric performance of these materials. An example of hybrid machine–human approach to search for new compounds with a potential application such as thermoelectric materials combines chemical intuition with machine learning. Brute force calculations can provide a guide to search for new compounds and we need not be limited to existing compounds found in databases. Given the experimental challenges in investigating quaternary and other multicomponent systems, these calculations serve as a good starting point for explorations. The great advantage of the recommendation engine is that it does not require knowledge of a crystal structure *a priori* since recommendation probability is based on composition. Experimental measurements of the physical properties show promise for the predicted thermoelectric materials. These properties are not just limited to thermal conductivity.

8.7 References

[1] Carrete, J.; Li, W.; Mingo, N.; Wang, S.; Curtarolo, S. *Phys. Rev. X* **2014**, *4*, 011019-1–011019-9.

[2] Meredig, B.; Agrawal, A.; Kirklin, S.; Saal, J.; Doak, J.; Thompson, A.; Zhang, K.; Choudhary, A.; Wolverton, C. *Phys. Rev. B* **2014**, *89*, 094104-1–094104-7.

[3] Meredig, B.; Wolverton, C. *Chem. Mater.* **2014**, *26*, 1985–1991.

[4] Tkachuk, A. V.; Mar, A. *Inorg. Chem.* **2005**, *44*, 2272–2281.

[5] Graf, T.; Felser, C.; Parkin, S. S. *Prog. Solid State Chem.* **2011**, *39*, 1–50.

[6] Gaultois, M. W.; Oliynyk, A. O.; Mar, A.; Sparks, T. D.; Mulholland, G. J.; Meredig, B. *APL Materials*, accepted.

[7] Oliynyk, A. O.; Stoyko, S. S.; Mar, A. *J. Solid State Chem.* **2013**, *202*, 241–249.

[8] Oliynyk, A. O.; Djama-Kayad, K.; Mar, A. *J. Alloys Compd.* **2014**, *602*, 130–134.

[9] Oliynyk, A. O.; Stoyko, S. S.; Mar, A. *Inorg. Chem.* **2013**, *52*, 8264–8271.

[10] Oliynyk, A. O.; Stoyko, S. S.; Mar, A. *Inorg. Chem.* **2015**, *54*, 2780–2792.

[11] Gaultois, M. W.; Sparks, T. D.; Borg, C. K.; Seshadri, R.; Bonificio, W. D.; Clarke, D. R. *Chem. Mater.* **2013**, *25*, 2911–2920.

Chapter 9

Deceptively simple and endlessly complicated: machine learning prediction and experimental confirmation of novel Heusler compounds

A version of this chapter has been submitted to Chemistry of Materials.

9.1. Introduction

Heusler compounds form a large class of intermetallics that exhibit versatile properties. The first compound, Cu_2MnAl, was discovered in 1898 by Friedrich ("Fritz") Heusler, a German mining engineer, and attracted attention – before its structure or composition was understood – because it is ferromagnetic even though it is formed from metals that are nonferromagnetic.[1,2] There seem to be simple rules for relating the electron count to the physical properties,[3] permitting the prediction of half-metallic ferromagnets,[4] ferrimagnets,[5] semiconductors,[6] and superconductors.[7,8] Given their tunable semiconducting properties (made possible by adjusting the chemical composition to attain a desired electron count so that the band gap varies from 0 to a few eV),[3] these compounds are currently being heavily investigated for sustainable technologies such as solar energy and thermoelectric conversion.[9,10] Exciting new applications for Heusler compounds include spintronics,[11,12] superconductivity,[7,8] magnetocalorics,[13] and topological insulators.[14] Thus, these compounds are advancing the frontiers of science and providing solutions to materials engineering challenges in the future.

To gauge interest in this area, a plot of Heusler compounds reported structurally (culled from Pearson's Database[15]) shows a peak in the 1980's, when magnetic properties were examined, followed by a recent renaissance, when exotic properties were discovered (Figure 9-1).

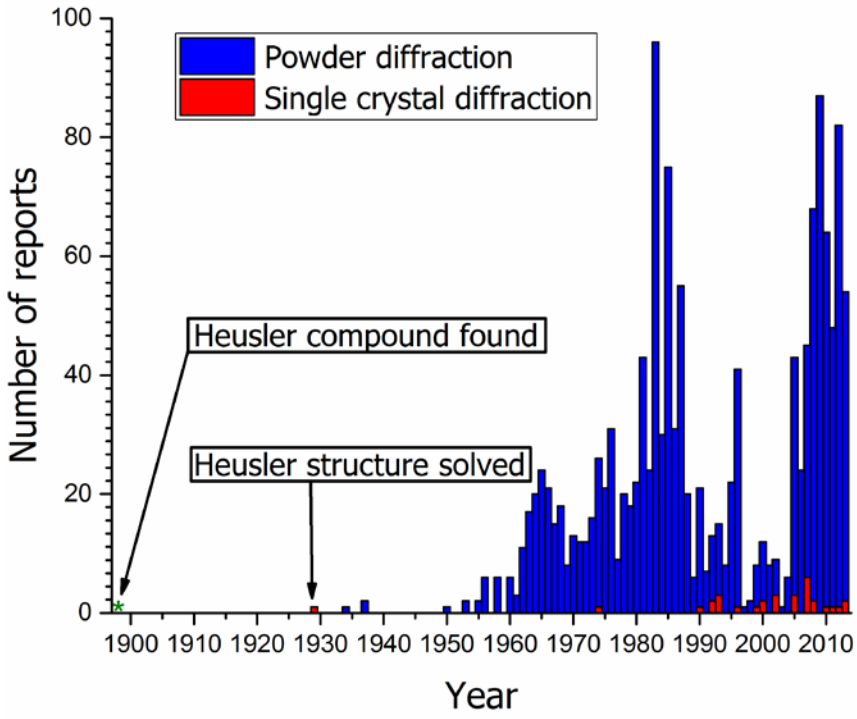

Figure 9-1 Number of structural reports of Heusler compounds found in Pearson's Database (Release 2015/2016) per year.[15]

In Friedrich Heusler's time, these compounds were thought to be solid solutions adopting the structure of one of the metal components.[2] More than 20 years passed before the first crystal structure was elucidated,[16] and many years still before an appreciation of the subtleties was attained. There are two families of Heusler compounds: half-Heusler compounds *ABC*, and (full-)Heusler compounds AB_2C. The components are metals, where typically *A* is a large electropositive metal, *B* is a transition metal, and *C* is an electronegative metal (usually a p-block metalloid). We focus our

attention on the latter, referred to simply as Heusler compounds. The Heusler structure (also called Cu_2MnAl-type) is a superstructure of the CsCl-type (Figure 9-2).

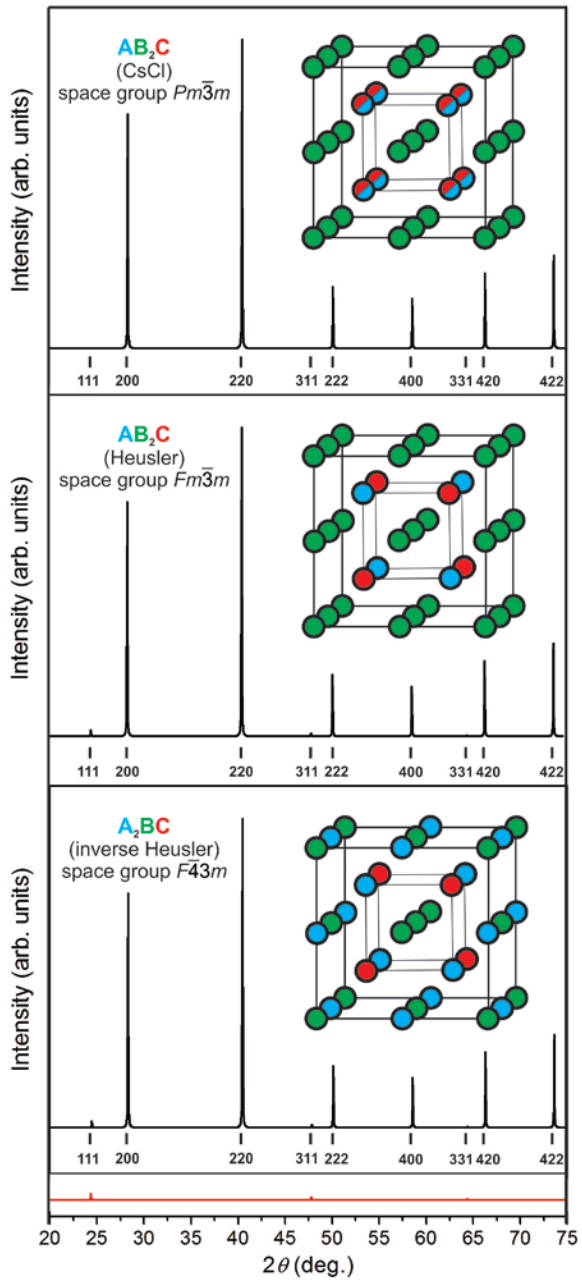

Figure 9-2 Simulated powder XRD patterns for $LiAg_2Al$ in (a) CsCl-type, (b) Heusler (Cu_2MnAl-type), and (c) inverse Heusler (Hg_2CuTi- or Li_2AgSb-type) structures. The difference plot between the XRD patterns for CsCl-type and Heusler structures is shown in blue at the bottom. Note that the patterns for Heusler and inverse Heusler structures have the same sets of peaks differing only slightly in intensities.

In AB_2C, the B atoms form a primitive cubic sublattice; the A and C atoms are arranged in a disordered fashion within body centres in the CsCl-type but in an ordered fashion in the Heusler structure. The CsCl-type structure contains two sites within a primitive cubic lattice (space group $Pm\bar{3}m$) whereas the Heusler structure contains three sites within a face-centered cubic lattice (space group $Fm\bar{3}m$). There is a complication: inverse Heusler compounds A_2BC are formed with the content of A doubled and that of B halved relative to the normal Heusler compounds AB_2C. The inverse Heusler structure (called Hg_2CuTi- or Li_2AgSb-type) consists of four sites within a face-centered cubic lattice and has lower symmetry (space group $F\bar{4}3m$). Many other variants of these basic structures are possible, involving distortions, split positions, and more complex ordering, which entice chemists and physicists to frolic in this rich playground of compounds.

Like golf, these structures are deceptively simple and endlessly complicated.[17] Indeed, their simplicity makes it difficult to detect the subtle differences. For example, $LiAg_2Al$ was reported as an inverse Heusler compound,[18] but the simulated powder X-ray diffraction (XRD) patterns for $LiAg_2Al$ in CsCl-type, Heusler, and inverse Heusler structures are nearly identical (Figure 9-2). The presence of weak superstructure peaks (111, 311, 331), barely observable except perhaps with synchrotron radiation XRD, distinguishes CsCl-type from Heusler or inverse Heusler structures. In turn, Heusler and inverse Heusler structures have identical sets of peaks differing almost imperceptibly in intensities, or for $LiAg_2Al$, these intensities are numerically identical. It is difficult to measure powder XRD patterns accurately, given that uncertainties in the intensities (e.g., arising from preferred orientation, severe absorption, or detector noise) can exceed the

difference needed to distinguish these structures. Sometimes, assumptions are made about the structure but they may not be correct (as is the case for $LiAg_2Al$, discussed later). A more accurate method is single-crystal XRD, but out of 1415 reports of Heusler compounds, only 31 (or 2%) have been characterized this way. Even single-crystal XRD is not infallible, because very weak intensities may still be hard to detect. Determining the correct structures of these compounds is vitally important to improving their performance in materials applications, because subtle structural differences can greatly influence their physical properties.

Given this difficulty in structure determination, prior work has exploited first-principles quantum chemical calculations, in which the structural preference is dictated by small energetic differences;[12] this could be viewed as a "brute force" approach to addressing the problem. For some categories of Heusler compounds, simple and chemically intuitive rules have been developed that relate electron count to their structures and properties,[3] but these rules are not necessarily applicable to the whole set of compounds. Here, we propose to apply data-mining and machine-learning techniques with these aims: (1) assign the correct structure of Heusler vs. inverse Heusler compounds for some arbitrary combination of elements, (2) predict the existence of new Heusler compounds, and (3) evaluate the reliability of structure assignments for the entire set of compounds AB_2C reported in crystallographic databases ("data sanitizing"). Importantly, we also test these predictions through experimental methods (synthesis, structure determination, and physical properties). In general, predicting what structure will form for a given combination of elements is one of the "grand challenges" of chemistry.[19] This goal has broader implications for advancing materials science, because

compounds with specific properties can be discovered more quickly without having to explore vast reaches of chemical space.

9.2 Experimental

9.2.1 Structure prediction

The Heusler prediction engine was built using a materials informatics approach from three integral components: training data, chemical descriptors, and a machine-learning algorithm. The key idea behind materials informatics is that, given enough examples (training data) and informative numerical representation of the materials (descriptors), a machine-learning algorithm can determine patterns to predict how unseen examples will behave. Careful development and selection of all three parts are necessary to create a useful predictive engine. Training data can be characterized by their quality and quantity. A sufficient quantity is required to be able to statistically detect a pattern: more complex patterns demand more examples. High quality data are also crucial, because errors create extra noise that can obscure patterns. The training data used in this engine are a compilation of experimentally confirmed structures for compounds with a formula of AB_2C. Crystallographic data for all such compounds were extracted from Pearson's Crystal Data[15] and the ASM Alloy Phase Diagram Database,[20] with the following criteria imposed for the input set of compounds used in the structure predictor: (i) the phases do not contain hydrogen, noble gases, and elements with $Z > 83$ (radioactive and actinide elements), and (ii) the phases exhibit exact 1:2:1 stoichiometry, contain 3 components, and are thermodynamically stable. A total of 1948 compounds crystallizing in 208 unique structure types were found to satisfy these criteria and were

confirmed to exist experimentally under ambient temperatures and pressures. The input file contained information about the composition and structure type of these compounds. Out of these, the most populous are Heusler compounds (341 entries, or 18%) and the second most populous are $NaFeO_2$-type compounds (255 entries, or 13%). There are 94 compounds each having only one reported entry, meaning that they crystallize in their own unique structure types.

Once a training set is compiled, the next challenge is to represent these examples in a machine-understandable way. Typically, descriptors are properties of a material that can be used to compare one compound to another, such as crystal structure or average atomic mass. Choosing a good set of descriptors is an essential part of materials informatics. The relationship between descriptor choice and model quality,[21] compounded with the lack of a standard representation, has led to a growing body of literature emphasizing the importance of descriptors.[22,23] Moreover, materials datasets tend to be much smaller than traditional machine-learning datasets, which makes complex patterns harder to detect with a suboptimal collection of descriptors. Descriptors allow for integration of chemical knowledge to help the model by describing materials in dimensions where patterns are likely to be found, so that the patterns can be detected with fewer data. Careful choice of a descriptor set takes advantage of prior knowledge to identify *where* the pattern is, allowing the algorithm to then determine *what* the pattern is. For example, because atomic size is known to be an important factor in determining chemical structure, descriptors such as the difference in atomic radii are included to capture this information for the model in the structure predictor. Finally comes the choice of machine-learning algorithm. We used the random forest algorithm,[24]

a technique that has been successfully applied to materials informatics.[25,26] This algorithm is an example of an ensemble method, which trains multiple predictors and combines their results to make a single final prediction. In the case of random forest, each of these sub-predictors is a decision tree trained on a fraction of the training data. The decision tree structure is able to capture complex interactions between descriptors. By averaging over the predictions of an ensemble of these decision trees, the random forest algorithm incorporates the different trends found by each tree, resulting in a complex and robust model. We use the standard *k*-fold cross-validation technique to characterize the performance of the models. This technique evaluates the model on examples that were unseen during training in order to accurately gauge model performance. To perform *k*-fold cross-validation, the data are split into *k* equal segments, called folds. For each of these folds, a model is trained on all data except the selected fold. Predictions are made for the data in the fold that were not included in the model training. The predictions are then compared to the known values for those examples.

9.2.2 Synthesis and structural characterization

From the recommendations offered above, the most promising Heusler compositions were identified for experimental validation. However, candidates involving substitution of similar elements were excluded to apply a fair test of the model (e.g., if FeB_2C and NiB_2C are known Heusler compounds, the unknown but chemically obvious compound CoB_2C containing the intervening transition metal was not considered). The ternary gallides MRu$_2$Ga and RuM_2Ga (where M is a first-row transition metal) were targeted for synthesis because their probability of forming Heusler compounds is

predicted to be high, their existence cannot be extrapolated simply through periodic trends from previously known compounds, and they are dissimilar to previous *M*–*M*′–Ga phases which mostly contain first-row transition metals for both *M* and *M*′ components. Conversely, to test for false negative predictions, the series LaM_2Ga (where *M* is again a first-row transition metal) was also targeted for synthesis because their probability of forming Heusler compounds is predicted to be low. $TiRu_2Ga$ sample was synthesized to test thermoelectric recommendation engine[27] in large quantities for thermal conductivity measurements. Full Heusler structures were not previously considered to be low thermal conductors however according to recommendations made by machine learning approach (with a similar algorithm presented in the current work) $TiRu_2Ga$ phase has a high potential to demonstrate thermal conductivity value $\kappa < 10$ $Wm^{-1}K^{-1}$.

Mixtures of Ru powder (99.95%, Alfa-Aesar) or La pieces (99.9%, Hefa), powders of various first-row transition metals *M* (Ti to Ni, >99.5%, Alfa-Aesar or Cerac), and Ga pieces (99.95%, Alfa-Aesar) were combined in ratios according to the formulas indicated above with a total mass of 0.2 g, pressed into pellets, and melted on a copper hearth under argon atmosphere in an Edmund Bühler MAM-1 arc melter. The ingots were placed in fused-silica tubes, which were evacuated and sealed. Annealing was done in one step at 800 °C, followed by quenching in cold water. The samples were ground to powders and examined by powder XRD on an Inel diffractometer equipped with a Cu $K\alpha_1$ radiation source and a curved position-sensitive detector.

Single crystals of $TiRu_2Ga$ were selected and confirmed by energy-dispersive X-ray (EDX) analysis, performed on a JEOL JSM-6010LA scanning electron microscope,

to have a composition ($Ti_{24(2)}Ru_{49(3)}Ga_{27(3)}$) in good agreement with the formula of a Heusler compound. Single-crystal diffraction data were collected at room temperature on a Bruker PLATFORM diffractometer equipped with a SMART APEX II CCD area detector and a graphite-monochromated Mo $K\alpha$ radiation source, using ω scans at 8 different ϕ angles with a frame width of 0.3° and an exposure time of 15 s per frame. The structure was solved and refined with use of the SHELXTL (version 6.12) program package.[28] Face-indexed absorption corrections were applied. The cubic space group $Fm\bar{3}m$ was chosen on the basis of Laue symmetry, intensity statistics, and systematic absences.

9.2.3 Thermal properties

Thermal conductivity, κ, of the samples was calculated from the standard relationship $\kappa = \rho\alpha C_p$ where ρ is the density, α is the thermal diffusivity and C_p is the heat capacity at constant pressure. Density values were taken from Pearson's Crystal Database estimated by single crystal diffraction report. Heat capacity was determined at the University of Utah using a Netzsch Sirius 3500 temperature modulated differential scanning calorimeter (TM-DSC) and additionally on a Perkin Elmer Pyris 1 DSC at the University of Alberta. Small fragments were cut from the annealed arc-melted ingots and calorimetry was performed from room temperature up to 600°C. Thermal diffusivity was measured on annealed arc-melted ingots. Samples were first polished to be coplanar with a thickness of 1 to 2 mm and then cut into disc shapes with either 8 or 12 mm diameters via electrical discharge machining. The thermal diffusivity of the discs was then measured using the laser flash method with a Netzsch LFA 457 instrument with a Cape-

Lehman[29] pulse length and heat loss correction model. Samples were coated with graphite on both sides to promote uniform absorption and emission. Measurements were taken from room temperature up to 600°C in 100°C increments.

9.3 Results and Discussion

Predicting the existence and structure of unknown compounds is an ongoing challenge in chemistry. On one extreme, semiclassical approaches assume that the structure depends on chemical concepts like atomic size and electron count which are used to create structure maps;[30-32] although intuitively appealing, there is a risk that the choice of parameters is biased or too simple. At another extreme, first-principles quantum mechanical calculations are performed to determine the total energies of alternative structures;[33,34] however, the gain in accuracy is offset by a loss in easy understanding through general chemical concepts and by a need for powerful computational resources. Intermediate approaches such as principal component analysis and machine-learning methods are now being applied to this general problem.[35,36]

9.3.1 Assignment of Heusler, Inverse Heusler, and Non-Heusler Compounds

We have constructed a prediction engine that suggests the structure of compounds AB_2C by exploiting a random forest algorithm. The distinguishing feature of our approach is that *the prediction is made from the descriptors based on the composition alone*. The model required less than 1 minute to train the dataset, and about 45 minutes to make the full set of predictions, *viz.* <0.01 s per compound. We performed 20-fold cross-validations for this model, and the distribution of probability values (color-coded

by the actual class) is shown in Figure 9-3. The model is exceptionally successful in making correct predictions, giving high probabilities for candidates observed to be Heusler compounds experimentally, low probabilities for those that are not; it is even able to correctly predict inverse Heusler compounds to be non-Heusler compounds.

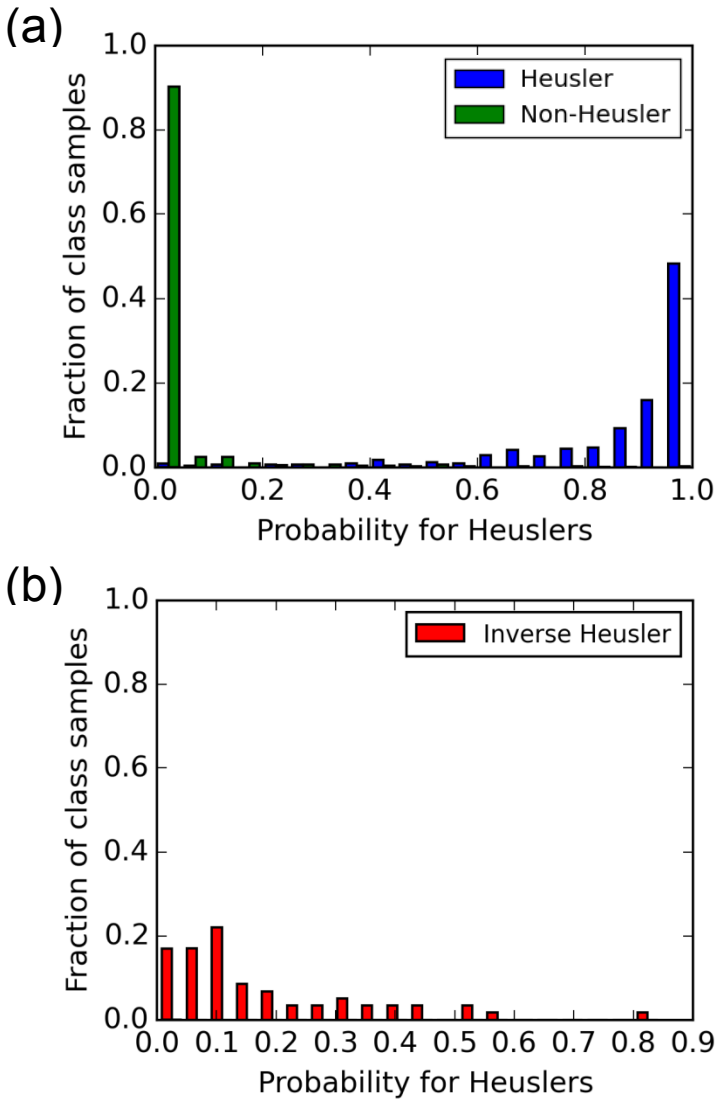

Figure 9-3 Distribution of probabilities for forming Heusler compounds evaluated in the validation process of the Heusler prediction engine for (a) Heusler vs. non-Heusler structures and (b) inverse Heusler structures, as assigned in crystallographic databases and literature.

Analyzing the descriptors (variables) that were most effective in separating Heusler structures from others in the prediction engine gives interesting insight. The most important such descriptors are the position of element *B* (in the formula AB_2C) in the periodic table, the total number of electrons (especially number of p-electrons), and the ratio of atomic sizes for the *A* and *B* components (and secondarily the ratio of atomic sizes for *A* and *C*). Since the electron configuration of element *B* is given by its group number or position in the periodic table, the first two descriptors essentially correspond to electron count, which is known to influence the energetic preference for Heusler compounds[19] and their various physical properties (magnetism,[4,5] superconductivity,[7,8] topological insulator behaviour[14]), depending on the combination of elements. A size factor, given by the third descriptor, dictates formation of Heusler vs inverse Heusler structures, in which the occupations of *A* and *B* atoms are partly interchanged. (As noted earlier, Heusler and inverse Heusler structures are not easy to distinguish experimentally from their powder XRD patterns.) However, it would be misleading to conclude that these are the only important factors. The whole point of the machine-learning algorithm is to capture complex, nonlinear relationships that cannot be reduced to a small number of factors influencing the formation of Heusler compounds (inherent in semiclassical approaches), while not having to expend costly computational effort (inherent in first-principles quantum calculations). Specifically, Heusler compounds often contain d- and f-block elements that can be tricky to model with density functional theory. The Heusler prediction engine offers several key advantages compared to the previous approaches: (1) it is fast, giving predictions with fractions of a second; (2) it requires no structural information, the very thing that needs to be predicted; (3) it uses only descriptors based

on elemental properties (or combinations thereof), which are well tabulated in the literature; and (4) it evaluates quantitative probabilities for the formation of a hypothetical compound. With this tool, experimentalists can exploit machine-learning guidance to complement their chemical intuition in designing compounds. In this way, they can accelerate the search for new materials, they can reduce the risks when the syntheses are difficult, costly, or dangerous to perform, and they can get new ideas to "think outside the box."

9.3.2 Prediction of new heusler compounds

For experimental validation, several compounds were selected belonging to two series of unknown gallides MRu$_2$Ga and RuM_2Ga (M = Ti–Ni), which have probabilities of >50% of being Heusler compounds, including both positive and some non-obvious positive predictions (Figure 9-4). Arc-melting and annealing reactions (at 800 °C) led to the successful preparation of all members of MRu$_2$Ga and RuM_2Ga (except for M = Ni) with Heusler structures, as confirmed by powder X-ray diffraction (Figure 9-5) on all samples and single-crystal X-ray diffraction on TiRu$_2$Ga as a representative member (Figure 9-6). The phase analysis is complicated by severe X-ray absorption caused by the presence of the large proportion of heavy elements. The two Ni-containing members (NiRu$_2$Ga, RuNi$_2$Ga) were not confirmed experimentally, but neither could the powder XRD patterns of these samples be assigned to any existing phase. In fact, Ni-containing intermetallic systems are often anomalous in that they exhibit a much richer variety of phases with diverse compositions,[37,38] not captured within the purview of this prediction engine. It is possible that under the synthetic conditions used, which were not optimized,

equilibria were at play involving formation of neighbouring phases with close composition to the Heusler structure.

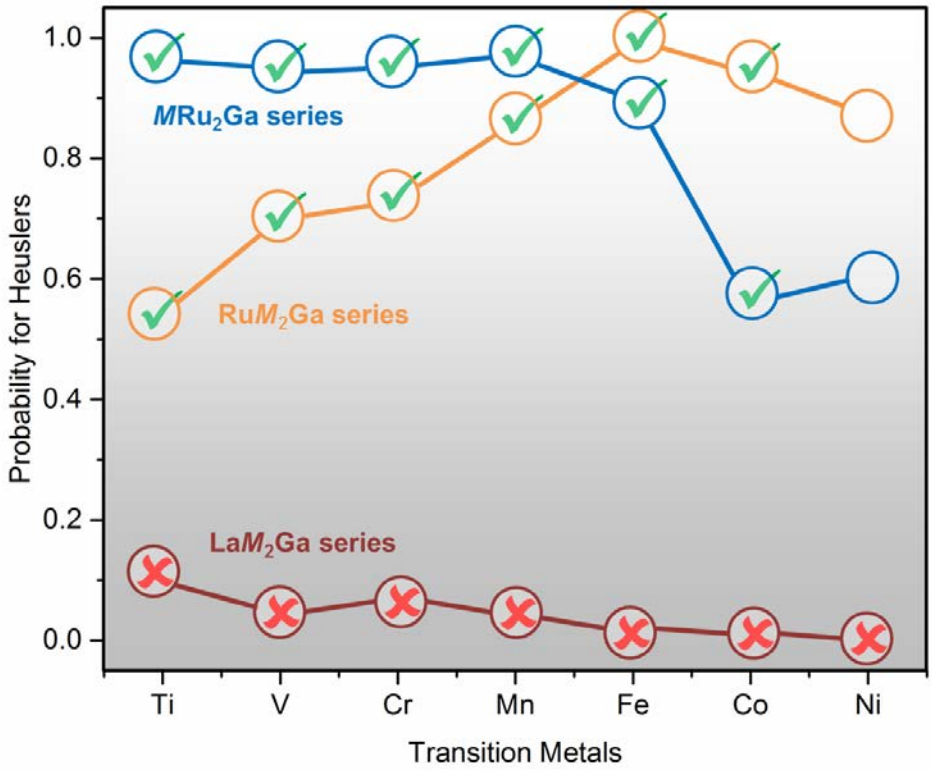

Figure 9-4 Probability of forming Heusler compounds for three series of gallides, and experimental confirmation through arc-melting and annealing at 800 °C (check marks indicate successful preparation of Heusler compound, and crosses indicate absence of Heusler compound).

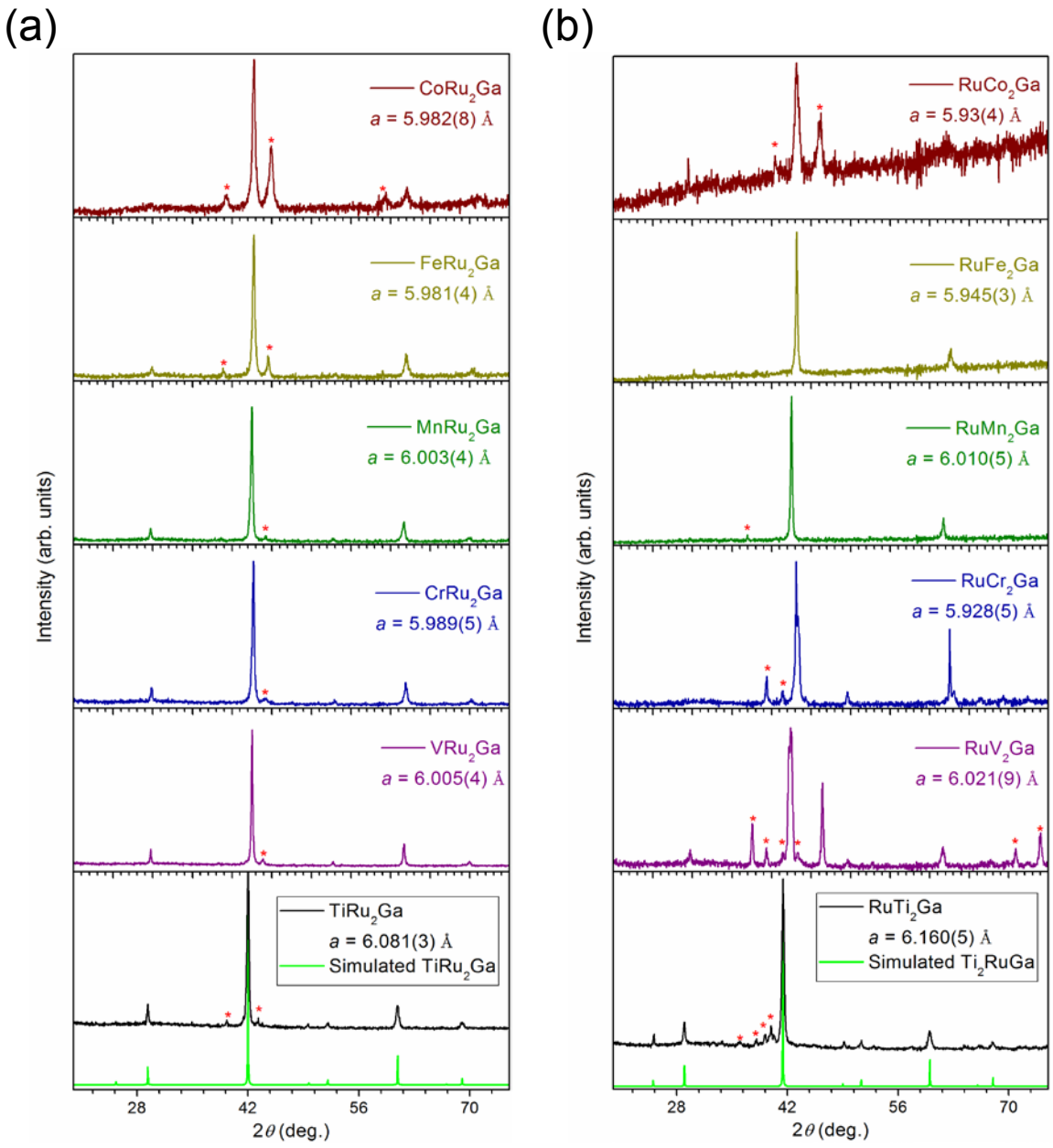

Figure 9-5 Powder XRD patterns for (a) MRu$_2$Ga and (b) RuM_2Ga (M = Ti–Co) series with Heusler structures. Red asterisks indicate small amounts of secondary phases (typically Ru and RuGa$_2$).

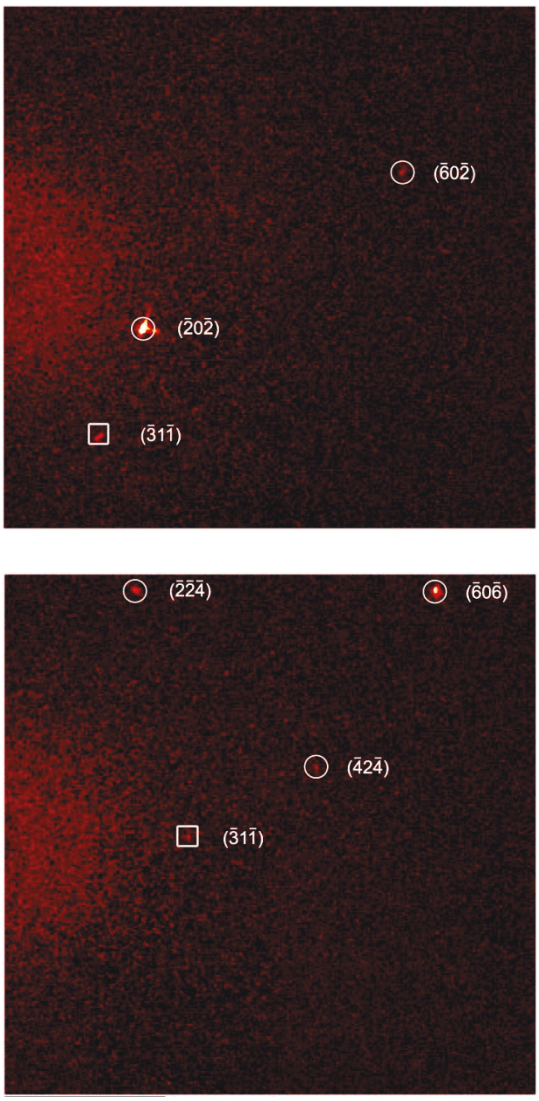

Figure 9-6 CCD frames from single-crystal diffraction data collection of $TiRu_2Ga$. The observation of weak superstructure reflections $\overline{3}1\overline{1}$ (enclosed in squares) provides evidence for a Heusler structure instead of a CsCl-type structure. The relative intensities in the simulated powder XRD pattern cannot be directly compared with those on these images which also depend on the diffractometer angles.

Experimental validation for negative predictions is also important, to ensure that the predictor engine does not give false-negative results. To test for these, compounds belonging to a third series LaM_2Ga (M = Ti–Ni) were selected, which have probabilities

of <20% of being Heusler compounds (Figure 9-4). The reactions attempted did not lead to formation of any ternary compounds, but rather to binary phases (LaGa, La_5Ga_3, $LaGa_2$, and elemental *M*). Indeed, as *post hoc* rationalization, inspection of the few phase diagrams experimentally investigated here (La–V–Ga,[39] La–Mn–Ga,[40] La–Fe–Ga[41]) reveals no ternary phases in these systems.

9.3.3 Data sanitizing

Structural confirmation of Heusler compounds is exceedingly tricky, as illustrated earlier by the nearly identical powder XRD patterns of the CsCl-type, Heusler, and inverse Heusler structures (Figure 9-2), and rarely performed by single-crystal diffraction. Thus, there are often uncertain or even incorrect assignments when structural investigation is deficient or absent. This could pose problems if conclusions about materials properties are made based on erroneous assumptions. The Heusler prediction engine can be applied to identify suggest correct structural assignments of existing compounds reported in the literature and in databases.

CsCl-type vs. Heusler. Heusler compounds AB_2C (where *A* and *C* atoms are ordered) can be misidentified as CsCl-type (where *A* and *C* atoms are disordered), or vice versa. Sometimes, it is possible to apply the rule that if two binary alloys *AB* and *BC* exist with CsCl-type structures, then they can form an ordered Heusler compound AB_2C. These uncertainties can be rectified by the prediction engine. For example, $Mn_{0.5}RhGa_{0.5}$ (or $MnRh_2Ga$) was reported in the literature as a Heusler compound[42] but was entered, perhaps accidentally, as CsCl-type in Pearson's Crystal Data[15]. In a list of combinations AB_2C sorted by probability in the prediction engine, $MnRh_2Ga$ is 95% probable to adopt

a Heusler structure. Thus, this prediction engine serves a valuable function to flag questionable entries in crystallographic databases.

Heusler vs. inverse Heusler. Heusler AB_2C and inverse Heusler compounds A_2BC have the same overall composition (1:2:1). In databases,[15] $LiAg_2Al$ was listed as an inverse Heusler compound on the basis of powder XRD,[18] but this assignment is suspect because the prediction engine suggests that it should be a Heusler compound at an 85% probability (the anomalous high entry in Fig. 3b). The experimental ambiguity is understandable because, as discussed earlier, the simulated powder XRD patterns for $LiAg_2Al$ are fortuitously identical for Heusler and inverse Heusler structures (Figure 9-2). There is also a generalization that Heusler structures AB_2C tend to contain a transition metal as the *B* component, whereas inverse Heusler structures A_2BC tend to contain a large electropositive metal as the *A* component. Given that Ag is a transition metal and Li is not a large or strongly electropositive metal atom, the assignment of $LiAg_2Al$ as a Heusler compound is more chemically sensible.

9.3.4 Thermal conductivity of $TiRu_2Ga$

Heusler compounds are promising thermoelectric materials but the challenge is to reduce their thermal conductivities. For the novel Heusler compound $TiRu_2Ga$, which was also predicted to be a good thermoelectric by a separate recommendation engine,[27] the thermal conductivity varies from 13 W m^{-1} K^{-1} at room temperature to as low as 4 $Wm^{-1}K^{-1}$ at 600 °C (Figure 9-7). This is a remarkable achievement, given that the lowest thermal conductivity previously observed in full Heusler compounds (according to thermoelectric database[43]) was 8.12 $Wm^{-1}K^{-1}$ at room temperature for $NbCo_2Sn$.[44]

Unusually, the heat capacity for $TiRu_2Ga$ decreases with temperature and the thermal diffusivity increases with temperature, though the thermal conductivity itself has the expected general trend of decreasing with temperature. Further measurements of other physical properties are in progress to evaluate the feasibility of this potential thermoelectric material.

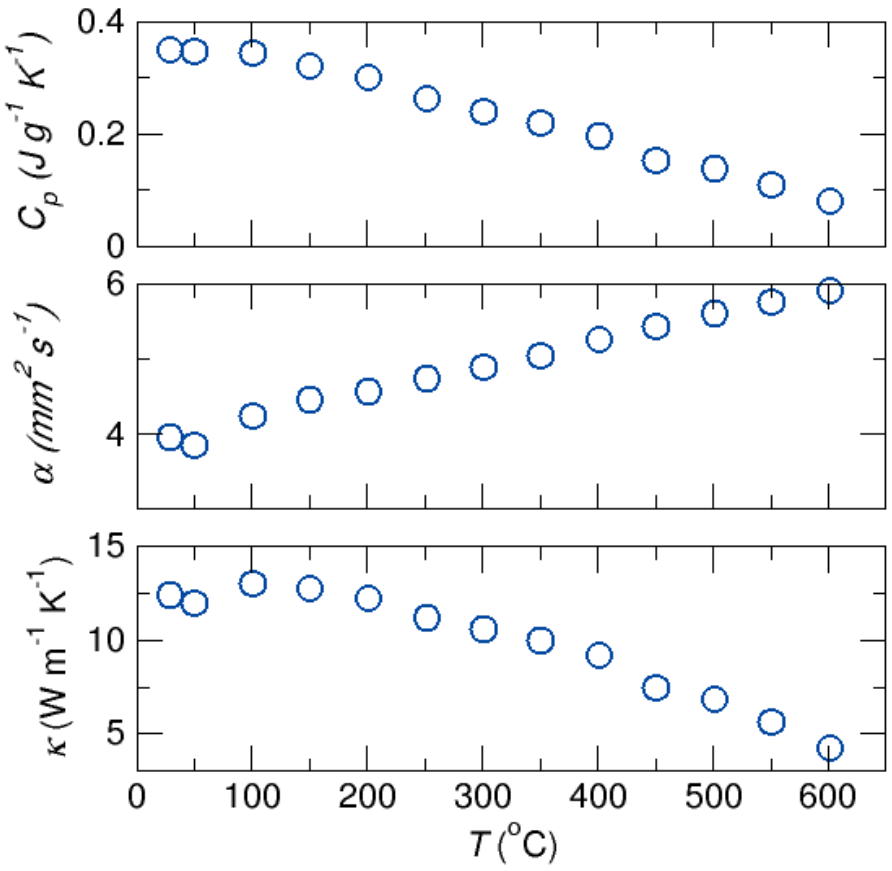

Figure 9-7 Thermal conductivity of the novel Heusler compound $TiRu_2Ga$.

9.4 Conclusions

A machine-learning prediction engine exploiting a random forest algorithm was applied to evaluate the probabilities at which compounds with the formula AB_2C will adopt Heusler structures, from descriptors based on the composition alone. This approach was exceptionally successful in distinguishing between Heusler and non-Heusler compounds, including the prediction of heretofore unknown compounds and flagging erroneously assigned entries in the literature and in crystallographic databases. Compared to approaches which were limited in scope (semiclassical) or computationally demanding (quantum calculations), the Heusler predictor is fast, requires no structural input, uses descriptors based on elemental properties, and evaluates quantitative probabilities. Novel predicted candidates $M\mathrm{Ru_2Ga}$ and $\mathrm{Ru}M_2\mathrm{Ga}$ (M = Ti–Ni) were synthesized and confirmed to be Heusler compounds; one member, $\mathrm{TiRu_2Ga}$, exhibited remarkably low thermal conductivities comparable to the best performance of existing Heusler compounds. The results have significant broader impact in accelerating the search for not only Heusler compounds (which have diverse applications for sustainable energy, among many), but also materials candidates for other applications, by offering ideas "outside the box."

References

[1] Heusler, F.; Stark, W.; Haupt, E. *Verh. Deut. Phys. Ges.* **1903**, *5*, 220–223.

[2] Bradley, A. J.; Rodgers, J. W. *Proc. R. Soc. London, Ser. A* **1934**, *144*, 340–359.

[3] Graf, T.; Felser, C.; Parkin, S. S. P. *Prog. Solid State Chem.* **2011**, *39*, 1–50.

[4] Kübler, J.; Williams, A. R.; Sommers, C. B. *Phys. Rev. B* **1983**, *28*, 1745–1755.

[5] Wurmehl, S.; Kandpal, H. C.; Fecher, G. H.; Felser, C. *J. Phys.: Condens. Matter* **2006**, *18*, 6171–6181.

[6] Ouardi, S.; Fecher, G. H.; Felser, C.; Kübler, J. *Phys. Rev. Lett.* **2013,** *110*, 100401-1–100401-5.

[7] Winterlik, J.; Fecher, G. H.; Felser, C. *Solid State Commun.* **2008**, *145*, 475–478.

[8] Aoki, Y.; Sato, H. R.; Sugawara, H.; Sato, H. *Physica C: Supercond.* **2000**, *333*, 187–194.

[9] Yang, J.; Li, H.; Wu, T.; Zhang, W.; Chen, L.; Yang, J. *Adv. Funct. Mater.* **2008**, *18*, 2880–2888.

[10] Larson, P.; Mahanti, S. D.; Sportouch, S.; Kanatzidis, M. G. *Phys. Rev. B* **1999**, *59*, 15660–15668.

[11] Galanakis, I.; Dederichs, P. H.; Papanikolaou, N. *Phys. Rev. B* **2002**, *66*, 134428-1–134428-10.

[12] Kandpal, H. C.; Fecher, G. H.; Felser, C. *J. Phys. D: Appl. Phys.* **2007**, *40*, 1507–1523.

[13] Ren, J.; Li, H.; Feng, S.; Zhai, Q.; Fu, J.; Luo, Z.; Zheng, H. *Intermetallics* **2015**, *65*, 10–14.

[14] Chadov, S.; Qi, X.; Kübler, J.; Fecher, G. H.; Felser, C.; Zhang, S. C. *Nat. Mater.* **2010**, *9*, 541–545.

[15] Villars, P.; Cenzual, K. Pearson's *Crystal Data – Crystal Structure Database for Inorganic Compounds (on DVD), Release 2015/16*, ASM International, Materials Park, Ohio, USA.

[16] Harang, L. *Z. Kristallogr.* **1927**, *65*, 261–285.

[17] Palmer, A. "*Golf is deceptively simple and endlessly complicated; it satisfies the soul and frustrates the intellect. It is at the same time rewarding and maddening – and it is without a doubt the greatest game mankind has ever invented.*"

[18] Lacroix-Orio, L.; Tillard, M.; Belin, C. *Solid State Sci.* **2004**, *6*, 1429–1437.

[19] U.S. Department of Energy, Grand Challenge #3: How do remarkable properties of matter emerge from complex correlations of the atomic or electronic constituents and how can we control these properites? (http://science.energy.gov/bes/efrc/research/grand-challenges/).

[20] Villars, P.; Okamoto, H.; Cenzual K. (Eds.), *ASM Alloy Phase Diagrams Database,* ASM International, Materials Park, OH, 2016 (http://www.asminternational.org).

[21] Hansen, K.; Biegler, F.; Ramakrishnan, R.; Pronobis, W.; von Lilienfeld, O.A.; Muller, K.-R.; Tkatchenko, A. *J. Phys. Chem. Lett.* **2015**, *6*, 2326–2331.

[22] Curtarolo, S.; Hart, G. L. W.; Nardelli, M. B.; Mingo, N.; Sanvito, S.; Levy, O. *Nat. Mater.* **2013**, *12*, 191–201.

[23] Ghiringhelli, L. M.; Vybiral, J.; Levchenko, S. V.; Draxl, C.; Scheffler, M. *Phys. Rev. Lett.* **2015**, *114*, 105503-1–105503-5.

[24] Breiman, L.; *Machine Learning* **2001**, *45*, 5–32.

[25] Carrete, J.; Li, W.; Mingo, N.; Wang, S.; Curtarolo, S. *Phys. Rev. X* **2014**, *4*, 011019-1–011019-9.

[26] Meredig, B.; Agrawal, A.; Kirklin, S.; Saal, J. E.; Doak, J. W.; Thompson, A.; Zhang, K.; Choudhary, A.; Wolverton, C. *Phys. Rev. B* **2014**, *89*, 094104-1–094104-7.

[27] Gaultois, M. W.; Oliynyk, A. O.; Mar, A.; Sparks, T. D.; Mulholland, G. J.; Meredig, B. *APL Materials*, accepted.

[28] Sheldrick, G. M. *SHELXTL*, version 6.12; Bruker AXS Inc.: Madison, WI, 2001.

[29] Cape, J. A.; Lehman, G. W. *J. Appl. Phys.* **1963**, *34*, 1909–1913.

[30] Phillips, J. C. *Helv. Phys. Acta* **1985**, *58*, 209–215.

[31] Pettifor, D. G. *Solid State Commun.* **1984**, *51*, 31–34.

[32] Villars, P. *J. Less-Common Met.* **1983**, *92*, 215–238.

[33] Oganov, A. R.; Lyakhov, A. O.; Valle, M. *Acc. Chem. Res.* **2011**, *44*, 227–237.

[34] Hautier, G.; Fischer, C. C.; Jain, A.; Mueller, T.; Ceder, G. *Chem. Mater.* **2010**, *22,* 3762–3767.

[35]Rajan, K. *Mater. Today* **2005**, *8*, 38–45.

[36] Broderick, S.; Rajan, K. Sci. Technol. *Adv. Mater.* **2015**, *16*, 013501-1–013501-8.

[37] Oryshchyn, S. V.; Le Sénéchal, C.; Députier, S.; Bauer, J.; Guérin, R.; Akselrud, L. G. *J. Solid State Chem.* **2001**, *160*, 156–166.

[38] Zelinska, M.; Zhak, O.; Oryshchyn, S.; Polianska, T.; Pivan, J.-Y. *Z. Naturforsch. B* **2007**, *62*, 1143–1152.

[39] Svechnikov, V. N.; Pan, V. M.; Spektor, A. T. *Russ. Metall.* **1971**, *1*, 133–137.

[40] Markiv, V. Ya.; Belyavina, N. N.; Shevchenko, I. P. *Russ. Metall.* **1994**, *3*, 148–151.

[41] Raghavan, V. *Indian Inst. Met.* **1992**, *6B*, 823–826.

[42] Suits, J. C. *Phys. Rev. B* **1976**, *14*, 4131–4135.

[43] Gaultois, M. W.; Sparks, T. D.; Borg, C. K. H.; Seshadri, R.; Bonificio W. D.; Clarke D. R. *Chem. Mater.* **2013**, *25*, 2911-2920.

[44] Kimura, Y.; Tamura, Y.; Kita, T. *Appl. Phys. Lett.* **2008**, *92*, 012105-1–012105-3.

Chapter 10

Classifying crystal structures of binary compounds AB through cluster resolution feature selection and support vector machine analysis

A version of this chapter has been submitted to Chemistry of Materials.

10.1. Introduction

A fundamental goal in chemistry is identifying what compounds form given an arbitrary combination of elements and what structure they adopt. Even for the simplest case – binary compounds AB, where A and B are any elements – the problem is complex because many factors influence structures. In the early days of crystallography, when structure determination was difficult, it was hoped that by correlating atomic properties and systematizing empirical information, "*perhaps we had come to a time when we could predict what the structures are without X-ray diffraction patterns.*"[1] Size factors were first invoked through radius ratio rules to rationalize structures of ionic solids AB,[2] but they fail to account for the greater prevalence of NaCl-type structures than predicted. Later, other atomic and physical properties were included, such as electronegativities and valence electron numbers, giving a more nuanced picture and generating structure maps (e.g., Mooser-Pearson, Phillips-van Vechten, Pettifor, Zunger, Villars)[3-5] that succeeded in segregating structure types. For example, focusing on intermetallic compounds AB, Villars considered 182 variables and tested combinations thereof to identify three expressions – difference in Zunger pseudopotential radii sums, difference in Martynov-

Batsanov electronegativity, and sum of valence electrons – that separated 988 compounds into 20 structure types with <3% violations, an impressive achievement.[5] The elucidation of these maps is a semiclassical or semiempirical approach. At the other extreme, first-principles electronic structure calculations can be performed to evaluate the stability of compounds;[6,7] this approach is feasible if powerful computational facilities are available but can provide guidance to discovering new compounds. Because predictions are only valuable if they are tested experimentally, it is important to coordinate these activities together.

An intermediate approach that could be valuable in structure prediction is chemometrics, in information is extracted from databases to predict optimal experimental conditions,[8-9] in applications such as identifying jet fuels,[10] classifying gasoline components,[11-15] and discovering biomarkers.[16,17] In materials science, the wealth of information in databases[18,19] offers opportunities for data mining, to address problems such as engineering semiconductor band gaps,[20] enhancing hardness of nitrides,[21] and designing zeolite topologies.[22] Cluster analysis and principal component analysis (PCA)[23,24] have been widely used to identify inherent patterns in chemical data. Arguably the most popular data exploratory technique, PCA has the advantage of dimensionality reduction for large datasets. Supervised pattern recognition approaches such as linear discriminant analysis and partial least squares discriminant analysis (PLS-DA)[25] have also been applied to chemical data.

A relatively modern supervised learning technique is support vector machines (SVM), which is well-suited for classification. SVM is a boundary-based method that

aims to maximize the gap (a hyperplane in higher dimensional space) separating samples within two classes;[26] it does not model the entire class but selects a subset of samples (called support vectors) within a class marking its boundary. SVM has been rarely applied to chemical problems and to our knowledge, never before to crystallography. Compared to linear discriminant analysis methods, SVM is more flexible because the kernel function (used to build the model through a radial or linear basis) can be changed to optimize the performance. Automatic tuning of the kernel function to maximize the separation boundaries between classes improves classification.

Prior to chemometric analysis, it is important to eliminate noise and irrelevant variables when selecting variables,[27] commonly through use of Fisher (*F*-ratio) scores, the ratio of between-group variability (explained variance) to within-group variability (unexplained variance),[10] or selectivity (*S*-ratio) scores, which evaluates the usefulness of each variable in a regression model.[28] Variables with higher scores contribute more to distinguishing classes. However, the score only estimates potential importance. Another parameter measuring model quality is cluster resolution, which is the product of non-colliding confidence ellipses generated around samples clustered by class assignments in any reduced dimensionality score space (e.g., PCA space). Through an algorithm called cluster resolution feature selection (CR-FS),[29] the effect of each variable on class separation is evaluated automatically and objectively by a hybrid backward elimination/forward selection of variables. In the backward elimination step, a subset of the top-ranked variables is selected, from which an initial cluster resolution is calculated to evaluate the model quality. The lowest ranked variables among this subset are successively eliminated and the cluster resolution is re-calculated. If the model quality

improves, the variable is discarded; otherwise it is retained. In the forward selection step, those variables whose inclusion improves the model quality are added, while those that do not are discarded. Through this process, the contribution of all variables to model quality can be evaluated.

Here we revisit the longstanding problem of predicting the structures of binary AB compounds, with several goals. First, CR-FS algorithm applied in PCA space was used to determine what combinations of variables (atomic and physical properties) best optimize the discrimination of structure types, and thereby evaluate the reliability of previous structure maps[5] and gain insight on factors influencing structural preference. Second, predictors retained after feature selection were used to build PLS-DA and SVM models, with the superior one chosen to predict the structure of a new compound. Third, we confirm the existence of a heretofore unknown AB compound through experiment. Although more than half of the possible AB compounds (out of all combinations of elements) remain uninvestigated, the latest report of a newly synthesized binary CsCl-type structure AB compound was that of RhZn, over 15 years ago.[30] Guidance in accelerating the investigation of missing AB compounds would then be extremely valuable.

10.2 Experimental

10.2.1 Chemometric analysis of AB compounds

Crystallographic data of AB compounds were extracted from Pearson's Crystal Data[18] and ASM Alloy Phase Diagram Database;[19] additional data (up to September 2015) were obtained from searches on SciFinder.[31] All combinations AB were considered provided that: (i) they did not contain hydrogen, noble gases, and elements with $Z > 83$ (radioactive elements and actinides) and (ii) they exhibit exact 1:1 stoichiometry. Out of 2926 AB compounds satisfying these conditions, 974 exist experimentally under ambient temperatures and pressures, crystallizing in 107 unique structure types.

Variables used to describe atomic properties were chosen from those which have well-defined values for all or most elements (or which can be interpolated, such as for the lanthanide series). They generally fall into a small number of categories: (i) electronegativities in different scales,[32-36] (ii) various types of radii,[2] and (iii) properties derived from position in the periodic table[37] (e.g. number of valence electrons, group number, and others). Mathematical expressions (such as sums or differences for two elements A and B) derived from these properties were also treated as variables. In total, 56 variables were considered.

The data for these AB combinations and variables were represented in a 974×56 matrix. To ensure good statistical reliability, only those compounds (706) crystallizing in structure types containing more than 30 representatives were retained in this analysis: 257 in CsCl, 205 in NaCl, 102 in TlI, 42 in β-FeB, 36 in NiAs, 33 in ZnS, and 31 in CuAu structure types. The data were normalized, mean-centred, and scaled to unit

variances. The pre-processed data were split into two parts: two-thirds (470) for training (i.e., variable selection and model building), and one-third (236) for external validation. Within a third of the training data, variables were ranked according to their *F*-ratio. The entire training set data were subjected to the CR-FS algorithm implemented in PCA score space. The 20 most highly ranked were used for backward elimination and the remained were tested during forward selection. PLS-DA and SVM models were generated within the training set data using only those variables retained by CR-FS. The SVM classification was performed with radial basis function and a venetian blind cross-validation with 10-fold data split to optimize the model. The ability of SVM vs. PLS-DA models to predict new compounds was compared using the validation set data. Then, using only variables that passed feature selection, a prediction was made on an unknown compound (RhCd).

Data handling and feature selection were performed using in-house written algorithms in Matlab 2015a (The Mathworks, Natick, MA). SVM models were generated using PLS Toolbox Version 8.0.1 (Eigenvector Research Inc., Wenatchee, WA). Results for objective comparison were class predicted probabilities of the SVM models.[38] All computations were performed on a Windows PC, running on an Intel® Core™ i7-4790K CPU and 32 GB RAM.

10.2.2 Synthesis and Characterization of RhCd

From the chemometric analysis above, RhCd is predicted to adopt a CsCl-type structure. A pressed pellet of Rh powder (99.95%, Alfa-Aesar) and filed Cd pieces (99.95%, Alfa-Aesar) mixed in a 1:1 molar ratio (total mass of 0.2 g) was placed in a

fused-silica tube, which was evacuated and sealed. The tube was heated to 800 °C, kept there for one week, and quenched in cold water. The product was examined by powder X-ray diffraction (XRD) performed on an Inel diffractometer and by energy-dispersive X-ray (EDX) analysis on a JEOL JSM-6010LA scanning electron microscope.

Small single crystals, confirmed by EDX to have composition RhCd, were selected. Intensity data were collected on a Bruker PLATFORM diffractometer equipped with a SMART APEX II CCD area detector an a graphite-monochromated Mo $K\alpha$ radiation source, using ω scans at 8 different ϕ angles with a frame width of 0.3° and an exposure time of 15 s per frame. The structure was solved and refined with use of the SHELXTL (version 6.12) program package.[39] Face-indexed absorption corrections were applied. The cubic space group $Pm\bar{3}m$ was chosen on the basis of Laue symmetry, intensity statistics, and systematic absences.

10.3 Results and discussion

10.3.1 Cluster resolution feature selection

The CR-FS algorithm is well-suited to simultaneously optimize the classification of multiple classes,[29,40-42] as is the case here, where there are seven common structure types (identified by numbered labels: CsCl (1), NaCl (2), ZnS (3), CuAu (10), TlI (14), β-FeB (15), NiAs (17)). Before objectively evaluating each descriptor, the 56 variables used to describe atomic properties are first ranked according to Fisher (*F*-ratio) or selectivity ratio (*S*-ratio) scores (Figure 10-1). The choice of which ratio to use was not extremely critical because both tended to arrive at the same results.

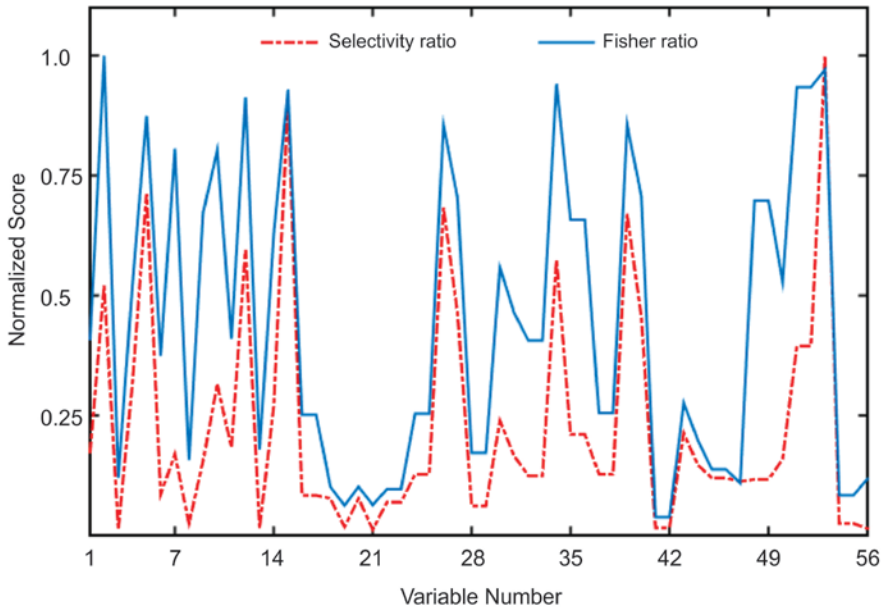

Figure 10-1 Fisher (blue solid line) and selectivity (red dashed line) ratio scores for 56 descriptors.

The variables selected according to *F*-ratio scores consist of those retained in the backward elimination step (red stars) and those added in the forward selection step (blue circles) (Figure 10-2). Some high-ranked variables were eliminated while some low-ranked ones were added, indicating that high *F*-ratios only suggest but do not guarantee their potential importance to the intended classification model. After backward elimination and forward selection, 31 out of 56 variables were retained. These variables were selected on a training set of data. The initially high-ranked variables that were removed through backward elimination were average Martynov-Bastanov or Mulliken electronegativities, Pauling electronegativities (and expressions derived from them), interatomic distances, and differences of Zunger radii sums (r_S+r_P). Conversely, the initially low-ranked variables that were included through forward selection were average numbers of valence electrons and Zunger radii sums (and some expressions derived from them).

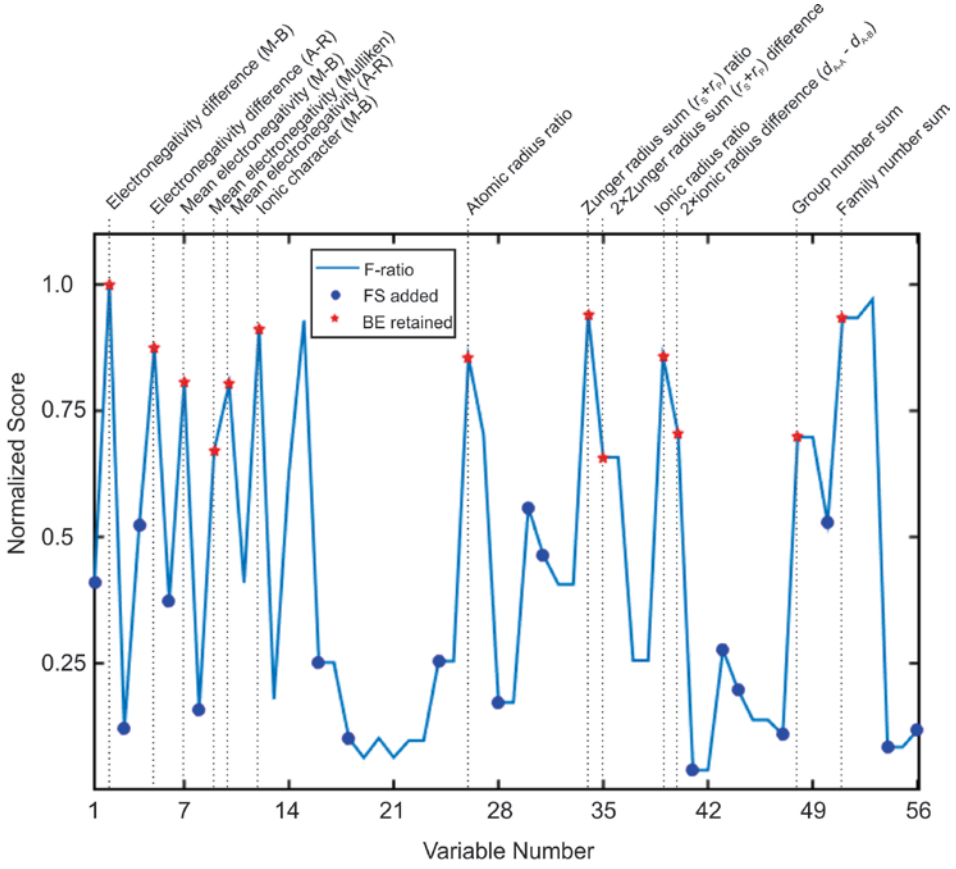

1. ●Electronegativity difference (Pauling scale)	13. Ionic character (Gordy scale)	37. Ionic radius sum (d_{A-B})
2. ★Electronegativity difference (Martynov-Batsanov scale)	14. Ionic character (Mulliken scale)	38. Mean ionic radius
3. ●Electronegativity difference (Gordy scale)	15. Ionic character (Allred-Rochow scale)	39. ★Ionic radius ratio
4. ●Electronegativity difference (Mulliken scale)	16. ●Sum of valence electrons	40. ★2×ionic radius difference (d_{A-A} - d_{A-B})
5. ★Electronegativity difference (Allred-Rochow scale)	17. Mean number of electrons	41. ●Crystal radius sum (d_{A-B})
6. ●Mean electronegativity (Pauling scale)	18. ●Atomic number sum	42. Mean crystal radius
7. ★Mean electronegativity (Martynov-Batsanov scale)	19. Atomic number difference	43. ●Crystal radius ratio
8. ●Mean electronegativity (Gordy scale)	20. Mean atomic number	44. ●2×crystal radius difference (d_{A-A} - d_{A-B})
9. ★Mean electronegativity (Mulliken scale)	21. Atomic weight difference	45. Period number sum
10. ★Mean electronegativity (Allred-Rochow scale)	22. Mean atomic weight	46. Mean period number
11. Ionic character (Pauling scale)	23. Atomic weight sum	47. ●Period number difference
12. ★Ionic character (Martynov-Batsanov scale)	24. ●Atomic radius sum (d_{A-B})	48. ★Group number sum
	25. Mean atomic radius	49. Mean group number
	26. ★Atomic radius ratio	50. ●Group number difference
	27. 2×atomic radius difference (d_{A-A} - d_{A-B})	51. ★Family number sum
	28. ●Covalent radius sum (d_{A-B})	52. Mean Family number
	29. Mean covalent radius	53. Family number difference
	30. ●Covalent radius ratio	54. ●Quantum number (l) sum
	31. ●2×covalent radius difference (d_{A-A} - d_{A-B})	55. Mean quantum number (l) mean
	32. Zunger radius sum (r_S+r_P) sum	56. ●Quantum number (l) difference
	33. Mean Zunger radius sum (r_S+r_P)	
	34. ★Zunger radius sum (r_S+r_P) ratio	
	35. ★2×Zunger radius sum (r_S+r_P) difference	
	36. Zunger radius sum (r_S+r_P) difference	

Figure 10-2 Fisher ratio scores for all variables (listed in the table) selected during backward elimination (red stars) and forward selection (blue circles).

10.3.2 PLS-DA prediction

To predict the structure type that a compound is likely to adopt, PLS-DA is applied as a classification technique. Plots of the scores of PLS-DA, namely the latent values, provide information about the underlying patterns in the data; that is, they serve as structure maps in which compounds with similar properties are projected close to each other in latent values score spaces. This guidance can be very valuable in cases where the experimental synthesis is high-risk (e.g. with radioactive elements like Tc) or expensive (e.g. with precious metals like Rh). As a test, we arbitrarily chose a hypothetical compound RhCd, which has not been previously reported and for which no phase diagram investigations (in the Rh–Cd system) have been conducted. This compound is located (at the point marked by the black hexagram in Figure 10-3a) within the prediction probability of the PLS-DA model for the CsCl-type structure. Samples lying within the confidence ellipse of the model indicate that they can be predicted with a higher degree of confidence. However, this point also falls at the peripheries of the predicted probabilities of CuAu- and NiAs-type structures, which overlap slightly with CsCl-type structures. Note that the CuAu-type structure is essentially a tetragonally distorted version of the cubic CsCl-type structure with the inequivalent *a*- and *c*-parameters being only slightly different. It is not surprising that these two structure types are difficult to distinguish experimentally (as they have similar X-ray diffraction patterns) and theoretically.

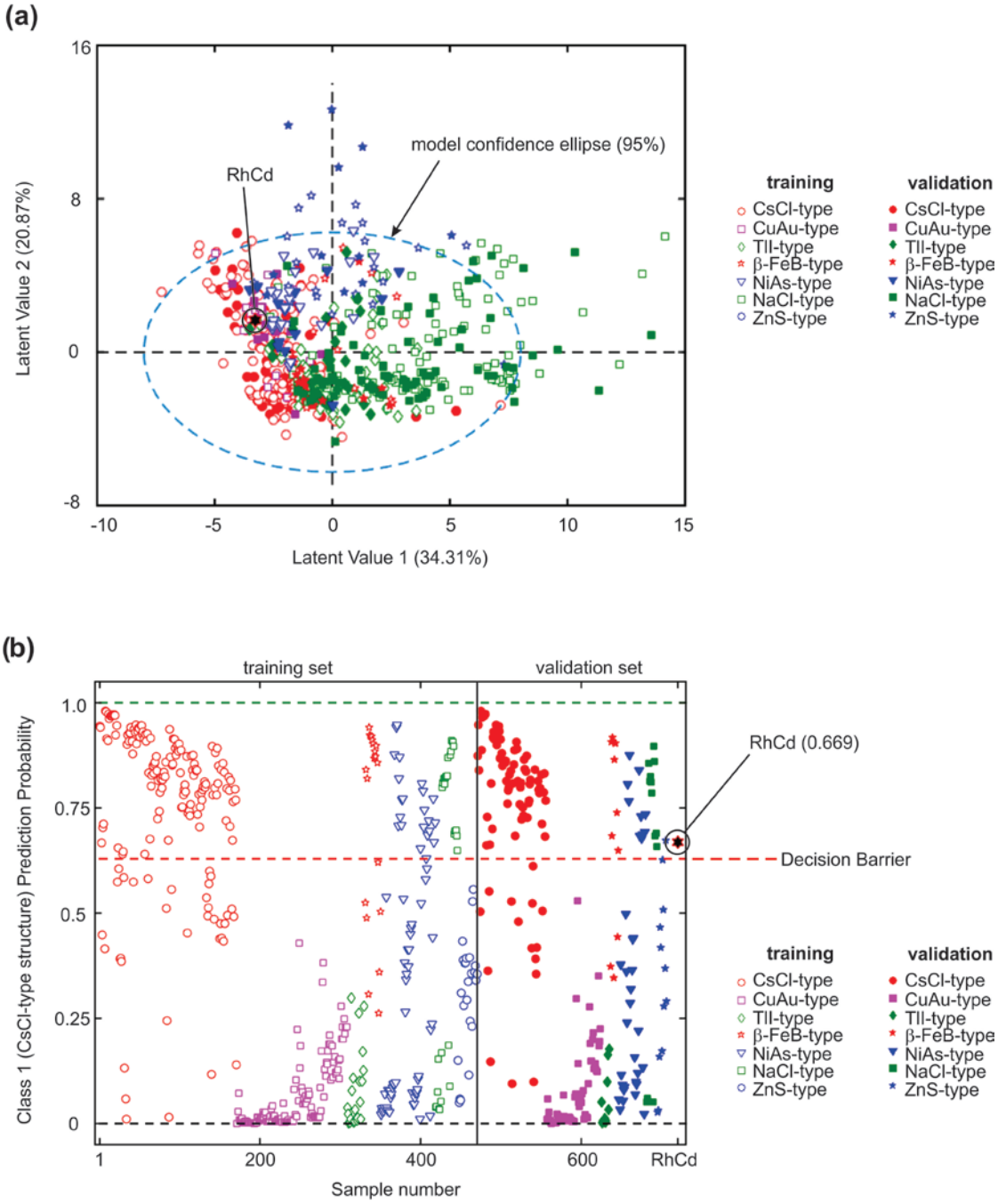

Figure 10-3 (a) Latent value scores for AB compounds and (b) predicted probability for CsCl-type structures for PLS-DA models using 31 selected features.

The results can also be visualized as plots of the sample number on the abscissa and the prediction probability on the ordinate, as shown for the CsCl-type structure using the variables selected (Figure 10-3b). The probability should be close to unity for samples predicted to belong to a given class and close to zero for all other samples. The PLS-DA model predicted the training set data with sensitivity of 95.91% and specificity of 66.56%. Although the model predicts the CsCl-type structure largely correctly, the false positive rate is very high and the overall model accuracy was 77.23%. When the model was applied to the validation set (containing 236 data), the sensitivity was 96.51%, the specificity was 66.00%, and the accuracy was 77.12%. Even though there seemed to be some improvement in predicting the validation set data, the prediction probability for the test compound RhCd is 0.669. This prediction could be better.

10.3.3 SVM Prediction

We present here for the first time an application of SVM to crystal structure prediction. Using the same training and validation set data as in the PLS-DA model, the SVM classification model was also generated to predict various structure types. The prediction probabilities for the CsCl-type structure were much starker (Figure 10-4). For the training set data, the sensitivity was 100.0%, the specificity was 99.33%, and the accuracy was 99.57%; for the validation set data, the sensitivity was 94.19%, the specificity was 92.67%, and the accuracy was 93.22%. Thus, the model performance was significantly better with SVM than with PLS-DA methods. Prior to feature selection, SVM models generated with all 56 variables gave prediction sensitivity, specificity, and accuracy of 42.69%, 100%, and 79.15%, respectively. When this model was applied to

the validation set, prediction sensitivity, specificity, and accuracy were 44.19%, 98.00%, and 78.39%, respectively. That is, this excellent performance was only possible with judicious feature selection.

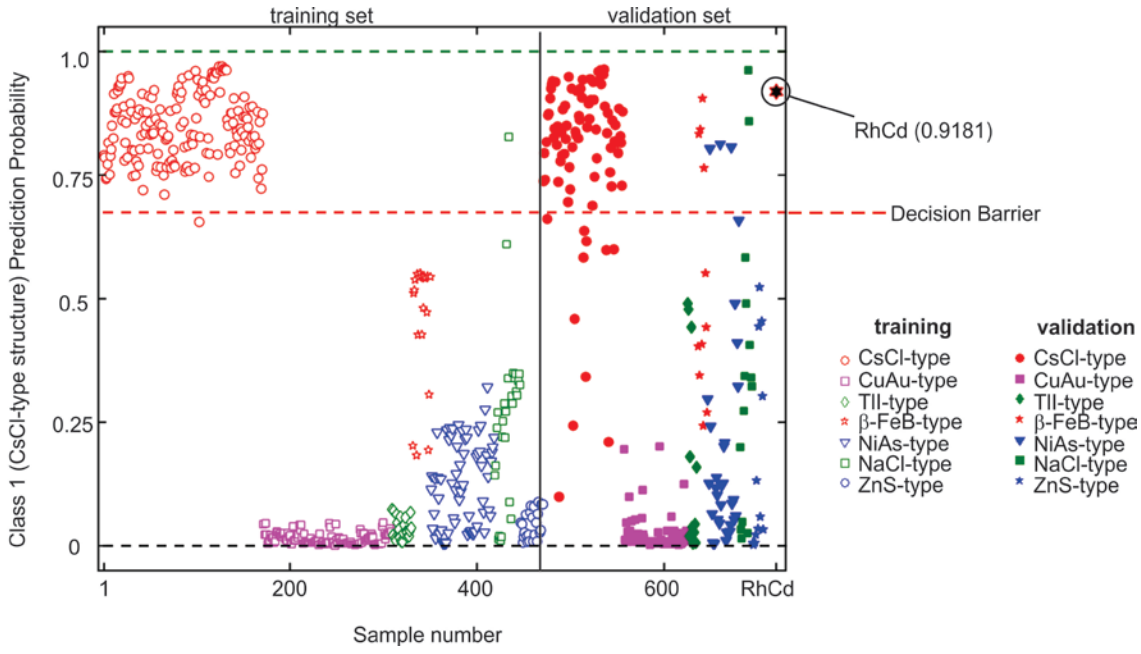

Figure 10-4 Predicted probability for CsCl-type structures for SVM using 31 selected features.

10.3.4 Prediction and experimental verification of RhCd

From the analysis above, 31 out of 56 variables were important for separating CsCl-type structures from others (Figure 10-3a). As has been emphasized in the past, the CsCl-type structure is, notwithstanding the ionic character of the prototype compound CsCl itself, essentially a metallic one adopted by hundreds of intermetallics, exhibiting the highest coordination geometries (cubic, CN8) among AB-type structures. Bond character (as gauged by electronegativity differences) and radius ratios are thus key

factors. Although PCA/PLS-DA has been used elsewhere to classify structures over limited types of compounds,[43] its application to the broader set of data here was not as successful. For hypothetical RhCd, the prediction that it adopts the CsCl-type structure was only 0.669 and the overall quality of the PLS-DA model was not great (Figure 10-3b). The SVM model yielded significant improvement in sensitivity, specificity, and accuracy (>92%) after feature selection, and gave a much higher probability of 0.918 of a CsCl-type structure for RhCd (Figure 10-4). Thus, SVM achieves a clearer separation between structure types and gives more definitive predictions.

The synthesis of RhCd was attempted by reaction of the elements at 800 °C. The products were examined by SEM, EDX, and powder XRD (Figure 10-5). Small single crystals, <50 μm in their longest dimension, were obtained. Their average composition is 47(2)% Rh and 53(2)% Cd, in excellent agreement with the formula RhCd. The powder XRD pattern confirms that RhCd adopts the CsCl-type structure. Small amounts of Rh metal (<9%) were found as a byproduct; this is understandable given that Cd metal is volatile and a small amount was found sublimed on the walls of the fused-silica tube. The structure was refined from single-crystal diffraction data. With an assignment of fully occupied Rh at 0, 0, 0 and Cd at ½, ½, ½ in space group $Pm\bar{3}m$, an excellent agreement factor (R_1 = 0.008) was obtained. (Note that because there are only 13 unique reflections and 4 refinable parameters, the data-to-parameter ratio is low.)

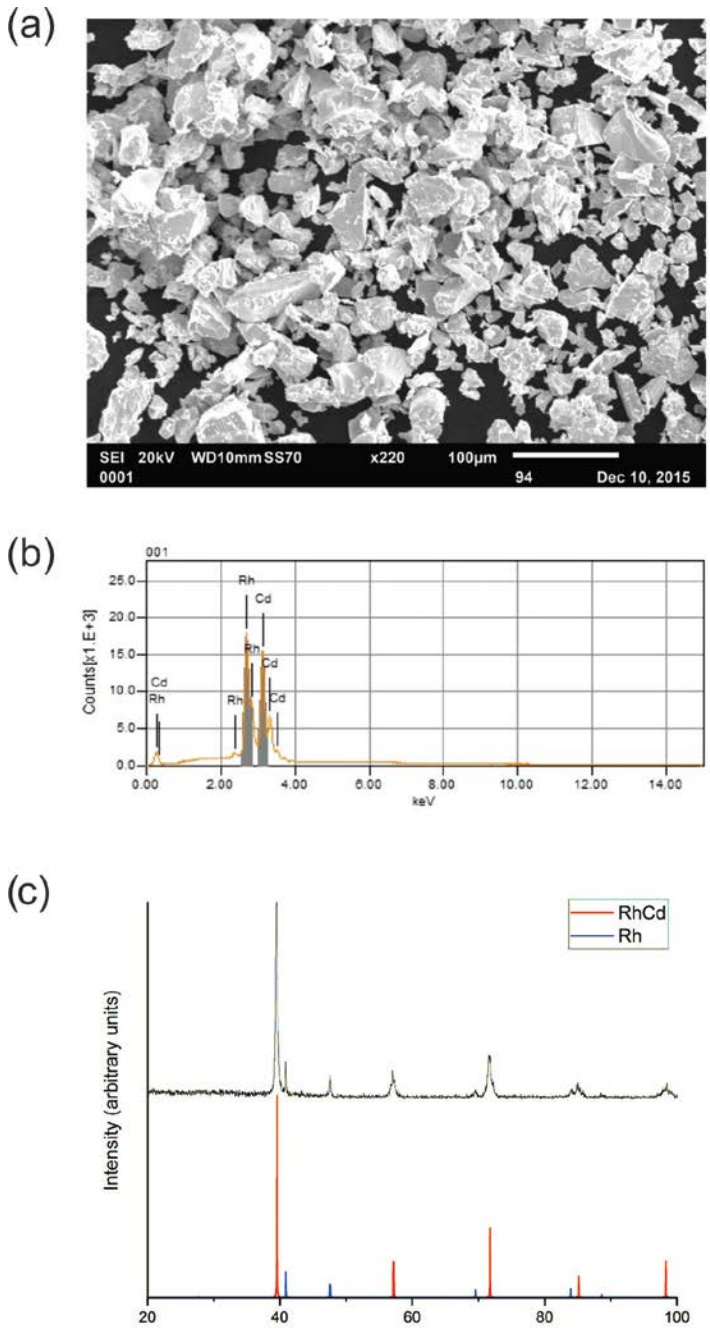

Figure 10-5 New binary compound RhCd. (a) SEM image of crystals, (b) EDX spectrum indicating presence of equal ratios of Rh and Cd in crystals, and (c) powder XRD pattern confirming CsCl-type structure.

10.3.5 Factors Influencing Structures of AB Compounds

It is instructive to compare the variables selected by CR-FS with those used in earlier schemes to derive structure maps of AB compounds. Previously, Villars noted that the most common variables used in such structure maps can be grouped according to pattern of behaviour with position in the periodic table and represented by five prototypical properties: (A) radius, (B) atomic number, (C) atomization energy, (D) electronegativity, and (E) number of valence electrons.[5] Of these, excellent separation of structure types was achieved using expressions involving radius, electronegativity, and number of valence electrons. Because these earlier structure maps were deduced by trial-and-error and chemical intuition, it was not certain if other combinations of properties could give better separation; however, inclusion of additional variables from classes B and C (atomic number, atomization energy) could be ruled out. Our results confirm that cluster resolution is optimized by properties related to radius and electronegativity, which were high-ranked variables, and by number of valence electrons, which was, surprisingly, a low-ranked variable.

Of course, there are many scales of radii and electronegativities,[2,32-37] and different ways of expressing number of valence electrons. In structure maps, an arbitrary decision had to be made in selecting one of these scales, based on the subset of AB compounds being examined. In CR-FS, the selection of these scales is performed in an unbiased manner. It may appear that introducing too many different scales conveying similar information worsens the model because many low-ranked variables could be retained. However, as in all statistical methods, some redundancy is desirable to provide

stability in the iterative selection of variables; thus variables are eliminated not because they are low-ranked but because they contribute to model quality.

Among the ~20 different scales that have been developed for electronegativity, 5 were chosen that are appropriate for intermetallics (which constitute the majority of AB compounds, given that the periodic table consists of mostly metals): Pauling,[32] Martynov-Batsanov,[33] Gordy,[34] Mulliken,[35] and Allred-Rochow.[36] Only two – Martynov-Batsanov and Allred-Rochow – survived the model used to optimize cluster resolution, in the form of electronegativity differences ($\Delta\chi$) or ionic character ($f = 1 - e^{-\frac{1}{4}(X_A - X_B)^2}$, where X_A and X_B electronegativities of A and B atoms). It is interesting that the Pauling scale, which is the most familiar and widely used among chemists, is simply not as effective. The Allred-Rochow scale relates the attraction of valence electrons in an atom to electrostatic force, evaluated from effective nuclear charge (estimated using Slater's rules) and covalent radius (obtained experimentally); it differs from the Pauling scale largely with respect to the precious metals, which have corrected values that are not the same as in sulfur and phosphorus. The Martynov-Batsanov scale is evaluated from average ionization energies of valence electrons; because it was specifically developed for crystalline inorganic substances, it is reassuring that it works well to separate structure types of AB compounds, as was also concluded by Villars.[5]

The size variables selected by CR-FS were a combination of atomic, covalent, and ionic radii, reflecting a compromise to capture the diversity of bonding in AB compounds. However, we also considered Zunger pseudopotential radii.[44] In this scale,

orbital radii are obtained by quantum calculations within a pseudopotential (Simons-Bloch) in which core electrons are frozen. For an atom A, the radii sum $(r_s + r_p)^a$ is defined. Although the difference of Zunger radii sums, $(r_s + r_p)^a - (r_s + r_p)^B$, was chosen by Villars as a coordinate in his structure map,[5] it did not survive in the model optimization. Instead, the sum of Zunger radii sums, $(r_s + r_p)^a + (r_s + r_p)^B$, was a high-ranked variable that was effective for cluster resolution.

Electron count is an important factor for normal valence compounds following the octet rule.[45] Thus, the total number of valence electrons, ΣVE_{AB}, was a third coordinate in Villars' structure map.[5] In our study, the average number of valence electrons, $\overline{VE}_{AB}$, was an initially low-ranked variable selected in model optimization. These two expressions convey similar information originating from position of elements in the periodic table, but the average is more effective in separating structure types for compounds formed from disparate vs closely related elements. To expand on this idea, we introduced a family number that classifies elements into: (1) alkali metals, (2) alkaline-earth metals, (3) f-block metals, (4) d-block metals, (5) p-block metals, (6) p-block metalloids, (7) p-block nonmetals, (8) chalcogens, and (9) noble gases. This classification is not the same as group number (1–18 or IA–VIIIA/IB–VIIIB), but it reflects better the drastic differences in chemical behaviour in the p-block in which elements in the same group can form quite different compounds and structures. (The concept is comparable to that of Mendeleev numbers, which are sequential integers assigned to each element so that those of similar chemical properties are grouped close together.) As expected, variables based on this family number make a significant contribution to separating structure types.

10.4 Conclusions

Crystallographic prediction models were built from partial least-squares discriminant analysis (PLS-DA) and, for the first time, support vector machine (SVM) techniques for the seven most populated structures of AB compounds: CsCl, NaCl, ZnS, CuAu, TlI, β-FeB, NiAs. Cluster resolution feature selection was applied in which variables were chosen in an unbiased manner by a forward selection/backward elimination algorithm; previously identified important variables in earlier structure maps (a semiclassical approach) were confirmed, and previously overlooked variables were found to improve model quality. For the validation set data, PLS-DA gave sensitivity of 96.51%, specificity of 66.00%, and accuracy of 77.12%, whereas SVM gave sensitivity of 94.19%, specificity of 92.67%, and accuracy of 93.22%, which is a significant improvement. An unknown compound, RhCd, was synthesized and correctly confirmed to adopt a CsCl-type structure, as predicted by PLS-DA (0.669) and more confidently by SVM (0.918). SVM shows promise as a powerful crystallographic predictor, with broader impact to solve the problem of determining what compounds form for an arbitrary combination of elements.

10.5 References

[1] Pauling, L. "*The empirical information made it clear that there was some possible systematization to the interatomic distances and also to other aspects of the crystal structures, and I thought perhaps we had come to the time when we could predict what the structures are without x-ray diffraction patterns.*" in: O'Keeffe, M.; Navrotsky A. (Eds.), Structure and Bonding in Crystals, Volume 1, Academic Press, New York, 1981, pp. 1–12.

[2] Pauling, L. *The Nature of the Chemical Bond*, third ed., Cornell University Press, Ithaca, 1960.

[3] Phillips, J.C. *Helv. Phys. Acta* **1985**, *58*, 209–215.

[4] Pettifor, D. G. *Solid State Commun.* **1984**, *51*, 31–34.

[5] Villars, P. *J. Less-Common Met.* **1983**, *92*, 215–238.

[6] Oganov, A. R.; Lyakhov, A. O.; Valle, M. *Acc. Chem. Res.* **2011**, *44*, 227–237.

[7] Hautier, G.; Fischer, C. C.; Jain, A.; Mueller, T.; Ceder, G. *Chem. Mater.* **2010**, *22,* 3762–3767.

[8] Wold, S. *Chemom. Intell. Lab. Syst.* **1995**, *30*, 109–115.

[9] Otto, M. *Chemometrics: Statistics and Computer Application in Analytical Chemistry*, second ed., Wiley-VCH, New York, 2007.

[10] Johnson, K. J.; Synovec, R. E. *Chemom. Intell. Lab. Syst.* **2002**, *60*, 225–237.

[11] Doble, P.; Sandercock, M.; Du Pasquier, E.; Petocz, P.; Roux, C.; Dawson, M. *Forensic Sci. Int.* **2003**, *132*, 26–39.

[12] Sandercock, P. M. L.; Du Pasquier, E. *Forensic Sci. Int.* **2003**, *134*, 1–10.

[13] Sandercock, P. M. L.; Du Pasquier, E. *Forensic Sci. Int.* **2004**, *140*, 43–59.

[14] Sandercock, P. M. L.; Du Pasquier, E. *Forensic Sci. Int.* **2004**, *140*, 71–77.

[15] Sinkov, N. A.; Harynuk, J. J. *Talanta* **2011**, *83*, 1079–1087.

[16] Li, X.; Xu, Z.; Lu, X.; Yang, X.; Yin, P.; Kong, H.; Yu, Y.; Xu, G. *Anal. Chim. Acta* **2009**, *633*, 257–262.

[17] Beckstrom, A. C.; Humston, E. M.; Snyder, L. R.; Synovec, R. E.; Juul, S. E. *J. Chromatogr. A* **2011**, *1218*, 1899–1906.

[18] P. Villars, K. Cenzual, Pearson's Crystal Data – Crystal Structure Database for Inorganic Compounds (on DVD), Release 2015/16, ASM International, Materials Park, Ohio, USA.

[19] Villars, P.; Okamoto, H.; Cenzual K. (Eds.), *ASM Alloy Phase Diagrams Database,* ASM International, Materials Park, OH, 2016 (http://www.asminternational.org).

[20] Srinivasan, S.; Rajan, K. *Materials* **2013**, *6*, 279–290.

[21] Petterson, F.; Suh, C.; Saxén, H.; Rajan, K.; Chakraborti, N. *Mater. Manuf. Processes* **2008**, *24*, 2–9.

[22] Lach-hab, M.; Yang, S.; Vaisman, I. I.; Blaisten-Barojas, E. *Mol. Inf.* **2010**, *29*, 297–301.

[23] Rajan, K. *Mater. Today* **2005**, *8*, 38–45.

[24] Broderick, S.; Rajan, K. Sci. Technol. *Adv. Mater.* **2015**, *16*, 013501-1–013501-8.

[25] Barker, M.; Rayens, W. *J. Chemom.* **2003**, *17*, 166–173.

[26] Boser, B. E.; Guyon, I. M.; Vapnik, V. N. *A training algorithm for optimal margin classifiers, Proceedings of the Fifth Annual ACM Workshop on Computational Learning Theory* **1992**, 144–152.

[27] Guyon, I.; Elisseeff, A. *J. Mach. Learn. Res.* **2003**, *3*, 1157–1182.

[28] Rajalahti, T.; Arneberg, R.; Kroksveen, A. C.; Berle, M.; Myhr, K.-M.; Kvalheim, O. M. *Anal. Chem.* **2009**, *81*, 2581–2590.

[29] Sinkov, N. A.; Johnston, B. M.; Sandercock, P. M. L.; Harynuk, J. *J. Anal. Chim. Acta* **2011**, *697*, 8–15.

[30] Gross, N.; Kotzyba, G.; Künnen, B.; Jeitschko, W. *Z. Anorg. Allg. Chem* **2001**, *627*, 155–163.

[31] Scifinder, 2015, Chemical Abstracts Service, Columbus, OH, 2015.

[32] Pauling, L. *J. Am. Chem. Soc.* **1932**, *54*, 3570–3582.

[33] Martynov, A. I.; Batsanov, S. S. *Zh. Neorg. Khim.* **1980**, *5*, 3171–3175.

[34] Ghosh, D. C.; Chakraborty, T. *J. Mol. Struct.: THEOCHEM* **2009**, *906*, 87–93.

[35] Mulliken, R. S. *J. Chem. Phys.* **1934**, *2*, 782–784.

[36] Allred, A. L.; Rochow, E. G. *J. Inorg. Nucl. Chem.* **1958**, *5*, 264–268.

[37] Emsley, J. *Nature's Building Blocks: An A-Z Guide to the Elements*, Oxford University Press, New York, 2011.

[38] Lin, C.; Weng, R. C. *Simple probabilistic predictions for support vector regression*, National Taiwan University, Taipei, 2004.

[39] Sheldrick, G. M. *SHELXTL*, version 6.12; Bruker AXS Inc.: Madison, WI, 2001.

[40] Sinkov, N. A.; Harynuk, J. J. *Talanta* **2013**, *103*, 252–259.

[41] Sinkov, N. A.; Sandercock, P. M. L.; Harynuk, J. *J. Forensic Sci. Int.* **2014**, *235*, 24–31.

[42] Adutwum, L. A.; Harynuk, J. *J. Anal. Chem.* **2014**, *86*, 7726–7733.

[43] Suh, C.; Rajan, K. *Mater. Sci. Technol.* **2009**, *25*, 466–471.

[44] O'Keeffe, M.; Navrotsky, A. *Structure and Bonding in Crystals*, Volume 1, Academic Press, New York, 1981.

[45] Abegg, R. *Z. Anorg. Allg. Chem.* **1904**, *39*, 330–380.

Chapter 11

Conclusions

11.1 Ternary germanides

Prior to this work, the most well studied *RE*–*M*–Ge systems were mainly focused on *M* = first-row transition metals, especially Fe, Co, Ni; systems containing *M* = early transition metal or 2nd and 3rd row transition metals were believed to contain not very many phases or to exhibit interesting properties. (Perhaps the prohibitive costs of elements like the precious metals may have also deterred research in these systems.) New results have now been obtained on *RE*–(Mn, Ru, Ir)–Ge systems, where previously only a few isolated phases were known and phase diagrams were incomplete, as described in chapters 2 and 3, in which $RE_3M_2Ge_3$ compounds were characterized. These compounds adopt the $Hf_3Ni_2Si_3$-type structure, in which Ge-centred trigonal prisms continue to serve as a common structural motif in germanides. Band structure calculations confirm that *M*–Ge interactions are the strongest in the structure. The relative complexity of the $Hf_3Ni_2Si_3$-type structure, which contains a combination of CrB- and $ThCr_2Si_2$-type building blocks, gives rise to many possible magnetic exchange interactions which may explain the unusual magnetic properties (field dependent and spin reorientation transitions) exhibited by some members of $RE_3M_2Ge_3$. These compounds show metallic behaviour for most *RE* members but interestingly $Y_3Ru_2Ge_3$ shows semiconducting behaviour. In fact, $Y_3Ru_2Ge_3$ shows quite low thermal conductivity (from 13 to 2 W m^{-1} K^{-1} in the range from 20 to 600 °C), unusual for an intermetallic compound, and may be a promising thermoelectric material to be further characterized.

Chapter 4 illustrates a rewarding outcome of exploratory synthesis, in which a phase with hypothetical composition RE_2MnGe_2 was proposed as a simple substitutional target given the existence of RE_2CoGe_2. Instead, a phase with slightly different composition $RE_{2.1}MnGe_{2.2}$ was obtained with an entirely new structure type. It exhibits static disorder in which single Ge atoms and Ge–Ge dumbbells are randomly distributed within a tunnel. Furthermore, $La_{2.1}MnGe_{2.2}$ appears to be a ferromagnetic with a transition temperature above 300 K; this is an unexpected finding given that none of the component elements are ferromagnetic themselves, but may result from complex interactions between d and f orbitals which need to be investigated in more detail.

The results up to this stage suggest that *RE*–Mn–Ge systems cannot be extrapolated simply from other *RE*–*M*–Ge systems, where *M* = Fe, Co, Ni. Therefore, a systematic study of their phase diagrams is warranted. Although sometimes pooh-poohed as old-fashioned and unsophisticated, phase diagram investigations are extremely thorough in establishing the existence of all possible thermodynamically stable compounds under specified conditions; if done carefully, no compounds will be missed except possibly for metastable ones. Unfortunately, few have the stamina, patience, and fortitude to carry out these studies these days. The Ce–Mn–Ge phase diagram was constructed at 800 °C and confirmed the existence of $Ce_3Mn_2Ge_3$ and $Ce_{2.1}MnGe_{2.2}$ as new ternary phases (in addition to the three previously known ones, $CeMn_2Ge_2$, CeMnGe, and Ce_2MnGe_6) and no other ones at this temperature. Probably other *RE*–*M*–Ge systems where *M* is an early transition metal (Ti, V, Cr) will show differences and deserved to be investigated.

11.2 Quaternary germanides

More complex structures can be expected if an additional element is introduced to form quaternary germanides, allowing greater control of properties. The p-block metalloid In was chosen as a fourth component because it is not likely to be disordered with Ge atoms and can be easily distinguished by different X-ray scattering factors. As a prelude to this study, the Ce–Mn–In–Ge phase diagram was surveyed for potential new compounds through the phase investigations described above. Two new quaternary phases, $Ce_4Mn_2InGe_4$ and $Ce_2Mn_2InGe_2$, were identified in chapter 5.

The further development of the substitutional chemistry of $Ce_4Mn_2InGe_4$ led to extension of many $RE_4M_2InGe_4$ series, as described in chapters 6 and 7. The *M* component is extremely diverse, encompassing not only Mn, but also all Fe triad elements, resulating in almost a hundred new compounds when *RE* substitutions are also considered. Again, the Ge-centred trigonal prisms figure as a prominent and recurring structural motif. These trigonal prisms can be used as an organizing principle to derive new structures or to relate to existing ones (e.g., $Tb_4RhInGe_4$), but no bonding information is implied in this approach. Alternatively, it is possible to focus on the *M*–Ge bonds, which are the strongest in the network and can be combined in various ways. The structural motif is now an infinite *M*Ge ladder; adjacent ladders are then connected by a Ge_n bridge (Figure 11-1). The number of Ge atoms, *n*, in the Ge_n bridge determines the symmetry of the structure. If n is odd, the *M*Ge ladders are related by reflection and the space group is orthorhombic; if n is even, they are related by twofold rotation and the space group is monoclinic. Thus there is a relationship between composition and structure, which evolves in two directions within the diagram. Proceeding along the line

towards *M*-poor compositions corresponds to longer Ge_n bridges, whereas proceeding along the line towards *RE*-poor compositions corresponds to condensing the *M*Ge ladders into wider sheets. Chapter 8 illustrates this idea to target and successfully prepare Dy_3RuGe_3, which adopts the Sc_3NiSi_3-type structure containing *M*Ge ladders connected by Ge_4 bridges, as a material with predicted low thermal conductivity.

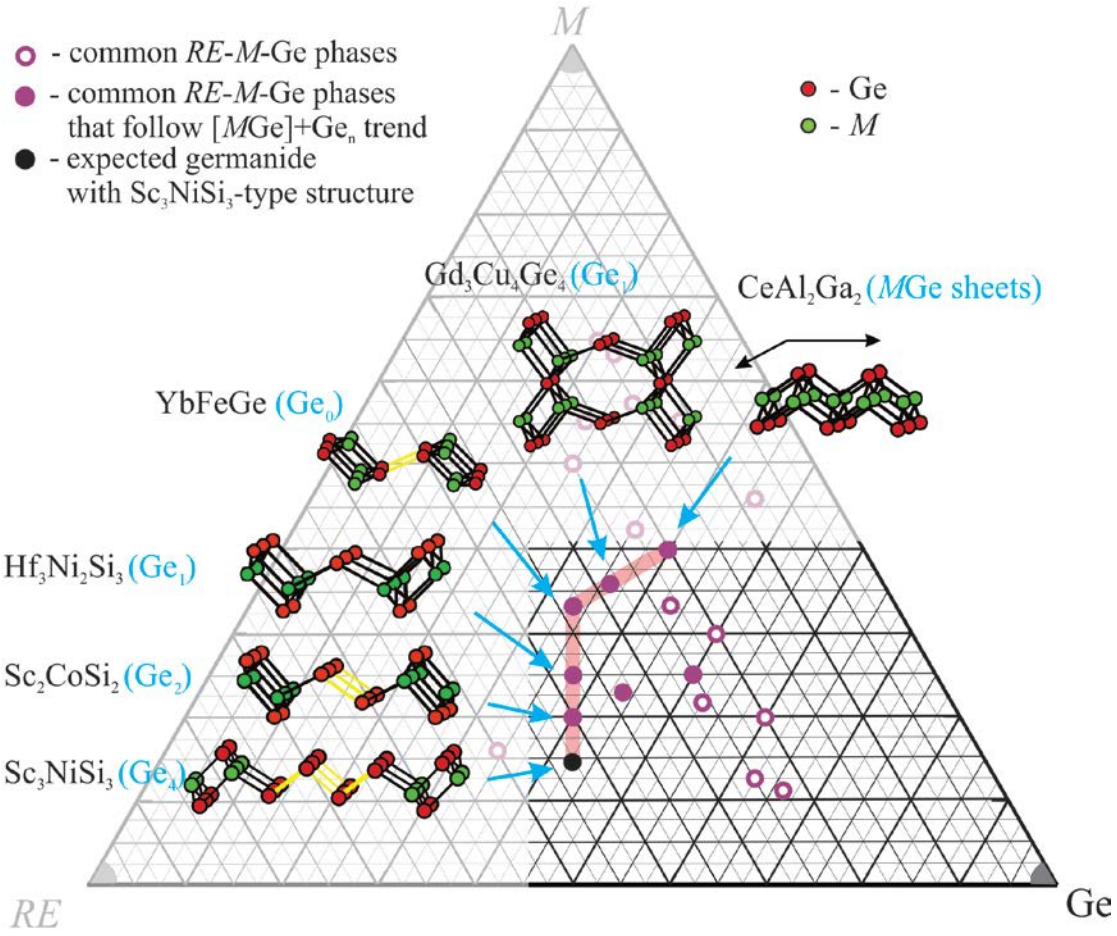

Figure 11-1 *RE*–*M*–Ge compostition diagram with common phases that follow *M*Ge + Ge_n trend.

11.3 Machine-learning approaches

Intermetallics, and germanides in particular, have not been generally identified in the past as good thermoelectric materials because their metallic nature results in low Seebeck coefficient, high thermal conductivity and zero band gap, which are undesirable features for this application. However, through a machine-learning algorithm, some germanides including many of the ones discovered here, were identified as counterintuitive candidates for thermoelectric materials. After four key thermoelectric properties (Seebeck coefficient, electrical conductivity, thermal conductivity, and band gap) were predicted, the $RE_3Ru_2Ge_3$ series was evaluated experimentally. Although most members of this series showed metallic behaviour and inadequately low thermal conductivity, $Y_3Ru_2Ge_3$ appeared to be promising because it showed semiconducting behaviour and remarkably low thermal conductivity. Thus, with no structural information, this machine-learning tool was helpful in identifying potential new thermoelectric materials designed in a non-intuitive way.

Chapters 9 and 10 extend the application of machine learning to other classes of materials beyond germanides, to test the generality of this approach and to evaluate novel algorithms (random forest algorithm, principal component analysis, support vector machine) rarely or never previously applied in materials science. First, the longstanding problem of predicting the structures of simple binary compounds *AB* is one that appears frequently in textbooks, which give the wrong impression of being solved. SVM was applied for the first time in crystallography to search for new *AB* compounds and to predict their structures. A key data preparation step is judicial selection of variables (by cluster resolution feature selection) which improves the accuracy of structure prediction

to an impressive level (93%) (Figure 11-2). Second, predicting the structures of a well known class of compounds – Heusler and inverse-Heusler phases – would have important and practical impact given their many applications. A random forest algorithm was successful in distinguishing between these two closely related structures, identifying questionable entries in databases, and predicting structures of new candidates. In both problems, these predictions were experimentally validated.

Table 11-1 SVM prediction model for *AB* compounds

Model	Sensitivity	Specificity	Accuracy
SVM (no CR-FS)	44.19%	98.00%	78.39%
SVM (with CR-FS)	94.19%	92.67%	93.22%

11.5 Future work

Although some of incomplete knowledge of germanide chemistry has now been rectified by the work in this thesis, more remains to be done. First, some *RE*–*M*–Ge ternary phase diagrams remain uninvestigated, especially those with *M* = precious metals; and even if the composition is reported, the structure could be undetermined (9 phases in Ce–Ru–Ge). Second, because some phases such as $RE_3Ru_2Ge_3$ exhibit low thermal conductivity and $Y_3Ru_2Ge_3$ shows semiconducting behaviour, it is worthwhile to measure properties of these and related compounds in more detail. Third, quaternary *RE*–*M*–In–Ge systems, and $RE_4M_2InGe_4$ series in particular, are compostitionally diverse, forming compounds with various *RE* and *M* metals. Because introduction of In metal led to formation of complex bonding networks, further substitution (e.g., with Cd or Ag) may result in equally interesting coordination by Ge_4 square units and likely a change in physical properties.

A really exciting direction of my research is further development of crystal structure predictors based on elemental properties and *a priori* data, which must be complemented by experimental validation. The ultimate goal is a prediction and visualization tool for all binary and ternary intermetallic systems. This tool could also be used to identify missing entries in crystallographic databases and to carry out data sanitizing (to weed out unreliable data). Such a prediction engine can offer recommendations to support a risky project or lead to truly revolutionary discoveries. Despite the fact that the structural study is my main goal, I would also want to implement the machine-learning approach to predict properties; for example, I am interested in discovering novel superhard materials via machine recommendations.

During my PhD program, I had a chance to study many areas in solid state science which include traditional structural approach towards new promising germanides and the cutting edge machine-learning techniques, the methods that determine how novel materials search will look like in a coming decade. Significant contributions in chemistry described in this thesis include the discovery of over three hundred new compounds, developing structural understanding of a promising class of germanide phases, measuring diverse physical properties, and proposing novel methods for material search.

Bibliography

[1] Chatterjee, B. *Diverse Topics in Science and Technology*, AuthorHouse UK, 2013.
[2] Sauthoff, G. *Intermetallics*, VCH, Wienheim, 1995.
[3] Bardeen, J.; Brattain, W. H. *Phys. Rev.* **1948**, *74*, 230–231.
[4] Qin, G.; Yuan, H.; Qin, Y.; Seo, J.; Wang, Y.; Ma, J.; Ma, Z. *IEEE Elec. Dev. Lett.* **2013**, *34*, 160–162.
[5] Kong, H.; Shi, X.; Uher, C.; Morelli; D.T. *J. Appl. Phys.* **2007**, *102*, 023702-1–023702-5.
[6] Strydom, A. M. *J. Phys.: Condens. Matter* **2007**, *19*, 386205-1–386205-15.
[7] Tegus, O.; Duong, N. P.; Dagula, W.; Zhang, L.; Brück, E.; Buschow, K. H. J.; de Boer, F. R. *J. Appl. Phys.* **2002**, *91*, 8528–8530.
[8] Venturini, G.; Méot-Meyer, M.; Marêché, J. F.; Malaman, B.; Roques B. *Mater. Res. Bull.* **1986**, *21*, 33–39.
[9] Singh, Y.; Ramakrishnan, S. *Phys. Rev. B* **2004**, *69*, 174423-1–174423-13.
[10] Kingery, W. D.; Bowen, H. K.; Ulmann, D. R. *Introduction to Ceramics*, 2nd ed., John Wiley & Sons, Academic Press, 1976.
[11] Yu, K.-O. *Modeling for Casting & Solidification Processing*, CRC, 2001.
[12] Canfield, P. C.; Fisk, Z. *Philos. Mag. B* **1992**, *65*, 1117–1123.
[13] Ferreira, S. O. *Advanced Topics on Crystal Growth*, InTech, 2013.
[14] Rudnev, V. *Handbook of Induction Heating*, CRC, 2003.
[15] Massa, W. *Crystal Structure Determination*, 2nd ed., Springer–Verlag: Berlin, 2004.
[16] West, A. R. *Basic Solid State Chemistry*, 2nd ed., Wiley: New York, 1999.
[17] Eckert, M. *Ann. Phys.* **2012**, *524*, A83–A85.
[18] Bragg, W. H.; Bragg W. L. *Proc. R. Soc. Lond. A* **1913**, *88*, 428–438.
[19] Rietveld, H. M. *J. Appl. Crystallogr.* **1969**, *2*, 65–71
[20] Akselrud, L. G.; Zavalii, P. Yu.; Grin, Yu. N.; Pecharski, V. K.; Baumgartner, B.; Wölfel, E. *Mater. Sci. Forum* **1993**, *133-136*, 335-342.
[21] Gibbs, J. W. *Scientific Papers*, Dover, New York, 1961.
[22] Russ, J. C. *Fundamentals of energy dispersive X-ray analysis*, Butterworth: London, 1984.
[23] Dronskowski, R. *Computational Chemistry of Solid State Materials*, Wiley-VCH, Weinheim, 2005.
[24] Tank, R.; Jepsen, O.; Burkhardt, A.; Andersen, O. K. *TB-LMTO-ASA Program*, version 4.7, Max Plank Institut für Festkörperforschung, Stuttgart, Germany, 1998.
[25] Dronskowski, R.; Blöchl, P. E. *J. Phys. Chem.* **1993**, *97*, 8617–8624.
[26] Vozar, L.; Hohenauer, W. *High Temp. – High Pressures* **2003**, *35*, 253–264.
[27] Parker, W. J.; Jenkins, R. J.; Butler, C. P.; Abbott, G. L. *J. Appl. Phys.* **1962**, *32*, 1679–1684.
[28] Cowan, R. D. *J. Appl. Phys.* **1962**, *34*, 926–927.

[29] Cape, J. A.; Lehman, G. W. *J. Appl. Phys.* **1963**, *34*, 1909–1913.
[30] Martin, D. H. *Magnetism in Solids*, M.I.T. Press, Cambridge, 1967.
[31] Johnson, K. J.; Synovec, R. E. *Chemom. Intell. Lab. Syst.* **2002**, *60*, 225–237.
[32] Doble, P.; Sandercock, M.; Du Pasquier, E.; Petocz, P.; Roux, C.; Dawson, M. *Forensic Sci. Int.* **2003**, *132*, 26–39.
[33] Sandercock, P. M. L.; Du Pasquier, E. *Forensic Sci. Int.* **2003**, *134*, 1–10.
[34] Sandercock, P. M. L.; Du Pasquier, E. *Forensic Sci. Int.* **2004**, *140*, 43–59.
[35] Sandercock, P. M. L.; Du Pasquier, E. *Forensic Sci. Int.* **2004**, *140*, 71–77.
[36] Sinkov, N. A.; Harynuk, J. J. *Talanta* **2011**, *83*, 1079–1087.
[37] Li, X.; Xu, Z.; Lu, X.; Yang, X.; Yin, P.; Kong, H.; Yu, Y.; Xu, G. *Anal. Chim. Acta* **2009**, *633*, 257–262.
[38] Beckstrom, A. C.; Humston, E. M.; Snyder, L. R.; Synovec, R. E.; Juul, S. E. *J. Chromatogr. A* **2011**, *1218*, 1899–1906.
[39] Srinivasan, S.; Rajan, K. *Materials* **2013**, *6*, 279–290.
[40] Petterson, F.; Suh, C.; Saxén, H.; Rajan, K.; Chakraborti, N. *Mater. Manuf. Processes* **2008**, *24*, 2–9.
[41] Lach-hab, M.; Yang, S.; Vaisman, I. I.; Blaisten-Barojas, E. *Mol. Inf.* **2010**, *29*, 297–301.
[42] Rajan, K. *Mater. Today* **2005**, *8*, 38–45.
[43] Broderick, S.; Rajan, K. Sci. Technol. *Adv. Mater.* **2015**, *16*, 013501-1–013501-8.
[44] Gaultois, M. W.; Oliynyk, A. O.; Mar, A.; Sparks, T. D.; Mulholland, G. J.; Meredig, B. *APL Materials*, accepted.
[45] Sparks, T. D.; Gaultois, M. W.; Oliynyk, A. O.; Brgoch, J.; Meredig, B. *Scr. Mater.* **2016**, *111*, 10–15.
[46] Ho, T. K. *IEEE Trans. Pattern Anal. Mach. Intell.* **1998**, *20*, 832–844.
[47] Hastie, T.; Tibshirani, R.; Friedman, J. *The Elements of Statistical Learning*, 2nd ed., Springer, 2008.
[48] Hotelling, H. *J. Educ. Psychol.* **1933**, *24*, 417–441.
[49] Abdi, H.; Williams, L. J. *Wiley Interdiscip. Rev. Comput. Stat.* **2010**, *2*, 433–459
[50] Cortes, C.; Vapnik, V. *Machine Learning* **1995**, *20*, 273–297
[51] Salamakha, P. S.; Sologub, O. L.; Bodak, O. I.; in: Gschneidner Jr., K. A.; Eyring L. (Eds.), *Handbook on the Physics and Chemistry of Rare Earths*, vol. 27, Elsevier, Amsterdam, 1999, pp. 1–223.
[52] Bie, H.; Zelinska, O. Ya.; Tkachuk, A. V.; Mar, A. *Chem. Mater.* **2007**, *19*, 4613–4620.
[53] Bie, H.; Mar, A. J. *Mater. Chem.* **2009**, *19*, 6225–6230.
[54] Bie, H.; Tkachuk, A. V.; Mar, A. *J. Solid State Chem.* **2009**, *182*, 122–128.
[55] Tegus, O.; Duong, N. P.; Dagula, W.; Zhang, L.; Brück, E.; Buschow, K. H. J.; de Boer, F. R. *J. Appl. Phys.* **2002**, *91*, 8528–8530.

[56] Kong, H.; Shi, X.; Uher, C.; Morelli, D. T. *J. Appl. Phys.* **2007**, *102*, 023702-1–023702-5.
[57] Strydom, A. M. *J. Phys.: Condens. Matter* **2007**, *19*, 386205-1–386205-15.
[58] Venturini, G.; Méot-Meyer, M.; Marêché, J. F.; Malaman, B.; Roques, B. *Mater. Res. Bull.* **1986**, *21*, 33–39.
[59] Singh, Y.; Ramakrishnan, S. *Phys. Rev. B* **2004**, *69*, 174423-1–174423-13.
[60] Sologub, O. L.; Prots', Yu. M.; Salamakha, P. S.; Bodak, O. I. *J. Alloys Compd.* **1994**, *209*, 107–109.
[61] Sologub, O. L.; Prots', Yu. M.; Salamakha, P. S.; Bodak, O. I. Stępień-Damm, J. *Pol. J. Chem.* **1995**, *69*, 423–426.
[62] Sologub, O. L.; Hiebl, K.; Rogl, P.; Noël, H. *J. Alloys Compd.* **1996**, *245*, L13–L17.
[63] Salamakha, P.; Sologub, O.; Stępień-Damm, J.; Stash, A. *Kristallografiya* **1996**, *41*, 1135–1136.
[64] Rodewald, U. Ch.; Pöttgen, R. *Solid State Sci.* **2003**, *5*, 487–493.
[65] Boulet, P.; Weitzer, F.; Hiebl, K.; Noël, H. *Physica B* **2000**, *292*, 302–319.
[66] Salamakha, P. S.; Bodak, O. I.; Pecharskii, V. K.; Bel'skii, V. K. *Izv. Akad. Nauk SSSR, Metally* (**1989**) 206–208.
[67] Hovestreydt, E.; Engel, N.; Klepp, K.; Chabot, B.; Parthé, E. *J. Less-Common Met.* **1982**, *85*, 247–274.
[68] Penc, B.; Hofmann, M.; Leciejewicz, J.; Ślaski, M.; Szytuła, A. *J. Alloys Compd.* **1999**, *287*, 18–24.
[69] Sheldrick, G. M. SHELXTL, version 6.12, Bruker AXS Inc., Madison, WI, 2001.
[70] Gelato, L. M.; Parthé, E. *J. Appl. Crystallogr.* **1987**, *20*, 139–143.
[71] Yarmolyuk, Ya. P.; Grin', Yu. N.; Gladyshevskii, E. I. *Kristallografiya* **1977**, *22*, 726–730.
[72] Welter, R.; Ijjalli, I.; Venturini, G.; Malaman, B. *J. Alloys Compd.* **1997**, *257*, 196–200.
[73] Chabot, B.; Engel, N.; Parthé, E. *J. Less-Common Met.* **1984**, *96*, 331–340.
[74] Gladyshevskii, E. I.; Kotur, B. Ya. *Kristallografiya* **1987**, *23*, 946–950.
[75] Zhao, J. T.; Parthé, E. *Acta Crystallogr., Sect. C* **1989**, *45*, 1853–1856.
[76] Paccard, D.; Le Roy, J.; Moreau, J. M. *Acta Crystallogr., Sect. B* **1982**, *38*, 2448–2449.
[77] Markiv, V. Ya.; Beloborodova, E. A.; Belyavina, N. N.; Alekseeva, N. V. *Dopov. Akad. Nauk Ukr.* (**1993**) 70–73.
[78] Bodak, O. I.; Oleksin, O. Ya.; Fedyna, M. F.; Pecharskii, V. K. *Neorg. Mater.* **1992**, *28*, 493–497.
[79] Kotur, B. Ya.; Andrusyak, R. I. *Neorg. Mater.* **1991**, *27*, 1433–1439.
[80] Morozkin, A. V.; Yao, J.; Mozharivskyj, Yu. *Intermetallics* **2012**, *21*, 115–120.
[81] Morozkin, A. V. *Intermetallics* **2012**, *25*, 136–138.

[82] Morozkin, A. V.; Nirmala, R.; Yao, J.; Mozharivskyj, Y.; Isnard, O. *J. Solid State Chem.* **2012**, *196*, 93–99.
[83] Sologub, O. L.; Stash, A.; Zavodnik, V. E.; Salamakha, P. S.; Bodak, O. I. *Coll. Abs. 6th Int. Conf. Crystal Chem. Intermet. Compd.* (Lvov) (**1995**) 96.
[84] Koterlyn, G. M.; Bodak, O. I.; Pavlyuk, V. V.; Stępień-Damm, J.; Pietraszko, A. *J. Alloys Compd.* **1999**, *291*, 110–116.
[85] Pavlyuk, V. V.; Bodak, O. I. *Neorg. Mater.* **1992**, *28*, 1119–1121.
[86] Seo, D.-K.; Corbett, J. D. *J. Am. Chem. Soc.* **2001**, *123*, 4512–4518.
[87] Rhode, M.; Wendorff, M.; Röhr, C. *Z. Anorg. Allg. Chem.* **2006**, *632*, 1195–1205.
[88] Pauling, L. *The Nature of the Chemical Bond*, 3rd ed., Cornell University Press, Ithaca, NY, 1960.
[89] Choe, W.; Miller, G. J.; Levin, E. M. *J. Alloys Compd.* **2001**, *329*, 121–130.
[90] Ghosh, K.; Ramakrishnan, S.; Chandra, G. *Phys. Rev. B* **1993**, *48*, 10435–10439.
[91] Salamakha, P. S.; in: Gschneidner Jr., K. A.; Eyring L. (Eds.), *Handbook on the Physics and Chemistry of Rare Earths*, vol. 27, Elsevier, Amsterdam, 1999, pp. 225–338.
[92] Oliynyk, A. O.; Stoyko, S. S.; Mar, A. *J. Solid State Chem.* **2013**, *202*, 241–249.
[93] Oliynyk, A. O.; Mar, A. *J. Solid State Chem.* **2013**, *206*, 60–65.
[94] Lei, X.-W.; Zhong, G.-H.; Li, M.-J.; Mao, J.-G. *J. Solid State Chem.* **2008**, *181*, 2448–2455.
[95] Grytsiv, A.; Kaczorowski, D.; Rogl, P.; Tran, V.; Godart, C.; Gofryk, K.; Giester, G. *J. Phys.: Condens. Matter* **2005**, *17*, 385–397.
[96] Villars, P.; Cenzual, K. *Pearson's Crystal Data – Crystal Structure Database for Inorganic Compounds*, release 2010/11, ASM International, Materials Park, OH, 2010.
[97] Slater, J. C.; *J. Chem. Phys.* **1964**, *41*, 3199–3205.
[98] Oliynyk, A. O.; Stoyko, S. S.; Mar, A. *Inorg. Chem.* **2013**, *52*, 8264–8271.
[99] Salvador, J. R.; Kanatzidis, M. G. *Inorg. Chem.* **2006**, *45*, 7091–7099.
[100] Attfield, J. P.; Férey, G. *J. Solid State Chem.* **1989**, *80*, 286–298.
[101] Venturini, G.; Welter, R.; Malaman, B. *J. Alloys Compd.* **1992**, *185*, 99–107.
[102] Lefèvre, C.; Venturini, G.; Malaman, B. *J. Alloys Compd.* **2003**, *354*, 47–53.
[103] Rossi, D.; Marazza, R.; Mazzone, D.; Ferro, R. *J. Less-Common Met.* **1978**, *59*, 79–83.
[104] Venturini, G.; Malaman, B.; Roques, B. *J. Solid State Chem.* **1989**, *79*, 136–145.
[105] Morozkin, A. V.; Seropegin, Yu. D.; Gribanov, A. V.; Barakatova, J. M. *J. Alloys Compd.* **1997**, *256*, 175–191.
[106] Welter, R.; Venturini, G.; Ressouche, E.; Malaman, B. *J. Alloys Compd.* **1995**, *228*, 59–74.
[107] Klosek, V.; Vernière, A.; Ouladdiaf, B.; Malaman, B. *J. Magn. Magn. Mater.* **2003**, *256*, 69–92.

[108] François, M.; Venturini, G.; Malaman, B.; Roques, B. *J. Less-Common Met.* **1990**, *160*, 197–213.
[109] Konyk, M. B.; Bodak, O. I. *J. Alloys Compd.* **2005**, *387*, 243–245.
[110] Salamakha, P. S.; Prots', Yu. M.; Sologub, O. L.; Bodak, O. I. *J. Alloys Compd.* **1994**, *215*, 51–54.
[111] Brabers, J. H. V. J.; Duijn, V. H. M.; de Boer, F. R.; Buschow, K. H. J. *J. Alloys Compd.* **1993**, *198*, 127–132.
[112] Chafik El Idrissi, B.; Venturini, G.; Malaman, B.; Ressouche, E. *J. Alloys Compd.* **1994**, *215*, 187–193.
[113] Kelemen, M. T.; Rösch, P.; Dormann, E.; Buschow, K. H. J. *J. Magn. Magn. Mater.* **2001**, *223*, 253–260.
[114] Narasimhan, K. S. V. L.; Rao, V. U. S.; Bergner, R. L.; Wallace, W. E. *J. Appl. Phys.* **1975**, *46*, 4957–4960.
[115] Szytuła, A.; Szott, I. *Solid State Commun.* **1981**, *40*, 199–202.
[116] Kolmakova, N. P.; Sidorenko, A. A.; Levitin, R. Z. *Low Temp. Phys.* (Transl. Fiz. Nizk. Temp. (Kiev)) **2002**, *28*, 653–668.
[117] Bodak, O. I.; Pecharskii, V. K.; Starodub, P. K.; Salamakha, P. S.; Mruz, O. Ya.; Bruskov, V. A. *Izv. Akad. Nauk SSSR, Metally* (**1986**) 214–216.
[118] Gladyshevskii, R. E.; Sologub, O. L.; Parthé, E. *J. Alloys Compd.* **1991**, *176*, 329–335.
[119] Morozkin, A. V.; Seropegin, Yu. D.; Bodak, O. I. *J. Alloys Compd.* **1986**, *234*, 143–150.
[120] Hiebl, K.; Sologub, O. *J. Magn. Magn. Mater.* **1998**, *186*, 56–64.
[121] Salamakha, P. S.; Sologub, O. L. *J. Alloys Compd.* **1999**, *287*, L1–L3.
[122] Pecharskii, V. K.; Bodak, O. I.; Bel'skii, V. K.; Starodub, P. K.; Mokra, I. R.; Gladyshevskii, E. I. *Kristallografiya* **1987**, *32*, 334–338.
[123] Morozkin, A. V.; Seropegin, Yu. D.; Portnoy, V. K.; Sviridov, I. A.; Leonov, A. V. *Mater. Res. Bull.* **1998**, *33*, 903–908.
[124] Salamakha, P.; Sologub, O.; Bocelli, G.; Otani, S.; Takabatake, T. *J. Alloys Compd.* **2001**, *314*, 177–180.
[125] Berke, H. *Angew. Chem. Int. Ed.* **2002**, *41*, 2483–2487.
[126] Sebastian, S. E.; Harrison, N.; Batista, C. D.; Balicas, L.; Jaime, M.; Sharma, P. A.; Kawashima, N.; Fisher, I. R. *Nature (London, U.K.)* **2006,** *441*, 617–620.
[127] Pavlyuk, V. V.; Pecharskii, V. K.; Bodak, O. I.; Bruskov, V. A. *Kristallografiya* **1987**, *32*, 70–73.
[128] Chondroudi, M.; Balasubramanian, M.; Welp, U.; Kwok, W.-K.; Kanatzidis, M. G. *Chem. Mater.* **2007**, *19*, 4769–4775.
[129] Chumalo, N.; Nychyporuk, G. P.; Pavlyuk, V. V.; Pöttgen, R.; Kaczorowski, D.; Zaremba, V. I. *J. Solid State Chem.* **2010**, *183*, 2963–2967.

[130] Dominyuk, N.; Zaremba, V. I.; Pöttgen, R.; Naturforsch. Z. *B: J. Chem. Sci.* **2011**, *66*, 433–436.
[131] Chondroudi, M.; Peter, S. C.; Malliakas, C. D.; Balasubramanian, M.; Li, Q. A.; Kanatzidis, M. G. *Inorg. Chem.* **2011**, *50*, 1184–1193.
[132] Dzevenko, M. V.; Galadzhun, Ya. V.; Zaremba, V. I.; Kalychak, Ya. M. *J. Alloys Compd.* **2005**, *397*, 161–164.
[133] Nychyporuk, G.; Zaremba, V.; Kalychak, Ya. *Visn. L'viv. Univ., Ser. Khim.* 2003, 43, 9–14.
[134] Salamakha, P. *J. Alloys Compd.* **1997**, *225*, 209–220.
[137] Markiv, V. Ya.; Beloborodova, E. A.; Belyavina, N. N.; Alekseeva, N. V. *Dopov. Akad. Nauk Ukr.* **1993**, *7*, 70–73.
[138] Starodub, P. K.; Zapotots'ka, L. M.; Bodak, O. I. *Visn. L'viv. Univ., Ser. Khim.* **1996**, *36*, 57–59.
[139] Konyk, M. B.; Romaka, L. P.; Romaka, V. V.; Serkiz, R. Ya. *Fiz. Khim. Tverd. Tila* **2012**, *13*, 956–962.
[140] Leciejewicz, J.; Szytuła, A.; Baźela, W.; Siek, S. *J. Magn. Magn. Mater.* **1990**, *89*, 29–32.
[141] Welter, R.; Venturini, G.; Ressouche, E.; Malaman, B. *J. Alloys Compd.* **1995**, *218*, 204–215.
[142] Nowik, I.; Levi, Y.; Felner, I.; Bauminger, E. R. *J. Magn. Magn. Mater.* **1995**, *147*, 373–384.
[143] Duraj, R.; Konyk, M.; Przewoźnik, J.; Romaka, L.; Szytuła, A. *Solid State Sci.* **2013**, *25*, 11–14.
[144] Oliynyk, A. O.; Djama-Kayad, K.; Mar, A. *J. Alloys Compd.* **2014**, *602*, 130–134.
[145] Villars, P. (editor-in-chief); Okamoto, H.; Cenzual K. (section editors), *ASM Alloy Phase Diagrams Center* (www1.asminternational.org/asmenterprise/apd), ASM International, Materials Park, OH, 2006.
[146] Arbuckle, J.; Parthé, E. *Acta Crystallogr.* **1962**, *15*, 1205–1207.
[147] Forsyth, J. B.; Brown, P. J. *J. Phys.: Condens. Matter* **1990**, *2*, 2713–2720.
[148] Gladyshevskii, E. I. *Zh. Strukt. Khim.* **1964**, *5*, 568–575.
[149] Salamakha, P. S. In *Handbook on the Physics and Chemistry of Rare Earths*; Gschneidner, K. A., Jr., Eyring, L., Eds.; Elsevier: Amsterdam, 1999; Vol. 27, pp 223–338.
[150] Zaremba, V. I.; Stępień-Damm, A.; Nichiporuk, G. P.; Tyvanchuk, Yu. B.; Kalychak, Ya. M. *Kristallografiya* **1998**, *43*, 13–16.
[151] Zaremba, V. I.; Kaczorowski, D.; Nychyporuk, G. P.; Rodewald, U. Ch.; Pöttgen, R. *Solid State Sci.* **2004**, *6*, 1301–1306.
[152] Zaremba, V. I.; Johrendt, D.; Rodewald, U. Ch.; Nychyporuk, G. P.; Pöttgen, R. *Solid State Sci.* **2005**, *7*, 998–1002.

[153] Tobash, P. H.; Lins, D.; Bobev, S.; Lima, A.; Hundley, M. F.; Thompson, J. D.; Sarrao, J. L. *Chem. Mater.* **2005**, *17*, 5567–5573.
[154] Guloy, A. M.; Corbett, J. D. *Inorg. Chem.* **1996**, *35*, 2616–2622.
[155] Nychyporuk, G.; Zaremba, V.; Kalychak, Ya.; Stępień-Damm, A.; Pietraszko, A. *J. Alloys Compd.* **2000**, *312*, 154–157.
[156] Mao, J.; Guloy, A. M. *J. Alloys Compd.* **2001**, *322*, 135–142.
[157] Mao, J.-G.; Goodey, J.; Guloy, A. M. *Inorg. Chem.* **2002**, *41*, 931–937.
[158] Zaremba, V. I.; Kaczorowski, D.; Nychyporuk, G. P.; Rodewald, U. Ch.; Heying, B.; Pöttgen, R. *Z. Anorg. Allg. Chem.* **2006**, *632*, 975–980.
[159] Kraus, W.; Nolze, G. *J. Appl. Crystallogr.* **1996**, *29*, 301–303.
[160] Akselrud, L. G.; Grin, Yu. N.; Zavalij, P. Yu.; Pecharsky, V. K.; Fundamenskii, V. S. *Abstracts of Papers*, 12th European Crystallographic Meeting, Moscow, USSR, Aug 20–29, 1989.
[161] Solokha, P.; De Negri, S.; Skrobanska, M.; Saccone, A.; Pavlyuk, V.; Proserpio, D. M. *Inorg. Chem.* **2012**, *51*, 207–214.
[162] You, T.-S.; Bobev, S. *J. Solid State Chem.* **2010**, *183*, 1258–1265.
[163] Zandbergen, H. W.; Andersen, S. J.; Jansen, J. *Science* **1997**, *277*, 1221–1225.
[164] Andersen, S. J.; Zandbergen, H. W.; Jansen, J.; Træholt, C.; Tundal, U.; Reiso, O. *Acta Mater.* **1998**, *46*, 3283–3298.
[165] You, T.-S.; Tobash, P. H.; Bobev, S. *Inorg. Chem.* **2010**, *49*, 1773–1783.
[166] Andersen, S. J.; Marioara, C. D.; Frøseth, A.; Vissers, R.; Zandbergen, H. W. *Mater. Sci. Eng., A* **2005**, *390*, 127–138.
[167] van Huis, M. A.; Chen, J. H.; Zandbergen, H. W.; Sluiter, M. H. F. *Acta Mater.* **2006**, *54*, 2945–2955.
[168] van Huis, M. A.; Chen, J. H.; Sluiter, M. H. F.; Zandbergen, H. W. *Acta Mater.* **2007**, *55*, 2183–2199.
[169] Lukachuk, M.; Pöttgen, R. *Z. Kristallogr.* **2003**, *218*, 767–787.
[170] You, T.-S.; Bobev, S. *J. Solid State Chem.* **2010**, *183*, 2895–2902.
[171] Siggelkow, L.; Hlukhyy, V.; Fässler, T. F. *J. Solid State Chem.* **2012**, *191*, 76–89.
[172] Guo, S.-P.; Meyers, J. J.; Tobash, P. H.; Bobev, S. *J. Solid State Chem.* **2012**, *192*, 16–22.
[173] Hoffmann, R.; Zheng, C. *J. Phys. Chem.* **1985**, *89*, 4175–4181.
[174] Johrendt, D.; Felser, C.; Jepsen, O.; Andersen, O. K.; Mewis, A.; Rouxel, J. *J. Solid State Chem.* **1997**, *130*, 254–265.
[175] Mudryk, Y.; Pecharsky, V. K.; Gschneidner, K. A., Jr. *Z. Anorg. Allg. Chem.* **2011**, *637*, 1948–1956.
[176] Rieger, W.; Nowotny, H.; Benesovsky, F. *Monatsh. Chem.* **1964**, *95*, 1502–1503.
[177] Pearson, W. B. *The Crystal Chemistry and Physics of Metals and Alloys*; Wiley: New York, 1972.

[178] Hyde, B. G.; Andersson, S. *Inorganic Crystal Structures*; Wiley: New York, 1989.
[179] You, T.-S.; Jung, Y.; Bobev, S. *Dalton Trans.* **2012**, *41*, 12446–12451.
[180] Allred, A. L. *J. Inorg. Nucl. Chem.* **1961**, *17*, 215–221.
[181] Carrete, J.; Li, W.; Mingo, N.; Wang, S.; Curtarolo, S. *Phys. Rev. X* **2014**, *4*, 011019-1–011019-9.
[182] Meredig, B.; Agrawal, A.; Kirklin, S.; Saal, J.; Doak, J.; Thompson, A.; Zhang, K.; Choudhary, A.; Wolverton, C. *Phys. Rev. B* **2014**, *89*, 094104-1–094104-7.
[183] Meredig, B.; Wolverton, C. *Chem. Mater.* **2014**, *26*, 1985–1991.
[184] Tkachuk, A. V.; Mar, A. *Inorg. Chem.* **2005**, *44*, 2272–2281.
[185] Graf, T.; Felser, C.; Parkin, S. S. *Prog. Solid State Chem.* **2011**, *39*, 1–50.
[186] Gaultois, M. W.; Oliynyk, A. O.; Mar, A.; Sparks, T. D.; Mulholland, G. J.; Meredig, B. *APL Materials*, accepted.
[187] Oliynyk, A. O.; Stoyko, S. S.; Mar, A. *Inorg. Chem.* **2015**, *54*, 2780–2792.
[188] Gaultois, M. W.; Sparks, T. D.; Borg, C. K.; Seshadri, R.; Bonificio, W. D.; Clarke, D. R. *Chem. Mater.* **2013**, *25*, 2911–2920.
[189] Heusler, F.; Stark, W.; Haupt, E. *Verh. Deut. Phys. Ges.* **1903**, *5*, 220–223.
[190] Bradley, A. J.; Rodgers, J. W. *Proc. R. Soc. London, Ser. A* **1934**, *144*, 340–359.
[191] Kübler, J.; Williams, A. R.; Sommers, C. B. *Phys. Rev. B* **1983**, *28*, 1745–1755.
[192] Wurmehl, S.; Kandpal, H. C.; Fecher, G. H.; Felser, C. *J. Phys.: Condens. Matter* **2006**, *18*, 6171–6181.
[193] Ouardi, S.; Fecher, G. H.; Felser, C.; Kübler, J. *Phys. Rev. Lett.* **2013,** *110*, 100401-1–100401-5.
[194] Winterlik, J.; Fecher, G. H.; Felser, C. *Solid State Commun.* **2008**, *145*, 475–478.
[195] Aoki, Y.; Sato, H. R.; Sugawara, H.; Sato, H. *Physica C: Supercond.* **2000**, *333*, 187–194.
[196] Yang, J.; Li, H.; Wu, T.; Zhang, W.; Chen, L.; Yang, J. *Adv. Funct. Mater.* **2008**, *18*, 2880–2888.
[197] Larson, P.; Mahanti, S. D.; Sportouch, S.; Kanatzidis, M. G. *Phys. Rev. B* **1999**, *59*, 15660–15668.
[198] Galanakis, I.; Dederichs, P. H.; Papanikolaou, N. *Phys. Rev. B* **2002**, *66*, 134428-1–134428-10.
[199] Kandpal, H. C.; Fecher, G. H.; Felser, C. *J. Phys. D: Appl. Phys.* **2007**, *40*, 1507–1523.
[200] Ren, J.; Li, H.; Feng, S.; Zhai, Q.; Fu, J.; Luo, Z.; Zheng, H. *Intermetallics* **2015**, *65*, 10–14.
[201] Chadov, S.; Qi, X.; Kübler, J.; Fecher, G. H.; Felser, C.; Zhang, S. C. *Nat. Mater.* **2010**, *9*, 541–545.

[202] Villars, P.; Cenzual, K. Pearson's *Crystal Data – Crystal Structure Database for Inorganic Compounds (on DVD), Release 2015/16*, ASM International, Materials Park, Ohio, USA.
[203] Harang, L. *Z. Kristallogr.* **1927**, *65*, 261–285.
[204] Palmer, A. "*Golf is deceptively simple and endlessly complicated; it satisfies the soul and frustrates the intellect. It is at the same time rewarding and maddening – and it is without a doubt the greatest game mankind has ever invented.*"
[205] Lacroix-Orio, L.; Tillard, M.; Belin, C. *Solid State Sci.* **2004**, *6*, 1429–1437.
[206] U.S. Department of Energy, Grand Challenge #3: How do remarkable properties of matter emerge from complex correlations of the atomic or electronic constituents and how can we control these properites? (http://science.energy.gov/bes/efrc/research/grand-challenges/).
[207] Villars, P.; Okamoto, H.; Cenzual K. (Eds.), *ASM Alloy Phase Diagrams Database,* ASM International, Materials Park, OH, 2016 (http://www.asminternational.org).
[208] Hansen, K.; Biegler, F.; Ramakrishnan, R.; Pronobis, W.; von Lilienfeld, O.A.; Muller, K.-R.; Tkatchenko, A. *J. Phys. Chem. Lett.* **2015**, *6*, 2326–2331.
[209] Curtarolo, S.; Hart, G. L. W.; Nardelli, M. B.; Mingo, N.; Sanvito, S.; Levy, O. *Nat. Mater.* **2013**, *12*, 191–201.
[210] Ghiringhelli, L. M.; Vybiral, J.; Levchenko, S. V.; Draxl, C.; Scheffler, M. *Phys. Rev. Lett.* **2015**, *114*, 105503-1–105503-5.
[211] Breiman, L.; *Machine Learning* **2001**, *45*, 5–32.
[212] Carrete, J.; Li, W.; Mingo, N.; Wang, S.; Curtarolo, S. *Phys. Rev. X* **2014**, *4*, 011019-1–011019-9.
[213] Cape, J. A.; Lehman, G. W. *J. Appl. Phys.* **1963**, *34*, 1909–1913.
[214] Phillips, J. C. *Helv. Phys. Acta* **1985**, *58*, 209–215.
[215] Pettifor, D. G. *Solid State Commun.* **1984**, *51*, 31–34.
[216] Villars, P. *J. Less-Common Met.* **1983**, *92*, 215–238.
[217] Oganov, A. R.; Lyakhov, A. O.; Valle, M. *Acc. Chem. Res.* **2011**, *44*, 227–237.
[218] Hautier, G.; Fischer, C. C.; Jain, A.; Mueller, T.; Ceder, G. *Chem. Mater.* **2010**, *22,* 3762–3767.
[219] Rajan, K. *Mater. Today* **2005**, *8*, 38–45.
[220] Broderick, S.; Rajan, K. Sci. Technol. *Adv. Mater.* **2015**, *16*, 013501-1–013501-8.
[221] Oryshchyn, S. V.; Le Sénéchal, C.; Députier, S.; Bauer, J.; Guérin, R.; Akselrud, L. G. *J. Solid State Chem.* **2001**, *160*, 156–166.
[222] Zelinska, M.; Zhak, O.; Oryshchyn, S.; Polianska, T.; Pivan, J.-Y. *Z. Naturforsch. B* **2007**, *62*, 1143–1152.
[223] Svechnikov, V. N.; Pan, V. M.; Spektor, A. T. *Russ. Metall.* **1971**, *1*, 133–137.
[224] Markiv, V. Ya.; Belyavina, N. N.; Shevchenko, I. P. *Russ. Metall.* **1994**, *3*, 148–151.

[225] Raghavan, V. *Indian Inst. Met.* **1992**, *6B*, 823–826.
[226] Suits, J. C. *Phys. Rev. B* **1976**, *14*, 4131–4135.
[227] Kimura, Y.; Tamura, Y.; Kita, T. *Appl. Phys. Lett.* **2008**, *92*, 012105-1–012105-3.
[228] Pauling, L. "*The empirical information made it clear that there was some possible systematization to the interatomic distances and also to other aspects of the crystal structures, and I thought perhaps we had come to the time when we could predict what the structures are without x-ray diffraction patterns*." in: O'Keeffe, M.; Navrotsky A. (Eds.), Structure and Bonding in Crystals, Volume 1, Academic Press, New York, 1981, pp. 1–12.
[229] Wold, S. *Chemom. Intell. Lab. Syst.* **1995**, *30*, 109–115.
[230] Otto, M. *Chemometrics: Statistics and Computer Application in Analytical Chemistry*, second ed., Wiley-VCH, New York, 2007.
[231] Johnson, K. J.; Synovec, R. E. *Chemom. Intell. Lab. Syst.* **2002**, *60*, 225–237.
[232] Doble, P.; Sandercock, M.; Du Pasquier, E.; Petocz, P.; Roux, C.; Dawson, M. *Forensic Sci. Int.* **2003**, *132*, 26–39.
[233] Sandercock, P. M. L.; Du Pasquier, E. *Forensic Sci. Int.* **2003**, *134*, 1–10.
[234] Sandercock, P. M. L.; Du Pasquier, E. *Forensic Sci. Int.* **2004**, *140*, 43–59.
[235] Sandercock, P. M. L.; Du Pasquier, E. *Forensic Sci. Int.* **2004**, *140*, 71–77.
[236] Sinkov, N. A.; Harynuk, J. J. *Talanta* **2011**, *83*, 1079–1087.
[237] Li, X.; Xu, Z.; Lu, X.; Yang, X.; Yin, P.; Kong, H.; Yu, Y.; Xu, G. *Anal. Chim. Acta* **2009**, *633*, 257–262.
[238] Beckstrom, A. C.; Humston, E. M.; Snyder, L. R.; Synovec, R. E.; Juul, S. E. *J. Chromatogr. A* **2011**, *1218*, 1899–1906.
[239] Srinivasan, S.; Rajan, K. *Materials* **2013**, *6*, 279–290.
[240] Petterson, F.; Suh, C.; Saxén, H.; Rajan, K.; Chakraborti, N. *Mater. Manuf. Processes* **2008**, *24*, 2–9.
[241] Lach-hab, M.; Yang, S.; Vaisman, I. I.; Blaisten-Barojas, E. *Mol. Inf.* **2010**, *29*, 297–301.
[242] Barker, M.; Rayens, W. *J. Chemom.* **2003**, *17*, 166–173.
[243] Boser, B. E.; Guyon, I. M.; Vapnik, V. N. *A training algorithm for optimal margin classifiers, Proceedings of the Fifth Annual ACM Workshop on Computational Learning Theory* **1992**, 144–152.
[244] Guyon, I.; Elisseeff, A. *J. Mach. Learn. Res.* **2003**, *3*, 1157–1182.
[245] Rajalahti, T.; Arneberg, R.; Kroksveen, A. C.; Berle, M.; Myhr, K.-M.; Kvalheim, O. M. *Anal. Chem.* **2009**, *81*, 2581–2590.
[246] Sinkov, N. A.; Johnston, B. M.; Sandercock, P. M. L.; Harynuk, J. *J. Anal. Chim. Acta* **2011**, *697*, 8–15.
[247] Gross, N.; Kotzyba, G.; Künnen, B.; Jeitschko, W. *Z. Anorg. Allg. Chem* **2001**, *627*, 155–163.

[248] Scifinder, 2015, Chemical Abstracts Service, Columbus, OH, 2015.
[249] Pauling, L. *J. Am. Chem. Soc.* **1932**, *54*, 3570–3582.
[250] Martynov, A. I.; Batsanov, S. S. *Zh. Neorg. Khim.* **1980**, *5*, 3171–3175.
[251] Ghosh, D. C.; Chakraborty, T. *J. Mol. Struct.: THEOCHEM* **2009**, *906*, 87–93.
[252] Mulliken, R. S. *J. Chem. Phys.* **1934**, *2*, 782–784.
[253] Allred, A. L.; Rochow, E. G. *J. Inorg. Nucl. Chem.* **1958**, *5*, 264–268.
[254] Emsley, J. *Nature's Building Blocks: An A-Z Guide to the Elements*, Oxford University Press, New York, 2011.
[255] Lin, C.; Weng, R. C. *Simple probabilistic predictions for support vector regression*, National Taiwan University, Taipei, 2004.
[256] Sinkov, N. A.; Harynuk, J. J. *Talanta* **2013**, *103*, 252–259.
[257] Sinkov, N. A.; Sandercock, P. M. L.; Harynuk, J. *J. Forensic Sci. Int.* **2014**, *235*, 24–31.
[258] Adutwum, L. A.; Harynuk, J. *J. Anal. Chem.* **2014**, *86*, 7726–7733.
[259] Suh, C.; Rajan, K. *Mater. Sci. Technol.* **2009**, *25*, 466–471.
[260] O'Keeffe, M.; Navrotsky, A. *Structure and Bonding in Crystals*, Volume 1, Academic Press, New York, 1981.
[261] Abegg, R. *Z. Anorg. Allg. Chem.* **1904**, *39*, 330–380.
[262] Salamakha, P. S.; Sologub, O. L.; Bodak, O. I. Chapter 173 Ternary rare-earth-germanium systems, *Handbook on the Physics and Chemistry of Rare Earths, Volume* **1999**, *27*, 1–223.
[263] Parthé, E.; Chabot, B.; Hovestreydt, E. *Acta Cryst. B* **1983**, *29*, 596–603.

Apendix 1

Supplementary Data for Chapter 2

Table A1-1 EDX analyses of $RE_3M_2Ge_3$ crystals. [a]

Compound	at. % *RE*	at. % *M*	at. % Ge
$Y_3Ru_2Ge_3$	35(1)	27(1)	38(1)
$Gd_3Ru_2Ge_3$	36(1)	25(1)	39(1)
$Tb_3Ru_2Ge_3$	36(1)	24(1)	40(1)
$Dy_3Ru_2Ge_3$	36(1)	25(1)	39(1)
$Ho_3Ru_2Ge_3$	35(1)	28(1)	37(1)
$Er_3Ru_2Ge_3$	37(1)	25(1)	38(1)
$Tm_3Ru_2Ge_3$	36(1)	24(1)	40(1)
$Lu_3Ru_2Ge_3$	37(1)	25(1)	38(1)
$Y_3Ir_2Ge_3$	36(1)	26(1)	38(1)
$Gd_3Ir_2Ge_3$	36(1)	24(1)	39(1)
$Tb_3Ir_2Ge_3$	37(1)	24(1)	38(1)
$Dy_3Ir_2Ge_3$	35(1)	27(1)	38(1)
$Ho_3Ir_2Ge_3$	37(1)	25(1)	38(1)
$Er_3Ir_2Ge_3$	35(1)	28(1)	37(1)
$Tm_3Ir_2Ge_3$	38(1)	26(1)	36(1)

[a] Expected composition is 37.5% *RE*, 25.0% *M*, and 37.5% As.

Apendix 2

Supplementary Data for Chapter 3

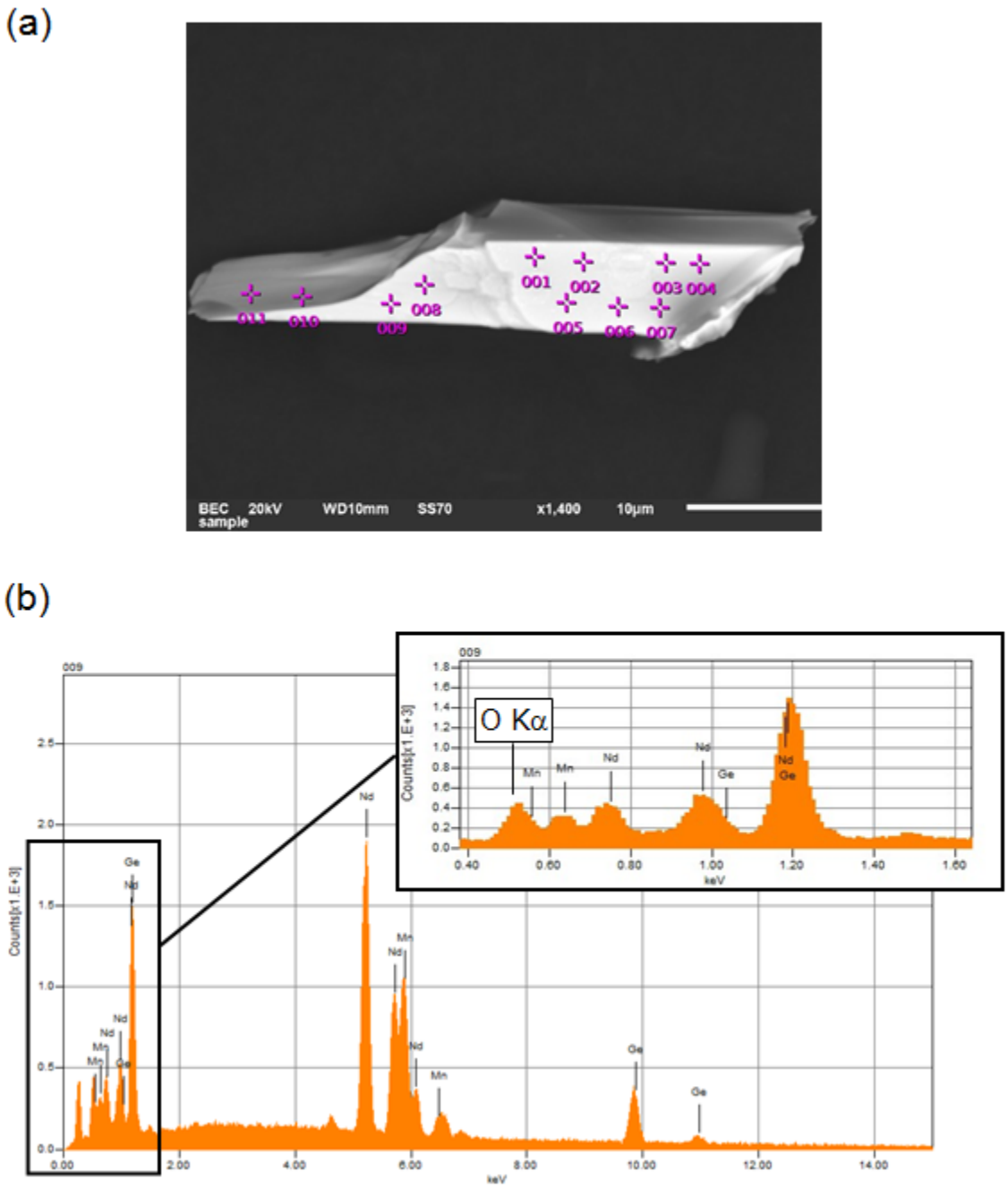

Figure A2-1 (a) SEM image and (b) EDX spectrum (point 009) with inset at low energies for single crystal of $Nd_4Mn_2Ge_5O_{0.6}$.

Apendix 3

Supplementary Data for Chapter 4

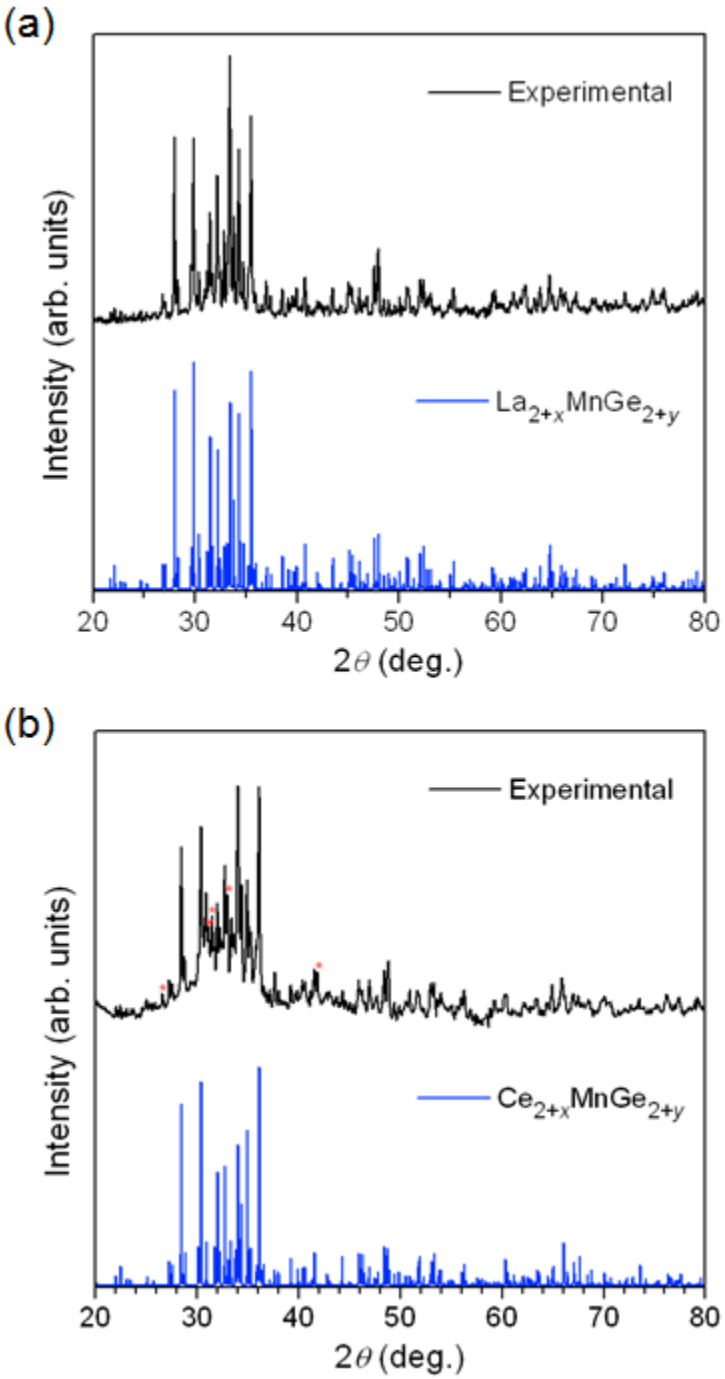

Figure A3-1 Powder XRD patterns for (a) $La_{2+x}MnGe_{2+y}$ and (b) $Ce_{2+x}MnGe_{2+y}$. Unidentified peaks in (b) are marked with asterisks.

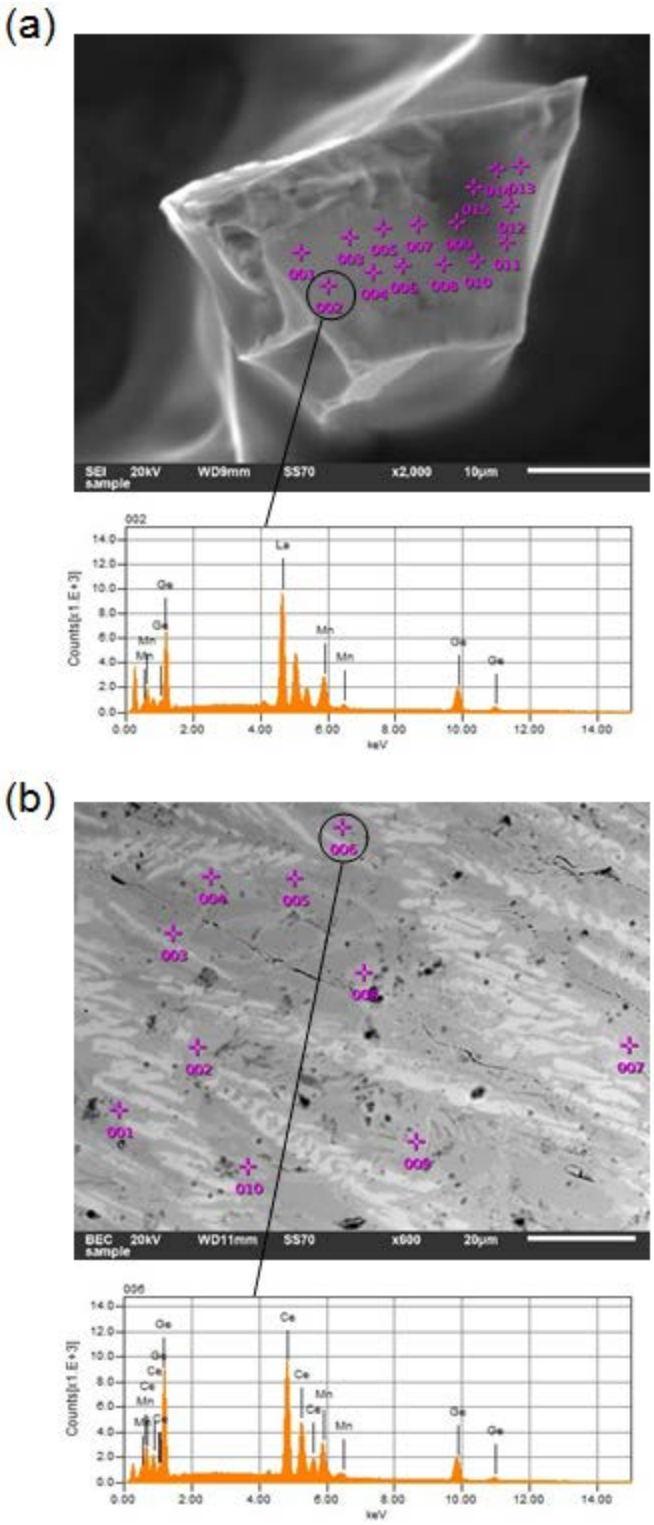

Figure A3-2 SEM images and EDX spectra for (a) single crystal of $La_{2+x}MnGe_{2+y}$ and (b) polished sample of an arc-melted "$Ce_{40}Mn_{20}Ge_{40}$" ingot after annealing.

Apendix 4

Supplementary Data for Chapter 5

Table A4-1 Loading compositions and phase compositions from XRD and EDX analyses in Ce–Mn–In system at 800 °C.

Loading composition	Overall EDX composition	Phases
$Ce_{10}Mn_{30}In_{60}$	$Ce_{24}Mn_{6}In_{70}$	In, $CeIn_3$, $Mn_{9.75}In_{3.25}$
$Ce_{20}Mn_{20}In_{60}$	$Ce_{24}Mn_{20}In_{56}$	$CeIn_3$, $CeIn_2$, $Mn_{9.75}In_{3.25}$
$Ce_{30}Mn_{10}In_{60}$	$Ce_{42}Mn_{10}In_{48}$	Ce_5In_4, Ce_3In_5, $CeIn_{1.33}Mn_{0.67}$
$Ce_{20}Mn_{30}In_{50}$	$Ce_{22}Mn_{26}In_{52}$	$CeIn_2$, $Mn_{9.75}In_{3.25}$, β-Mn
$Ce_{30}Mn_{20}In_{50}$	$Ce_{32}Mn_{18}In_{50}$	$CeIn_{1.33}Mn_{0.67}$, $CeIn_2$, β-Mn
$Ce_{35}Mn_{10}In_{55}$	$Ce_{32}Mn_{7}In_{61}$	$CeIn_{1.33}Mn_{0.67}$, $CeIn_2$, Ce_3In_5
$Ce_{40}Mn_{10}In_{50}$	$Ce_{33}Mn_{8}In_{59}$	$CeIn_{1.33}Mn_{0.67}$, Ce_3In_5
$Ce_{50}Mn_{10}In_{40}$	$Ce_{46}Mn_{12}In_{42}$	$CeIn_{1.33}Mn_{0.67}$, Ce_5In_4, β-Mn
$Ce_{55}Mn_{10}In_{35}$	$Ce_{54}Mn_{14}In_{32}$	Ce_5In_4, Ce_2In, β-Mn
$Ce_{60}Mn_{10}In_{30}$	$Ce_{63}Mn_{11}In_{26}$	Ce_2In, Ce_3In, β-Mn
$Ce_{65}Mn_{10}In_{25}$	$Ce_{65}Mn_{4}In_{31}$	Ce_2In, Ce_3In, β-Mn
$Ce_{60}Mn_{20}In_{20}$	———	Ce_3In, β-Mn, Ce
$Ce_{55}Mn_{20}In_{25}$	$Ce_{54}Mn_{21}In_{25}$	Ce_2In, Ce_3In, β-Mn
$Ce_{40}Mn_{45}In_{15}$	———	Ce_3In, β-Mn, Ce
$Ce_{60}Mn_{30}In_{10}$	$Ce_{40}Mn_{42}In_{18}$	Ce_3In, β-Mn
$Ce_{30}Mn_{60}In_{10}$	$Ce_{18}Mn_{75}In_{7}$	Ce_3In, β-Mn
$Ce_{10}Mn_{80}In_{10}$	———	β-Mn, Ce_5In_4, Ce_2In
$Ce_{10}Mn_{70}In_{20}$	———	β-Mn, $CeIn_{1.33}Mn_{0.67}$
$Ce_{20}Mn_{50}In_{30}$	$Ce_{40}Mn_{43}In_{17}$	Ce_2In, β-Mn
$Ce_{10}Mn_{50}In_{40}$	$Ce_{11}Mn_{58}In_{31}$	$CeIn_2$, $Mn_{9.75}In_{3.25}$, β-Mn

Table A4-2 Loading compositions and phase compositions from XRD and EDX analyses in Mn–In–Ge system at 800 °C.

Loading composition	**Overall EDX composition**	**Phases**
$Mn_{20}In_{10}Ge_{70}$	$Mn_{26}In_{10}Ge_{64}$	Ge, Mn_5Ge_3, In
$Mn_{10}In_{20}Ge_{70}$	$Mn_{14}In_{18}Ge_{68}$	Ge, Mn_5Ge_3, In
$Mn_{30}In_{20}Ge_{50}$	$Mn_{41}In_{8}Ge_{51}$	Ge, Mn_5Ge_3, In
$Mn_{50}In_{10}Ge_{40}$	$Mn_{55}In_{7}Ge_{38}$	Mn_5Ge_3, In
$Mn_{30}In_{30}Ge_{40}$	$Mn_{50}In_{8}Ge_{42}$	Mn_5Ge_3, In
$Mn_{55}In_{10}Ge_{35}$	$Mn_{60}In_{7}Ge_{33}$	Mn_5Ge_3, In
$Mn_{60}In_{10}Ge_{30}$	$Mn_{68}In_{3}Ge_{29}$	Mn_5Ge_2, In
$Mn_{65}In_{10}Ge_{25}$	$Mn_{70}In_{6}Ge_{24}$	Mn_5Ge_2, In
$Mn_{70}In_{10}Ge_{20}$	$Mn_{74}In_{6}Ge_{20}$	$Mn_{3.4}Ge$, In
$Mn_{75}In_{10}Ge_{15}$	$Mn_{73}In_{7}Ge_{20}$	$Mn_{3.4}Ge$, $Mn_{9.75}In_{3.25}$, In
$Mn_{80}In_{10}Ge_{10}$	$Mn_{80}In_{5}Ge_{15}$	$Mn_{3.4}Ge$, $Mn_{9.75}In_{3.25}$
$Mn_{70}In_{20}Ge_{10}$	$Mn_{81}In_{5}Ge_{14}$	$Mn_{3.4}Ge$, γ-Mn
$Mn_{60}In_{30}Ge_{10}$	$Mn_{52}In_{32}Ge_{16}$	Mn_5Ge_2, In
$Mn_{60}In_{20}Ge_{20}$	$Mn_{67}In_{13}Ge_{20}$	Mn_5Ge_2, In
$Mn_{50}In_{20}Ge_{30}$	$Mn_{47}In_{20}Ge_{33}$	Mn_5Ge_3, In
$Mn_{40}In_{30}Ge_{30}$	$Mn_{47}In_{13}Ge_{40}$	Ge, Mn_5Ge_3, In
$Mn_{40}In_{40}Ge_{20}$	$Mn_{61}In_{9}Ge_{30}$	Mn_5Ge_3, Mn_5Ge_2, In
$Mn_{30}In_{50}Ge_{20}$	$Mn_{58}In_{11}Ge_{31}$	Mn_5Ge_3, In

Table A4-3 Loading compositions and phase compositions from XRD and EDX analyses in Ce–In–Ge system at 800 °C.

Loading composition	**Overall EDX composition**	**Phases**
$Ce_{20}In_{10}Ge_{70}$	$Ce_{12}In_{18}Ge_{70}$	β-$CeGe_{2-x}$, Ge, In
$Ce_{20}In_{30}Ge_{50}$	$Ce_{26}In_{18}Ge_{56}$	β-$CeGe_{2-x}$, Ge, In
$Ce_{40}In_{10}Ge_{50}$	$Ce_{41}In_{13}Ge_{46}$	β-$CeGe_{2-x}$, Ce_2InGe_2
$Ce_{35}In_{20}Ge_{45}$	$Ce_{35}In_{25}Ge_{40}$	Ce_2InGe_2, β-$CeGe_{2-x}$
$Ce_{30}In_{30}Ge_{40}$	$Ce_{25}In_{34}Ge_{41}$	β-$CeGe_{2-x}$, In
$Ce_{35}In_{30}Ge_{35}$	$Ce_{32}In_{30}Ge_{38}$	Ce_2InGe_2, β-$CeGe_{2-x}$, In
$Ce_{47.5}In_{7.5}Ge_{45}$	$Ce_{49}In_8Ge_{43}$	Ce_2InGe_2, CeGe
$Ce_{50}In_{10}Ge_{40}$	$Ce_{54}In_{10}Ge_{36}$	Ce_2InGe_2, Ce_5Ge_4
$Ce_{55}In_{10}Ge_{35}$	$Ce_{57}In_{11}Ge_{32}$	Ce_5Ge_4, $Ce_{11}In_6Ge_4$
$Ce_{50}In_{20}Ge_{30}$	$Ce_{48}In_{26}Ge_{26}$	Ce_2InGe_2, $Ce_{11}In_6Ge_4$
$Ce_{60}In_{10}Ge_{30}$	$Ce_{63}In_{12}Ge_{25}$	$Ce_3In_{0.89}Ge_{1.11}$, Ce_5Ge_3
$Ce_{45}In_{30}Ge_{25}$	$Ce_{48}In_{34}Ge_{18}$	$Ce_{11}In_6Ge_4$, $Ce_3In_{4.33}Ge_{0.67}$
$Ce_{70}In_{10}Ge_{20}$	$Ce_{69}In_6Ge_{25}$	$Ce_3In_{0.89}Ge_{1.11}$, Ce_5Ge_3, Ce_3In
$Ce_{65}In_{15}Ge_{20}$	$Ce_{64}In_{17}Ge_{19}$	$Ce_3In_{0.89}Ge_{1.11}$, Ce_3In, Ce_2In
$Ce_{55}In_{30}Ge_{15}$	$Ce_{55}In_{30}Ge_{15}$	$Ce_3In_{0.89}Ge_{1.11}$, $Ce_{11}In_6Ge_4$
$Ce_{70}In_{20}Ge_{10}$	$Ce_{76}In_{19}Ge_5$	$Ce_3In_{0.89}Ge_{1.11}$, Ce_3In
$Ce_{65}In_{25}Ge_{10}$	$Ce_{66}In_{26}Ge_8$	$Ce_3In_{0.89}Ge_{1.11}$, Ce_3In, Ce_2In
$Ce_{60}In_{30}Ge_{10}$	$Ce_{61}In_{31}Ge_8$	$Ce_3In_{0.89}Ge_{1.11}$, Ce_5In_4
$Ce_{50}In_{40}Ge_{10}$	$Ce_{46}In_{43}Ge_{11}$	$Ce_3In_{4.33}Ge_{0.67}$, $Ce_{11}In_6Ge_4$, Ce_5In_4
$Ce_{40}In_{55}Ge_5$	$Ce_{41}In_{53}Ge_6$	$Ce_3In_{4.33}Ge_{0.67}$, Ce_5In_4, Ce_3In_5
$Ce_{80}In_{10}Ge_{10}$	————	Ce, Ce_3In, Ce_5Ge_3
$Ce_{40}In_{40}Ge_{20}$	$Ce_{31}In_{52}Ge_{17}$	Ce_2InGe_2, In
$Ce_{30}In_{50}Ge_{20}$	$Ce_{15}In_{65}Ge_{20}$	β-$CeGe_{2-x}$, In, Ce_2InGe_2
$Ce_{20}In_{50}Ge_{30}$	$Ce_{30}In_{41}Ge_{29}$	Ce_2InGe_2, In
$Ce_{10}In_{60}Ge_{30}$	$Ce_{17}In_{37}Ge_{46}$	β-$CeGe_{2-x}$, In, Ge
$Ce_{20}In_{60}Ge_{20}$	$Ce_{14}In_{63}Ge_{23}$	β-$CeGe_{2-x}$, In, Ce_2InGe_2
$Ce_{30}In_{60}Ge_{10}$	$Ce_{43}In_{51}Ge_6$	$Ce_3In_{4.33}Ge_{0.67}$, $CeIn_2$
$Ce_{35}In_{60}Ge_5$	$Ce_{28}In_{68}Ge_4$	$CeIn_3$, In, Ce_2InGe_2
$Ce_{30}In_{65}Ge_5$	$Ce_{31}In_{65}Ge_4$	$Ce_3In_{4.33}Ge_{0.67}$, $CeIn_2$, $CeIn_3$

Table A4-4 Loading compositions and phase compositions from XRD and EDX analyses in Ce–Mn–Ge system at 800 °C.

Loading composition	**Overall EDX composition**	**Phases**
$Ce_{60}Mn_{20}Ge_{20}$	————	Ce_5Ge_5, Ce, Mn
$Ce_{30}Mn_{50}Ge_{20}$	$Ce_{35}Mn_{43}Ge_{22}$	Mn, Ce_5Ge_3
$Ce_{20}Mn_{50}Ge_{30}$	$Ce_{25}Mn_{45}Ge_{30}$	$CeMn_2Ge_2$, CeMnGe, β-Mn
$Ce_{10}Mn_{20}Ge_{70}$	$Ce_9Mn_{27}Ge_{64}$	Ce_2MnGe_6, Ge, $Mn_{11}Ge_8$
$Ce_{25}Mn_5Ge_{70}$	$Ce_{28}Mn_5Ge_{67}$	β-$CeGe_{2-x}$, Ge, Ce_2MnGe_6
$Ce_{20}Mn_{20}Ge_{60}$	$Ce_{23}Mn_{17}Ge_{60}$	Ce_2MnGe_6, β-$CeGe_{2-x}$, $CeMn_2Ge_2$ (trace)
$Ce_{25}Mn_{10}Ge_{65}$	$Ce_{26}Mn_{10}Ge_{64}$	β-$CeGe_{2-x}$, Ce_2MnGe_6
$Ce_{35}Mn_5Ge_{60}$	$Ce_{38}Mn_5Ge_{57}$	β-$CeGe_{2-x}$, $CeMn_2Ge_2$, CeGe (trace)
$Ce_{15}Mn_{40}Ge_{45}$	$Ce_{19}Mn_{35}Ge_{46}$	Ce_2MnGe_6, $CeMn_2Ge_2$
$Ce_{30}Mn_{30}Ge_{40}$	$Ce_{33}Mn_{28}Ge_{39}$	$Ce_{43}Mn_{18}Ge_{39}$, $CeMn_2Ge_2$, CeGe (trace)
$Ce_5Mn_{55}Ge_{40}$	$Ce_6Mn_{55}Ge_{39}$	$CeMn_2Ge_2$, $Mn_{11}Ge_8$
$Ce_5Mn_{60}Ge_{35}$	$Ce_6Mn_{58}Ge_{36}$	$CeMn_2Ge_2$, Mn_5Ge_3
$Ce_5Mn_{65}Ge_{30}$	$Ce_7Mn_{61}Ge_{32}$	Mn_5Ge_2, $CeMn_2Ge_2$
$Ce_5Mn_{70}Ge_{25}$	$Ce_6Mn_{65}Ge_{29}$	$CeMn_2Ge_2$, $Mn_{3.4}Ge$
$Ce_5Mn_{75}Ge_{20}$	$Ce_5Mn_{75}Ge_{20}$	$CeMn_2Ge_2$, $Mn_{3.4}Ge$, γ-Mn
$Ce_5Mn_{80}Ge_{15}$	$Ce_5Mn_{80}Ge_{15}$	$CeMn_2Ge_2$, β-Mn, γ-Mn
$Ce_5Mn_{85}Ge_{10}$	$Ce_8Mn_{82}Ge_{10}$	CeMnGe, β-Mn
$Ce_{10}Mn_{50}Ge_{40}$	$Ce_{11}Mn_{47}Ge_{42}$	$CeMn_2Ge_2$, $Mn_{11}Ge_8$, Ce_2MnGe_6
$Ce_{10}Mn_{55}Ge_{35}$	$Ce_{11}Mn_{54}Ge_{34}$	$CeMn_2Ge_2$, Mn_2Ge
$Ce_{10}Mn_{60}Ge_{30}$	$Ce_{11}Mn_{58}Ge_{31}$	$Mn_{3.4}Ge$, $CeMn_2Ge_2$
$Ce_{10}Mn_{65}Ge_{25}$	$Ce_{10}Mn_{66}Ge_{24}$	γ-Mn, $CeMn_2Ge_2$
$Ce_{10}Mn_{70}Ge_{20}$	$Ce_{12}Mn_{64}Ge_{24}$	γ-Mn, $CeMn_2Ge_2$
$Ce_{15}Mn_{50}Ge_{35}$	$Ce_{17}Mn_{46}Ge_{36}$	$CeMn_2Ge_2$, Mn_5Ge_3
$Ce_{15}Mn_{55}Ge_{30}$	$Ce_{17}Mn_{52}Ge_{31}$	$CeMn_2Ge_2$, γ-Mn
$Ce_{30}Mn_{30}Ge_{40}$	$Ce_{36}Mn_{25}Ge_{39}$	$Ce_{43}Mn_{18}Ge_{39}$, $CeMn_2Ge_2$
$Ce_{50}Mn_{10}Ge_{40}$	$Ce_{55}Mn_8Ge_{37}$	CeMnGe, Ce_5Ge_3, $Ce_3Mn_2Ge_3$ (trace)
$Ce_{35}Mn_{30}Ge_{35}$	$Ce_{38}Mn_{26}Ge_{36}$	Ce_5Ge_3, $Ce_3Mn_2Ge_3$ ($Ce_{40}Mn_{25}Ge_{35}$), Ce
$Ce_{40}Mn_{25}Ge_{35}$	$Ce_{44}Mn_{23}Ge_{33}$	Ce_5Ge_3, CeMnGe
$Ce_{45}Mn_{20}Ge_{35}$	$Ce_{49}Mn_{16}Ge_{35}$	Ce_5Ge_3, CeMnGe
$Ce_{55}Mn_{10}Ge_{35}$	$Ce_{60}Mn_5Ge_{35}$	Ce_5Ge_3, Ce_4Ge_3
$Ce_{30}Mn_{40}Ge_{30}$	$Ce_{45}Mn_{26}Ge_{29}$	CeMnGe, Ce_5Ge_3
$Ce_{40}Mn_{30}Ge_{30}$	$Ce_{46}Mn_{24}Ge_{30}$	CeMnGe, Ce_5Ge_3
$Ce_{32.5}Mn_{30}Ge_{37.5}$	$Ce_{32}Mn_{31}Ge_{37}$	$Ce_3Mn_2Ge_3$, $CeMn_2Ge_2$
$Ce_{50}Mn_{10}Ge_{40}$	$Ce_{48}Mn_{12}Ge_{40}$	$Ce_{43}Mn_{18}Ge_{39}$, Ce_5Ge_4, Ce_5Ge_3 (trace)

$Ce_{50}Mn_5Ge_{45}$	$Ce_{47}Mn_8Ge_{45}$	$Ce_{43}Mn_{18}Ge_{39}$, CeGe, Ce_5Ge_4 (trace)
$Ce_{52.5}Mn_5Ge_{42.5}$	$Ce_{51}Mn_6Ge_{43}$	$Ce_{43}Mn_{18}Ge_{39}$, Ce_4Ge_3, Ce_5Ge_4
$Ce_{37.5}Mn_{25}Ge_{37.5}$	$Ce_{42}Mn_{23}Ge_{35}$	$Ce_3Mn_2Ge_3$ ($Ce_{40}Mn_{25}Ge_{35}$), CeMnGe, Ce_5Ge_3
$Ce_{37.5}Mn_{25}Ge_{37.5}$	$Ce_{40}Mn_{21}Ge_{39}$	$Ce_{43}Mn_{18}Ge_{39}$, $Ce_3Mn_2Ge_3$ ($Ce_{40}Mn_{25}Ge_{35}$), Ce_5Ge_3
$Ce_{37.5}Mn_{25}Ge_{37.5}$	$Ce_{40}Mn_{20}Ge_{40}$	$Ce_{43}Mn_{18}Ge_{39}$, $Ce_3Mn_2Ge_3$ ($Ce_{40}Mn_{25}Ge_{35}$)

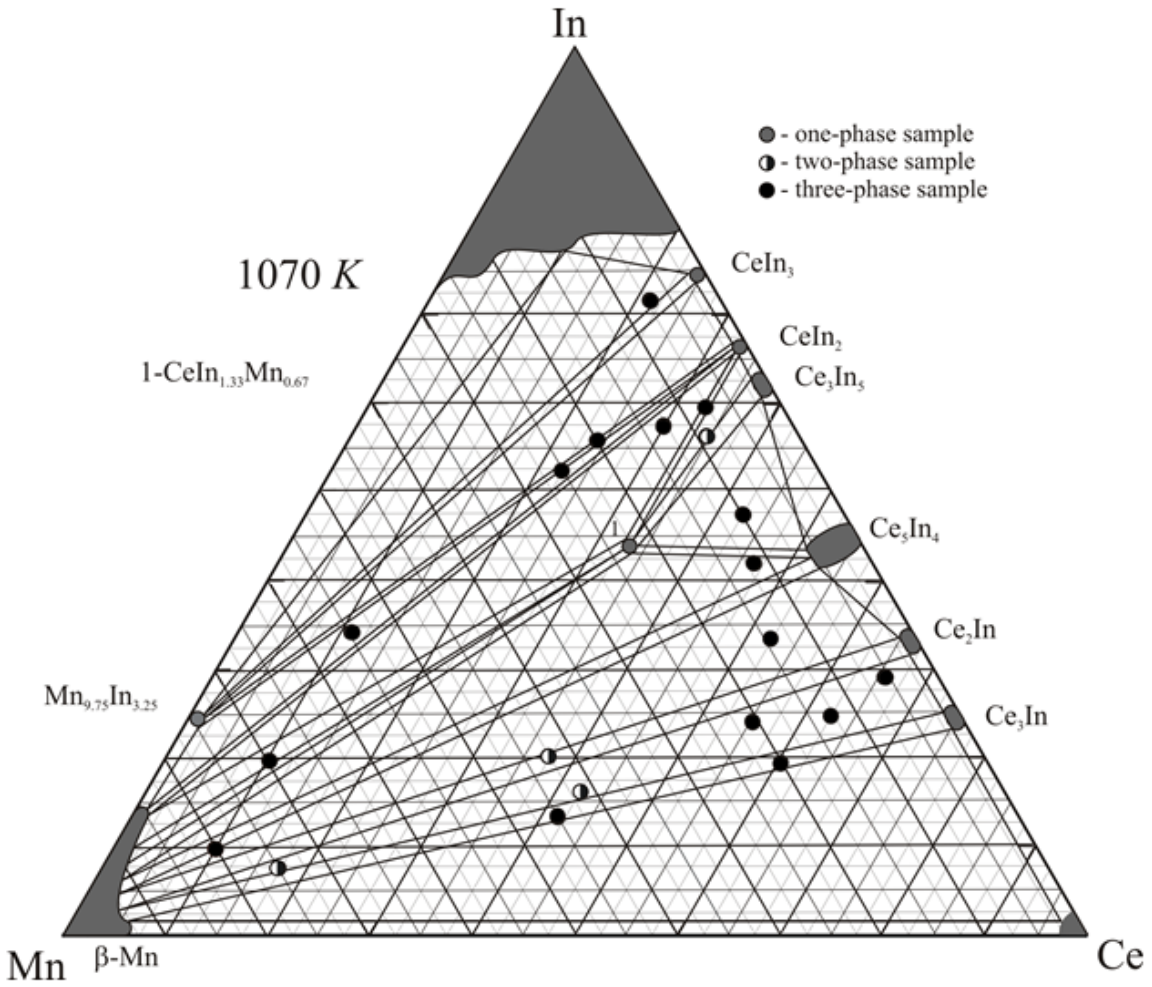

Figure A4-1 Analysis of samples in Ce–Mn–In phase diagram

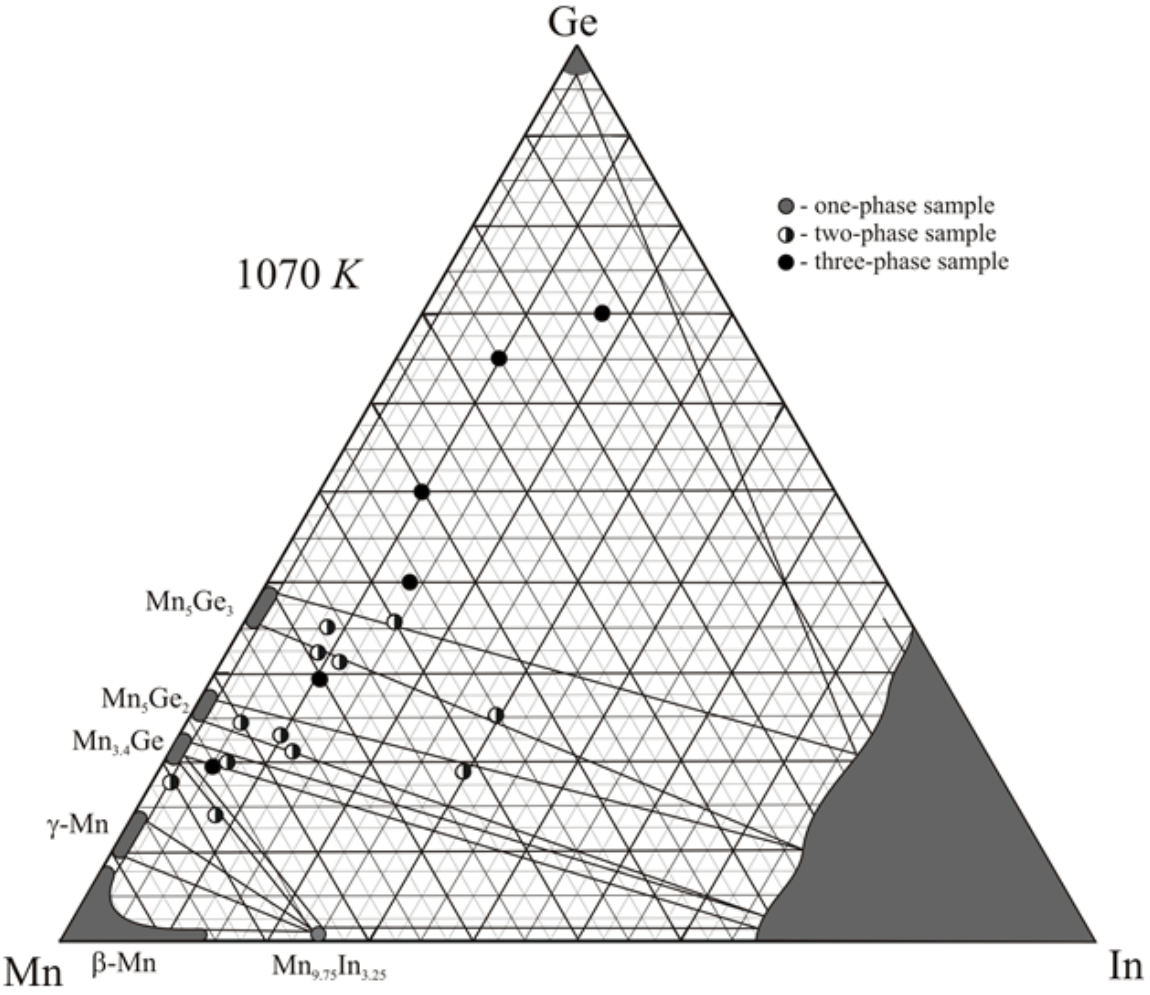

Figure A4-2 Analysis of samples in Mn–In–Ge phase diagram

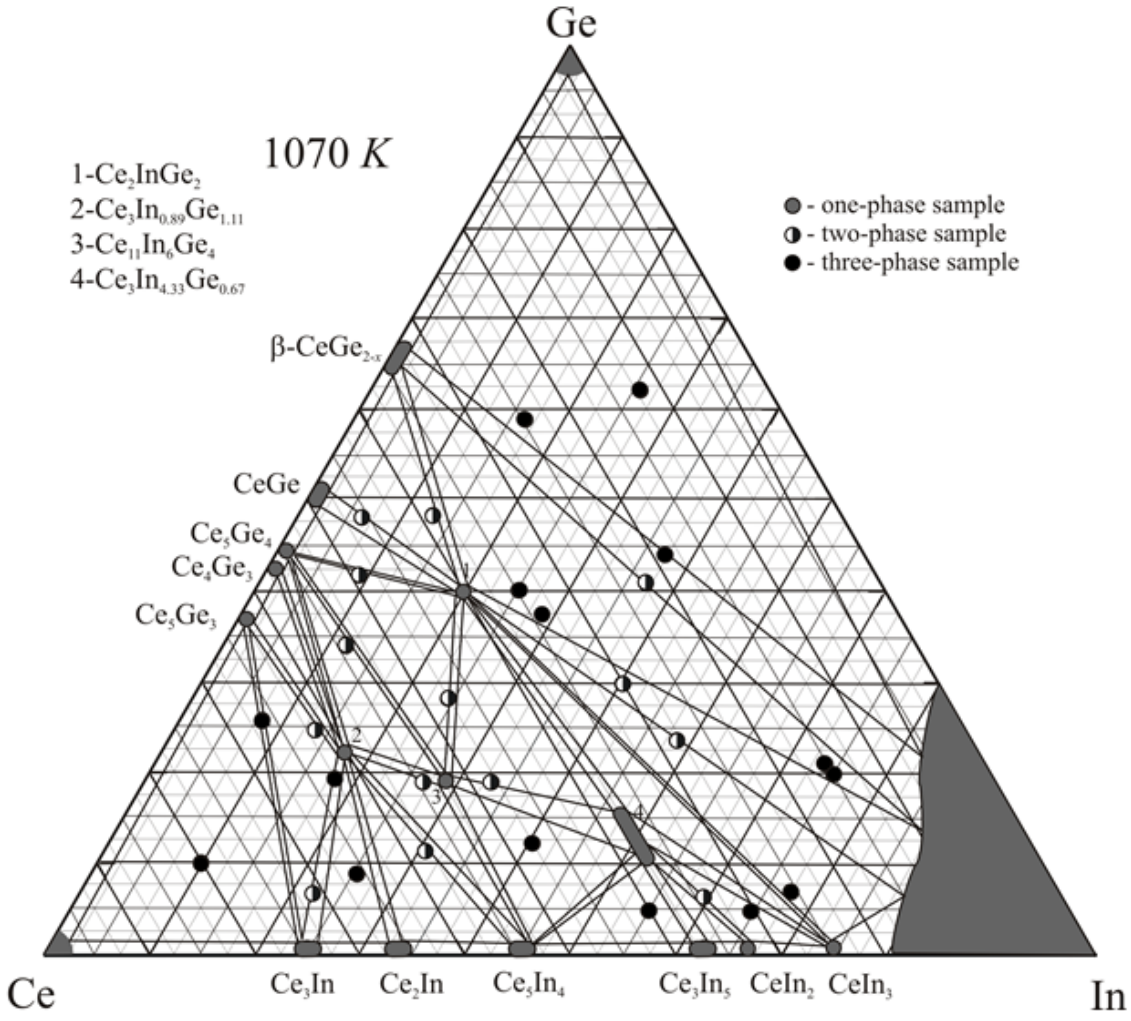

Figure A4-3 Analysis of samples in Ce–In–Ge phase diagram

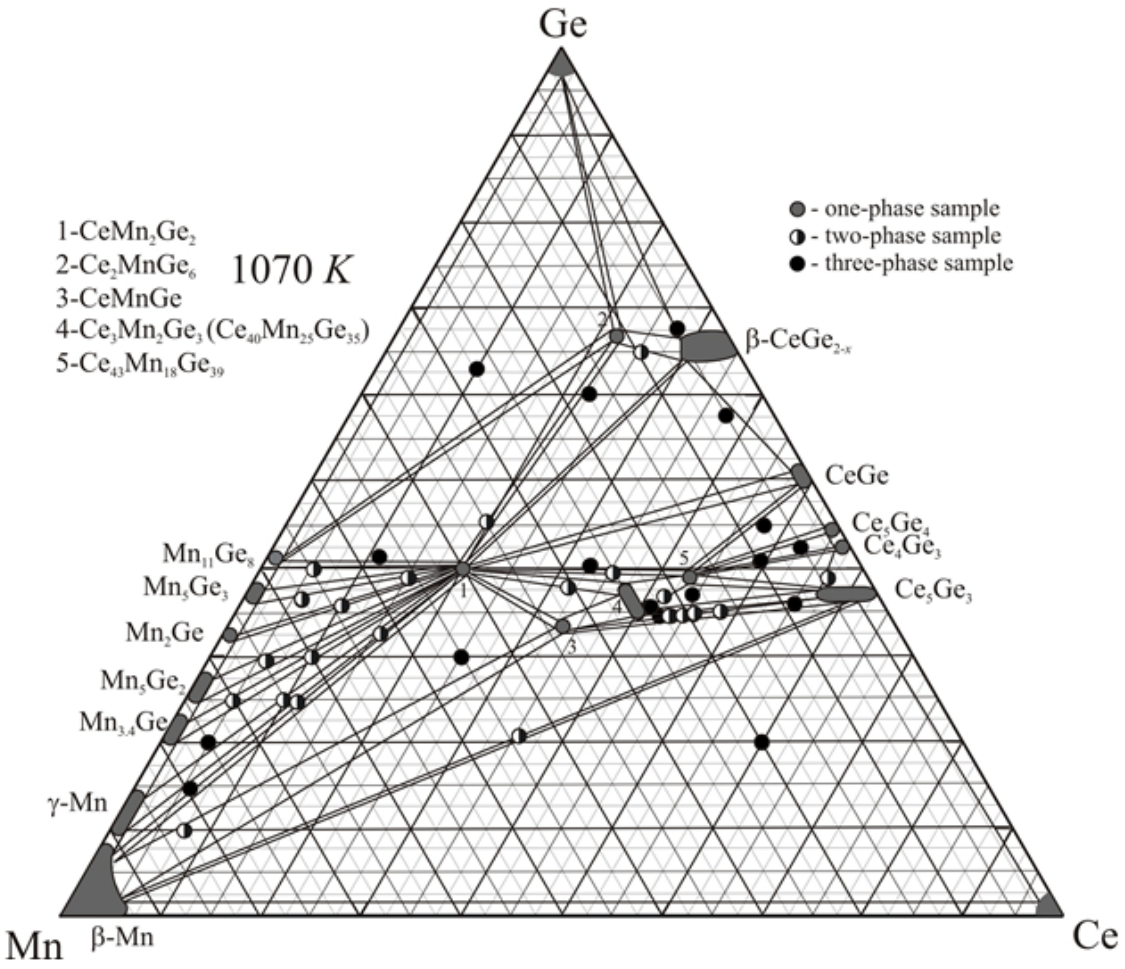

Figure A4-4 Analysis of samples in Ce–Mn–Ge phase diagram

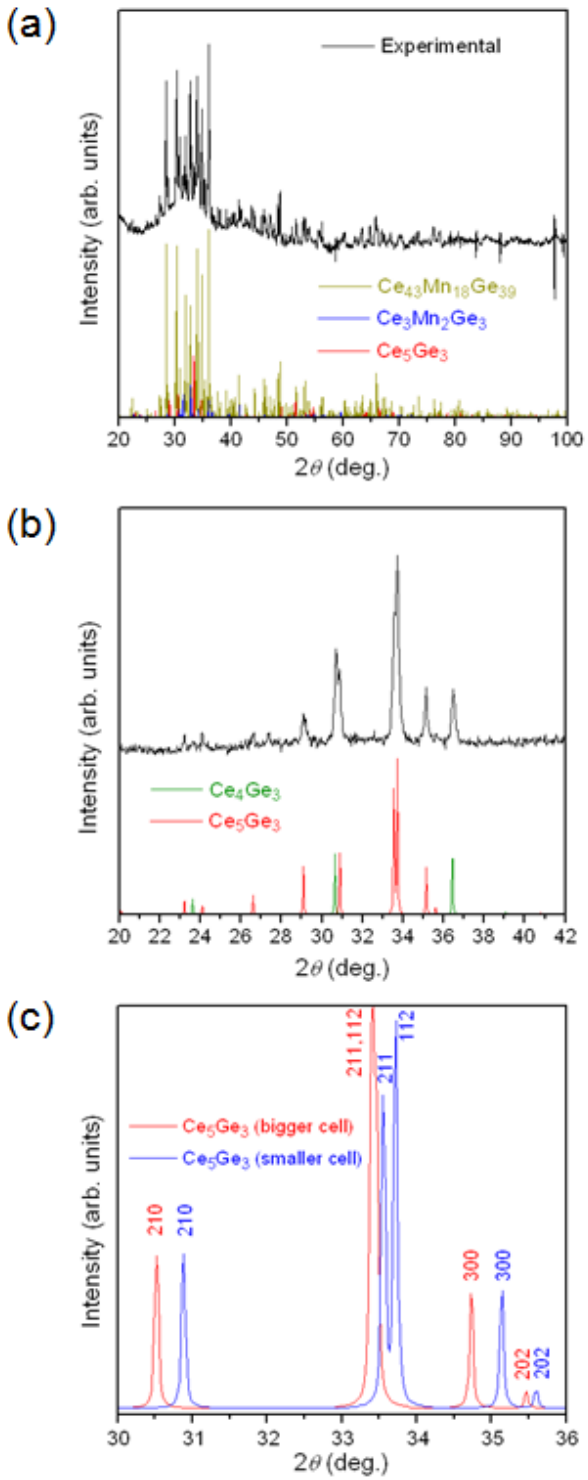

Figure A4-5 Solubility of Mn in Ce_5Ge_3 is indicated by powder XRD patterns of (a) a three-phase sample containing Ce_5Ge_3 with maximum 5% Mn content (confirmed by EDX analysis) and (b) a two-phase sample containing Ce_5Ge_3 without Mn. Different cell parameters are evident in (c) comparison of XRD patterns for limiting compositions of Ce_5Ge_3 (with 0–5% Mn).

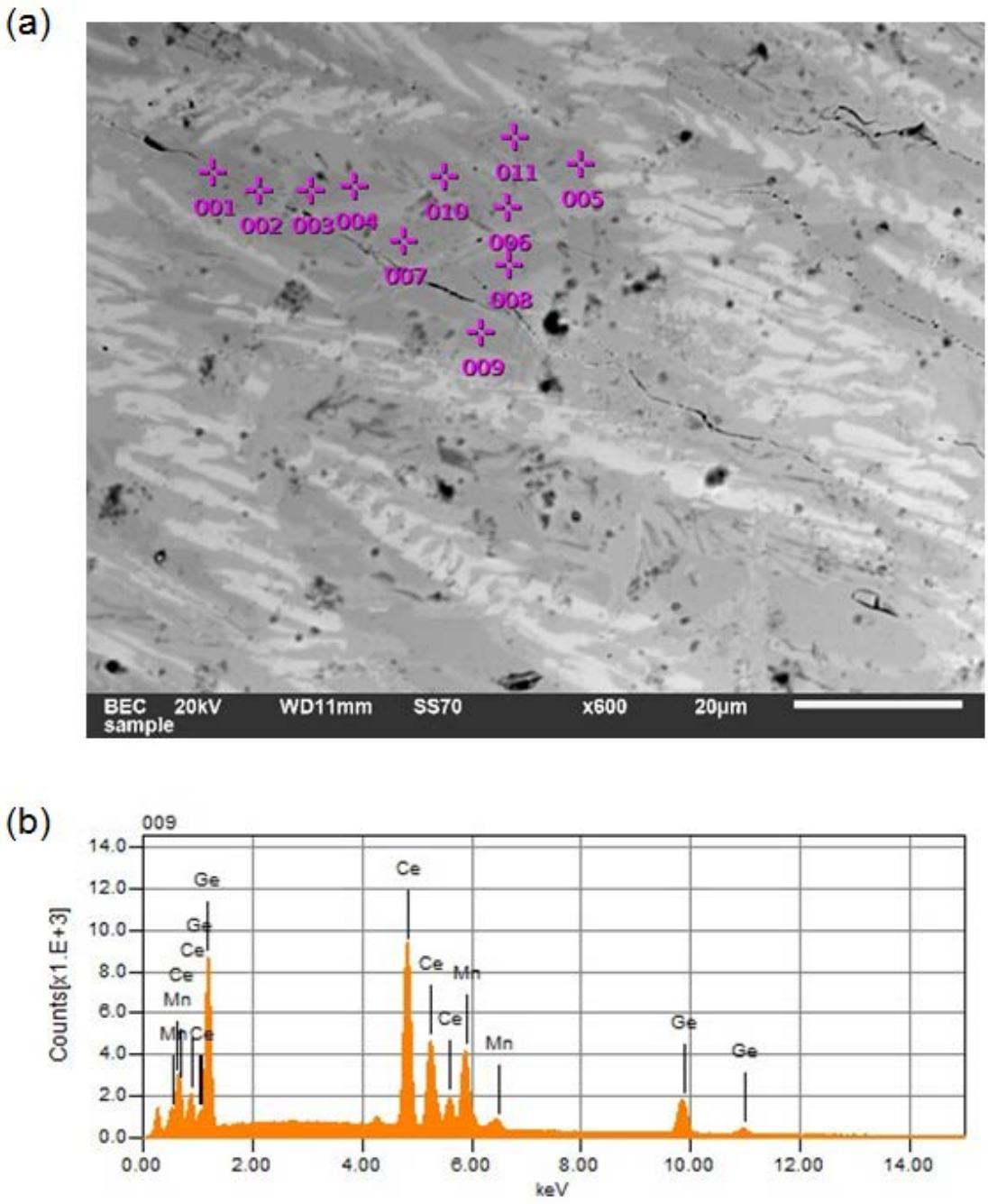

Figure A4-6 (a) SEM image of a three-phase sample consisting of $Ce_{40}Mn_{25}Ge_{35}$ ($Hf_3Ni_2Si_3$-type) in darkest grey regions, $Ce_{43}Mn_{18}Ge_{39}$ ($La_{2+x}MnGe_{2+y}$-type) in slightly less dark grey regions, and Ce_5Ge_3 (Mn_5Si_3-type) in light regions. (b) Representative EDX spectrum (point 009) of darkest grey regions, corresponding to an average composition of $Ce_{40(1)}Mn_{25(1)}Ge_{35(1)}$.

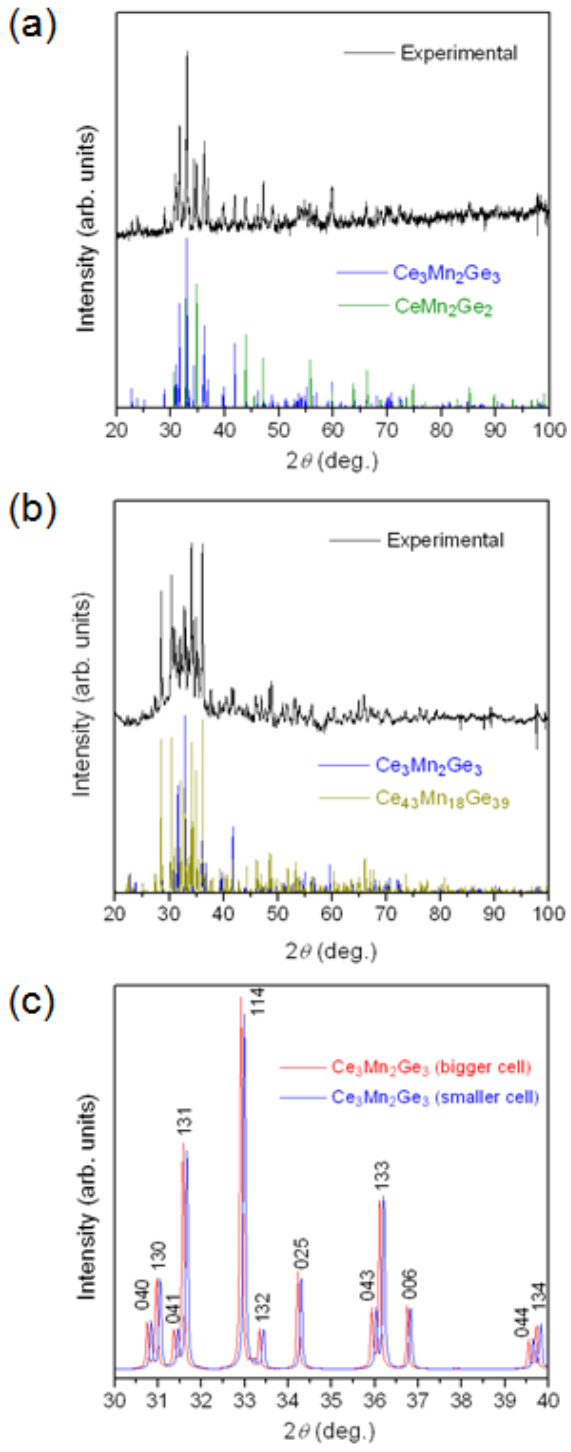

Figure A4-7 Homogeneity range in $Ce_3Mn_2Ge_3$ is indicated by powder XRD patterns of two-phase samples containing $Ce_3Mn_2Ge_3$ in equilbrium with (a) $CeMn_2Ge_2$ or (b) $Ce_{43}Mn_{18}Ge_{39}$. Different cell parameters of $Ce_3Mn_2Ge_3$ are evident in (c) comparison of XRD patterns for the limiting compositions of this phase ($Ce_{37.5}Mn_{25}Ge_{37.5}$ (smaller) and $Ce_{40}Mn_{25}Ge_{35}$ (bigger)).

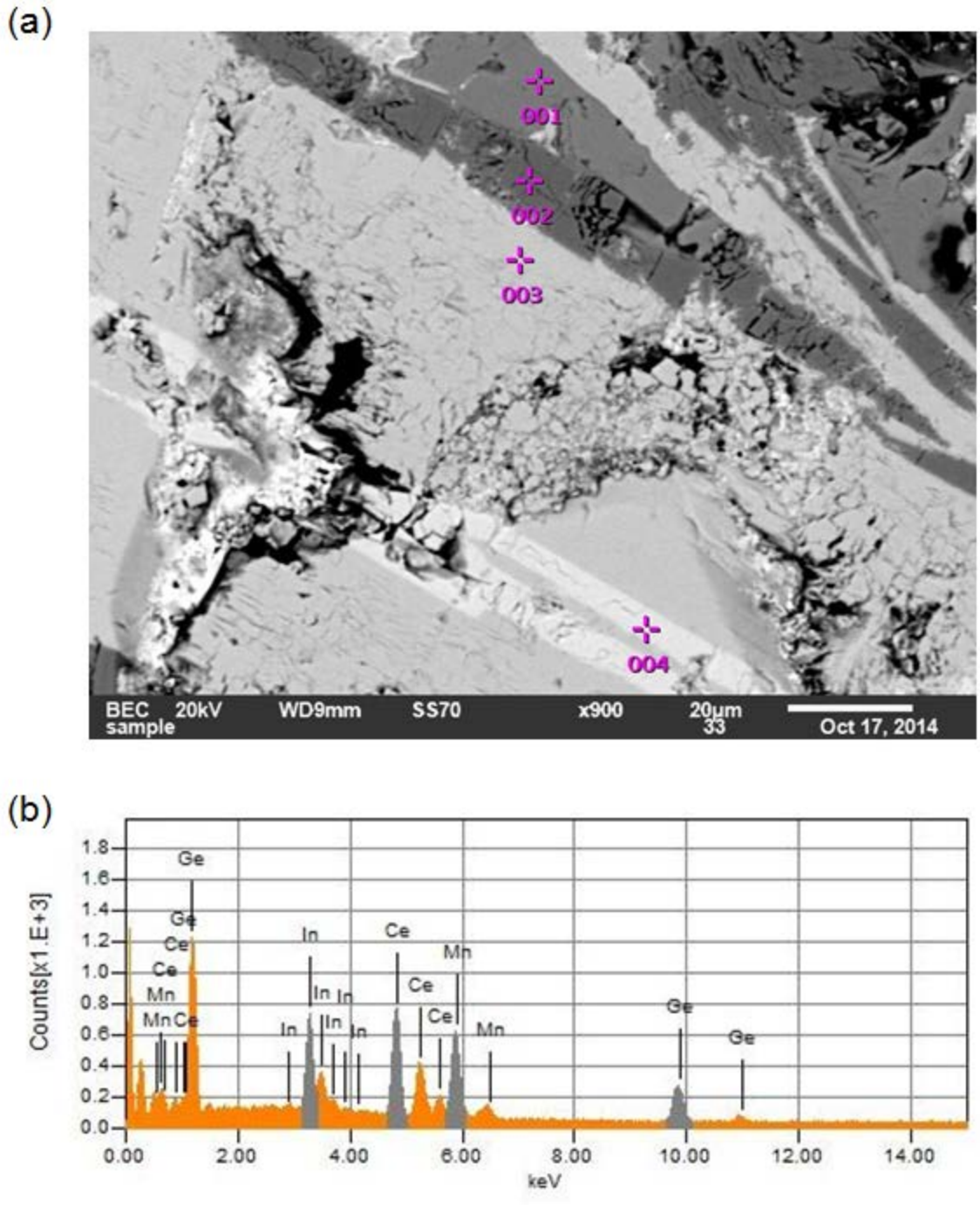

Figure A4-8 (a) SEM image of an annealed arc-melted ingot with overall composition "$Ce_{20}Mn_{30}In_{10}Ge_{40}$" containing four phases: Ge (darkest; point 002)), $Mn_{11}Ge_8$ (dark; point 001), Ce_2MnGe_6 (grey; point 003), and new quaternary phase $Ce_2Mn_2InGe_2$ (light; point 004). (b) EDX spectrum of $Ce_2Mn_2InGe_2$ (point 004).

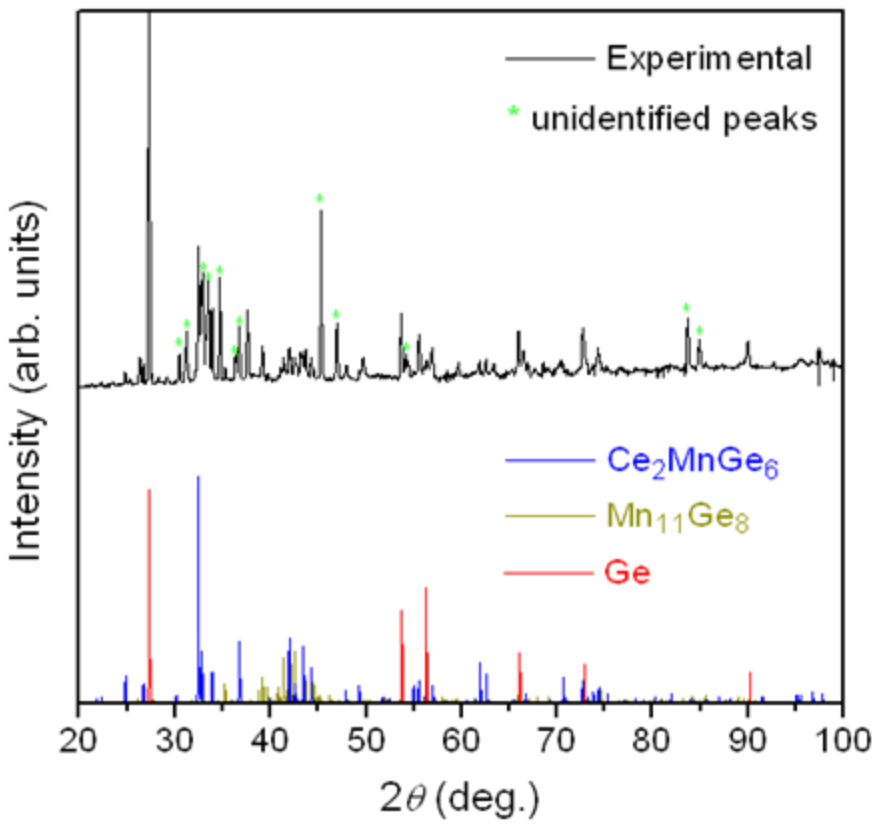

Figure A4-9 Powder XRD pattern for sample with overall composition "$Ce_{20}Mn_{30}In_{10}Ge_{40}$", containing Ge (red), $Mn_{11}Ge_8$ (dark yellow), Ce_2MnGe_6 (blue), and $Ce_2Mn_2InGe_2$ (green asterisks).

Apendix 5

Supplementary Data for Chapter 6

Table A5-1 Estimated fractional percentages (mol. %) of phases in arc-melted "$RE_4Mn_2InGe_4$" samples.

Sample (nominal composition)	$RE_4Mn_2InGe_4$	RE_2InGe_2	$REMn_2Ge_2$	REMnGe	$RE_{11}Ge_{10}$	RE_5Ge_4
$La_4Mn_2InGe_4$	54	28	18			
$Ce_4Mn_2InGe_4$	51	37	12			
$Pr_4Mn_2InGe_4$	60	40				
$Nd_4Mn_2InGe_4$	31	48	21			
$Sm_4Mn_2InGe_4$	35	31	18	16		
$Gd_4Mn_2InGe_4$	28	31	16		25	
$Tb_4Mn_2InGe_4$	23	42			35	
$Dy_4Mn_2InGe_4$	40	22			38	
$Ho_4Mn_2InGe_4$	45	16			39	
$Er_4Mn_2InGe_4$	40		20	20	20	
$Tm_4Mn_2InGe_4$	32		22	25	21	
$Lu_4Mn_2InGe_4$	34		30		23	13

Apendix 6

Supplementary Data for Chapter 7

Table A6-1 Crystallographic Data for $RE_4Fe_2InGe_4$ (*RE* = Ce–Nd, Sm, Gd)

formula	$Ce_4Fe_2In_{0.969(2)}Ge_4$	$Pr_4Fe_2In_{0.974(3)}Ge_4$	$Nd_4Fe_2In_{0.987(2)}Ge_4$	$Sm_4Fe_2In_{0.964(3)}Ge_4$	$Gd_4Fe_2In_{0.983(5)}Ge_4$
formula mass (amu)	1077.36	1080.52	1093.84	1118.28	1145.88
space group	*C*2/*m* (No. 12)	*C*2/*m* (No. 12)	*C*2/*m* (No. 12)	*C*2/*m* (No. 12)	*C*2/*m* (No. 12)
a (Å)	16.071(4)	16.0089(12)	15.9354(10)	15.770(4)	15.672(3)
b (Å)	4.3480(10)	4.3242(3)	4.3102(3)	4.2745(11)	4.2436(8)
c (Å)	7.2757(17)	7.2282(5)	7.2004(5)	7.1211(17)	7.0643(13)
β (°)	106.945(3)	106.8770(10)	107.0650(9)	107.011(3)	107.068(3)
V (Å^3)	486.34(19)	478.83(6)	472.78(6)	459.0(2)	449.12(14)
Z	2	2	2	2	2
T (K)	173(2)	173(2)	173(2)	173(2)	173(2)
ρ_{calcd} (g cm^{-3})	7.357	7.494	7.684	8.091	8.473
crystal dimensions (mm)	0.10 × 0.05 × 0.03	0.06 × 0.03 × 0.03	0.07 × 0.05 × 0.03	0.11 × 0.03 × 0.02	0.07 × 0.04 × 0.02
μ(Mo $K\alpha$) (mm^{-1})	35.58	37.48	39.31	43.45	47.80
transmission factors	0.144–0.431	0.264–0.434	0.133–0.495	0.150–0.521	0.109–0.469
2θ limits	5.30–66.44°	5.32–66.48°	5.35–66.36°	5.40–66.53°	5.44–66.02°
data collected	$-24 \le h \le 24$,	$-24 \le h \le 24$,	$-24 \le h \le 24$,	$-24 \le h \le 23$,	$-23 \le h \le 23$,
	$-6 \le k \le 6$,	$-6 \le k \le 6$,	$-6 \le k \le 6$,	$-6 \le k \le 6$,	$-6 \le k \le 6$,
	$-10 \le l \le 11$	$-10 \le l \le 10$	$-10 \le l \le 11$	$-10 \le l \le 10$	$-10 \le l \le 10$
no. of data collected	3484	3440	3336	3275	3133
no. of unique data, including $F_o^2 < 0$	1016 (R_{int} = 0.028)	1000 (R_{int} = 0.034)	982 (R_{int} = 0.026)	959 (R_{int} = 0.032)	929 (R_{int} = 0.053)
no. of unique data, with $F_o^2 > 2\sigma(F_o^2)$	908	847	879	842	738
no. of variables	37	37	37	37	37
$R(F)$ for $F_o^2 > 2\sigma(F_o^2)$ [a]	0.017	0.020	0.017	0.020	0.031
$R_w(F_o^2)$ [b]	0.039	0.039	0.037	0.041	0.069
goodness of fit	1.10	1.01	1.07	1.07	1.02
$(\Delta\rho)_{max}$, $(\Delta\rho)_{min}$ (e Å^{-3})	1.59, –1.38	2.19, –1.70	1.68, –0.99	1.54, –2.16	3.25, –2.95

[a] $R(F) = \sum||F_o| - |F_c|| / \sum|F_o|$. [b] $R_w(F_o^2) = [\sum[w(F_o^2 - F_c^2)^2] / \sum wF_o^4]^{1/2}$; $w^{-1} = [\sigma^2(F_o^2) + (Ap)^2 + Bp]$, where $p = [\max(F_o^2,0) + 2F_c^2] / 3$.

Table A6-2 Crystallographic Data for $RE_4Co_2InGe_4$ (*RE* = Ce–Nd, Sm, Gd)

formula	$Ce_4Co_2In_{0.986(3)}Ge_4$	$Pr_4Co_2In_{0.985(2)}Ge_4$	$Nd_4Co_2In_{0.965(2)}Ge_4$	$Sm_4Co_2In_{0.973(2)}Ge_4$	$Gd_4Co_2In_{0.970(4)}Ge_4$
formula mass (amu)	1083.52	1086.68	1100.00	1124.44	1152.04
space group	*C*2/*m* (No. 12)	*C*2/*m* (No. 12)	*C*2/*m* (No. 12)	*C*2/*m* (No. 12)	*C*2/*m* (No. 12)
a (Å)	15.9351(14)	15.8705(6)	15.7845(9)	15.6336(12)	15.548(6)
b (Å)	4.3361(4)	4.3247(2)	4.3028(3)	4.2723(3)	4.2483(16)
c (Å)	7.2602(6)	7.2264(3)	7.1824(4)	7.1131(6)	7.058(3)
β (°)	107.5309(12)	107.5111(5)	107.5115(8)	107.6415(10)	107.618(5)
V (Å^3)	478.35(7)	473.00(3)	465.20(5)	452.75(6)	444.3(5)
Z	2	2	2	2	2
T (K)	173(2)	173(2)	173(2)	173(2)	173(2)
ρ_{calcd} (g cm^{-3})	7.523	7.630	7.853	8.248	8.610
crystal dimensions (mm)	0.06 × 0.04 × 0.03	0.10 × 0.03 × 0.03	0.08 × 0.04 × 0.03	0.13 × 0.04 × 0.03	0.07 × 0.02 × 0.02
μ(Mo $K\alpha$) (mm^{-1})	36.61	38.38	40.40	44.52	48.78
transmission factors	0.245–0.454	0.100–0.498	0.168–0.440	0.050–0.477	0.136–0.532
2θ limits	5.36–66.20°	5.38–66.42°	5.41–66.15°	5.47–66.50°	5.49–66.51°
data collected	$-24 \le h \le 24$,	$-24 \le h \le 24$,	$-23 \le h \le 23$,	$-24 \le h \le 24$,	$-23 \le h \le 23$,
	$-6 \le k \le 6$,	$-6 \le k \le 6$,	$-6 \le k \le 6$,	$-6 \le k \le 6$,	$-6 \le k \le 6$,
	$-10 \le l \le 11$	$-11 \le l \le 10$	$-10 \le l \le 10$	$-10 \le l \le 10$	$-10 \le l \le 10$
no. of data collected	3360	3390	3306	3307	3157
no. of unique data, including $F_o^2 < 0$	988 (R_{int} = 0.035)	992 (R_{int} = 0.022)	968 (R_{int} = 0.030)	959 (R_{int} = 0.021)	934 (R_{int} = 0.046)
no. of unique data, with $F_o^2 > 2\sigma(F_o^2)$	841	905	851	897	771
no. of variables	37	37	37	37	37
$R(F)$ for $F_o^2 > 2\sigma(F_o^2)$ [a]	0.022	0.016	0.018	0.016	0.026
$R_w(F_o^2)$ [b]	0.045	0.034	0.037	0.033	0.054
goodness of fit	1.06	1.11	1.05	1.10	1.01
$(\Delta\rho)_{max}$, $(\Delta\rho)_{min}$ (e Å^{-3})	2.38, –1.58	1.38, –1.22	1.42, –1.47	1.76, –1.36	2.04, –2.22

[a] $R(F) = \sum||F_o| - |F_c|| / \sum|F_o|$. [b] $R_w(F_o^2) = [\sum[w(F_o^2 - F_c^2)^2] / \sum wF_o^4]^{1/2}$; $w^{-1} = [\sigma^2(F_o^2) + (Ap)^2 + Bp]$, where $p = [\max(F_o^2,0) + 2F_c^2] / 3$.

Table A6-3 Crystallographic Data for $RE_4Ru_2InGe_4$ (RE = Ce–Nd, Sm, Gd–Er)

formula	$Ce_4Ru_2In_{0.962(3)}Ge_4$	$Pr_4Ru_2In_{0.959(5)}Ge_4$	$Nd_4Ru_2In_{0.954(3)}Ge_4$	$Sm_4Ru_2In_{0.965(3)}Ge_4$	$Gd_4Ru_2In_{0.962(3)}Ge_4$
formula mass (amu)	1167.80	1170.96	1184.28	1208.72	1236.32
space group	$C2/m$ (No. 12)	$C2/m$ (No. 12)	$C2/m$ (No. 12)	$C2/m$ (No. 12)	$C2/m$ (No. 12)
a (Å)	16.174(4)	16.083(5)	16.014(6)	15.877(3)	15.773(4)
b (Å)	4.3794(10)	4.3605(13)	4.3463(16)	4.3178(7)	4.2875(11)
c (Å)	7.2321(17)	7.190(2)	7.160(3)	7.0936(12)	7.0393(18)
β (°)	106.144(3)	106.254(4)	106.353(5)	106.517(2)	106.635(4)
V (Å^3)	492.1(2)	484.1(2)	478.2(3)	466.23(13)	456.1(2)
Z	2	2	2	2	2
T (K)	173(2)	173(2)	173(2)	173(2)	173(2)
ρ_{calcd} (g cm^{-3})	7.882	8.033	8.225	8.610	9.002
crystal dimensions (mm)	0.19 × 0.04 × 0.02	0.12 × 0.03 × 0.02	0.09 × 0.02 × 0.02	0.09 × 0.02 × 0.02	0.13 × 0.02 × 0.02
μ(Mo $K\alpha$) (mm^{-1})	35.29	37.20	38.99	42.91	47.20
transmission factors	0.138–0.652	0.059–0.633	0.109–0.583	0.110–0.573	0.064–0.553
2θ limits	5.24–66.57°	5.28–66.15°	5.30–66.45°	5.35–66.45°	5.39–66.61°
data collected	$-24 \le h \le 24$, $-6 \le k \le 6$, $-11 \le l \le 11$	$-24 \le h \le 24$, $-6 \le k \le 6$, $-11 \le l \le 10$	$-24 \le h \le 24$, $-6 \le k \le 6$, $-10 \le l \le 10$	$-24 \le h \le 24$, $-6 \le k \le 6$, $-10 \le l \le 10$	$-24 \le h \le 24$, $-6 \le k \le 6$, $-10 \le l \le 10$
no. of data collected	3534	3430	3457	3389	3346
no. of unique data, including $F_o^2 < 0$	1025 (R_{int} = 0.030)	996 (R_{int} = 0.061)	994 (R_{int} = 0.038)	988 (R_{int} = 0.034)	972 (R_{int} = 0.044)
no. of unique data, with $F_o^2 > 2\sigma(F_o^2)$	878	783	833	849	800
no. of variables	37	36	37	37	37
$R(F)$ for $F_o^2 > 2\sigma(F_o^2)$ [a]	0.022	0.035	0.024	0.022	0.024
$R_w(F_o^2)$ [b]	0.051	0.081	0.053	0.044	0.044
goodness of fit	1.06	1.02	1.04	1.05	1.05
$(\Delta\rho)_{max}$, $(\Delta\rho)_{min}$ (e Å^{-3})	1.60, –1.69	3.72, –2.32	2.30, –2.26	2.11, –2.11	2.76, –2.50

formula	$Tb_4Ru_2In_{0.932(3)}Ge_4$	$Dy_4Ru_2In_{0.961(4)}Ge_4$	$Ho_4Ru_2In_{0.962(4)}Ge_4$	$Er_4Ru_2In_{0.980(5)}Ge_4$

formula mass (amu)	1243.00	1257.32	1267.04	1276.36
space group	*C*2/*m* (No. 12)	*C*2/*m* (No. 12)	*C*2/*m* (No. 12)	*C*2/*m* (No. 12)
a (Å)	15.6651(9)	15.612(3)	15.550(4)	15.526(5)
b (Å)	4.2639(2)	4.2519(9)	4.2349(12)	4.2254(14)
c (Å)	6.9895(4)	6.9641(15)	6.9425(19)	6.916(2)
β (°)	106.672(1)	106.728(3)	106.842(4)	106.850(4)
V (Å^3)	447.23(4)	442.73(16)	437.6(2)	434.2(2)
Z	2	2	2	2
T (K)	173(2)	173(2)	173(2)	173(2)
ρ_{calcd} (g cm^{-3})	9.230	9.432	9.617	9.762
crystal dimensions (mm)	0.14 × 0.05 × 0.03	0.07 × 0.03 × 0.03	0.10 × 0.03 × 0.02	0.13 × 0.02 × 0.02
μ(Mo $K\alpha$) (mm^{-1})	50.10	52.42	55.05	57.68
transmission factors	0.035–0.337	0.084–0.430	0.040–0.410	0.098–0.559
2θ limits	5.43–66.35°	5.45–66.18°	5.47–66.33°	5.48–66.34°
data collected	$-23 \le h \le 23$,	$-23 \le h \le 23$,	$-23 \le h \le 23$,	$-23 \le h \le 23$,
	$-6 \le k \le 6$,	$-6 \le k \le 6$,	$-6 \le k \le 6$,	$-6 \le k \le 6$,
	$-10 \le l \le 10$	$-10 \le l \le 10$	$-10 \le l \le 10$	$-10 \le l \le 10$
no. of data collected	3193	3134	3120	3164
no. of unique data, including $F_o^2 < 0$	944 (R_{int} = 0.026)	928 (R_{int} = 0.041)	930 (R_{int} = 0.034)	923 (R_{int} = 0.050)
no. of unique data, with $F_o^2 > 2\sigma(F_o^2)$	894	815	842	758
no. of variables	37	37	37	37
$R(F)$ for $F_o^2 > 2\sigma(F_o^2)$ [a]	0.019	0.024	0.023	0.030
$R_w(F_o^2)$ [b]	0.043	0.051	0.054	0.069
goodness of fit	1.10	1.06	1.07	1.04
$(\Delta\rho)_{max}$, $(\Delta\rho)_{min}$ (e Å^{-3})	1.84, –1.66	1.99, –2.68	2.16, –2.42	3.02, –2.68

[a] $R(F) = \sum||F_o| - |F_c|| / \sum|F_o|$. [b] $R_w(F_o^2) = [\sum[w(F_o^2 - F_c^2)^2] / \sum wF_o^4]^{1/2}$; $w^{-1} = [\sigma^2(F_o^2) + (Ap)^2 + Bp]$, where $p = [\max(F_o^2,0) + 2F_c^2] / 3$.

Table A6-4 Crystallographic Data for $Sm_4Rh_2InGe_4$ and $Tb_4RhInGe_4$

formula	$Sm_4Rh_2In_{0.973(3)}Ge_4$	$Tb_4RhInGe_4$
formula mass (amu)	1212.40	1143.77
space group	*C*2/*m* (No. 12)	*C*2/*m* (No. 12)
a (Å)	15.857(3)	20.2575(12)
b (Å)	4.3147(8)	4.2641(3)
c (Å)	7.0971(14)	10.2434(6)
β (°)	106.878(3)	104.9984(9)
V (Å^3)	464.65(16)	854.68(9)
Z	2	4
T (K)	173(2)	296(2)
ρ_{calcd} (g cm^{-3})	8.666	8.889
crystal dimensions (mm)	0.10 × 0.02 × 0.01	0.08 × 0.06 × 0.04
μ(Mo *K*α) (mm^{-1})	43.36	50.89
transmission factors	0.095–0.677	0.115–0.262
2θ limits	5.37–66.47°	4.12–66.23°
data collected	$-24 \le h \le 23$,	$-30 \le h \le 30$,
	$-6 \le k \le 6$,	$-6 \le k \le 6$,
	$-10 \le l \le 10$	$-15 \le l \le 15$
no. of data collected	3381	6268
no. of unique data, including $F_o^2 < 0$	977 (R_{int} = 0.032)	1802 (R_{int} = 0.035)
no. of unique data, with $F_o^2 > 2\sigma(F_o^2)$	852	1539
no. of variables	37	64
$R(F)$ for $F_o^2 > 2\sigma(F_o^2)$ [a]	0.020	0.024
$R_w(F_o^2)$ [b]	0.039	0.058
goodness of fit	1.02	1.04
$(\Delta\rho)_{max}$, $(\Delta\rho)_{min}$ (e Å^{-3})	1.66, –1.75	3.03, –1.81

[a] $R(F) = \sum||F_o| - |F_c|| / \sum|F_o|$. [b] $R_w(F_o^2) = [\sum[w(F_o^2 - F_c^2)^2] / \sum wF_o^4]^{1/2}$; $w^{-1} = [\sigma^2(F_o^2) + (Ap)^2 + Bp]$, where $p = [\max(F_o^2,0) + 2F_c^2] / 3$.

Table A6-5 Atomic Coordinates and Equivalent Isotropic Displacement Parameters (Å^2) [a] for $RE_4Fe_2InGe_4$ (*RE* = Ce–Nd, Sm, Gd)

	$Ce_4Fe_2InGe_4$	$Pr_4Fe_2InGe_4$	$Nd_4Fe_2InGe_4$	$Sm_4Fe_2InGe_4$	$Gd_4Fe_2InGe_4$
*RE*1 in 4*i* (*x*, 0, *z*)					
x	0.34776(2)	0.34777(2)	0.34754(2)	0.34772(2)	0.34742(4)
z	0.06007(4)	0.06093(4)	0.06215(4)	0.06255(4)	0.06412(8)
U_{eq}	0.00763(7)	0.00669(8)	0.00712(7)	0.00629(8)	0.00805(14)
*RE*2 in 4*i* (*x*, 0, *z*)					
x	0.58847(2)	0.58812(2)	0.58823(2)	0.58798(2)	0.58795(4)
z	0.37604(4)	0.37653(4)	0.37846(4)	0.37920(4)	0.38067(8)
U_{eq}	0.00721(7)	0.00636(8)	0.00687(7)	0.00596(8)	0.00781(14)
Fe in 4*i* (*x*, 0, *z*)					
x	0.21673(4)	0.21719(5)	0.21763(4)	0.21844(6)	0.21885(11)
z	0.62609(10)	0.62709(11)	0.62762(10)	0.62850(13)	0.6287(2)
U_{eq}	0.00811(13)	0.00670(16)	0.00743(14)	0.00617(16)	0.0086(3)
In in 2*a* (0, 0, 0)					
occupancy	0.969(2)	0.974(3)	0.987(2)	0.964(3)	0.983(5)
U_{eq}	0.00945(15)	0.00862(17)	0.00872(15)	0.00754(18)	0.0095(3)
Ge1 in 4*i* (*x*, 0, *z*)					
x	0.06576(3)	0.06585(4)	0.06590(3)	0.06620(4)	0.06630(8)
z	0.65284(7)	0.65361(8)	0.65421(7)	0.65557(9)	0.65600(17)
U_{eq}	0.00759(10)	0.00653(12)	0.00701(11)	0.00613(13)	0.0078(2)
Ge2 in 4*i* (*x*, 0, *z*)					
x	0.21179(3)	0.21072(4)	0.20913(3)	0.20748(4)	0.20590(8)
z	0.27952(7)	0.27811(9)	0.27565(7)	0.27217(10)	0.26973(18)
U_{eq}	0.00833(11)	0.00749(13)	0.00746(11)	0.00672(13)	0.0086(2)

[a] U_{eq} is defined as one-third of the trace of the orthogonalized U_{ij} tensor.

Table A6-6 Atomic Coordinates and Equivalent Isotropic Displacement Parameters (Å^2) [a] for $RE_4Co_2InGe_4$ (*RE* = Ce–Nd, Sm, Gd)

	$Ce_4Co_2InGe_4$	$Pr_4Co_2InGe_4$	$Nd_4Co_2InGe_4$	$Sm_4Co_2InGe_4$	$Gd_4Co_2InGe_4$
*RE*1 in 4*i* (*x*, 0, *z*)					
x	0.34577(2)	0.34602(2)	0.34651(2)	0.34636(2)	0.34635(3)
z	0.05737(5)	0.05798(3)	0.05893(4)	0.05959(3)	0.06106(6)
U_{eq}	0.00826(9)	0.00622(6)	0.00722(7)	0.00607(6)	0.00665(11)
*RE*2 in 4*i* (*x*, 0, *z*)					
x	0.58910(2)	0.58903(2)	0.58883(2)	0.58881(2)	0.58893(3)
z	0.37952(5)	0.38071(3)	0.38109(4)	0.38273(3)	0.38421(6)
U_{eq}	0.00767(9)	0.00559(6)	0.00647(7)	0.00549(6)	0.00631(11)
Co in 4*i* (*x*, 0, *z*)					
x	0.21787(6)	0.21840(4)	0.21867(5)	0.21945(4)	0.21972(8)
z	0.62480(12)	0.62559(9)	0.62575(10)	0.62585(9)	0.62681(16)
U_{eq}	0.00931(17)	0.00706(11)	0.00773(14)	0.00655(12)	0.0070(2)
In in 2*a* (0, 0, 0)					
occupancy	0.986(3)	0.985(2)	0.965(2)	0.973(2)	0.970(4)
U_{eq}	0.01026(19)	0.00807(13)	0.00910(16)	0.00742(14)	0.0078(2)
Ge1 in 4*i* (*x*, 0, *z*)					
x	0.06687(4)	0.06678(13)	0.06685(4)	0.06703(3)	0.06698(6)
z	0.65461(9)	0.65517(6)	0.65580(8)	0.65687(7)	0.65795(13)
U_{eq}	0.00836(14)	0.00621(9)	0.00696(11)	0.00595(10)	0.00688(18)
Ge2 in 4*i* (*x*, 0, *z*)					
x	0.21158(4)	0.21054(3)	0.20966(4)	0.20766(3)	0.20596(6)
z	0.28021(9)	0.27877(7)	0.27642(8)	0.27226(7)	0.26912(13)
U_{eq}	0.00867(14)	0.00636(9)	0.00715(11)	0.00609(10)	0.00716(18)

[a] U_{eq} is defined as one-third of the trace of the orthogonalized U_{ij} tensor.

Table A6-7 Atomic Coordinates and Equivalent Isotropic Displacement Parameters (Å^2) [a] for $RE_4Ru_2InGe_4$ (*RE* = Ce–Nd, Sm, Gd–Er)

	$Ce_4Ru_2InGe_4$	$Pr_4Ru_2InGe_4$	$Nd_4Ru_2InGe_4$	$Sm_4Ru_2InGe_4$	$Gd_4Ru_2InGe_4$
*RE*1 in 4*i* (*x*, 0, *z*)					
x	0.34953(2)	0.34947(4)	0.34959(3)	0.34901(2)	0.34881(3)
z	0.06118(5)	0.06241(9)	0.06348(6)	0.06477(5)	0.06621(6)
U_{eq}	0.00783(9)	0.00806(15)	0.00763(10)	0.00638(9)	0.00692(10)
*RE*2 in 4*i* (*x*, 0, *z*)					
x	0.58842(2)	0.58830(4)	0.58818(3)	0.58809(2)	0.58772(3)
z	0.37852(5)	0.38007(9)	0.38076(6)	0.38265(5)	0.38302(6)
U_{eq}	0.00739(9)	0.00748(15)	0.00719(10)	0.00604(9)	0.00642(10)
Ru in 4*i* (*x*, 0, *z*)					
x	0.21781(3)	0.21833(5)	0.21848(4)	0.21920(3)	0.21954(4)
z	0.62602(7)	0.62714(13)	0.62778(9)	0.62921(8)	0.63040(9)
U_{eq}	0.00745(11)	0.00719(19)	0.00664(13)	0.00540(11)	0.00622(13)
In in 2*a* (0, 0, 0)					
occupancy	0.962(3)	0.959(5)	0.954(3)	0.965(3)	0.962(3)
U_{eq}	0.00931(19)	0.0095(3)	0.0088(2)	0.0082(2)	0.0089(2)
Ge1 in 4*i* (*x*, 0, *z*)					
x	0.06541(4)	0.06523(7)	0.06505(5)	0.06489(5)	0.06471(6)
z	0.65348(10)	0.65444(18)	0.65481(12)	0.65616(11)	0.65732(13)
U_{eq}	0.00776(14)	0.0079(2)	0.00723(16)	0.00613(14)	0.00703(17)
Ge2 in 4*i* (*x*, 0, *z*)					
x	0.21169(4)	0.21014(8)	0.20896(5)	0.20642(5)	0.20446(6)
z	0.27628(10)	0.27471(18)	0.27264(12)	0.26868(11)	0.26595(13)
U_{eq}	0.00821(14)	0.0087(2)	0.00785(16)	0.00675(14)	0.00734(17)

	$Tb_4Ru_2InGe_4$	$Dy_4Ru_2InGe_4$	$Ho_4Ru_2InGe_4$	$Er_4Ru_2InGe_4$
*RE*1 in 4*i* (*x*, 0, *z*)				
x	0.34865(2)	0.34834(2)	0.34818(2)	0.34794(4)
z	0.06664(4)	0.06710(6)	0.06760(5)	0.06828(8)
U_{eq}	0.00661(8)	0.00655(10)	0.00653(10)	0.00911(14)
*RE*2 in 4*i* (*x*, 0, *z*)				
x	0.58726(2)	0.58756(2)	0.58723(2)	0.58744(3)
z	0.38282(4)	0.38425(6)	0.38370(5)	0.38492(8)
U_{eq}	0.00629(8)	0.00610(10)	0.00611(10)	0.00865(14)
Ru in 4*i* (*x*, 0, *z*)				
x	0.22007(3)	0.22032(4)	0.22041(4)	0.22059(6)
z	0.63194(6)	0.63215(10)	0.63283(9)	0.63335(13)
U_{eq}	0.00579(10)	0.00572(13)	0.00762(14)	0.00852(19)
In in 2*a* (0, 0, 0)				
occupancy	0.932(3)	0.961(4)	0.962(4)	0.980(5)
U_{eq}	0.00938(19)	0.0081(2)	0.0080(2)	0.0106(3)
Ge1 in 4*i* (*x*, 0, *z*)				
x	0.06446(4)	0.06451(5)	0.06444(5)	0.06421(8)
z	0.65897(9)	0.65897(14)	0.66003(13)	0.65998(19)
U_{eq}	0.00688(12)	0.00663(17)	0.00689(17)	0.0095(2)
Ge2 in 4*i* (*x*, 0, *z*)				
x	0.20247(4)	0.20184(6)	0.20063(6)	0.19976(9)
z	0.26350(9)	0.26189(14)	0.26062(13)	0.25934(19)
U_{eq}	0.00729(12)	0.00730(17)	0.00796(17)	0.0100(2)

[a] U_{eq} is defined as one-third of the trace of the orthogonalized U_{ij} tensor.

Table A6-8 Atomic Coordinates and Equivalent Isotropic Displacement Parameters (Å^2) [a] for $Sm_4Rh_2InGe_4$ and $Tb_4RhInGe_4$

atom	Wyckoff position	*x*	*y*	*z*	U_{eq} (Å^2) [a]
$Sm_4Rh_2InGe_4$					
Sm1	4*i*	0.34640(2)	0	0.06704(4)	0.00599(8)
Sm2	4*i*	0.58692(2)	0	0.38125(4)	0.00557(8)
Rh	4*i*	0.21977(3)	0	0.62518(7)	0.00583(10)
In [b]	2*a*	0	0	0	0.00730(18)
Ge1	4*i*	0.06472(4)	0	0.65732(9)	0.00574(13)
Ge2	4*i*	0.20301(4)	0	0.26094(9)	0.00617(13)
$Tb_4RhInGe_4$					
Tb1	4*i*	0.27830(2)	0	0.65591(4)	0.00787(9)
Tb2	4*i*	0.37132(2)	0	0.00695(3)	0.00703(9)
Tb3	4*i*	0.37279(2)	0	0.35947(4)	0.00842(9)
Tb4	4*i*	0.54120(2)	0	0.27206(4)	0.00884(9)
Rh	4*i*	0.24058(3)	0	0.10680(6)	0.00787(12)
In1	2*c*	0	0	½	0.01127(15)
In2	2*a*	0	0	0	0.01258(16)
Ge1	4*i*	0.06320(4)	0	0.78519(9)	0.00996(16)
Ge2	4*i*	0.13207(5)	0	0.18953(8)	0.00944(16)
Ge3	4*i*	0.14302(4)	0	0.44998(8)	0.00876(16)
Ge4	4*i*	0.80414(4)	0	0.14907(8)	0.00778(16)

[a] U_{eq} is defined as one-third of the trace of the orthogonalized U_{ij} tensor. [b] Occupancy of 0.973(3).

Table A6-9 Interatomic Distances (Å) in $RE_4Fe_2InGe_4$ (*RE* = Ce–Nd, Sm, Gd)

	$Ce_4Fe_2InGe_4$	$Pr_4Fe_2InGe_4$	$Nd_4Fe_2InGe_4$	$Sm_4Fe_2InGe_4$	$Gd_4Fe_2InGe_4$
*RE*1–Ge1 (×2)	3.0543(6)	3.0311(5)	3.0108(4)	2.9742(7)	2.9445(9)
*RE*1–Ge2	3.0591(8)	3.0459(7)	3.0362(6)	3.0084(9)	2.9867(13)
*RE*1–Ge2 (×2)	3.2200(7)	3.1976(5)	3.1760(4)	3.1294(7)	3.0093(10)
*RE*1–Fe	3.2248(9)	3.2245(9)	3.2053(7)	3.1659(11)	3.1435(18)
*RE*1–In (×2)	3.3951(6)	3.3810(3)	3.3742(3)	3.3404(6)	3.3257(6)
*RE*1–Fe (×2)	3.5205(8)	3.4933(7)	3.4749(6)	3.4409(9)	3.4076(13)
*RE*2–Ge1 (×2)	3.0568(6)	3.0377(5)	3.0213(4)	2.9924(7)	2.9644(9)
*RE*2–Fe	3.1351(11)	3.1244(9)	3.1068(7)	3.0692(11)	3.0479(18)
*RE*2–Ge2 (×2)	3.1558(6)	3.1374(5)	3.1211(4)	3.0887(7)	3.0633(10)
*RE*2–Fe (×2)	3.1780(7)	3.1703(7)	3.1534(5)	3.1329(8)	3.1099(13)
*RE*2–Ge1 (×2)	3.2574(7)	3.2383(5)	3.2238(4)	3.1920(8)	3.1694(10)
*RE*2–Ge2	3.4490(8)	3.4545(7)	3.4511(6)	3.4470(9)	3.4429(14)
*RE*2–In (×2)	3.4591(6)	3.4413(3)	3.4349(3)	3.4048(6)	3.3849(6)
Fe–Ge2 (×2)	2.4612(6)	2.4529(5)	2.4524(4)	2.4392(7)	2.4312(11)
Fe–Ge1	2.4900(10)	2.4852(10)	2.4809(8)	2.4640(12)	2.454(2)
Fe–Ge2	2.4996(10)	2.4944(10)	2.4980(9)	2.4924(12)	2.484(2)
In–Ge1 (×2)	3.0088(8)	2.9854(6)	2.9726(5)	2.9333(8)	2.9099(12)
In–Ge2 (×2)	3.4185(9)	3.3887(7)	3.3412(6)	3.2790(9)	3.2302(13)
Ge1–Ge1	2.5834(10)	2.5803(12)	2.5701(10)	2.5615(13)	2.547(2)

Table A6-10 Interatomic Distances (Å) in $RE_4Co_2InGe_4$ (*RE* = Ce–Nd, Sm, Gd)

	$Ce_4Co_2InGe_4$	$Pr_4Co_2InGe_4$	$Nd_4Co_2InGe_4$	$Sm_4Co_2InGe_4$	$Gd_4Co_2InGe_4$
*RE*1–Ge1 (×2)	3.0426(5)	3.0268(4)	3.0017(4)	2.9680(4)	2.9400(10)
*RE*1–Ge2	3.0454(8)	3.0387(5)	3.0226(6)	2.9965(6)	2.9769(13)
*RE*1–Ge2 (×2)	3.1927(6)	3.1763(4)	3.1514(5)	3.1048(4)	3.0753(11)
*RE*1–Co	3.1876(9)	3.1712(6)	3.1581(8)	3.1217(7)	3.1012(15)
*RE*1–In (×2)	3.3957(3)	3.3822(2)	3.3608(3)	3.3360(2)	3.3209(9)
*RE*1–Co (×2)	3.5304(8)	3.5153(5)	3.4955(6)	3.4674(5)	3.4338(12)
*RE*2–Ge1 (×2)	3.0399(6)	3.0258(4)	3.0090(4)	2.9806(4)	2.9598(10)
*RE*2–Co	3.0855(10)	3.0701(6)	3.0536(8)	3.0168(7)	2.9995(17)
*RE*2–Ge2 (×2)	3.1428(6)	3.1293(4)	3.1136(5)	3.0851(4)	3.0622(10)
*RE*2–Co (×2)	3.1434(7)	3.1364(5)	3.1225(6)	3.0958(5)	3.0776(11)
*RE*2–Ge1 (×2)	3.2508(6)	3.2360(4)	3.2165(5)	3.1878(4)	3.1687(11)
*RE*2–Ge2	3.3859(8)	3.3858(5)	3.3852(6)	3.3785(6)	3.3814(14)
*RE*2–In (×2)	3.4571(3)	3.4499(2)	3.4317(3)	3.4075(3)	3.3924(9)
Co–Ge2 (×2)	2.4439(5)	2.4405(3)	2.4338(4)	2.4262(4)	2.4234(10)
Co–Ge1	2.4800(11)	2.4790(7)	2.4699(9)	2.4586(8)	2.4503(17)
Co–Ge2	2.4734(11)	2.4715(8)	2.4699(9)	2.4656(8)	2.4683(17)
In–Ge1 (×2)	3.0056(7)	2.9870(5)	2.9657(6)	2.9335(5)	2.9044(13)
In–Ge2 (×2)	3.3725(8)	3.3425(6)	3.3075(7)	3.2372(6)	3.1907(14)
Ge1–Ge1	2.5884(13)	2.5810(9)	2.5731(10)	2.5570(9)	2.5493(19)

Table A6-11 Interatomic Distances (Å) in $RE_4Ru_2InGe_4$ (*RE* = Ce–Nd, Sm, Gd–Er)

	$Ce_4Ru_2InGe_4$	$Pr_4Ru_2InGe_4$	$Nd_4Ru_2InGe_4$	$Sm_4Ru_2InGe_4$	$Gd_4Ru_2InGe_4$
*RE*1–Ge1 (×2)	3.0605(7)	3.0360(11)	3.0178(9)	2.9849(6)	2.9536(8)
*RE*1–Ge2	3.0527(10)	3.0441(15)	3.0355(12)	3.0133(9)	2.9990(11)
*RE*1–Ge2 (×2)	3.2230(8)	3.2011(12)	3.1817(10)	3.1380(7)	3.1055(9)
*RE*1–Ru	3.2734(9)	3.2477(13)	3.2331(12)	3.1896(8)	3.1603(10)
*RE*1–In (×2)	3.3929(6)	3.3800(8)	3.3686(9)	3.3533(5)	3.3370(7)
*RE*1–Ru (×2)	3.5311(7)	3.5054(11)	3.4863(10)	3.4472(6)	3.4113(8)
*RE*2–Ge1 (×2)	3.0495(7)	3.0319(12)	3.0198(10)	2.9945(7)	2.9761(8)
*RE*2–Ru	3.1433(9)	3.1249(14)	3.1141(13)	3.0846(8)	3.0685(11)
*RE*2–Ge2 (×2)	3.1838(7)	3.1620(11)	3.1474(10)	3.1158(6)	3.0878(8)
*RE*2–Ru (×2)	3.2085(6)	3.1942(10)	3.1822(9)	3.1596(5)	3.1429(7)
*RE*2–Ge1 (×2)	3.2739(8)	3.2511(11)	3.2336(11)	3.2025(7)	3.1725(9)
*RE*2–Ge2	3.4922(10)	3.4880(16)	3.4890(13)	3.4890(9)	3.4947(12)
*RE*2–In (×2)	3.4867(6)	3.4736(8)	3.4614(9)	3.4389(5)	3.4123(7)
Ru–Ge2 (×2)	2.4792(6)	2.4740(9)	2.4728(9)	2.4685(5)	2.4626(7)
Ru–Ge1	2.5273(10)	2.5243(16)	2.5184(13)	2.5112(9)	2.5029(12)
Ru–Ge2	2.5037(11)	2.5004(17)	2.5042(14)	2.5073(10)	2.5078(13)
In–Ge1 (×2)	2.9789(9)	2.9552(14)	2.9401(12)	2.9051(8)	2.8757(10)
In–Ge2 (×2)	3.4512(10)	3.4039(15)	3.3660(13)	3.2896(9)	3.2324(11)
Ge1–Ge1	2.6063(14)	2.594(2)	2.5796(17)	2.5609(15)	2.5463(18)

	$Tb_4Ru_2InGe_4$	$Dy_4Ru_2InGe_4$	$Ho_4Ru_2InGe_4$	$Er_4Ru_2InGe_4$
*RE*1–Ge1 (×2)	2.9289(4)	2.9182(8)	2.9011(8)	2.8931(11)
*RE*1–Ge2	2.9908(7)	2.9761(11)	2.9735(11)	2.9666(15)
*RE*1–Ge2 (×2)	3.0743(5)	3.0577(9)	3.0413(9)	3.0287(12)
*RE*1–Ru	3.1269(5)	3.1120(9)	3.0956(10)	3.0837(13)
*RE*1–In (×2)	3.3192(2)	3.3138(6)	3.3044(7)	3.3025(8)
*RE*1–Ru (×2)	3.3829(4)	3.3687(7)	3.3514(8)	3.3355(10)
*RE*2–Ge1 (×2)	2.9654(5)	2.9505(8)	2.9468(8)	2.9342(11)
*RE*2–Ru	3.0494(6)	3.0343(9)	3.0263(11)	3.0196(14)
*RE*2–Ge2 (×2)	3.0597(5)	3.0504(8)	3.0324(8)	3.0227(11)
*RE*2–Ru (×2)	3.1348(4)	3.1203(7)	3.1126(7)	3.1032(10)
*RE*2–Ge1 (×2)	3.1433(5)	3.1362(8)	3.1181(9)	3.1112(12)
*RE*2–Ge2	3.5055(6)	3.4955(9)	3.5013(11)	3.5009(14)
*RE*2–In (×2)	3.3874(2)	3.3828(6)	3.3654(7)	3.3612(8)
Ru–Ge2 (×2)	2.4582(4)	2.4545(7)	2.4520(8)	2.4518(10)
Ru–Ge1	2.4985(8)	2.4927(11)	2.4866(12)	2.4876(17)
Ru–Ge2	2.5100(8)	2.5107(13)	2.5123(13)	2.5120(17)
In–Ge1 (×2)	2.8429(6)	2.8341(10)	2.8187(10)	2.8076(14)
In–Ge2 (×2)	3.1781(7)	3.1540(11)	3.1202(11)	3.1001(15)
Ge1–Ge1	2.5380(12)	2.5284(18)	2.5245(17)	2.513(3)

Table A6-12 Interatomic Distances (Å) in $Sm_4Rh_2InGe_4$ and $Tb_4RhInGe_4$

$Sm_4Rh_2InGe_4$			
Sm1–Ge1 (×2)	2.9777(6)	Sm2–Ge1 (×2)	3.1826(7)
Sm1–Ge2	2.9799(8)	Sm2–In (×2)	3.4219(5)
Sm1–Ge2 (×2)	3.1028(7)	Sm2–Ge2	3.554(9)
Sm1–Rh	3.1952(8)	Rh–Ge2 (×2)	2.4964(5)
Sm1–In (×2)	3.3891(5)	Rh–Ge2	2.5207(9)
Sm1–Rh (×2)	3.4434(6)	Rh–Ge1	2.5342(9)
Sm2–Ge1 (×2)	3.0029(6)	In–Ge1 (×2)	2.9013(8)
Sm2–Rh	3.0788(8)	In–Ge2 (×2)	3.2141(8)
Sm2–Ge2 (×2)	3.1119(6)	Ge1–Ge2	2.5569(13)
Sm2–Rh (×2)	3.1577(5)		
$Tb_4RhInGe_4$			
Tb1–Ge4	2.9166(9)	Tb4–Ge1 (×2)	2.9531(7)
Tb1–Ge2 (×2)	2.9768(7)	Tb4–Ge2 (×2)	3.0747(7)
Tb1–Ge3	2.9946(10)	Tb4–Ge3 (×2)	3.1900(7)
Tb1–Ge3 (×2)	3.0261(6)	Tb4–In1 (×2)	3.4209(3)
Tb1–Rh (×2)	3.3288(5)	Tb4–In2 (×2)	3.4358(3)
Tb2–Ge2 (×2)	2.9205(6)	Rh–Ge4 (×2)	2.4703(5)
Tb2–Ge1 (×2)	3.0622(7)	Rh–Ge4	2.5419(10)
Tb2–Rh	3.0761(7)	Rh–Ge2	2.5524(10)
Tb2–Ge4 (×2)	3.0891(6)	Rh–Rh (×2)	3.1481(8)
Tb2–Rh (×2)	3.1105(5)	In1–Ge1 (×2)	2.8701(9)
Tb2–In2 (×2)	3.3826(3)	In1–Ge3 (×2)	3.0700(9)
Tb2–Ge4	3.4498(9)	In2–Ge1 (×2)	2.8177(9)
Tb3–Ge3 (×2)	2.9634(6)	In2–Ge2 (×2)	2.8702(9)
Tb3–Ge1 (×2)	3.0687(7)	Ge1–Ge4	2.5958(12)
Tb3–Ge4 (×2)	3.0940(6)	Ge2–Ge3	2.6192(12)
Tb3–Rh	3.2068(7)		
Tb3–In1 (×2)	3.3673(3)		

Table A6-13 Estimated Fractional Percentages (mol %) of Phases in Arc-melted "$Nd_4M_2InGe_4$" and "$Sm_4M_2InGe_4$" Samples

Sample (nominal composition)	$RE_4M_2InGe_4$	RE_2InGe_2	REM_2Ge_2	REM_xGe_{2-x}	REMGe
$Nd_4Fe_2InGe_4$	73		20	7	
$Nd_4Co_2InGe_4$	91		9		
$Nd_4Ru_2InGe_4$	38	41	21		
$Nd_4Rh_2InGe_4$	42	18	11	29	
$Nd_4Ir_2InGe_4$	46	33	9	12	
$Sm_4Fe_2InGe_4$	100				
$Sm_4Co_2InGe_4$	100				
$Sm_4Ni_2InGe_4$	88			12	
$Sm_4Ru_2InGe_4$	100				
$Sm_4Rh_2InGe_4$	95				5

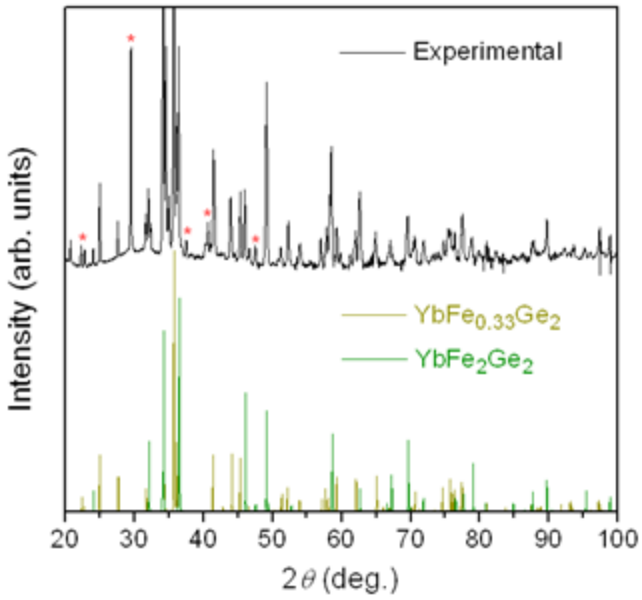

Figure A6-1 Powder XRD pattern for reaction with nominal composition $Yb_4Fe_2InGe_4$ at 800 °C. Unidentified peaks are marked by the red asterisks

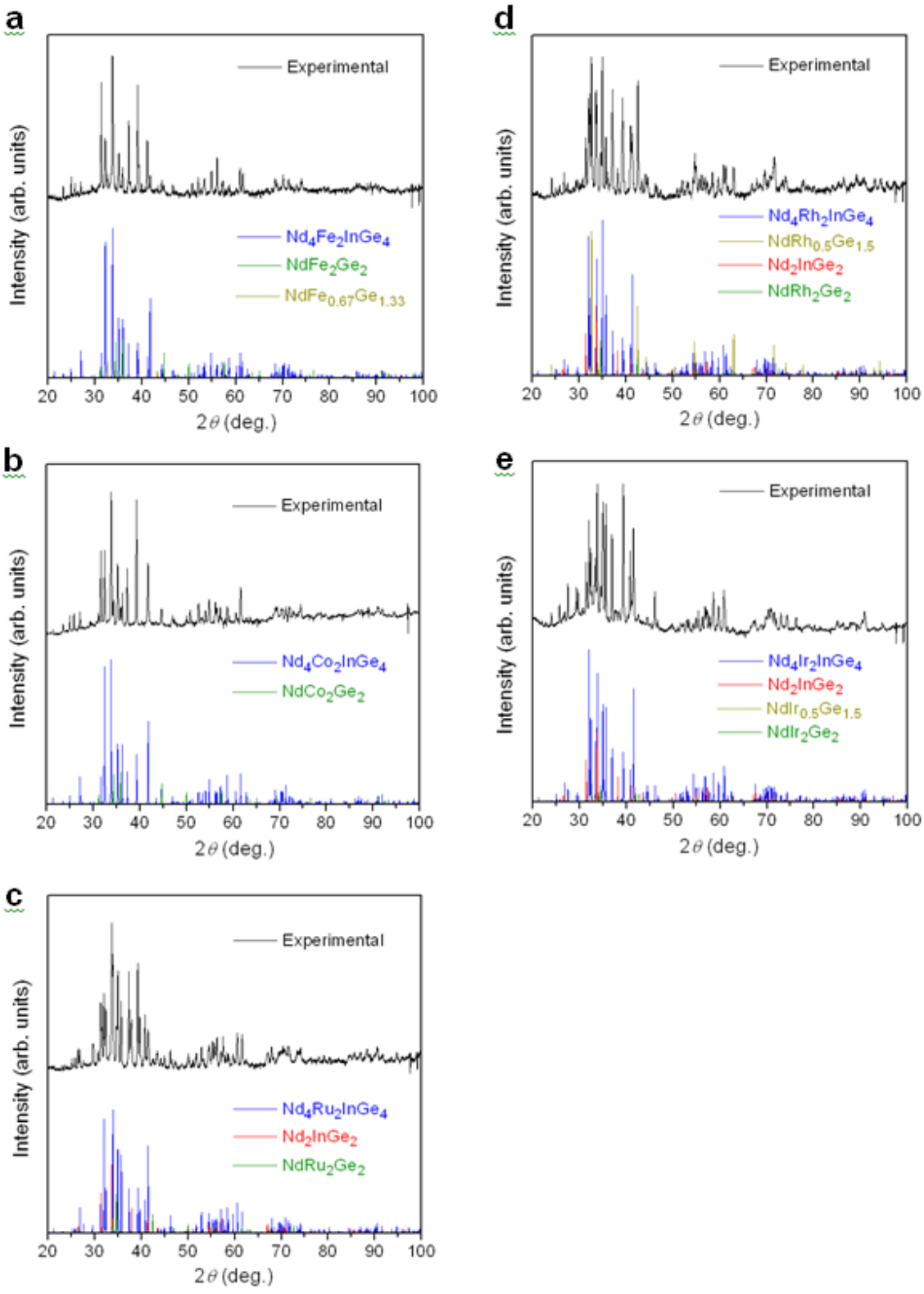

Figure A6-2 Powder XRD patterns for $Nd_4M_2InGe_4$ (M = Fe, Co, Ru, Rh, Ir)

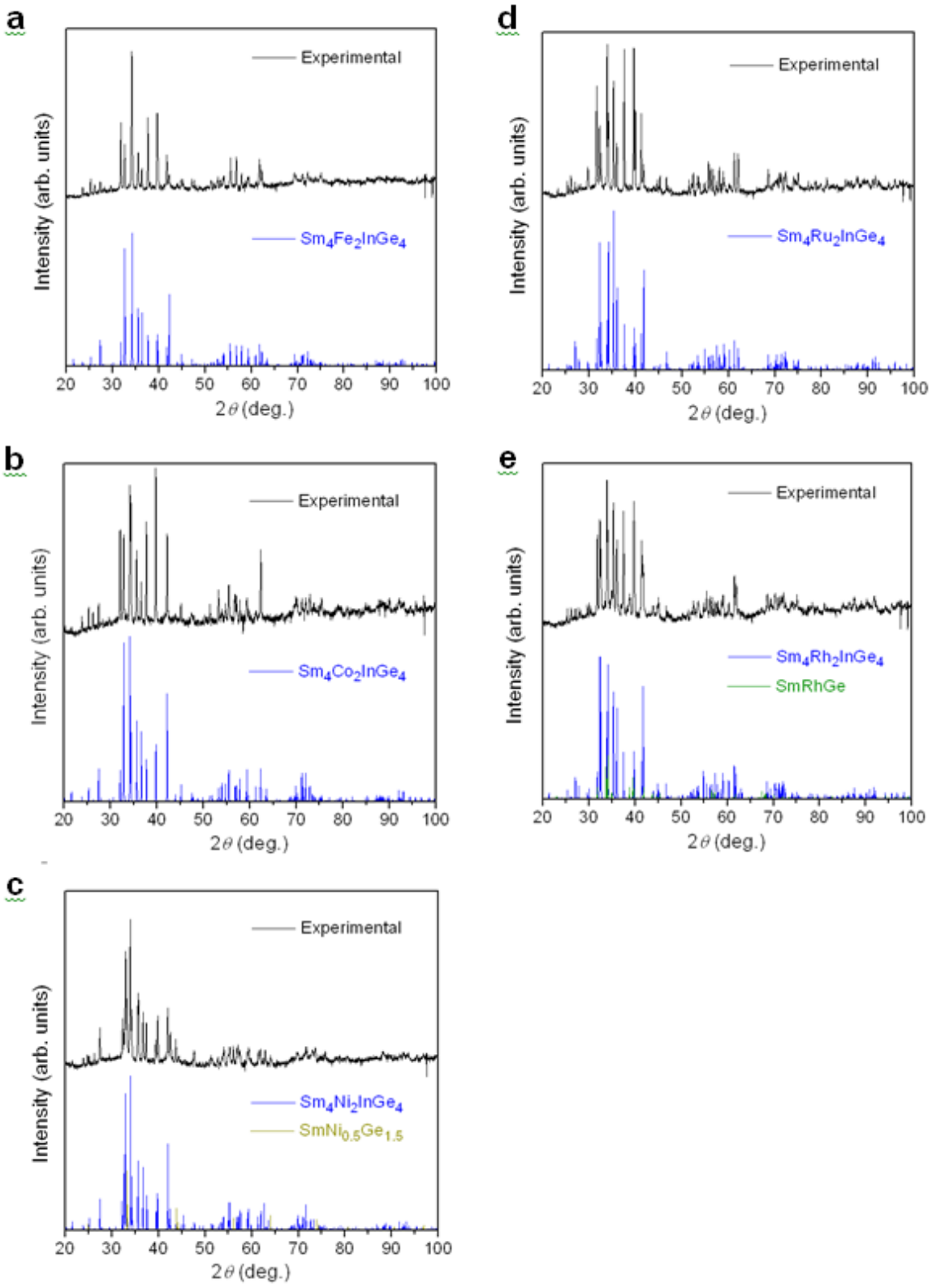

Figure A6-3 Powder XRD patterns for $Sm_4M_2InGe_4$ (M = Fe, Co, Ni, Ru, Rh)

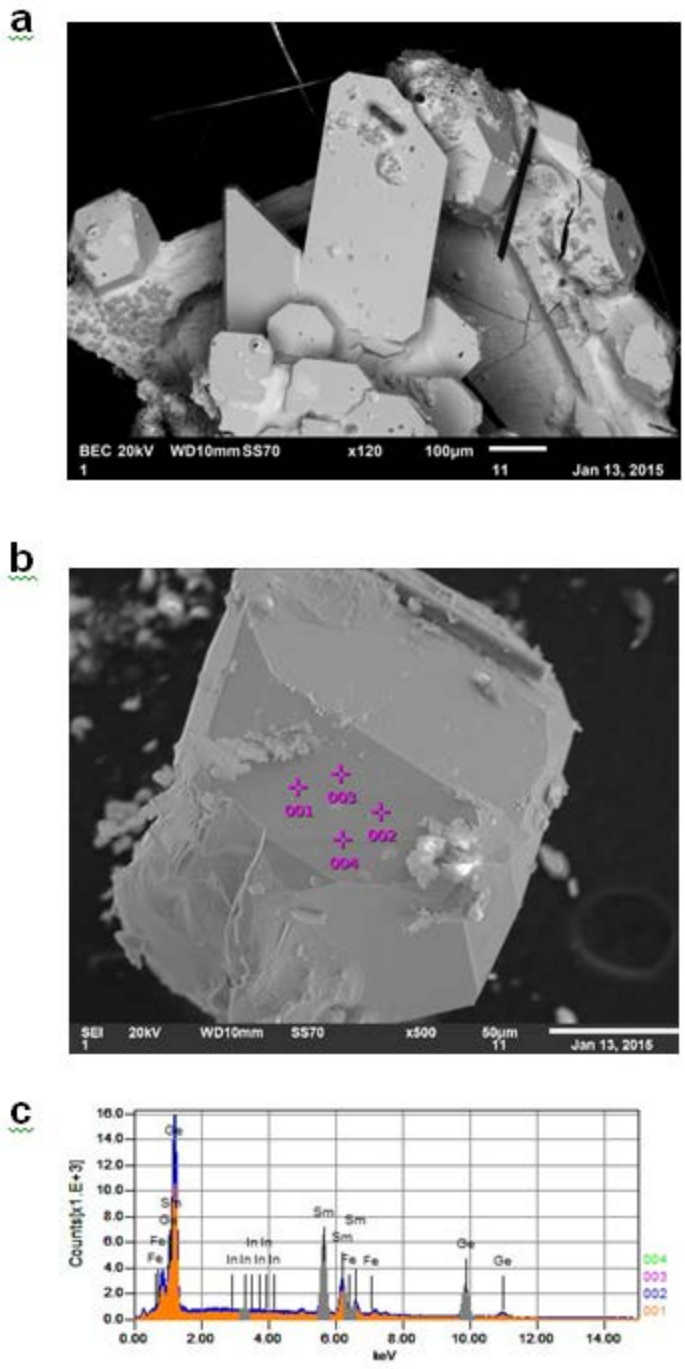

Figure A6-4 (a) Agglomerate of large crystals resulting from reaction with nominal composition "$Sm_4Fe_2In_xGe_4$" in presence of excess In acting as flux. (b) Selected crystal with four points chosen for EDX analysis. (c) EDX spectra revealing that these crystals are Sm_5Ge_3, confirmed by absence of Fe and In peaks.

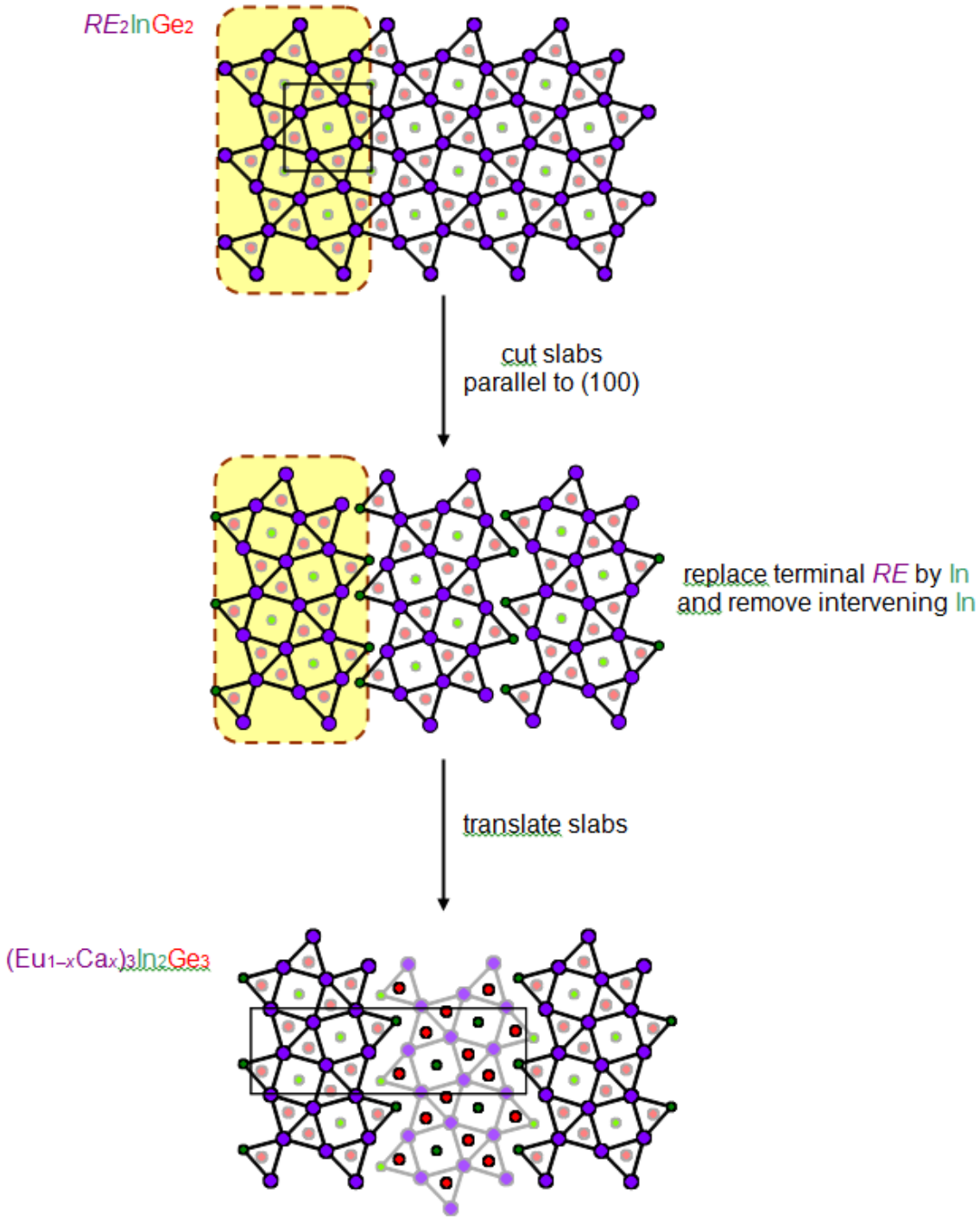

Figure A6-5 Derivation of $(Eu_{1-x}Ca_x)_3In_2Ge_3$ from RE_2InGe_2 following the same procedure to draw structural relationships to $RE_4M_2InGe_4$ and $RE_4RhInGe_4$.